

Optical trapping and manipulation exploiting liquid crystalline systems



Raúl Josué Hernández Hernández

Dipartimento di Fisica

Università della Calabria

A thesis submitted for the degree of

Philosophiæ Doctor (PhD)

Supervisor: Prof. Gabriella Cipparrone

1. Reviewer: Prof. Gino Mariotto

2. Reviewer: Prof. Andrei Th. Ionescu

3. Reviewer: Prof. Karen Volke Sepúlveda

4. Reviewer: Prof. Lorenzo Caputi

Day of the defense: December 7, 2012

Signature from head of PhD committee:

To my family...
my parents María and Marcelo,
my brother Alejandro
and my sister Ivonne.
Also to all the people in Calabria.

Abstract

This thesis and all the research contained within, pretends to develop new ideas and concepts on liquid crystals (LC) and optical trapping and manipulation. The combination between optical tweezers and LC systems promises unique and exciting results.

The content on the thesis is presented for those with some experience in the fields of liquid crystal and optical manipulation, and for those who are interested in begin to learn about these matters, proposing an overview of much existing work and a correlation between different science branches like soft matter, photonics and optical control.

Two main research lines has been developed involving liquid crystalline systems and polarized optical tweezers.

In the first part, nematic LC droplets in water have been adopted to study the mechanical properties of light fields with a polarization gradient, *i.e.* optical tweezers based on polarization holographic techniques with non conventional trapping in an extended interferometric optical trap. For this purpose, LC emulsions in water were prepared, obtaining droplets with radial or bipolar director configuration, which result in optically isotropic or anisotropic particles. Exploiting the vectorial nature of the light and its interaction with LC droplets, an unconventional opto-hydrodynamical control and trapping has been demonstrated. The planned experiments shown that a hydrodynamic force, known as Magnus force, never considered in optical micromanipulation experiments, can play an important role in the optical micromanipulation and should be considered whenever particles are forced to spin and dragged in a fluid.

In the second part, the study was mainly focused into developing an innovative and versatile soft matter object, namely chiral-solid microspheres. They were created by combining very simple self-assembling and photoinduced processes of the soft matter, *i.e.* photopolymerizing cholesteric LC droplets in water emulsion. The ability to control the internal helical geometry using chemical agents in the precursor LC emulsion enables to obtain solid microspheres with radial, conical, or cylindrical configurations of the helical structures that exhibit unique optical properties. Their

exclusive capabilities were demonstrated by optical manipulation experiments involving optical tweezers. A unique and dichotomous behavior has been revealed by polarized circularly polarized tweezers: an attractive or repulsive optical force is exerted by varying the light polarization. Moreover, the application of the chiral-solid microspheres as optical microresonators for creating microlasers was also demonstrated. The high performance as well as the novel and exclusive properties make these chiral microparticles good candidates for developing new concepts in colloidal materials science, microphotonics, microlasers, optical trapping and manipulation, micro- and optofluidics and microsensors.

Abstract

Lo scopo di questa tesi e della ricerca in essa contenuta è quello di generare nuove idee e concetti innovativi sui cristalli liquidi, l'intrappolamento e la manipolazione ottica. Il binomio manipolazione ottica e sistemi liquido-cristallini, infatti, promette risultati unici e affascinanti.

Questo lavoro è rivolto sia a coloro i quali hanno già esperienza nei campi dei cristalli liquidi e della manipolazione ottica, sia a quelli che vogliono acquisire conoscenza in queste materie, proponendo una analisi di gran parte del lavoro esistente ed una correlazione fra diverse branche, quali materia soffice, fotonica e controllo ottico.

La tesi contiene due argomenti di ricerca prevalenti: i sistemi liquido cristallini e le pinze ottiche polarizzate.

Nella prima parte sono state analizzate le proprietà meccaniche dei campi elettromagnetici con un gradiente di polarizzazione usando gocce di cristallo liquido nematico. Si è studiato, così, uno schema non convenzionale di intrappolamento ottico basato su tecniche olografiche di polarizzazione. A questo scopo sono state realizzate emulsioni di cristallo liquido in acqua, ottenendo gocce con configurazione interna radiale o bipolare, che hanno rispettivamente un comportamento ottico isotropo o anisotropo. Sfruttando la natura vettoriale della luce e la sua interazione con le gocce, è stato dimostrato un inaspettato controllo opto-idrodinamico. Gli esperimenti realizzati hanno messo in luce che, una forza idrodinamica, nota come forza Magnus, mai considerata in esperimenti di micromanipolazione, può giocare un ruolo rilevante in questi contesti e dovrebbe essere considerata in caso di particelle mantenute in rotazione e trascinate in un fluido.

Nella seconda parte lo studio è stato focalizzato sullo sviluppo di microparticelle solide chirali di forma sferica. Esse sono state create sfruttando semplici processi di self-assembling e fotoindotti tipici della materia soffice, cioè mediante la fotopolimerizzazione di gocce di cristallo liquido colesterico in ambiente acquoso. La capacità di controllare la geometria supramolecolare interna usando opportuni agenti chimici nelle emulsioni liquido cristalline, permette di ottenere microsferiche con configurazioni radiali, coniche o cilindriche delle strutture elicoidali. Esperimenti di micromanipolazione hanno evidenziato interessanti proprietà ottiche delle particelle. In particolare, l'utilizzo di pinze ottiche polarizzate circolarmente ha evidenziato un originale

e dicotomico comportamento delle microsfele: una forza ottica attrattiva o repulsiva si manifesta sulla particella variando l'elicità della luce. Inoltre il loro utilizzo come microrisonatori ottici ha dimostrato la possibilità di creare microlaser. Le loro elevate prestazioni così come le loro esclusive proprietà, rendono queste micro particelle chirali ottime candidate per lo sviluppo di concetti innovativi nella scienza dei materiali colloidali, in microfotonica e microlaser, manipolazione e intrappolamento ottici, micro e opto fluidica e microsensori.



Contents

1	Introduction	1
1.1	Liquid crystals: introduction and basic concepts	1
1.2	Liquid crystals phases	4
1.3	Physical properties of LC	7
1.4	Alignment and elastic deformations of LCs	9
1.4.1	Elastic constants	10
1.4.2	Liquid crystals in confined volumes: spherical droplets	11
1.5	Optical manipulation: introduction and basic concepts	13
1.5.1	Radiation pressure	13
1.5.2	Light manipulation at microscale: initial techniques	13
1.6	Optical tweezers	15
1.6.1	Ray optics regime ($d \gg \lambda$)	15
1.6.2	Rayleigh regime ($d \ll \lambda$)	19
1.6.2.1	Scattering force	19
1.6.2.2	Gradient force	20
1.7	Experimental optical tweezers	23
1.7.1	Dynamic Optical tweezers	26
1.8	Optical angular momentum (OAM)	27
2	Optical tweezers and micro hydrodynamics on LC droplets	31
2.1	Introduction	31
2.1.1	Navier-Stokes equations	32
2.2	Magnus force in optical manipulation	33
2.2.1	Model and experiment description	34
2.2.2	Trajectories analysis	41
2.2.3	Results and discussions	44
2.3	Optical tweezers and polarization holography	44
2.3.1	Two beams with orthogonal polarizations	45
2.3.2	Experimental description	50
2.3.3	Results and discussions	52

2.4	Conclusions	55
3	Chiral assembled microspheres of LC	57
3.1	Introduction	57
3.2	Chiral liquid crystals	58
3.2.1	Chirality	58
3.2.2	Doping nematic LCs with chiral molecules	59
3.2.3	Selective reflection in CLC	60
3.2.4	Cholesteric pitch and particle size diameter	63
3.3	CLC particles: sample preparation and experimental description	65
3.4	Optical characterization	66
3.5	Conclusions	73
4	Chiral LC microspheres and optical manipulation	75
4.1	Introduction	75
4.1.1	Photonic bandgap in CLC	75
4.1.2	Optical tweezers setup	76
4.2	Experimental results and discussion	77
4.2.1	Dynamics for radial optically isotropic particles	78
4.3	Force simulation for radial isotropic particles	80
4.4	Optically anisotropic particles	88
4.4.1	Rotation of optically non symmetric spheres of CLC	92
4.4.1.1	Fluid particles and trajectories	92
4.4.1.2	Solid particles and trajectories	97
4.5	Conclusions	103
5	Photonic applications of CLC: micro lasers	105
5.1	Introduction	105
5.2	Optical microcavities	106
5.2.1	Circular and spherical Bragg microcavities	108
5.3	Liquid crystal band-edge lasers	109
5.4	Sample preparation and experimental setup	112
5.5	Results and discussion	114
5.6	Conclusions	117
6	General conclusions and prospectives	119
6.1	List of publications	121
6.2	Participation in Conferences	122
	Appendices	125

CONTENTS

A Properties of Liquid Crystals (Table)	125
B Program for optical forces	127
List of Figures	137
Bibliography	141

Part 1

Introduction

1.1 Liquid crystals: introduction and basic concepts

Matter experiences very different states of aggregation: the most commonly known are solid, liquid and gaseous, each of them characterized by its own well defined assembling rules. In the solid phase (like a crystal), each atom is locked into a definite location in the crystal lattice, realizing a highly ordered and strongly anisotropic structure. On the contrary, the liquid phase is very disordered: the atoms can freely move within the liquid without being locked into well-defined positions and thus the liquid is an isotropic phase. Between these two phases, the matter can experience other states of aggregation, states characterized by intermediate properties to which we will refer as soft condensed matter or simply soft matter. Their peculiarity is that they are viscoelastic, this mean that they don't possess the stiffness of the solids nor show the same rheological behavior of the liquids and the level of prevalence among intermediate properties will depend from the specific material. The material of interest in the present thesis will be the liquid crystals.

Liquid crystals (LCs) are a state of matter that has properties between those of a conventional amorphous liquid and those of a solid crystal^[1]. The history of this intermediate state begun in 1888 when was first observed in cholesteryl benzoate, a crystalline solid. It becomes a turbid cloudy liquid, or a LC after being heated to 145 °C; above 179 °C the liquid becomes isotropic and clear. Later, the sequence is reversed when the substance is cooled and color changes occur on both heating and cooling. The cloudy intermediate phase contains domains that seem to have a crystal-like molecular structure.

LCs arise under certain conditions in organic substances having sharply anisotropic molecules, that is, highly elongated (rodlike) molecules or flat (dislike) molecules with orientational and sometimes positional order. As was mentioned before, they represent an equilibrium phase of matter in which the molecules are arranged with a degree of order that falls in between

the complete positional disorder of a liquid and the long-ranged, three dimensional order of a crystal. LCs are very interesting because possess rheological properties analogous to fluids but are birefringent like crystals (with the great difference that the direction of optical axis is not fixed and can vary from point to point within them) and show giant optical nonlinearities. One can figure LCs like fluids possessing extra internal degrees of freedom; for instance, it may flow like a liquid, but their molecules may be oriented in a crystal-like way.

For the sake of simplicity, we will only consider the case of LCs made of rodlike molecules. If we define a unit vector \mathbf{n} known as the molecular director or director, to represent the long axis of each molecule, then the director is the statistical average direction of alignment of the molecules over a small volume element around the point. This vector is defined as:

$$\mathbf{n}(\theta, \phi) = (\sin \theta \cos \phi, \sin \theta \sin \phi, \cos \theta). \quad (1.1)$$

The director \mathbf{n} is bidirectional; $+\mathbf{n}$ and $-\mathbf{n}$ are equivalent. In an homogeneous LC, the director is a constant throughout the medium, while in the inhomogeneous LC the director \mathbf{n} can change from point to point and due to this is a function of space.

The fundamental units or molecules that induces structural order of a LC are called mesogens, they are usually highly anisotropic in shape which gives rise the preferred orientations of nearby molecules. As examples of this molecules, the structure of a small elongated organic molecule: the *p*-azoxyanisole (PAA), is shown in figure 1.1; from a (rough) steric point of view, this is a rigid rod of length $\sim 20 \text{ \AA}$ and width $\sim 5 \text{ \AA}$. Another example of elongated molecule is the *N*-(*p*-methoxybenzylidene)-*p*-butylaniline (MBBA). Both, PAA and MBBA are “nematogens”, *i.e.* it means that they give rise to the nematic type of mesophase.

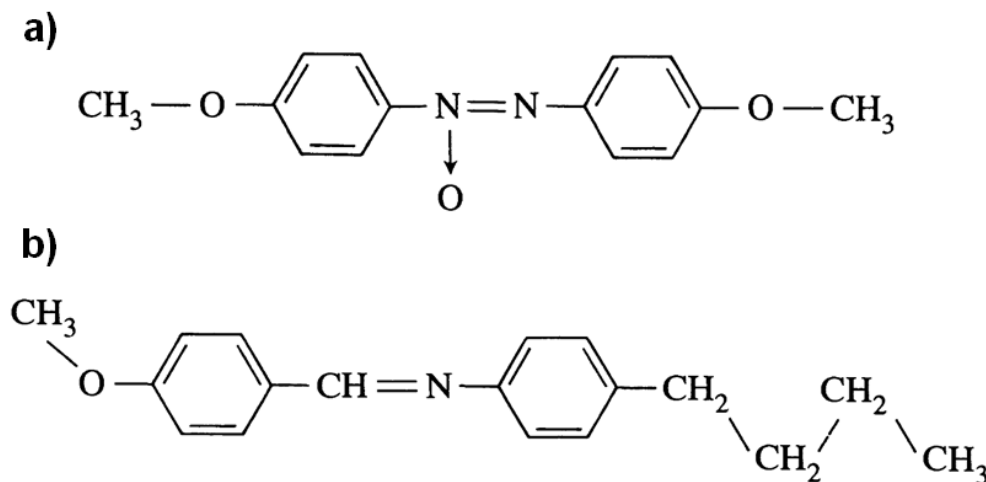


Figure 1.1: Molecular structure of a) PAA and b) MBBA -

Order parameter

From this point, we will take the physical representation or simplification for the long chain molecules as ellipsoids or cylinders. One of the inherent properties of LC is that molecules possess a long-range orientational order, described by the director \mathbf{n} , the extend of this long-range order is described by the order parameter S of a LC defined as

$$S = \frac{1}{2} \langle 3 \cos^2 \theta - 1 \rangle \quad (1.2)$$

where θ is the angle between the long axis of an individual molecule and the director \mathbf{n} and the angular brackets denote statistical average over all molecules. For perfectly parallel alignment, $S = 1$, while for totally random orientations, $S = 0$. In the nematic phase, the order parameter S has an intermediate value that is strongly temperature dependent. It is evident that $S = 0$ at the clearing point. The values of the order parameter S also depend on the structure of the molecules^[1,2]. For an isotropic liquid, averaging molecular orientations gives no result, since there are as many molecules lying along one axis as another. The molecular ordering usually persists only for a fairly narrow temperature range, and is related to the intrinsic molecular shape. The figure 1.2¹, represent the molecular orientation with the temperature.

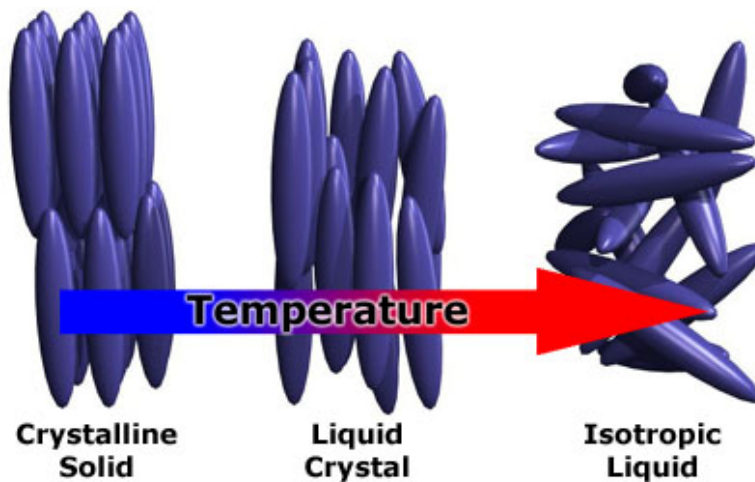


Figure 1.2: Liquid crystal transition - Geometry of molecular orientation with temperature transition.

Generally speaking, there are three phases of liquid crystals, known as nematic phase, smectic phase and cholesteric phase. In the following section, schematics for these phases will be shown.

¹Images reprinted from Barret Research Group^[3]

1.2 Liquid crystals phases

The most disordered type of liquid crystalline is surely the nematic phase, which has no positional order (the centers of mass of the rod-like molecules are arranged like in an isotropic liquid) but in which the molecules are, on the average oriented about a particular direction. Thus the only kind of ordering that survives in such mesophase is the orientational molecular ordering. For illustrative purposes, a scheme representing the mesogens as ellipsoidal rods oriented in roughly the same direction, shows conceptually what order in the nematic phase is like (figure 1.3).

The nematic phase has no positional order but has orientational order. That is, the mesogens all point in the same direction, essentially expressing the molecular anisotropy as a phase anisotropy. A given molecule's orientation is not constant, and all the mesogens do not point in exactly the same direction. In the nematic phase, averaging molecular orientations gives a definite preferred direction, which is referred to as the director. It is important to remember that liquid crystals are liquids, meaning that although there is an average order, molecules are constantly flowing, and moving, changing position and orientation. As we will later see, the different degrees of positional ordering lead to very different optical properties.



Figure 1.3: Liquid crystal in nematic phase - A schematic representing mesogens as ellipsoidal rods, oriented in roughly the same direction, shows conceptually what order in the nematic phase is like

Smectic phases have orientational order, and some degree of positional order. These phases are distinguished by the presence of layers perpendicular to the director. The figure 1.4 shows the chemical structure of a species with several smectic phases. The Smectic A phase has layers oriented at 90 degrees to the director. The Smectic C phase has a director tilted with respect to the layers.

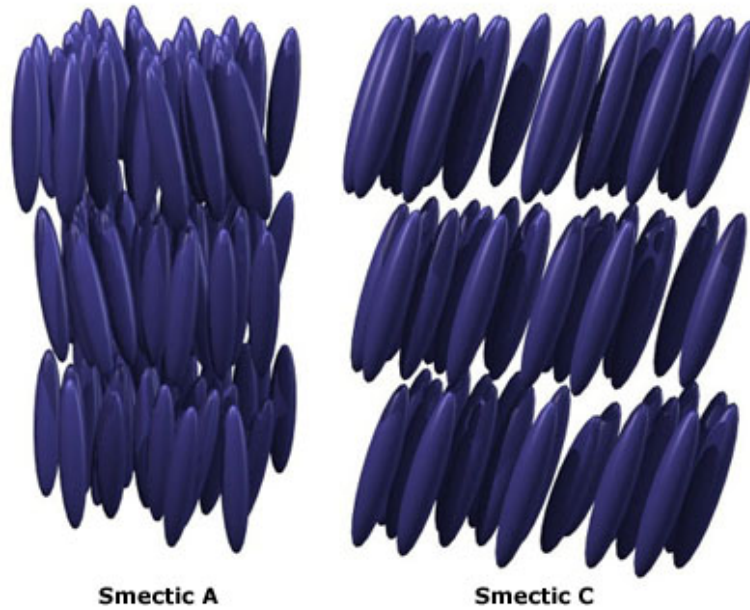


Figure 1.4: Liquid crystal in smectic phase - Representation of molecular orientation

Chiral liquid crystal molecules have the potential to form chiral mesophases¹. Normally, chiral molecules lead to chiral phases, where the director twists as it progresses through the phase. If the molecules of a system in such mesophase are chiral, their centers of mass will be randomly distributed within the fluid but, as a consequence of the microscopical chirality, a structure develops with well defined macroscopic chirality, which leads to the larger-scale twisting of the internal order. The chiral nematic phase is also called the cholesteric phase (since the phase was first discovered in cholesterols).

The structure of the twisting nematic layers is shown below in the figure 1.5. In a) there is a representation of the structure with individual planes (cross-sections) displaying a typical nematic arrangement, but with the lack of axial symmetry due to chirality, the director \mathbf{n} is rotated slightly between adjacent planes, usually forming a helical superstructure with the helical axis χ normal to the directors. This variation of director is usually periodic, and it is known as the “pitch” p being double the period of the angle of the director. The different nematic molecules in b) have been colored differently so as to differentiate their orientation on the layers.

Light circularly polarized with the same handedness as a cholesteric material, traveling parallel to the helical axis will generally experience more matter than light of the opposite handedness would, resulting in very different refractive indices, reflectance and transmittance for light of different circular polarizations^[1,2]. Due to electrodynamic interactions, linearly polarized light will have its plane of polarization rotated when passing along a cholesteric helix, being rotated

¹A brief definition of chirality is given in section 3.2.1, and more details about chiral LC will be presented on future chapters, for the moment is just important to note the structure arrangement of this LC phase

as the director rotates^[2]. More details about this, will be discussed on the following sections. While the cholesteric LCs can be considered as the twisted nematics and the twist can vary in

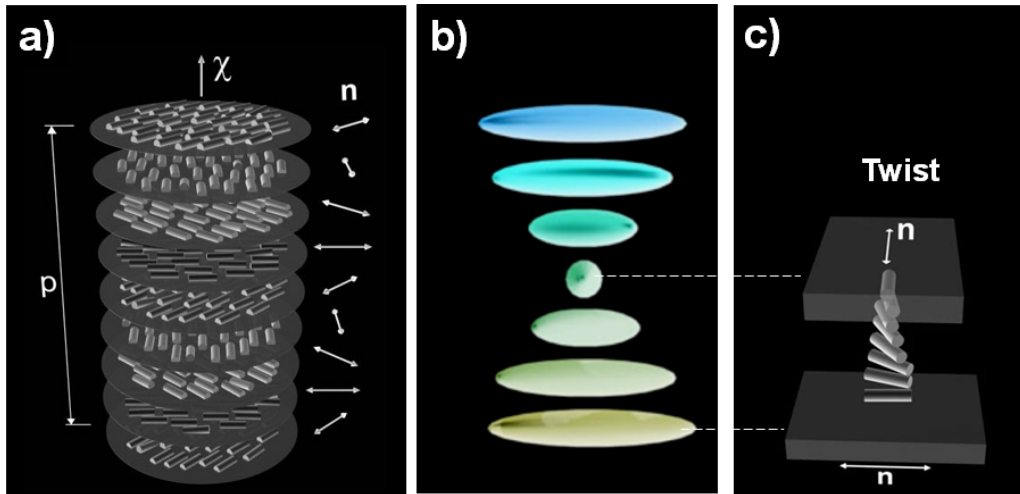


Figure 1.5: Liquid crystal in cholesteric phase - a) Structure of cholesteric liquid crystals p is the pitch; \mathbf{n} is director; ξ is helical axis direction. b) Is a more idealized view of the nematic twisting of the cholesteric phase. c) Show the twist of the nematic director \mathbf{n}

wide range, the complex structure of the cholesterics leads to much more complicated defects and textures than in the nematics. Other liquid crystalline mesophases are more ordered than those described above: smectic and the columnar phases, for example, will possess also a positional ordering. There are many different types of LC phases, but in what follows, we will not pay attention to these other kind of liquid crystals and just will focus on the nematic and cholesteric phases which are distinguished by their different physical properties and in particular, distinct optical properties (see figure 1.6).

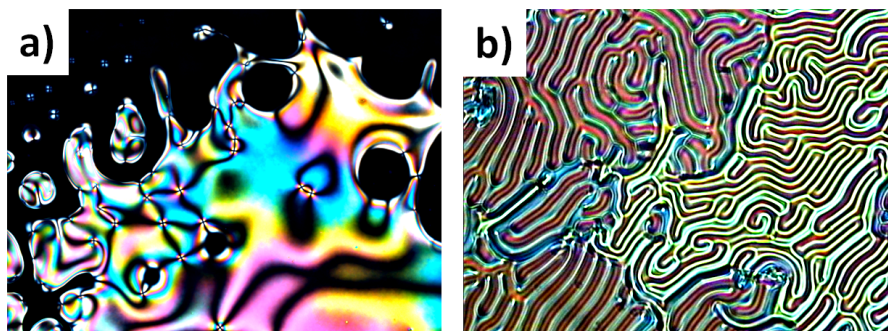


Figure 1.6: Microscope pictures of different textures for different LC phases - a) Nematic liquid crystalline phase of 5CB (35.4°C) showing the Schlieren texture observed between crossed polarizer and analyzer, image reprinted from^[4]; b) Cholesteric phase showing the fingerprint texture.

1.3 Physical properties of LC

Dielectric constants

Because of the orientational ordering of the rodlike molecules, the nematic LCs are uniaxially symmetric, with the axis of symmetry parallel to the axes of the molecules (director \mathbf{n}). As a result of the uniaxial symmetry, the dielectric constants differ in value along the preferred axis (ε_{\parallel}) and perpendicular to this axis (ε_{\perp}). The dielectric anisotropy is defined as:

$$\Delta\varepsilon = \varepsilon_{\parallel} - \varepsilon_{\perp} \quad (1.3)$$

The sign and magnitude of the dielectric anisotropy $\Delta\varepsilon$ are of the utmost importance in the applicability of the LC material in LCDs using one of the various electro-optic effects. For LC with positive dielectric anisotropy ($\varepsilon_{\perp} < \varepsilon_{\parallel}$), lowest electrostatic energy occurs at $\theta = 0$ when the director is parallel to the applied electric field.

Viscosity - Rotational Viscosity

The viscosity of fluid can be understood as the internal resistance to flow, defined as the ratio of shearing stress to the rate of shear. It arises from the intermolecular forces in the fluid. Like most liquids, the viscosity increases at low temperatures as a result of lower molecular kinetic energy. An important parameter is the rotational viscosity coefficient γ_1 , which provides a resistance to the rotational motion of the LC molecules. For most nematic LC, the magnitude of the rotational viscosity is in the range 0.02-0.5 $Pa \cdot s$ (comparable to the light machine oils). As a reference, water at 20°C has a viscosity of 1.002 $mPa \cdot s$. The viscosity unit of $Pa \cdot s$ (Pascal·s) corresponds to 1 $N \cdot s/m^2$ in SI (Systemé International) units, or 10 poise (1 Poise \equiv 1 $dyn \cdot s/cm^2$ in cgs units). In addition, LC with high values of $\Delta\varepsilon$ usually exhibit higher viscosities.

Refractive index

In a glass flask, nematic LCs appears as an opaque milky fluid. The scattering of light is due to random fluctuation of the refractive index of the sample containing many domains of the nematic LC. Such sample exhibits uniaxial optical symmetry with two principal refractive indices n_o and n_e . The ordinary refractive index n_o is for light with electric field polarization perpendicular to the director and the extraordinary refractive index n_e is for light with electric field polarization parallel to the director. The birefringence (or optical anisotropy) is defined as

$$\Delta n = n_e - n_o. \quad (1.4)$$

If $n_o < n_e$, the LC is said to be positive birefringent, whereas if $n_o > n_e$, it is said to be negative birefringent. The existence of the optical anisotropy is due mainly to the anisotropic molecular structures.

For a given sample with a certain thickness and birefringence, when observing it on microscope through crossed polarizers we will see a bright white with several dark patches. The contrasting areas or regions in the photographs on figure 1.7 correspond to domains where the LC molecules are oriented in different directions, the alignment direction is dictated by the external field or confining surfaces. This effect can be seen in the microscope photographs; with the Schlieren brushes which are the distinctive dark cross shapes that appear throughout the images. The center of a cross is in fact a disclination¹ in the LC, the surrounding dark regions occurs where the orientation of the crystals is parallel to either the polarizer or analyzer. A further property of disclinations in nematic LCs is that when one of the polarizers is rotated, the Schlieren brushes appear to rotate themselves (figure 1.7 a-e), *i.e.* every 90° the areas that were the lightest become the darkest and vice versa. On the photos the characteristic brushes (threads) are seen originated and terminated at some points. This points are linear singularities or disclinations. The disclinations with opposite signs can be differentiated by the fact that their brushes appear to rotate in opposite directions.

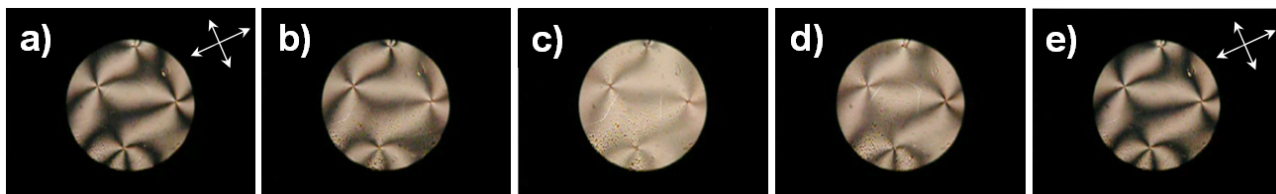


Figure 1.7: Nematic LC observed between polarizer and analyzer - In a) and e) the polarizer and analyzer are always crossed (indicated by the white arrows). Their positions with respect to photos b)-d) differ by a small angle, on c) the polarizer and analyzer are almost parallel.

Within a domain, the molecules are well ordered and when they are not oriented they form defects. The concept of defects came about from crystallography, where defects are disruptions of ideal crystal lattice such as vacancies (point defects) or dislocations (linear defects). In numerous liquid crystalline phases, there is variety of defects and many of them are not observed in the solid crystals.

Chiral nematic LCs also exhibit birefringence, however due to their chirality the manner in which they split light into components is slightly different. When light is traveling along the helical axis of a chiral nematic it does not undergo regular “linear” birefringence. This is because as the director vector \mathbf{n} rotates the two components rotate along with it, and having traveled through one pitch or 360° , the components experience exactly the same overall refractive index.

¹Disclination refers to a discontinuity in the orientation on the molecular director. The discontinuity may be located at one point, on a line, or on a surface and is referred to as a point, line, or sheet disclination^[1]

The result is that one component does not end up traveling faster than the other, so we don't see any optical path difference. However, in a chiral material light can become circularly polarized. In this case, the light does not split into two perpendicular components, but into two components that are constantly rotating in opposite directions.

1.4 Alignment and elastic deformations of LCs

A LC placed in contact with a confining medium (solid, vapor, immiscible liquid), will tend to order in ways that reflect interactions defined by the chemistry and geometry of the interfacial region. This phenomenon is referred to as the anchoring of LCs by interfaces. Since almost any surface causes the director \mathbf{n} orient in a specific direction near the surface. The molecules alignment at surfaces propagates over macroscopic distances. The easiest way (that doesn't needs the action of external fields) is forcing the orientation that interfaces (properly prepared) impose on the layer of LCs with whom they are in contact. In most practical cases surface forces at boundaries are much stronger than bulk elastic forces and their effect is enough to impose a well-defined direction to the director \mathbf{n} at the surfaces. This is the case of strong anchoring. The effect of the anchoring, in this case, will be to impose a given direction to the director at boundaries but has not to be taken into account by adding extra free energy terms to the free energy. In the case of weak anchoring, instead, one has to take into account both bulk and surface terms in the free energy. There are three main types of the LC director \mathbf{n} alignment near to the solid wall or at the free surface. These are planar, homeotropic and tilted orientations (figure 1.8)^[5].

To orient the LC, it is necessary to treat the surface in some way. The surface, which is in a contact with mesophase is usually considered to be flat on the microscopic scale, and the position of the director near it is determined by polar θ and azimuthal ϕ angles (figure 1.8 d). All procedures of solid substrate treatment can be roughly divided into two major groups: mechanical treatment and chemical treatment.

- **Planar alignment** - The director with planar orientation lies in the plane of the surface or phase separation border. In this case two possible orientations exist: one, homogeneous planar orientation, when the director is oriented uniformly over the surface and ϕ is fixed; another, heterogeneous planar orientation, when the orientation of the director is not uniform over the surface and ϕ has different values in different points of the surface. For a free surface any direction in the plane of the surface may be allowed, while for a solid substrate a particular direction in the plane may be imposed by the crystalline structure of the surface. The simplest way to get homogeneous planar orientation of the director is to rub surface with velvet cloth in some defined direction.

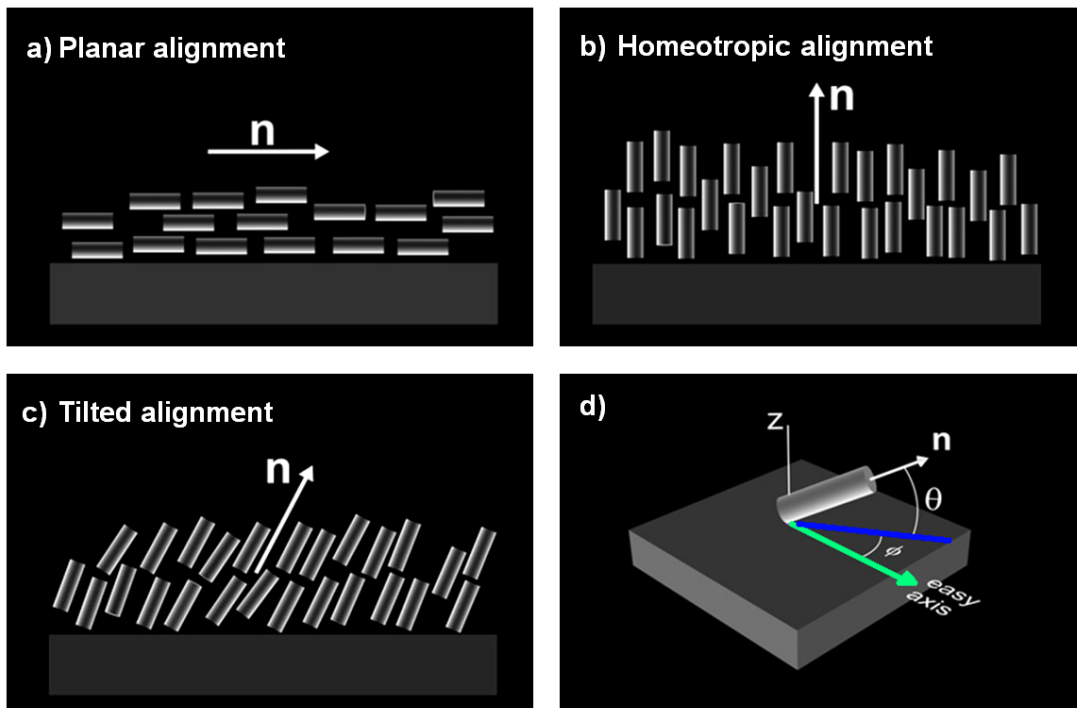


Figure 1.8: Types of liquid crystals orientation near surface - \mathbf{n} is the molecular director. a) Planar alignment; b) homeotropic alignment. c) Tilted alignment, d) Position of director \mathbf{n} in space

- **Homeotropic alignment** - When the director \mathbf{n} is oriented homeotropically, the polar angle $\theta = 90^\circ$. In order to get homeotropic orientation, the substrates can be treated with surfactant, for example like OTS (octa-decyltrichlorosilane) or DMOAP (N, N-Dimethyl-N-octadecyl-3-aminopropyltrimethoxysilyl chloride); which is a cationic alkosylane that induces homeotropic anchoring on the surface of the material.

In case of tilted orientation θ is fixed and ϕ might change. The preferred direction of the director \mathbf{n} at the surfaces set by alignment is called “easy axis”.

1.4.1 Elastic constants

Given that LC possess a tendency for a long-range lineal order, it costs energy to induce curvature in the director field. Following the notation of Oseen-Frank theory^[6,7], the elastic energy density in a planar slab an arbitrary curvature of a director field could be described in terms of three basic deformations: splay, twist and bend (figure 1.9).

The contribution for each deformation to the overall energy density F is given by:

$$F = \frac{1}{2} \left[k_{11} (\nabla \cdot \mathbf{n})^2 + k_{22} (\mathbf{n} \cdot \nabla \times \mathbf{n})^2 + k_{33} (\mathbf{n} \times \nabla \times \mathbf{n})^2 \right] \quad (1.5)$$

The elastic constants k_{11} (splay), k_{22} (twist) and k_{33} (bend) can be measured in various ways and indicate the resistance of a nematic mixture to these various elastic deformations. The

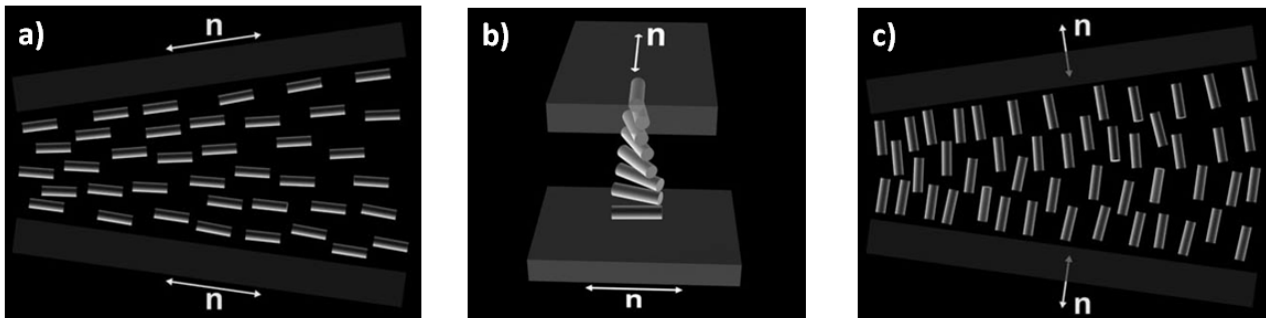


Figure 1.9: Elastic distortions in liquid crystals - Schematic illustrations of the orientations of mesogens experiencing a) splay, b) twist and c) bend deformations.

equation (1.5) is the basis for the theoretical treatment of defects and textures of nematic LCs. For a stable distortions, the solution of the above equation have to yield a relative minimum in the free energy. The confinement of liquid crystals imposed by surface boundary conditions is at the heart of most LC device applications. This confinement can come in the form of boundary conditions enforced by planar substrates or curved boundary conditions. Confined LC systems differ from macroscopic bulk liquid crystals because of their large surface-to-volume ratio.

1.4.2 Liquid crystals in confined volumes: spherical droplets

The configuration of the LC droplets is the focus of much current research. In general, many different configurations have been observed and they also depend on factors such as droplet size and shape, surface anchoring and applied fields. The nematic LC orders inside the droplet according to the boundary conditions and the resulting configuration strongly depends on the delicate interplay between surface and the elastic deformations. To obtain an emulsion of LC is necessary to put a small amount of the LC into pure water and by virtue of its hydrophobicity, a nematic LC droplet naturally acquires a spherical shape with an internal bipolar structure when dispersed in water as shows the figure 1.10 (first column on left)¹. In pure water, the LC molecules align parallel to the water-LC interface and the structure is bipolar. By increasing the surfactant concentration, the surface anchoring of LC molecules gradually changes towards the perpendicular molecular orientation. Starting from a zero concentration of the surfactant in the emulsion (bipolar), the surface anchoring continuously changes form planar to the intermediate states until the completely homeotropic^[9](last column in right) on figure 1.10, influencing the bulk orientation of the LC director in the droplet.

In a bipolar droplet both splay and bend deformations are present; the splay deformation is obviously present near the poles of the droplet where the director field fans out away from the

¹The images correspond to reference^[8] as well as the choice of particular surfactant SDS (Sodium Dodecyl Sulfate; Sigma-Aldrich); however the droplets structures and behavior are general for nematic LCs with surfactants

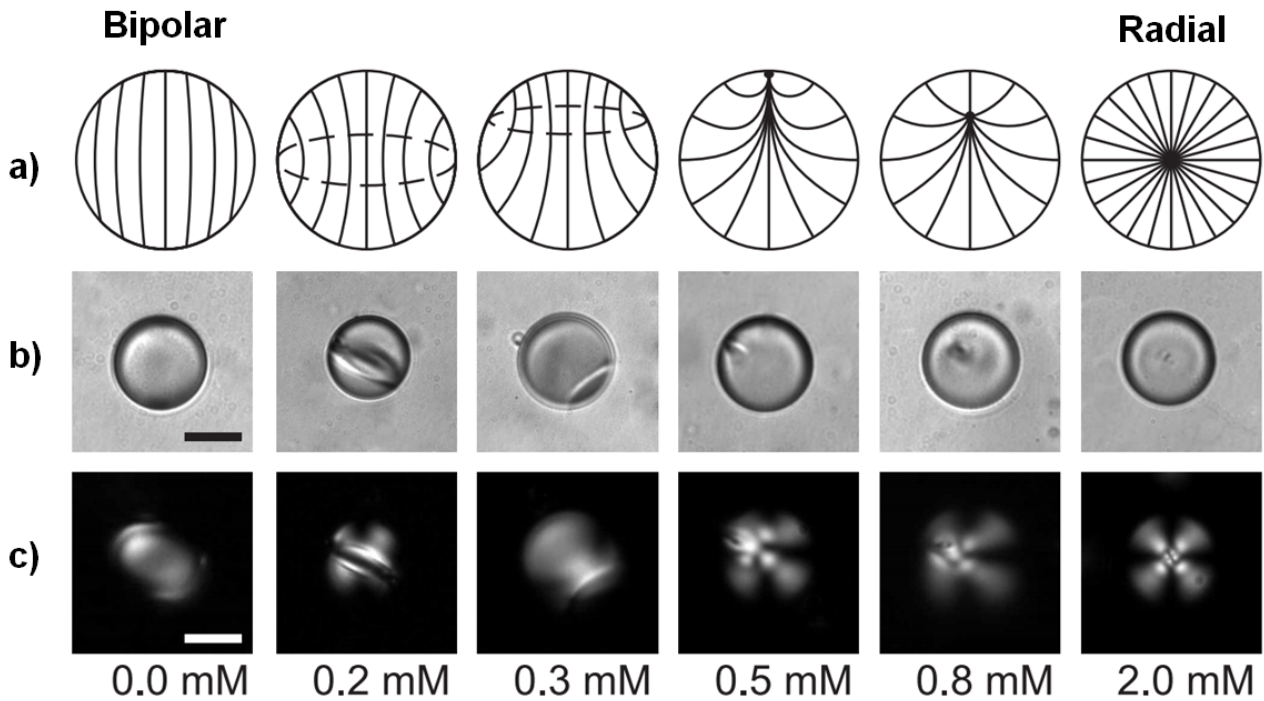


Figure 1.10: Examples of nematic liquid crystals confined to spherical droplets at increasing surfactant concentrations - Row (a) represent the molecular configuration on the droplets; the lines represent the orientation of the long axes of the LC molecules. The dots are point defects, where the orientation is not defined. (b) Non-polarized optical microscope images of $\sim 17 \mu\text{m}$ diameter microdroplets of 5CB in water and SDS. The “inner” ring is observable at 0.2 mM of SDS. The point defect evolves at the surface and sinks into the center at 0.8 mM concentration of SDS. Scale bar $10 \mu\text{m}$. (c) The same images as in (b), taken between crossed polarizers.

defect. The bend deformation dominates along the lines connecting the two poles. In a purely radial droplet, on the other hand, only splay exists. Volovik and Lavrentovich^[10] pointed out that the defects in nematic droplets could be classified as either hedgehogs or boojums. A hedgehog can exist either on the surface of a droplet or in its interior, while boojums can exist only on a surface. The defect inside a radial structure is a hedgehog, while the point defects on the surface of bipolar droplets are boojums. The two types of defects can interconvert, as long as certain topological conservation laws are satisfied. These topological assignments offer a formal method of classification of the defects within nematic droplets. Those readers interested in topological classifications can consult several references on this subject^[10–12].

In chiral materials the presence of a twist in the director field is the lowest energy state, with the pitch determined by the material properties of the nematic. Additional twisting (or untwisting) by an external force requires energy. Chiral materials usually adopt twisted structures in droplets. Depending on the emulsion, the droplets can have a typical diameter distribution varying from 1 to tens of μm , which correspond to the typical sizes of particles for optical manipulation.

1.5 Optical manipulation: introduction and basic concepts

1.5.1 Radiation pressure

The first observations of radiation pressure, *i.e.* the force exerted by electromagnetic radiation on matter, date back to 1609 when German astronomer Johannes Kepler noticed that the tails of comets always point away from the Sun, being blown by what he believed to be a kind of solar breeze. The fact that electromagnetic radiation exerts a pressure upon a surface exposed to it was deduced theoretically by James Clerck Maxwell in 1873^[13], those explanations and treatments have in common the phenomenon of radiation pressure at macro scale. But even before the invention of lasers, there were also observations with elaborate experimental apparatus to prove the existence of radiation pressure qualitatively (Lebedev 1901^[14]; Nichols and Hull 1901^[15]) and quantitatively (Nichols and Hull 1903^[16]). However, it wasn't until years later with the arriving of the laser technology that it was possible to observe the same phenomena and the remarkable features at the micro scale with the use of laser light.

1.5.2 Light manipulation at microscale: initial techniques

In 1969, the first experiment to observe laser radiation pressure was done by Arthur Ashkin from the AT&T Bell Labs in Holmdel, NJ^[17]. On this experiment, Ashkin found that when

the laser beam hits a particle near the edge of the beam, the particle was drawn into the beam axis and proceeded to move to the output glass face of the cell, where it stopped. If the power was turned off and the particles wandered away to the beam position, they were quickly pulled back to the beam axis when the power was turned on again. If one wiggled the beam back and forth as a particle was moving along the beam, the particle followed the beam just guided by the light. The set up is depicted in figure (1.11a), using a greatly diluted solution in water of $2.5 \mu\text{m}$ or at times $10 \mu\text{m}$ diameter latex spheres placed in a glass cell made from microscope slides.

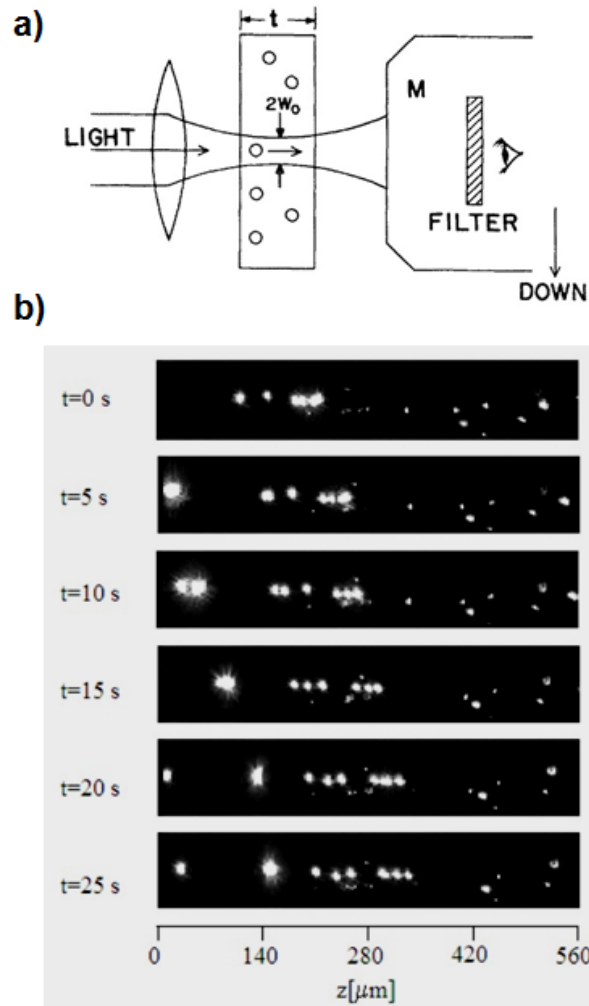


Figure 1.11: Acceleration and trapping of particles by radiation pressure - a) Images taken from the article of Ashkin^[17] with geometry of glass cell, $t = 120 \mu\text{m}$, for observing micron particle motions in a focused laser beam with a microscope M. b) Sequence of microscope images showing the optical acceleration and trapping of particles of latex with diameter of $2 \mu\text{m}$ ^[18], analog to the former image on a)

After, when a modest laser power of a few hundred milliwatts cw was focused on these spheres, they moved along quite rapidly at velocities given by Stokes's law, using low power microscopes viewing from the side along the beam axis. In this case, the relation of refractive indices is

such that ($n_{sphere} > n_{medium}$), so the sphere acts as a focusing lens. If one reverses the relative magnitudes of the index media, the sphere becomes a diverging lens, the sign of the radial deflection forces reverse, and the sphere should be pushed out of the beam. Combining two counter-propagating laser beams (so-called dual beam trap), he demonstrated the possibility of moving and even stable spatial confinement of dielectric particle of high refractive index immersed in a low-refractive index medium. This optical guiding of particles along laser beams was demonstrated in both a liquid and air. Later on in 1971, Ashkin obtained the stable optical levitation in air by trapping a microparticle using only one laser beam, where gravitational forces counteract the radiation pressure^[19,20].

1.6 Optical tweezers

The historically most important insight on these basic traps, was that microscopic transparent particles with an index of refraction higher than the surroundings cannot only be pushed by the radiation pressure, but they can also be moved against the direction light propagation towards the focus of the laser to remain confined, leading to the demonstration of a “single beam gradient force trap” which is nowadays known as optical tweezers^[21–23]. In optical tweezers, a single laser beam is very tightly focused through a high numerical aperture lens and by this means can establish gradient forces counteracting the scattering forces in propagation direction. This simple and elegant implementation of an optical trap enables the stable, three-dimensional optical trapping of dielectric particles. From their original seminal paper, Ashkin and co-workers demonstrated that a focused laser beam could be used to trap, hold and move microscopic dielectric particles in all three dimensions^[23–25]. Based on these fundamental findings, a whole field of optical micromanipulation has developed. On the one hand, optical tweezers have been further developed towards versatile, multifunctional tools by means of time-sharing approaches, holographic beam-shaping, manipulation of viruses and bacterias, and an uncountable number of technological refinements. On the other hand, a wide range of alternative approaches has emerged that go beyond the concept of single or multiple discrete optical tweezers but provide optical landscapes, tailored to a specific problem.

1.6.1 Ray optics regime ($d \gg \lambda$)

Optical tweezers can be qualitatively understood in terms of geometric ray optics. By adopting an approach similar to that of a ray-tracing package used for lens design, the effect of a complete optical beam can be modeled using a bundle of rays, with each individual ray weighted according to its intensity. In the geometric ray optics regime, the size of the particle is much larger than the wavelength of the light, and a single beam can be tracked throughout the particle. This situation is for example given when whole cells, which are microns or tens of microns in size,

are trapped using infrared light while are suspended in solution. The incident laser beam is decomposed into individual rays with appropriate intensity, momentum and direction. These rays propagate in a straight line in uniform, nondispersive media and can be described by geometrical optics. This yields to a good qualitative picture but can also describe optical tweezers quantitatively if the limits of the regime are respected.

With reference to figure 1.12, we consider a spherical-transparent particle of refractive index n_s which is immersed in a medium of refractive index n_m , interacting with a light field that has an inhomogeneous intensity distribution in a plane transverse to the optical axis, such as a collimated Gaussian beam. After that one ray of light travels through the particle, the linear momentum has changed in direction and magnitude (as depicted in figure 1.12a), by the conservation of momentum, the momentum difference is picked up by the particle. Each

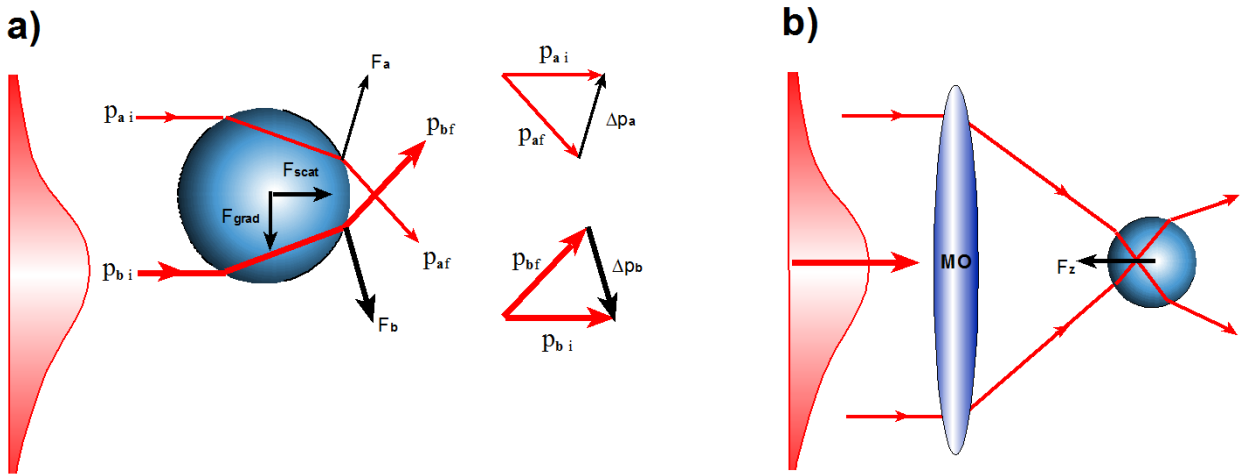


Figure 1.12: Basic principle of optical tweezers in the geometric optics regime - a) A transverse intensity gradient will result in a gradient force \vec{F}_{grad} pointing towards the region of highest intensity. **b)** Strong focusing through a microscope objective (MO) can result in a backward force along the optical axis \vec{F}_z

incoming ray is associated with the linear momentum \vec{p} , for a ray of power P , traveling in a medium with the refractive index n_m , we have the magnitude for each ray equal to:

$$p = \frac{n_m P}{c} \quad (1.6)$$

Tracing two rays \vec{p}_{ai} and \vec{p}_{bi} that are incident symmetrically on the sphere but have different intensities, the rays \vec{p}_a and \vec{p}_b hit the sphere and apart from minor surface reflections that we neglect, both rays are refracted by the sphere as show the figure 1.12a¹. After passing through the sphere, both rays emerges from it to the external medium with linear momentum \vec{p}_{af} and

¹Here we consider $n_s > n_m$. If the ratio of the refractive index of the particle to that of the surrounding medium is not close to one but sufficiently large, diffraction effects can be neglected, which is thoroughly explained in^[26,27] and assumed for further discussion. If we had a low index particle in a high index medium, we expect that the refraction at the interface will reverse.

\vec{p}_{bf} in a different direction than the incident. By conservation of momentum this gives rise to the force \vec{F}_a in the direction of the momentum change. While the ray \vec{p}_b gives rise to a higher force \vec{F}_b . Taking the vector sum of \vec{F}_a with \vec{F}_b and so on for the many other pairs of rays incident on the particle, we get a net force on the sphere directed towards the optical axis where the intensity is high. In the case when both rays are incident symmetric with the same intensity, the net resultant force has only a forward component due to the rotational symmetry of the problem, we call this \vec{F}_{scat} the scattering force, since this arises from the scattering of light momentum. The net force's component perpendicular to the beam propagation is called the gradient force \vec{F}_{grad} , the gradient force's direction is toward the area of highest light intensity; i.e. toward the beam axis in case of Gaussian beam profile, and toward the focus of the laser if the beam is focused. The external rays of a light beam contribute relatively much more to the gradient force, while the central rays contribute more to the scattering force.

Now considering a tightly focused beam as represented in figure 1.12b, as is typical of optical tweezers. The spherical particle acts as a weak positive lens and changes the degree of divergence or convergence of the focused light field. If the angle of the incident rays is high enough, this can result in the axial force \vec{F}_z that point backward if the particle is positioned behind the focus of the rays. By this means, a stable trapping position for the particle is achieved, i.e. in this case the particle will experience a reaction force along the intensity gradient and feels a restoring force like a spring with a mass because at any (small) displacement of the particle will result in a symmetric a restoring force toward the equilibrium position^[21,26]. This symmetry is broken if the particle is not centered exactly on the optical axis of the Gaussian beam as shown in figure (1.13).

From a closer inspection, it becomes obvious that forces are actually applied at discontinuities in refractive indices, *i.e.* at the surface. The net force is due to the combination of all surface forces. For a rigid object, such as a glass bead, the net force is the only force that matters. For a soft object, the forces on the surface become important and lead to a deformation of the object^[28]. This is the basis for the optical tool known as “Optical Stretcher”.

This simple rays optics picture for the forces explains all the observed phenomena by Ashkin. It applies for high index of refraction particles in a surrounding medium of low index of refraction. However, the geometric optics only poorly describes the light field in the vicinity of the focus and furthermore neglects any effects of diffraction and interference^[29,30]. Hence, geometric optics can only describe the limiting regime of particles that are large compared to the wavelength of the light field ($d \gg \lambda$)^[26]. For quantitatively accurate results, as a rule of thumb usually the smallest dimension of the particle should be at least 20 times the optical wavelength^[31].

In the discussion above, we used the momentum changes associated with the reflection and refraction of light to provide a qualitative explanation of the trapping force of optical tweezers.

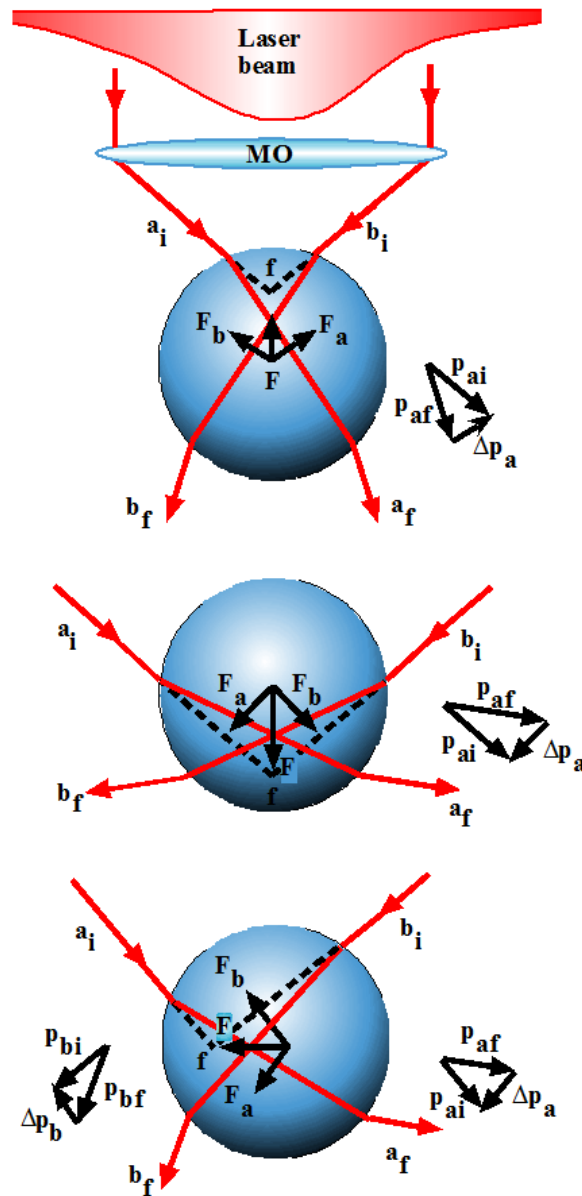


Figure 1.13: Optical tweezers with a rays model - The figure shows three configurations with different incidence angles giving rise to stable optical trap

1.6.2 Rayleigh regime ($d \ll \lambda$)

The alternative model description of optical tweezers is where the radius of the particle is sufficiently smaller than the wavelength of the light ($d \ll \lambda$). The approximation called a dipole or Rayleigh approximation can be applied to describe the behavior of the particle in an electromagnetic wave. Under this condition, the distinction between the components of reflection, refraction and diffraction can be ignored, since the perturbation of the incident wavefront is minimal, the particle or small dielectric sphere can be treated as an induced, simple point dipole and the radiation force exerted on the dipole can be divided into two components: a so-called scattering force component and a gradient force component which are associated with momentum changes of the electromagnetic wave due to the scattering by the dipole and Lorenz force acting on the induced dipole, respectively^[21,26,32].

1.6.2.1 Scattering force

As the electric field oscillates harmonically in time, the induced point dipole follows synchronously the electric field and then, the particle acts as an oscillating electric dipole which radiates secondary or scattered waves in all directions. This scattering event changes both magnitude and direction of the energy flux of the electromagnetic wave. The corresponding momentum transfer also occurs and the scattering force associating with these changes is exerted on the particle. This scattering force is given by^[32,33]:

$$\vec{F}_{scat}(\vec{r}) = \frac{C_{pr}}{c/n_m} \langle \vec{S}(\vec{r}, t) \rangle_T = \hat{z} \left(\frac{n_m}{c} \right) C_{pr} I(\vec{r}), \quad (1.7)$$

where C_{pr} is the cross section for the radiation pressure of the particles, \vec{S} is the Poynting vector and \hat{z} is the unit vector in the beam propagation direction. In the case of small dielectric particles in the Rayleigh regime where the particles scatters the light isotropically, C_{pr} is equal to the scattering cross section C_{scat} and is given by^[34]:

$$C_{pr} = C_{scat} = \frac{8}{3} \pi (kr)^4 r^2 \left(\frac{m^2 - 1}{m^2 + 2} \right)^2. \quad (1.8)$$

By substituting the equation (1.8) into the equation (1.7), the scattering force is given in terms of the intensity distribution of the beam by:

$$\vec{F}_{scat}(\vec{r}) = \hat{z} \left(\frac{n_m}{c} \right) \frac{8}{3} \pi (kr)^4 r^2 \left(\frac{m^2 - 1}{m^2 + 2} \right)^2 I(\vec{r}). \quad (1.9)$$

with the wavenumber $k = 2\pi/\lambda$. If the particle has absorbing properties, an additional force arises which also depends on the intensity but proportional to r^3 rather than r^6 ^[29,35]. This force is in the beam-direction propagation.

The sum of these forces, including the gradient force, can be separated into a transverse component \vec{F}_r and axial component \vec{F}_z as depicted in figure 1.14.

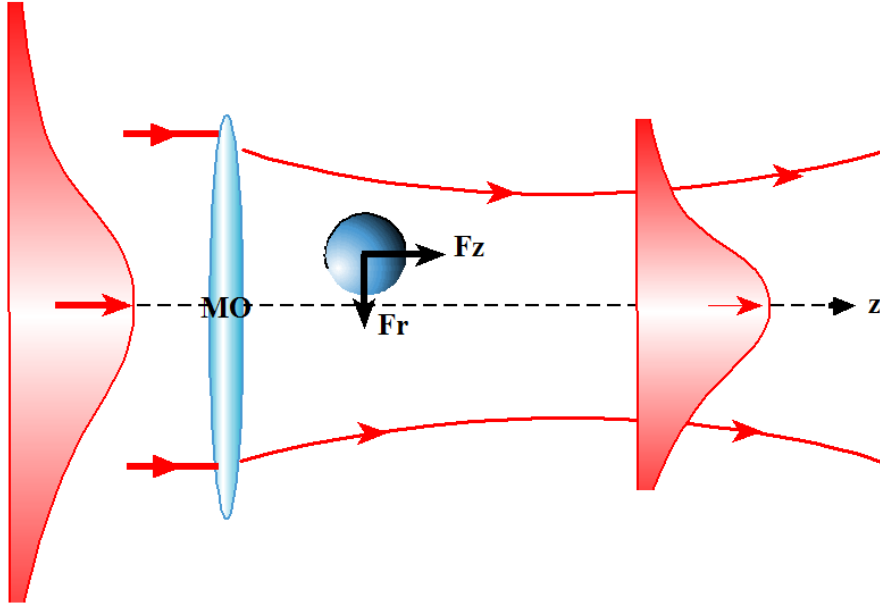


Figure 1.14: Basic principle of optical tweezers in the Rayleigh regime - A particle with refractive index higher than the surrounding medium $n_{sphere} > n_{medium}$ is exposed to a light field- a mildly focused Gaussian beam- then experiences an attractive transverse force \vec{F}_r towards the maximum intensity region (beam focus) and a force along the beam axis \vec{F}_z . The optical forces are in the order of $\sim pN$.

1.6.2.2 Gradient force

In this Rayleigh regime, particles can be seen as infinitesimal induced point dipoles that interact with the light field. The polarizability of the particle gives a measure of induced electric dipole momenta through the linear relationship:

$$\vec{p}(\vec{r}, t) = \alpha \vec{E}(\vec{r}, t). \quad (1.10)$$

Considering a homogeneous isotropic sphere with radius r and refractive index n_s inserted in a medium with refractive index n_m , interacting with an homogeneous electric field \vec{E} . Then its polarizability α is connected with its relative refractive index $m = n_s/n_m$ by the Clausius-Mossotti¹ relation^[36]:

$$\alpha = 4\pi r^3 \varepsilon \frac{m^2 - 1}{m^2 + 2} \quad (1.11)$$

where $\varepsilon = \varepsilon_0 n_m^2$ is the permittivity of medium. The force due to the Lorentz force acting on the dipole, induced by the electromagnetic field $\vec{E}(\vec{r}, t)$ of the laser is:

$$\vec{F}(\vec{r}, t) = \left(\vec{p}(\vec{r}, t) \cdot \nabla \right) \vec{E}(\vec{r}, t) \quad (1.12)$$

from this relationship and using the identity

$$\nabla \vec{E}^2 = 2 \left(\vec{E} \cdot \nabla \right) \vec{E} + 2 \vec{E} \times \left(\nabla \times \vec{E} \right), \quad (1.13)$$

¹It should be correctly named as Lorentz-Lorenz equation (1880) because the refractive index is used

with $\nabla \times \vec{E} = 0$ as a result of the Maxwell's equations. The equation (1.12) becomes

$$\vec{F}(\vec{r}, t) = \frac{1}{2} \alpha \nabla \vec{E}^2(\vec{r}, t) \quad (1.14)$$

The gradient force that the particle experiences in a steady state is the time-averaged version of the electric field and is given by:

$$\langle \vec{E}^2(\vec{r}, t) \rangle_t = \frac{1}{2} |\vec{E}(\vec{r})|^2, \quad (1.15)$$

which yields to

$$\vec{F}_{grad}(\vec{r}) = \langle \vec{F}(\vec{r}, t) \rangle_t = \frac{1}{2} \alpha \nabla \langle \vec{E}^2(\vec{r}, t) \rangle_t = \frac{1}{4} \alpha \nabla |\vec{E}(\vec{r}, t)|^2. \quad (1.16)$$

Furthermore, the light intensity $I(\vec{r})$ or the irradiance at the position $\vec{r} = (x, y, z)$. This is defined as a time-averaged version of the Poynting vector and is given by

$$I(\vec{r}) = \hat{z} \frac{n_m \varepsilon_0 c}{2} |E(\vec{r})|^2, \quad (1.17)$$

where again n_m is the refractive index of the exposed material, ε_0 is the permittivity of free space and c is the speed of light. These results lead to the force equation:

$$\vec{F}_{grad}(\vec{r}) = \frac{1}{2n_m \varepsilon_0 c} \alpha \nabla I(\vec{r}). \quad (1.18)$$

For small particles, this equation is also valid for a time-varying electric field and in this case, replacing α according to equation (1.11), the force can be written in terms of the intensity I of the light field:

$$\vec{F}_{grad}(\vec{r}) = \frac{2\pi n_m r^3}{c} \left(\frac{m^2 - 1}{m^2 + 2} \right) \nabla I(\vec{r}). \quad (1.19)$$

This force obviously depends on the gradient of the intensity and, hence, naturally is called gradient force. For a static field, this expression would give the total force^[31]. In the case of time-varying fields, the oscillating dipole can be considered as an antenna that radiates energy. In contrast to the scattering force of equation (1.9), the gradient force consist of the three rectangular components which act as restoring forces directed towards the beam-waist center in a case of $m > 1$ (high-index particles) and are proportional to r^3 .

With an increasing degree of focusing, the three-dimensional intensity gradients increase, the (axial) gradient force becomes stronger than the scattering force, and three-dimensional trapping can become possible. Comparing the scaling of the gradient force (equation 1.19) and the scattering force (equation 1.9) with the particle radius, one could expect that small particles below a certain threshold can always be trapped. This is not the case because there is an additional force due to the Brownian molecular motion of the particle. The thermal kinetic energy associated with the Brownian motion is $k_B T$, with the Boltzmann's constant k_B and the

temperature T . This energy has to be compared to the depth of the optical trapping potential well, generated by the conservative gradient force¹:

$$U = -\frac{2\pi n_m r^3}{c} \left(\frac{m^2 - 1}{m^2 + 2} \right) I + C, \quad (1.20)$$

where C is an arbitrary integration constant. Furthermore, the drag force (viscous force) due to the dynamic viscosity η , which is $\vec{F}_D = -6\pi\eta r \vec{v}$ for a spherical particle with radius r and thus less efficiently damp the Brownian motion. As illustrated in figure 1.15a, the particle automatically scans or “explores” the shape of the potential well. On figure 1.15b shows the number $N(x)$ that a particle was observed at a particular position x , which gives the probability function $p(x)$. Often, an optical potential induced by optical tweezers can be approximated as harmonic (figure 1.15c). In this approximation, the force that a particle feels is directly proportional to its displacement Δx from the equilibrium position ($x = 0$) and the factor k which is the stiffness of the optical trap; i.e. $|\vec{F}| = k\Delta x$. The force measurement in this configuration means measuring the new equilibrium position and thus Δx as illustrated in figure 1.15d. As the displaced particle still underlies Brownian motion, the measured force always is a superposition of external forces and forces due to Brownian motion.

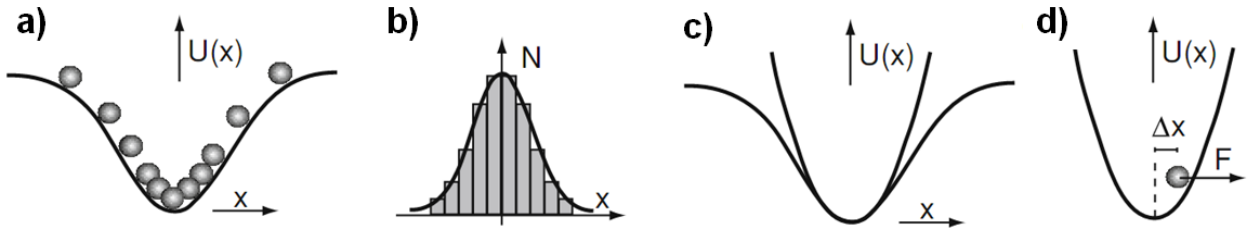


Figure 1.15: Optical potential and force measurement - A trapped particle has a higher probability of presence at the potential minimum a), resulting in an according histogram of positions b). For typical configurations and applications, the potential well can be approximated as harmonic c), resulting in a linear relation between external forces acting on the particle and the particle’s displacement d).^[37]

Both the geometric optical approximation and the Rayleigh approximation allow for an intuitive understanding of the physical principles of optical trapping. The correspondence between the ray tracing treatment and the Lorentz force treatment can be obtained by recalling that the index of refraction difference that produces reflection and refraction can be derived from a model where the dielectric is composed of an array of bound electrons. The electric field due to the light causes the electrons to oscillate around their equilibrium positions. The acceleration due to this oscillation produces a propagating electric field. The total field propagating in the medium is then the sum of the initial electric field and the electric field radiated by all of the

¹The potential energy is derived by integrating the equation (1.19), assuming that the gradient force is conservative.

oscillating electrons. The net result is a phase shift of the field in the medium with respect to the field in free space, corresponding to an index of refraction different from 1^[36]. Thus our initial method calculated the change in the momentum of the light due to the rescattering of the light by the atoms, and then used momentum conservation to calculate the force on the atoms. The second treatment, based on the Lorentz force, directly calculates the force on the atoms resulting from the rescattering. Both approaches and their quantitative validity is restricted for typically trapped particles. For particles in the intermediate regime, in the order of the optical wavelength ($d \approx \lambda$), a more rigorous treatment based on fundamental electromagnetic theory is required for the quantitatively correct description of optical tweezers (see references^[38,39] and appendix B).

1.7 Experimental optical tweezers

In this thesis we shall focus on the use of optical tweezers acting on LC emulsions and particles. There are many excellent review papers that give an overview of optical tweezers, the theory of optical tweezers, their construction, their application, and recent developments. Building a simple optical tweezers system is relatively straightforward. An optical tweezer has as working principle the intensity gradient of the electric field due to the focusing of the laser beam by the microscope objective. Once the gradient force rises along the propagation axis, the beam is capable to counteract the optical scattering force and the other inherent forces on the system such as the particle weight and thermal fluctuations. The dielectric particle is confined in 3D near to the focus beam. To achieve a better focusing in a single spot is necessary to use a high numerical aperture on the microscope ($N.A. \approx 1.2$). On figure 1.16 are depicted the optical elements to build a single optical tweezer and their working principle. The full description of the system and the details for more sophisticated configuration can be founded in references^[40–43]. While in figure 1.18, is shown an example of optical trapping and manipulation of a single micro silica particle using a laser beam fixed.

Some properties of the trapping laser are important to consider: a high power and single mode output, a good pointing stability, and low power fluctuations. Infrared lasers are often used in biological samples, because laser light with a wavelength between 900 and 1200 nm has relatively low absorption and scattering in biological material and therefore, damage to the sample is limited. It is important that the beam hits the back aperture of the microscope objective always with the same diameter and at the same, centered position in order to keep the optical trap operating and its properties unchanged^[26,43].

To create the high intensity gradients required for three-dimensional optical trapping, high NA objectives are needed. Lower NA objectives will confine particles on the optical axis, but they will not trap a particle near the focus. A high transmittance of the trapping laser light is also

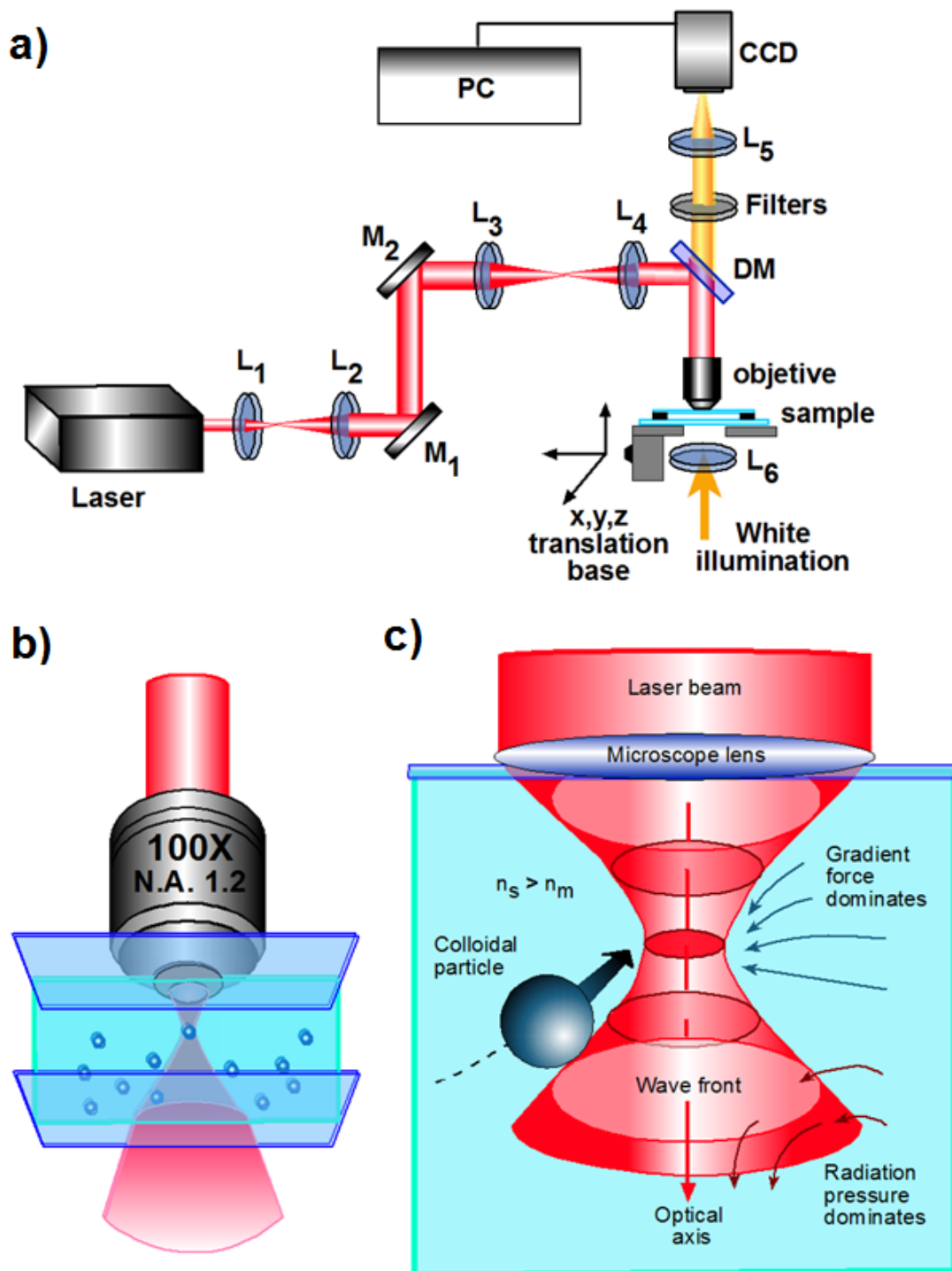


Figure 1.16: Optical tweezers diagram - The image show a diagram of optical tweezers. a) The experimental setup for an inverted optical tweezers. b) A representation of the cell with particles and focusing light. c) A particle with refractive index higher than the surrounding medium $n_{sphere} > n_{medium}$ is attracted towards the maximum intensity region (beam focus).

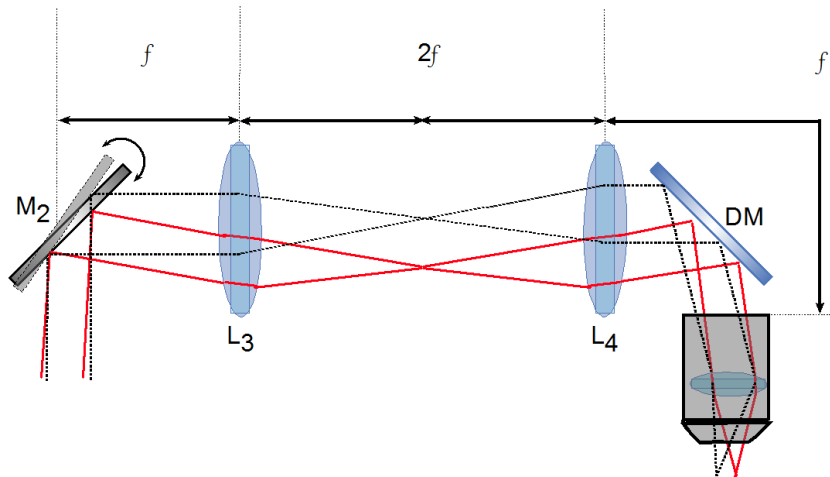


Figure 1.17: Conjugated planes system - Technical realization with a Keplerian telescope (L_3 and L_4 with beam manipulation in the conjugate plane of the microscope objective)

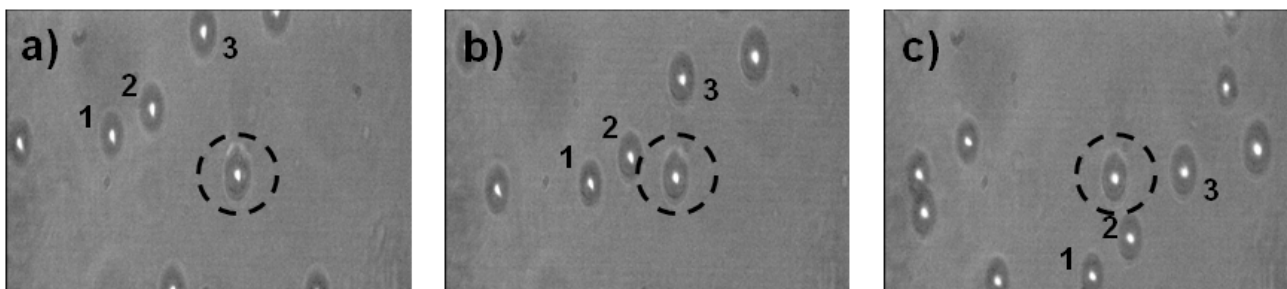


Figure 1.18: Particle trapped with optical tweezers - Sequence of microscope photographs showing a particle of $5 \mu m$ diameter suspended in water and trapped in the focal spot of the laser beam (at the center of the dotted circle). a) The position of the trap is fixed and the particle remains stable in that position, b-c) displacing the sample, in the plane (x, y) orthogonal to the incident beam, a selective control of position with respect to the other particles (labelled as 1,2,3) is achieved.

important. As trapping performance is sensitive to aberrations, especially along the optical axis, often plan apochromat oil immersion lenses are used. These objectives provide excellent optical trapping performance and high-resolution imaging when they are used in samples with a small or no refractive index mismatch between the solvent and the microscope cover slip. In almost all optical tweezers systems, the objective used for trapping is also used for imaging. The laser is coupled into the objective using a dichroic mirror that is chosen so that it reflects the trapping laser and transmits the light used for imaging. When one objective is used for trapping and imaging, the trapping and imaging planes are coupled to each other. The sample generally consist of an emulsion of solid micro particles in water inside a small container closed, usually made of a microscope glass slide and a coverslip with a thin spacer between them.

1.7.1 Dynamic Optical tweezers

Once the particle is confined with the optical tweezer, is possible to control their position in three dimensions inside the sample in two different ways: fixing the spot beam and just moving the sample with an x, y, z precision translator (as shown in figure 1.18) or fixing the sample and move the position of the beam by changing the wavefront and the incidence angle at the rear aperture on the microscope objective (as figures 1.17 and 1.19). If the incident beam is collimated, the focused beam is located at the objective focal plane, in contrast, if the incident beam is slightly divergent or convergent on the back aperture, the focused beam will be located at different planes along the propagation axis. Although single optical tweezers at a fixed position already enable many applications, it is often desirable to have a trap that can be displaced in the sample chamber. This can be achieved by using the mirror M_2 and the rear aperture of the objective when are on the conjugated planes of the telescope formed by the lenses L_3 and L_4 , such that tilting the mirror M_2 the incident angle of the incoming beam varies on the entrance pupil. On this way is possible to control the tweezer position along the axis x, y, z . The mirror DM is a dichroic mirror that only reflects the laser beam and allow to pass the light from the illumination source. Then with the ocular L_5 and the camera CCD is possible to observe the particles inside the sample on real time while their are manipulated.

In figure (1.19a) the basic configuration of optical tweezers is depicted. A collimated laser beam is focused through a lens with short focal length, which usually is a microscope objective, into a sample that contains a fluid with dispersed particles. In order to move the focal spot and thus the optical trap to a different position in the plane orthogonal to the beam axis, the incident laser beam needs to have an angle with respect to the beam axis as shown in figure (1.19b). A diverging or converging beam, on the other hand, would shift the focal plane along the beam axis figure (1.19c). This can be obtained using an afocal telescope of two lenses in order to create an optically conjugated plane of the back aperture of the microscope objective (Figure 1.17).

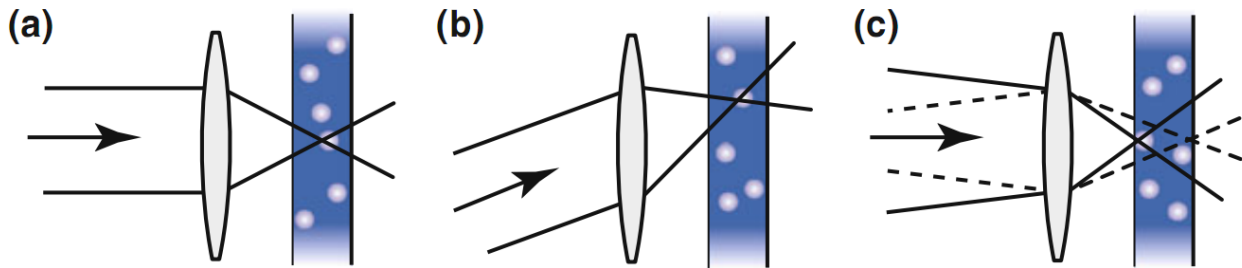


Figure 1.19: Basic principle of position control in optical tweezers - On images a) to c) The position of the laser focus and hence the optical trap is translated three-dimensionally by variation of the incidence angle and divergence of the laser beam. As a result the position of the trap can be controlled

The position control can be automated if computer-controlled scanning mirrors are used^[44–46]. Other powerful application is time-shared optical tweezers, where the laser beam is directed to one position, held there for a short time and then directed to the next position, if this is done iteratively and if the absence of the laser beam is short enough to prevent the particles escaping due to Brownian motion, many particles can be trapped simultaneously^[44,46–48]. One ingenious way to realize control of beam angle and beam divergence in one particular plane without mechanical manipulation is diffraction at computer-generated holograms, also known as diffractive optical elements (DOEs) in this context. The hologram can be imprinted statically in optical materials^[49,50], e.g. by lithographic methods, or alternatively displayed by a computer-controlled spatial light modulator (SLM)^[51,52].

1.8 Optical angular momentum (OAM)

Of particular interest from the fundamental physical point of view is the ability of the light fields to transfer not only linear momentum but also angular momentum to an object by light absorption and refraction. A photon’s angular momentum is determined by its spin angular momentum (SAM) associated with its circular polarization^[53] and by its orbital angular momentum (OAM) associated with the spatial distribution of the wave phase^[54].

Optical angular momentum can be transferred to matter by various physical principles like reflection, absorption, or transmission. The conservation of angular momentum demands that the object acquires this momentum at the expense of the outgoing photon, whose angular momentum is changed/reduced by \hbar ($2\hbar$ upon reflection). Consequently, photons of circular polarization change their state to linear upon transmission, while the particle begins to spin in the direction of the incoming photons. If the light is not (completely) absorbed, the difference between incident and scattered light gives the amount of transferred optical angular momentum. SAM is strongly related to the polarization state of light, where each photon of a circularly

polarized beam carries an angular momentum $\sigma\hbar$, where $\sigma = \pm 1$ for the left- and right-handed polarizations, respectively and the sign is given by the chirality. An experimental proof of this relation was shown in the famous experiment by Beth^[53]. The SAM content of a light wave can be altered by birefringent properties of a particle. If a particle, for example, transforms (a portion of) linearly polarized incident light into circularly polarized light, the SAM of the light wave increases by \hbar per photon and the particle feels the opposite amount of angular momentum in order to conserve the total amount of angular momentum. OAM on the other hand, can be transferred if a particle changes the wave front tilt of the incident light wave, in the case of a screw wavefront dislocation with $\exp(i\ell\phi)$ azimuthal phase dependence, also called an optical vortex, the pitch of the screw defines the topological charge ℓ . The orbital angular momentum is given by $\ell\hbar$ per photon^[55,56]. A direct experimental validation of this relation was done with optical tweezers only quite recently^[57] compared to the experimental proof of spin angular momentum. Both, SAM and OAM decouple in the paraxial approximation^[58,59] but may be transferred into each other in strongly focused beams^[60]. While spin angular momentum always is intrinsic in the sense that its value does not depend on the choice of calculation axis, OAM may be either intrinsic or extrinsic^[61].

In the case of LCs, the bipolar molecular alignment of the nematic liquid crystal intrinsically renders it optically anisotropic, hence birefringent, which is the key optical property that allows light momentum transfer to a micro-object trapped by laser tweezers^[62,63]. During our research, we performed several experiments with bipolar droplets on LC E7 to repeat the observation of droplets rotation due to the transfer of angular momentum, some of the results will be presented on the next chapter. To go beyond, on the following image sequence fixing the position of the laser focus and the sample, through the structure on the nematic CLC droplet (E7 doped with ZLI-811) and the white arrow can be observed from a) to h), the rotation of the CLC droplet immersed in water due to the transfer of angular momentum. The images were taken with a 40x microscope objective lens and the interval time for each frame is about 3 seconds at low power of 30 mW.

The equation of motion that links the torque $\vec{\Gamma}$ of the object with its angular velocity $\vec{\Omega}$ and moment of inertia I is given by

$$\vec{\Gamma} = I \frac{d\vec{\Omega}}{dt} + D\vec{\Omega} \quad (1.21)$$

where D is the damping factor (the drag coefficient for the rotational movement). For a spinning sphere, $D = 8\pi\eta r^3$, where r is the radius and η is the viscosity of the fluid. For a steady state, the time derivative drops out and the terminal angular velocity is proportional to the torque divided by the damping factor. This factor is highly dependent on the object's shape and the properties of the environment in which it moves. Hence, the spinning of the droplet by circularly polarized laser tweezers can be used to measure locally the viscosity of the environment in which it spins. To know the viscosity for a droplet of radius r , the measurement of torque provides a direct determination of the laser-trapping force \vec{F} from $\vec{\Gamma} = \vec{F} \times \vec{r}$.

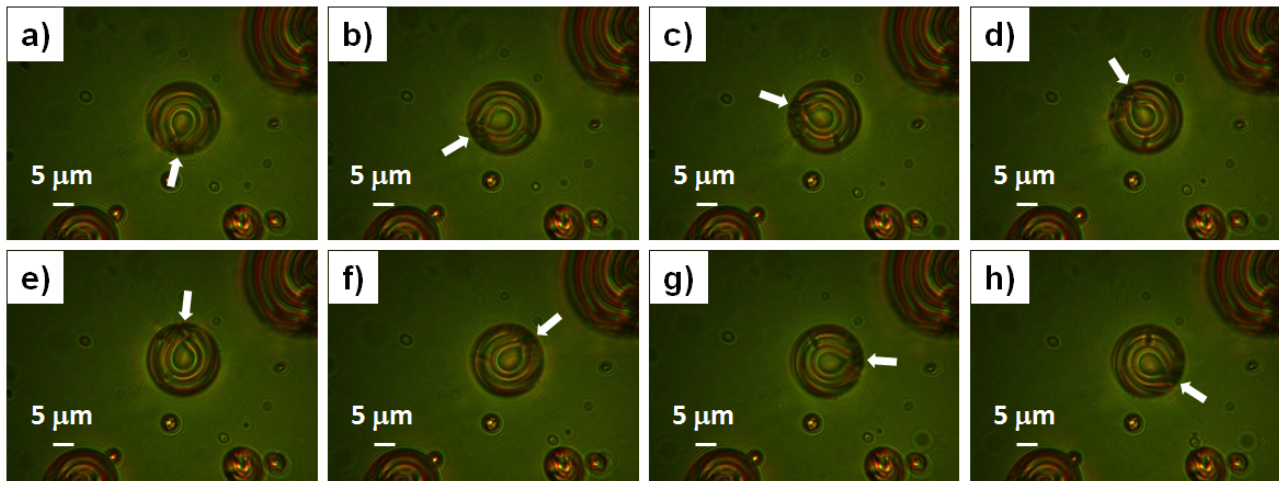


Figure 1.20: Transfer of angular momentum by light - Clockwise rotation of a nematic CLC in water due to the transfer of angular momentum

Probably the most exciting field of applications of optical angular momentum in the field of micromanipulation is the continuous driving of micro machines and microfluidic systems.

Part 2

Optical tweezers and micro hydrodynamics on LC droplets

2.1 Introduction

The motion of objects in a fluid is encountered quite frequently in nature, in geophysical and astrophysical situations, but also in several engineering applications, chemical engineering, or environmental mechanics^[64–70]. The areas of study and applications that have mainly addressed the experiments and the theoretical modeling of motion in a fluid until now refer to situations in which objects are suspended in shear and vortical flows and where the Reynolds number (Re) involved is high or moderate^[65–68].

As the object travels through a fluid, the viscosity of the fluid acts on the moving object with a force that resists to the motion of the object. Since Galileo Galilei, spheres have been used by physicists to probe movement and friction^[71]. In particular, the motion of a solid sphere (radius r , velocity \vec{v} , density ρ_s) in a quiescent liquid (viscosity η , density ρ) is the paradigm for characterizing the laws of friction at low and high Reynolds numbers. Two common approaches for modeling this resistive force are the Stokes' and Newton's models. In 1845, Sir George Gabriel Stokes published the equations of a viscous flow^[72]. Stokes determined the resistive force, or viscous drag force of a sphere falling under the force of gravity in a fluid, either liquid or gas, to be directly proportional to the sphere's velocity. For low Reynolds number ($Re = \rho v r / \eta \ll 1$), he established that the magnitude of the drag force experienced by the solid during its motion is given by $F_D = 6\pi\eta v r$. On the other hand, for high Reynolds numbers, Newton^[73] was probably the first to propose an heuristic expression for the drag magnitude as $F_D = 1/2 C_D \rho v^2 \pi r^2$, where C_D is a coefficient provided by the experiments. Newton, showed that the drag force is proportional to the square of the velocity of the object and acts in the direction opposite to the direction of the velocity. Nowadays, Newton's model is associated with higher velocities and turbulent, or non-steady flows.

For spheres moving in a flow, besides the drag force acting parallel to the velocity (which is due to the slip velocity between the object and the surrounding fluid), is associated also a transverse force to the slip velocity known as lift or Magnus force due to a cross-flow by the vorticity in the ambient flow or due to the spinning of the particles about its axis when travel in the fluid. This effect was first found by Robins^[74] and then rediscovered almost a century later by Magnus^[75], who finally got the credit for the effect^[76]. On this spirit, the focus of this chapter and the articles on which is based, represent an attempt to provide a new approach on the study of the dynamics of spinning LC droplets immersed in water interacting with an optical field, considering the equations of motion of spherical particles in a viscous fluid and including the hydrodynamic forces and torques. In the conventional approach, the optical forces and torques are mainly considered for optical tweezers performances and the dynamics of trapped particles, while the ambient fluid only yields a damping effect through the viscous force^[77–79]. In contrast, we show that the hydrodynamic Magnus force, can play an important role in the optical trapping and manipulation and it should be considered whenever particles are forced to spin and dragged in a fluid, as well as shear and vortical flows are involved.

2.1.1 Navier-Stokes equations

The essential fluid physics of the system is dictated by a competition between various phenomena, which is captured by a series of dimensionless numbers expressing their relative importance. Before beginning with the specific subjects, we very briefly review the importance and basic fluid properties as well as the dimensional parameters that characterize them. Because fluids are continuum materials and the discrete quantities like mass and force give way to continuous fields like density ρ and force density f that are defined per unit volume, the concept of a small fluid element is often invoked by analogy with discrete mechanics. Forces on such elements arise from fluid stresses \mathbf{T} (forces per unit area or stress tensor) exerted on the element surfaces, in addition to externally applied body forces \vec{f} exerted on the bulk of the element which typically consist of gravity forces, but may also include other types (such as electromagnetic forces). Then, the velocity field for a Newtonian fluid in an inertial frame of reference, obeys the general Navier-Stokes equations which essentially represent the continuum version of $\vec{F} = m\vec{a}$ on a per unit volume basis:

$$\rho \left(\frac{\partial \vec{v}}{\partial t} + \vec{v} \cdot \nabla \vec{v} \right) = \nabla \cdot \mathbf{T} + \vec{f} = -\nabla p + \eta \nabla^2 \vec{v} + \vec{f}, \quad (2.1)$$

where \vec{v} is the flow velocity, ρ is the fluid density, p is the pressure and where the inertial acceleration terms appear on the left and forces on the right. When inertial forces are small compared to viscous forces, which is usually the case in micro fluidic devices and optical trapping systems, the nonlinear term can be neglected, leaving the Stokes equation as:

$$\rho \frac{\partial \vec{u}}{\partial t} = \nabla \cdot \mathbf{T} + \vec{f} = -\nabla p + \eta \nabla^2 \vec{u} + \vec{f}. \quad (2.2)$$

In both cases, mass conservation requires

$$\frac{\partial \rho}{\partial t} + \nabla \cdot (\rho \vec{\mathbf{u}}) = 0. \quad (2.3)$$

giving the incompressibility condition $\nabla \cdot \vec{\mathbf{u}} = 0$ for slowly flowing fluid with nearly constant density like water.

As a result that the flow is laminar and that it is sufficiently “slow” the inertial effects will not be considered. This simplification is justified with water as the typical working fluid, with typical velocities of $1 \mu\text{m}/\text{s}$ to $1 \text{cm}/\text{s}$ and typical sizes in μm , the Reynolds numbers range between $\mathcal{O}(10^{-6})$ and $\mathcal{O}(10)$. These low values of Re affirm that viscous forces typically overwhelm inertial forces, and the resulting flows are linear. When Re is very small, the nonlinear terms in equation (2.1) disappear, resulting in linear and predictable Stokes flow of equation (2.2).

2.2 Magnus force in optical manipulation

A spinning particle experiences a Magnus lift force when subjected to a uniform cross-flow^[69]. This rotation-induced lift force can also be explained as an inertial effect arising from the differential pressure associated with the high-speed and low-speed sides of the sphere. However, only a few papers have studied the motion of particles in a fluid at small Reynolds number and even less take it in account as the case encountered in optical manipulation experiments. Rubinow and Keller^[69] evaluated the lift force on a spinning spherical particle when the particle is launched with initial linear and angular velocities in a static viscous fluid. Solving the Navier-Stokes equations for the motion of the fluid around the particle, they found that in addition to the drag force, a spinning particle experiences a force orthogonal to the direction of motion given by:

$$\vec{\mathbf{F}}_M = \pi R^3 \rho \vec{\boldsymbol{\Omega}} \times \vec{\mathbf{v}} [1 + \mathcal{O}(Re)] \quad (2.4)$$

known as Magnus force, where R is the radius of the spherical particle, $\vec{\boldsymbol{\Omega}}$ its angular velocity, $\vec{\mathbf{v}}$ its linear velocity, $Re = \frac{\rho \nu R}{\eta}$ is the Reynolds number and ρ and η are the density and the viscosity of the fluid, respectively. In a different work, Saffman considered the lift force on a small sphere in a slow shear flow^[70], in the theoretical models reported in these papers is stated that in the case of micrometric particles at small Reynolds number where $Re < 1$ and $R \sim 10^{-6} \text{m}$, the Magnus force can be neglected with respect to the drag (or viscous) force.

For this reason, the researchers working in the field of optical manipulation have always ignored this force. However, we noted that the situations considered by the theoretical studies on the Magnus force do not reflect the conditions of the optical micromanipulation experiments, where an external agent (*i.e.* the light) rotates and/or translates the particles in a static fluid. This makes the rotation and/or translation rates of the particle independent parameters that can be exploited on the experiments. Taking in account such conditions, we have evaluated the

Magnus force adopting a simple modeling approach in an experiment based on the measure of the forces and by a method of trajectories analysis^[80], showing that it is unexpectedly much larger than the one predicted by the existing theories and therefore, cannot be neglected in such kind of situations.

2.2.1 Model and experiment description

Because optical tweezers and micromanipulation techniques provide an extremely useful tool for micro-rheology; facilitating the study of the hydrodynamic interactions between colloids in suspensions and allow the study of one isolated particle in rotation. The idea for the experiment is based on an anisotropic optical trap (specifically an extended line trap), which also carries angular momentum, and therefore is able to set in rotation a particle and drag it in a fluid.

The experiment exploits a holographic optical trap based on the interference of two Gaussian laser beams with parallel circular polarization. The resulting light fringes pattern enables one-dimensional optical trapping of particles with proper size and refractive index to be established within the interference fringes^[81,82]. Due to the polarization of the light, the birefringent or absorbing particles are put in rotation because of the transfer of the spin angular momentum^[55]. A displacement of the interference fringes enables that the rotating particles in the fluid can be dragged along the trapping direction, *i.e.* perpendicularly to the light fringes and their angular velocity. The experimental system used for the laser trapping experiment is depicted in figure 2.1.

An argon laser beam at $\lambda = 488$ nm is directed towards a Mach-Zehnder interferometer formed by the non polarizer beam splitter BS1 that separates the incident beam into two, one beam is directed to the mirror M1 and the other one is directed to the mirror M2 to be reflected towards a second non polarizer beam splitter BS2. The quarter-wave plate ($\lambda/4$) just before the microscope objective changes the polarization state of the light beams from linear to circular (left L or right R for both beams). After the BS2, there are three beams, two of them are almost parallel and directed with the mirrors M3 and M4 towards the dichroic mirror DM which reflects them into the 40X microscope objective to focus the two beams almost parallel in order to interfere on the sample plane, the remaining beam after BS2 and orthogonal to the former two beams is blocked by a screen and is not used.

In the interferometer, the mirror M1 is mounted onto a piezoelectric system controlled electrically by an arbitrary function generator, this allow to move the mirror (M1) of the Mach-Zehnder interferometer to translate the interference light fringes. M2, M3 and M4 are fixed mirrors. All the measurements have been performed displacing the interference pattern with a time modulated function, usually a smooth sinusoidal function gave the best results. Also,

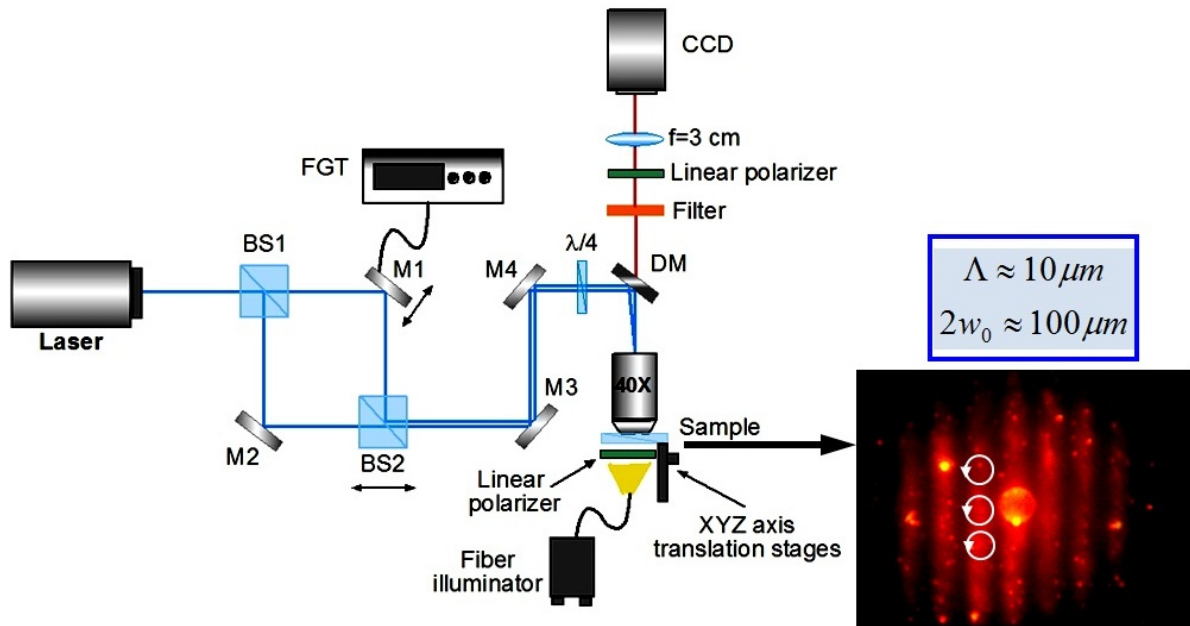


Figure 2.1: Experimental setup - Experimental set up for the Magnus effect with two circular parallel polarizations at small angle. The inset show a microscope image of the beam spot in a sample with fluorescent dye to measure the spatial periodicity Λ and the size of the interference fringes

only to control the thick of the fringes¹ or spatial periodicity Λ , we could adjust the tilts screws on the mirror M1, to match the thick with the diameter size of the particle to trap. The sample position is adjusted with a precision x, y, z -axis translation stage. A computer controlled charge couple device (CCD) camera and a fiber illumination system have been used to image the sample placed between crossed polarizer and analyzer.

The sample is an emulsion of nematic liquid crystal E7 in distilled water, a system already adopted for optical manipulation experiments^[63,83]. A relevant aspect of this system is that droplets with radial and bipolar nematic configuration, can be found in the same emulsion (figure 2.3). Spherical droplets of nematic LC with diameter ranging from $1 \mu m$ to $20 \mu m$ can be obtained and are transparent in the whole visible range, with radial or bipolar configuration of the nematic director^[63,83,84].

Optical microscopy of nematic LCs serves to determine the alignment properties of these fluids. If a nematic fluid is placed between crossed polarizers, the nematic will induce a phase shift in the light, and the nematic will typically appear bright on a dark background. An exception arises when the local director fields is aligned parallel to either the polarizer or analyzer so that no phase shift occurs. If the liquid crystal anchoring is normal to the internal surface of the droplet, this leads to the radial configuration resulting in birefringence patterns that exhibit a

¹See inset on figure 2.1

characteristic dark cross, while for bipolar configuration the optical anisotropic droplet show a brilliant spot that changes when the polarizer orientation changes. (See figure 2.2)

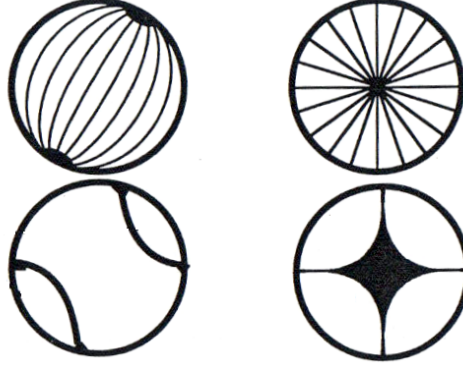


Figure 2.2: Representation of nematic droplets with radial and bipolar configuration

- In the upper part are represented the internal configuration for the bipolar (left side) and radial (right side) nematic droplets. For the same particles down is represented the bright and dark zones observed under crossed polarizers

A powerful method of probing droplet structure is to calculate the appearance of droplets viewed under a polarizing microscope^[85]. To begin, a director field within the droplet must be defined; this can be done either numerically or with an analytical function. The nematic material is then divided into many thin slices, with the layer direction perpendicular to the incoming light (defining a \hat{z} direction). The thickness of each layer is chosen to be small enough so that the nematic orientation can be assumed constant within each layer, the orientation of the nematic changes from slice to slice. Each point within a slice is treated as a birefringent slab, with the optic axis and birefringence magnitude depending on the local director orientation. The effect of each slab is to change both the orientation and the phase of the polarization vector entering the layer. The calculation of the transmission of light through a droplet viewed between crossed polarizers can be performed using^[85]:

$$\begin{bmatrix} E_x \\ E_y \end{bmatrix}_{out} = \begin{bmatrix} 0 & 0 \\ 0 & 1 \end{bmatrix} \mathbf{J}_N \mathbf{J}_{N-1} \dots \mathbf{J}_2 \mathbf{J}_1 \begin{bmatrix} 1 & 0 \\ 0 & 0 \end{bmatrix} \begin{bmatrix} E_x \\ E_y \end{bmatrix}_{in}. \quad (2.5)$$

Here, the optical field entering the droplet is represented by a 2×1 vector with components E_x and E_y . The incoming electric field E is multiplied by the matrix for a horizontal polarizer, followed by multiplication by a series of Jones matrices, where \mathbf{J}_i refers to the Jones matrix of the i -th vertical slice. Multiplication of this result by the matrix for a vertically-oriented analyzer produces the outgoing E field. The intensity I of the light is calculated by:

$$I = E_x E_x^* + E_y E_y^* \quad (2.6)$$

The Jones matrix \mathbf{J} for each thin layer of nematic is defined by:

$$\mathbf{J} = \begin{bmatrix} \cos^2 \gamma \exp(i\phi_e) + \sin^2 \gamma \exp(i\phi_o) & \cos \gamma \sin \gamma [\exp(i\phi_e) - \exp(i\phi_o)] \\ \cos \gamma \sin \gamma [\exp(i\phi_e) - \exp(i\phi_o)] & \sin^2 \gamma \exp(i\phi_e) + \cos^2 \gamma \exp(i\phi_o) \end{bmatrix} \quad (2.7)$$

2.2 Magnus force in optical manipulation

the matrix \mathbf{J} , projects the electric field components of the light onto the ordinary and extraordinary axes of the liquid crystal, and is given in terms of the quantities

$$\phi_o = \frac{2\pi}{\lambda} n_o \Delta z \quad (2.8)$$

$$\phi_e = \frac{2\pi}{\lambda} n_e(\beta) \Delta z \quad (2.9)$$

$$n_e^2(\beta) = \frac{n_o n_e}{\sqrt{n_o^2 \sin^2 \beta + n_e^2 \cos^2 \beta}} \quad (2.10)$$

where γ is the azimuthal angle between the extraordinary axis and the \mathbf{x} direction, while ϕ_o and ϕ_e , respectively are the ordinary and extraordinary phase shifts induced by the nematic layer. The ordinary phase advance ϕ_o is given in the equation (2.8), where λ is the wavelength of light, n_o is the ordinary refractive index of the nematic, and Δz is the width of the nematic layer. The extraordinary phase advance ϕ_e is given by the equation (2.9), where $n_e(\beta)$ is the value of the local extraordinary index. The magnitude of the extraordinary phase shift depends on the angle β the director adopts relative to the \mathbf{z} axis, given by the equation (2.10). This calculation neglects any refraction, reflection, or diffraction by the droplets, so it is most appropriate for large droplets with the modest birefringence values. The calculation is performed for a single wavelength^[85].

In a nematic droplet, using the optical microscope observation between crossed polarizers, is possible to characterize the internal configurations in the nematic liquid crystal droplets suspended in water. In many cases, as in bipolar or radial droplets, it is simple to determine an approximate internal structure by this simple experiment, as shows the figure 2.3.

After that the two beams are focused by the microscope objective, the resulting light pattern perform one dimensional optical trapping within the light interference fringes^[84]; while the light pressure in the longitudinal direction ($\hat{\mathbf{z}}$) and the gradient force along the light stripes ($\hat{\mathbf{y}}$) are weak. The intensity distribution of the interference pattern with spatial periodicity Λ in the plane (x, y) can be written as:

$$I = \frac{4P_0}{\pi\omega_0^2} \cos^2 \left(\frac{\pi}{\Lambda} x \right) \exp \left[- \frac{2(x^2 + y^2)}{\omega_0^2} \right] \quad (2.11)$$

where P_0 is the total light power and ω_0 is the Gaussian spot size of the interfering beams. In a very simple approach adequate for a small object, the dipole moment induced in the particle responds to field gradients, yielding to a force proportional to the intensity gradient and then the optical force can be written as:

$$\begin{aligned} \vec{\mathbf{F}}_M = D \left\{ \left[- \frac{\pi}{\Lambda} \sin \left(\frac{2\pi x}{\Lambda} \right) - \frac{4x}{\omega_0^2} \cos^2 \left(\frac{\pi}{\Lambda} x \right) \right] \times \exp \left[- \frac{2(x^2 + y^2)}{\omega_0^2} \right] \right\} \hat{\mathbf{x}} \\ + D \left\{ \left[- \frac{4y}{\omega_0^2} \cos^2 \left(\frac{\pi}{\Lambda} x \right) \right] \times \exp \left[- \frac{2(x^2 + y^2)}{\omega_0^2} \right] \right\} \hat{\mathbf{y}} \end{aligned} \quad (2.12)$$

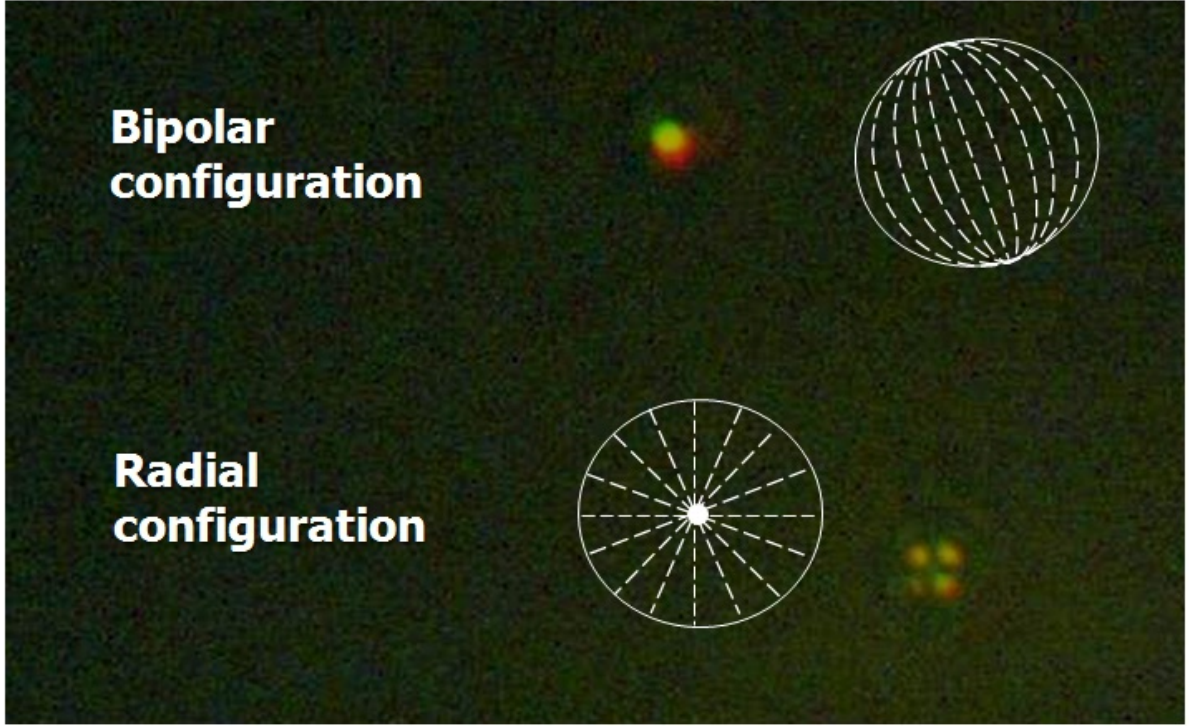


Figure 2.3: Liquid crystal droplets with radial and bipolar internal configurations under crossed polarizers - The image shows a microscope image of the emulsion of LC in water with two droplets on the same emulsion showing the two configurations radial and bipolar (same as showed in figure 1.10). Also is showed a representation of the molecular configuration

where $D = \left(2\pi R^3/c\right)n_f \left\{ \left[\left(n_p/n_f\right)^2 - 1 \right] / \left[\left(n_p/n_f\right)^2 + 2 \right] \right\} \left(4P_0/\pi\omega_0^2\right)$, n_p and n_f are the refractive indices of the particle and the fluid, respectively. The x component of the optical force is dominated by the term $\sim \sin(2\pi x/\Lambda)$ which exhibits the same spatial periodicity Λ as the interference pattern in equation (2.11), but phase shifted by $\frac{\Lambda}{4}$, thus enabling the trapping in the bright fringes. Owing to the Gaussian intensity profile, a y component of the optical force exists, which acts as a restoring force toward the center of the fringes, even if it is much weaker than the x component.

The piezoelectric actuated mirror mount electrically driven by a function generator, allows to the mirror M1 in the Mach-Zehnder interferometer to be moved in order to shift the interference fringes along the x axis. The measurement of the displacement of a spinning particle trapped in a fringe has been performed by swinging the interference pattern with a sinusoidal time modulated function. According to the experimental scheme, we can describe the motion of the trapped particle starting from the equations of the motion of a spherical particle in an isotropic fluid, subjected to the optical force and torque:

$$m \frac{d\vec{v}}{dt} = \vec{F}_D + \vec{F}_M + \vec{F}_{op} \quad (2.13)$$

$$I \frac{d\vec{\Omega}}{dt} = \vec{\tau}_D + \vec{\tau}_{op} \quad (2.14)$$

2.2 Magnus force in optical manipulation

where m is the mass of the sphere and I the moment of inertia. \vec{F}_D is the viscous force, which can be written as $\vec{F}_D = -b\vec{v}$, where $b = 6\pi R\eta$ in the case of a spherical particle¹ and $\vec{\tau}_D$ and $\vec{\tau}_{op}$ are the viscous and optical torques. $\vec{F}_M = C_M\rho\vec{\Omega} \times \vec{v}$ is the Magnus force experienced by a particle rotating with angular velocity $\vec{\Omega}$ and translating with a linear velocity \vec{v} within a static fluid, where C_M is a parameter including the physical and geometrical features of the particle. Here we consider the case of particles spinning at a constant angular velocity $\vec{\Omega}$ ($\vec{\tau}_D + \vec{\tau}_{op} = 0$), in which the translational motion of the particle along the fringes can be described considering the equation (2.13).

In the figure (2.4) are represented the optical and Magnus forces acting on an anticlockwise spinning particle [a) and b)] and on a clockwise spinning particle [c) and d)] within an interference fringe to show the combination of the trapping and translational effects. In figure (2.4) [b) and d)] the directions of the particle's motion due to these forces combination are depicted for the respective signs of constant linear and angular velocities, in the case of a non-negligible effect of the Magnus force. The trapped particle is forced to move in the \hat{x} direction together with the fringe according to the sinusoidal function $x(t) = A \sin(\omega t)$, where A is the amplitude of the oscillatory displacement and ω is the pulsation. Therefore, the x component of the linear velocity of the particle $v_x(t) = A \omega \cos(\omega t)$ is an independent parameter. The projection on the y direction for the equation (2.13) is:

$$m \frac{dv_y}{dt} = -bv_y + F \cos(\omega t) - Ky \quad (2.15)$$

where the y component of the optical force $F_{op,y} = -Ky$ has been derived from equation (2.12) truncated to the first linear term, and can be considered as a simple restoring force and K includes all the geometrical and physical parameters of the equation (2.12); the Magnus force component $F_{M,y} = F \cos(\omega t)$ is a sinusoidal driving force, where

$$F = C_M\rho\Omega A\omega \quad (2.16)$$

The equation (2.15) describes the motion of a classical forced and damped harmonic oscillator. The steady state solution of the equation (2.15) is $y(t) = Y_0 \sin(\omega t + \phi)$, with the maximum displacement Y_0 related to the amplitude of the driving (Magnus) force by the expression:

$$Y_0 = \frac{F}{\sqrt{(K - m\omega^2)^2 + b^2\omega^2}} \quad (2.17)$$

where we have define the phase shift between the y and x components of the displacement as $\phi = \arctan[b \omega / (K - m\omega^2)]$.

¹For example, for a 1 μm diameter bead in water ($\eta = 0.001 N \cdot s \cdot m^{-2}$), $\gamma = 9.4 \times 10^{-9} N \cdot s \cdot m^{-1}$. A correction to this relationship, known as Faxen's law, is required in close proximity to surfaces (such as the cover slip). Because the damping effect is dependent on the velocity of the bead, rather than its position, it does not affect the distribution of positions but, it might affect the behavior of the bead over time, and therefore also the power spectrum of bead motion^[32]. However, in our experiment the trapping zone was away from the surfaces.

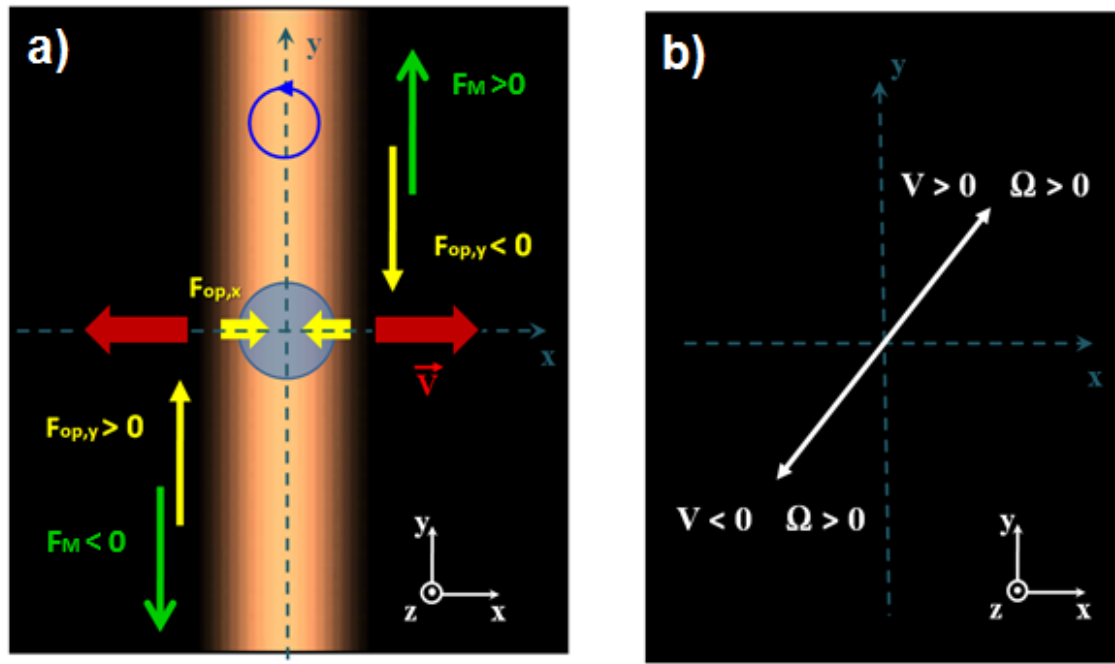
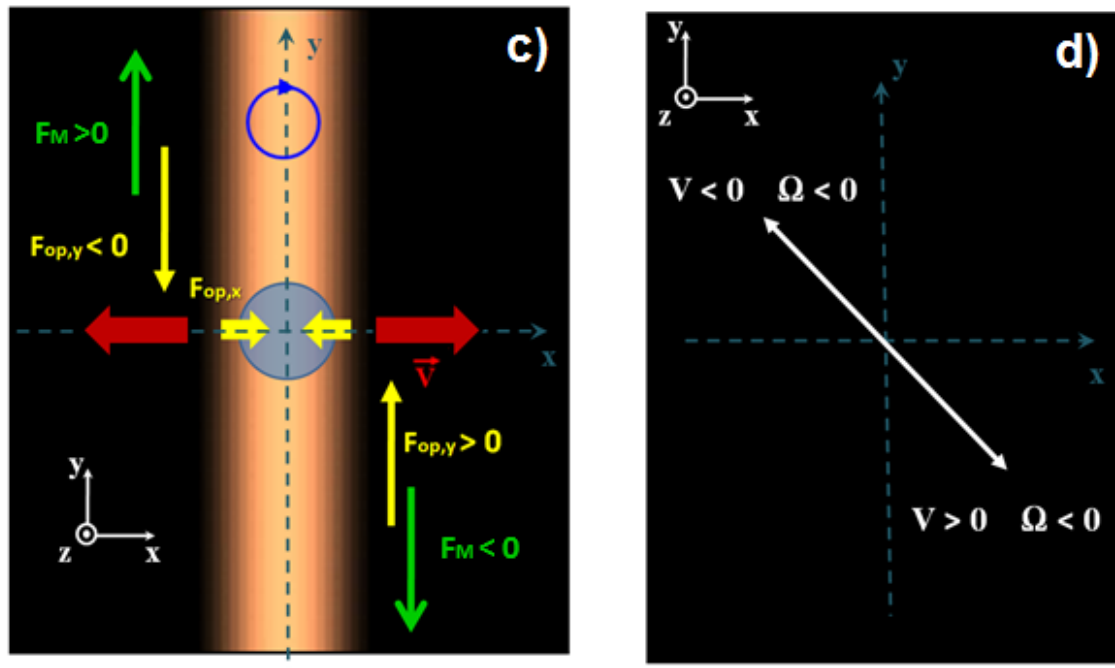
Anisotropic anticlockwise spinning (birefringent) particle

Anisotropic clockwise spinning (birefringent) particle


Figure 2.4: Scheme for Magnus force - (a) Scheme of the forces acting on the anticlockwise spinning particle ($\vec{\Omega} = \Omega \hat{z}, \Omega > 0$ in blue circle with arrow) when is trapped in an interference fringe (orange) and is translated with velocity \vec{v} (red arrows) along the grating wave vector direction, *i.e.* perpendicularly with respect to the light fringe. The components of both forces, the optical force (yellow arrows) \vec{F}_{op} and Magnus force (green arrows) \vec{F}_M , along the y axis are sketched in the case of a movement along \hat{x} and $-\hat{x}$. (b) Scheme of the expected displacement of the particle (white diagonals): a left (right) displacement of the fringe corresponds to a y displacement downward (upward) of the particle spinning anticlockwise. (c) and d) The situation is reversed for a clockwise rotation of the particle.

2.2.2 Trajectories analysis

From the previous mathematical model and with the analysis of several samples resulting in different videos, we can measure the maximum displacement from the equilibrium position. For the cases of anticlockwise rotation, clockwise rotation and the particular case of no rotation. The software program used for the video analysis was Able Particle Tracker v3.0. The images were taken directly from the original videos captured by the CCD (DCU223C Thorlabs) with resolution 1024×768 pixels and sensitive area with dimensions $4.76 \text{ mm} \times 3.57 \text{ mm}$. Resulting in a pixel square of size $4.65 \mu\text{m}$. The images do not have the same scale but the size of the particles is given for each measure.

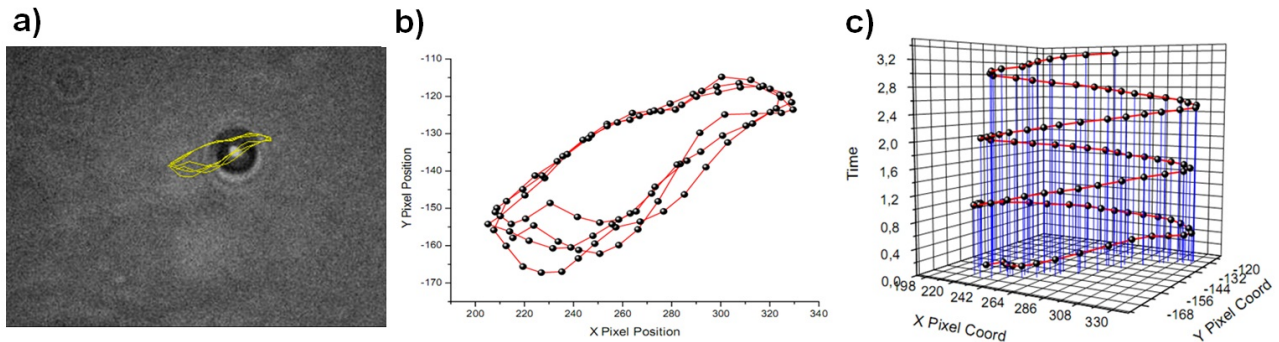


Figure 2.5: Trajectory for anticlockwise spinning LC droplet with diameter $\sim 5 \mu\text{m}$ due to Magnus force - a) Image of the trajectory obtained from the video sequence analysis. b) Graphic of the position X, Y in time for the trajectory. (c) Evolution of trajectory in time.

As a summary of results, the figures (2.6a) and (2.6b) show the representative displacement of a birefringent LC droplet with a diameter of $\sim 5 \mu\text{m}$, rotating in an anticlockwise direction ($\vec{\Omega} > 0$) with angular speed of $\sim 30 \text{ rad/s}$, observed when the droplet trapped is sinusoidally dragged to left (2.6a) and to right (2.6b) with amplitude $A = 10 \mu\text{m}$ and pulsation $\omega \sim 1.6 \text{ rad/s}$.

The displacement of the spinning particle to the left ($v_x < 0$) and to the right ($v_x > 0$) is associated with a correlated downward (2.6a) and upward (2.6b) displacement along the y direction, respectively, in agreement with the scheme reported in figure (2.4b). In figures (2.6c) and (2.6d) the displacements of a droplets that rotates with opposite angular velocity (i.e., clockwise $\vec{\Omega} < 0$), are in correspondence with $v_x < 0$ and $v_x > 0$. The observed shifts along the y axis are reversed with respect to $\vec{\Omega} > 0$ (see also figure 2.4d).

The LC droplets with radial director configuration does not rotate in circularly polarized light; therefore no displacement along the y axis is observed even if they are trapped in the fringes and dragged along the x axis as shown in figures 2.7 and 2.8.

In this case, the radial droplets in spite to be trapped and translated with the same parameters that the anisotropic droplets on the fringes pattern, do not show neither vertical displacement

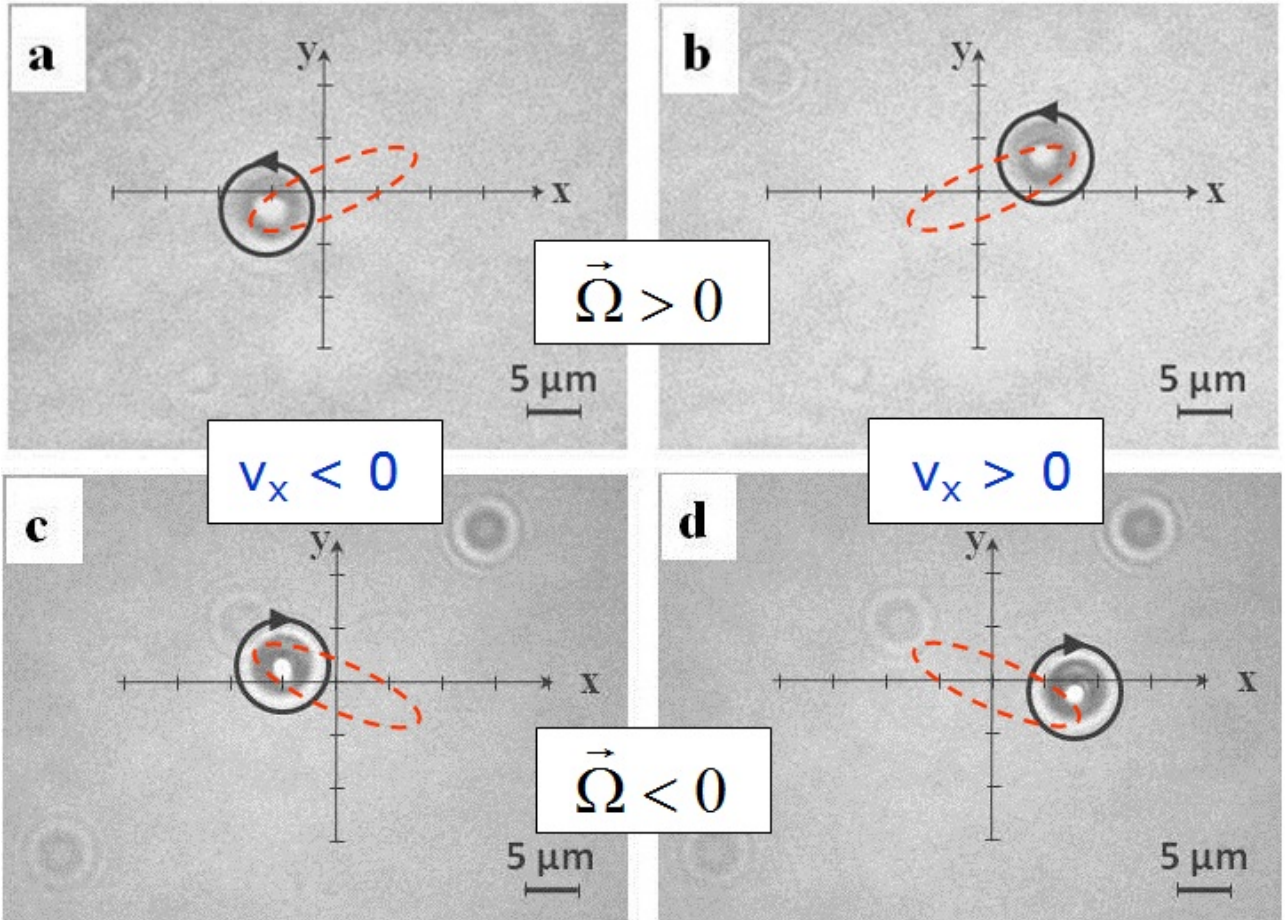


Figure 2.6: Displacement of spinning LC droplet due to Magnus force - Maximum displacement of the spinning droplet along the y direction in the case of a droplet rotating in an anticlockwise sense [a) and b)]; and for clockwise rotation [c) and d)], when the translation of the particle is along $-\hat{x}$, [a) and c)] or \hat{x} , [b) and d)].

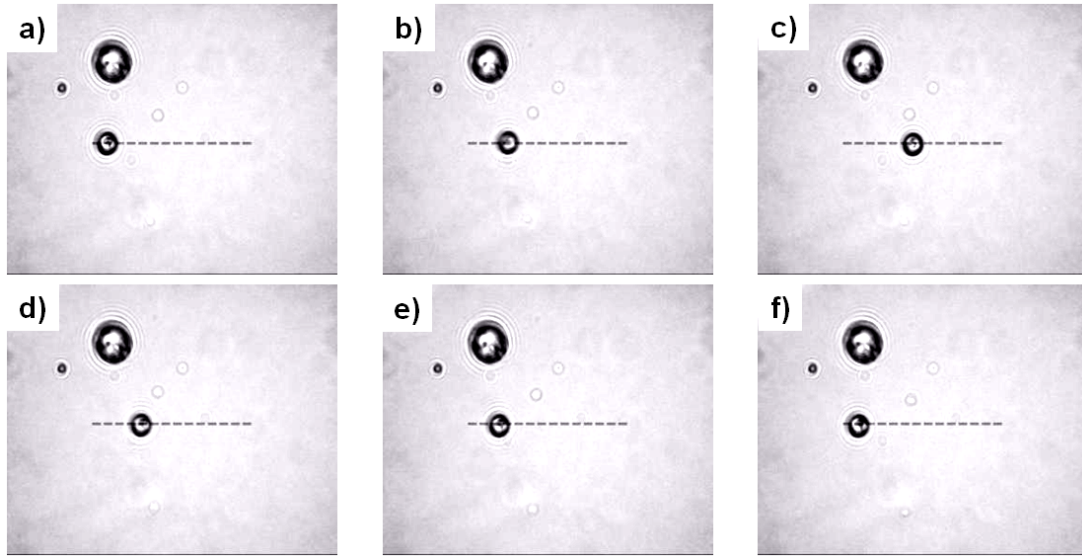


Figure 2.7: Microscope sequence images for a non spinning LC droplet with radial configuration - The images a)-f) show a LC droplet with radial configuration and diameter $\sim 5 \mu m$ trapped in one of the fringes with circular state of polarization inside the pattern. The particle is sinusoidally dragged to left and right with amplitude $A = 15 \mu m$ and pulsation $\omega \sim 1.6 \text{ rad/s}$. The dotted line serves as reference to indicate a horizontal line.

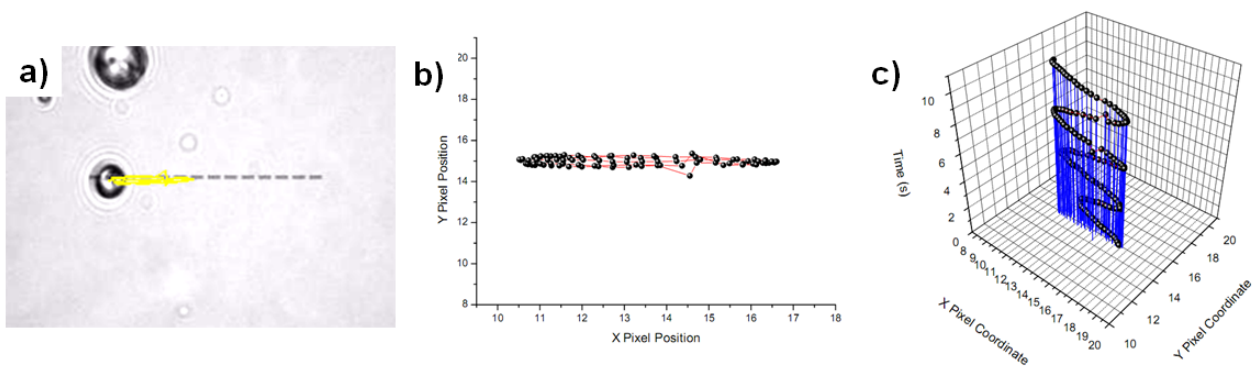


Figure 2.8: Trajectory for a non spinning LC droplet with radial configuration - a) Image of the trajectory in the plane (x, y) obtained from the video image sequence analysis. b) Graphic of the position in time for the trajectory, (c) Evolution of trajectory in time.

or the elliptical trajectory. In this case is clear that because the rotation is absent, the effect of the Magnus force is not exhibited.

2.2.3 Results and discussions

The values of physical and geometrical parameters of the media and of the light field involved in the experiment are: the mass of the LC droplet, $m = 10^{-13} \text{ kg}$; the mean refractive index of the liquid crystal (E7) $n_p \approx 1.63$; the refractive index of the water $n_f \approx 1.33$; the viscosity of the water $\eta \approx 10^{-3} \text{ N} \cdot \text{s}/\text{m}^2$; the total power of the laser beams $P_0 \approx 100 \text{ mW}$; the spot size of the interference pattern, $w_0 \approx 100 \mu\text{m}$; the spatial periodicity $\Lambda \approx 10 \mu\text{m}$. Considering these experimental data, the calculated values of b and K have the same order of magnitude, $10^{-8} \text{ N m}^{-1}\text{s}$ and 10^{-8} N m^{-1} respectively. According to equation 2.17, the order of magnitude of the Magnus force $F \sim 10^{-14} \text{ N}$ has been estimated measuring a y -displacement $Y_0 \sim 1 \mu\text{m}$ in figures (2.6a) and (2.6b).

The value of C_M in equation 2.16 stemming from the experiment is about 10^{-14} m^3 , while in consideration of the theory by Rubinov and Keller (see the equation 2.4) the expected value of C_M should be on the order of 10^{-16} m^3 . The discrepancy between the theory^[69] and the present experiment^[80] could be ascribed to the fact that in the former the rotation and translation of the particles are forced by an external field (*i.e.*, the optical field) or to the presence of nonlinear coupling terms between the drag and lift forces^[86].

The experimental finding proof that the strength of the optical trap (K) is a relevant parameter to reveal the Magnus effect. In fact, a strong trapping along both the x and y axes would hinder the effectiveness of the Magnus force, thus reducing the value of Y_0 . As a consequence, in the case of a weak intensity gradient, the Magnus force can be applied to perform also particle trapping, as recently was suggested in the reference^[84] and whose details shall be presented in the next section.

2.3 Optical tweezers and polarization holography

It is well known that an optical trap is an instrument of manipulation and analysis based on an intensity gradient usually called optical tweezers^[21]. The gradient of light combined with additional forces due to light scattering and gravity, creates a stable trap position close to the focal point of the beam that draws dielectric (transparent) particles towards the focus. This conventional trapping operation on optical tweezers allow to capture and stably manipulate micro-particles while the medium (usually water) yields a damping effect through the viscous force. In this way, the experimental study of small particles have been improved in many research fields^[62,87-89].

Although the optical tweezers have reached a high technological level, the intensity gradient is at the basis of their conventional trapping operation principle. Studies of the helical modes suggested that a phase gradient can be also used for optical manipulation^[89]. And recently, one experiment exploiting polarization patterns^[84], addressed to investigate new trapping and manipulation capabilities based on polarization gradients.

Such as the previous section when besides the optical forces, the involvement of an hydrodynamical force named Magnus force was employed to demonstrate a new approach. On this section will be presented the investigation of the capabilities for optical trapping and manipulation offered by polarization gradients in two configurations, created via vectorial holography^[90]. The holographic tweezers studied in the experiment are based on a more gentle approach to the optical manipulation and then the effect of possible hydrodynamics forces on the particles should not be neglected, the features of these holographic tweezers have been investigated exploiting also liquid crystal (LC) droplets in water. The proposed experiment enables to verify the presence of optical forces related to the polarization gradient leading to the observation of an unconventional trapping due to solely optical forces, but that can be explained with the aid of the hydrodynamic forces on rotating particles, originated from the optical force field.

The polarization holography relies on the interference of asymmetrically polarized beams^[90–92]. Among several configurations, here we consider the interference of two Gaussian beams with orthogonal linear polarizations, s and p respectively, and the interference of two beams with opposite circular polarizations (left L and right R), having in both cases equal intensity, and crossing at a small angle θ between them, see figure (2.9).

2.3.1 Two beams with orthogonal polarizations

The resulting optical electric field and intensity profile in an homogeneous and isotropic medium are respectively^[90,91]

$$\vec{E}_{s,p} = E_0 \left[\cos \frac{\theta}{2} \exp(-i\delta) \hat{\mathbf{x}} + \exp(i\delta) \hat{\mathbf{y}} - \sin \frac{\theta}{2} \exp(-i\delta) \hat{\mathbf{z}} \right] \exp(-i\beta) \quad (2.18)$$

$$I_{s,p} = 2E_0^2 \quad (2.19)$$

while for orthogonal circular polarization R and L, we have in analog way:

$$\begin{aligned} \vec{E}_{R,L} = \frac{E_0}{\sqrt{2}} \left[\cos \frac{\theta}{2} \left(\exp(-i\delta) + \exp(i\delta) \right) \hat{\mathbf{x}} + i \left(\exp(-i\delta) - \exp(i\delta) \right) \hat{\mathbf{y}} \right. \\ \left. + \sin \frac{\theta}{2} \left(\exp(-i\delta) - \exp(i\delta) \right) \hat{\mathbf{z}} \right] \exp(-i\beta) \end{aligned} \quad (2.20)$$

$$I_{R,L} = 2E_0^2 \left[1 - \sin^2(\theta/2) \cos(2\delta) \right] \quad (2.21)$$

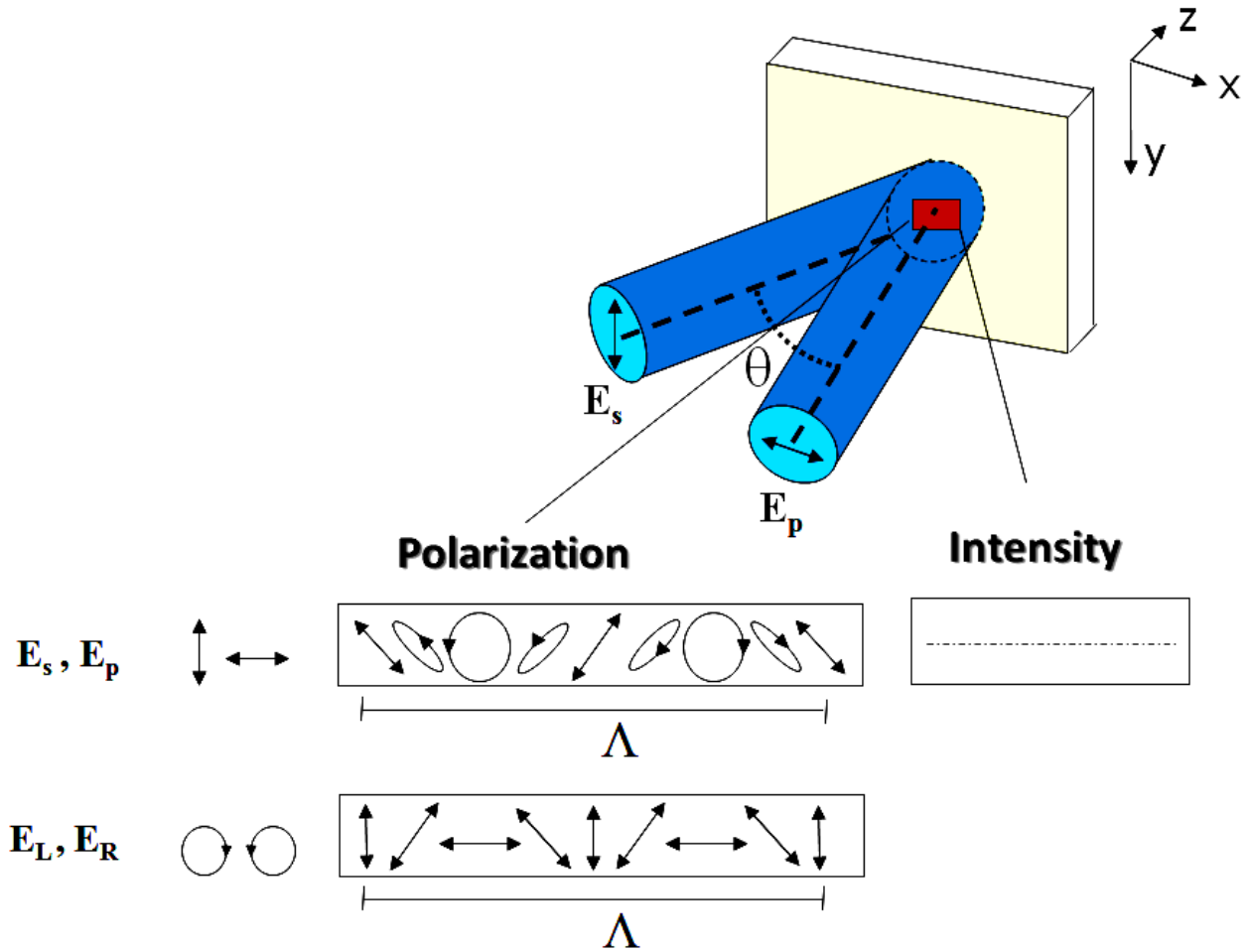


Figure 2.9: Polarization holography due to the interference of two beams at small angle - Two examples used in the experiments for polarization holography (linear s and p and opposite circular L and R). For linear orthogonal polarization s and p , the resulting polarization pattern goes through polarization state -1 to 1. Only for s and p polarizations, the intensity is constant.

2.3 Optical tweezers and polarization holography

where $\beta = \frac{2\pi n}{\lambda} \cos \frac{\theta}{2} z$, $\delta = \frac{2\pi n}{\lambda} \sin \frac{\theta}{2} x = \frac{\pi}{\Lambda} x$ and $\Lambda = \frac{\lambda}{2n \sin \frac{\theta}{2}}$ is the spatial periodicity of the pattern. To evaluate the mechanical properties of such light fields, the linear and angular momentum densities are calculated. The linear momentum density carried by the light in the interference region is given by:

$$\vec{g} = \frac{1}{c^2} \text{Re}\{\vec{E}^* \times \vec{H}\}. \quad (2.22)$$

Evaluating the magnetic fields in the interference region for both cases from the equations of the electric field given in equation (2.18) and equation (2.20), the linear momentum density are respectively:

$$\vec{g}_{s,p} = \frac{1}{c^2} \sqrt{\frac{\epsilon}{\mu}} E_0^2 \left[\left(\sin \theta \cos \frac{2\pi x}{\Lambda} \right) \hat{y} + \left(2 \cos \frac{\theta}{2} \right) \hat{z} \right], \quad (2.23)$$

$$\vec{g}_{R,L} = \frac{1}{c^2} \sqrt{\frac{\epsilon}{\mu}} E_0^2 \left(2 \cos \frac{\theta}{2} \right) \hat{z}, \quad (2.24)$$

In the case of linear orthogonal interfering beams in equation (2.23), besides the usual longitudinal z -component, a transverse y -component occurs for $\vec{g}_{s,p}$, which is spatially modulated versus the x -coordinate along with the polarization pattern (black ellipsoids in upper part of figure 2.10), and is responsible for the transverse force field along \hat{y} (green arrows).

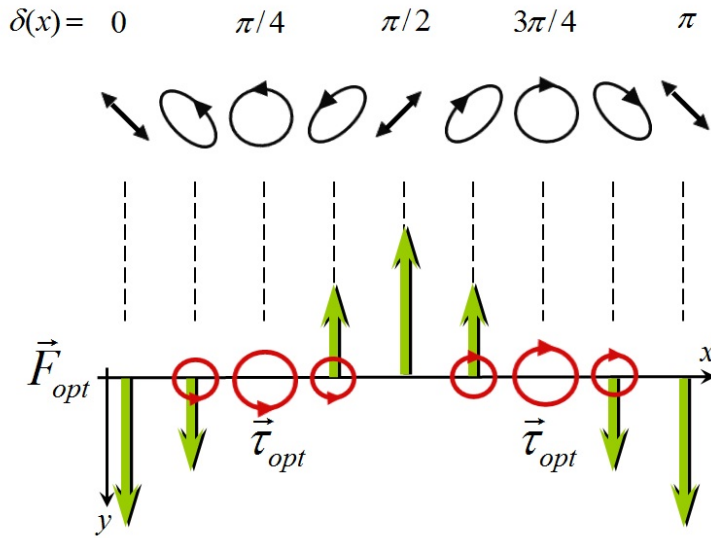


Figure 2.10: Polarization gradient with optical force and optical torque - Upper part shows the scheme of the polarization pattern versus the half phase difference $\delta(x)$. Lower part represent the modulation of the optical force \vec{F}_{op} (green arrows) felt by a particle with diameter lower than $\lambda/2$. The optical torque $\vec{\tau}_{op}$ is indicated (red circles and sense of rotation) for the spinning particles when are trapped in an interference fringe with circular-elliptical polarization in the polarization grating states along \hat{x} direction.

In the case of opposite circular interfering beams, any spatially modulated component occurs on equation (2.24), but only a uniform longitudinal component, the radiation pressure, as in the case of the superposition of two light beams randomly linearly polarized. This result

suggests that no effects related to the polarization gradient are expected, if the ellipticity is uniform.

The angular momentum density follows from the linear momentum density as^[59]:

$$\vec{j} = \vec{r} \times \vec{g}, \quad (2.25)$$

then, in the case of linear s and p interference, only a z modulated component is present:

$$j_z = \frac{1}{c^2} \sqrt{\frac{\epsilon}{\mu}} E^2 (\sin \theta) x \cos \frac{2\pi x}{\Lambda}, \quad (2.26)$$

so, the total angular momentum J_z , obtained by the integration of j_z over the interference region, exhibits two contributions: the orbital component associated with the spatial distribution of the wave and the spin component associated with the ellipticity of light. When a particle is located in the optical field given in equation (2.18), there is a transfer of linear and angular momentum from light to matter depending on the particle position, shape and size. Therefore the optical force

$$\vec{F}_{op} = Q \frac{2A}{c} \left[\hat{y} \sin \theta \int \int \cos \frac{2\pi x}{\Lambda} dx dy + \hat{z} 2 \cos \frac{\theta}{2} \int \int dx dy \right] \quad (2.27)$$

and torque

$$\vec{\tau}_{op} = Q' \frac{2A}{c} \hat{z} \sin \theta \int \int x \cos \frac{2\pi x}{\Lambda} dx dy \quad (2.28)$$

arises over the particle in the xy -plane, where Q and Q' are the parameters accounting for the linear and angular momentum transferred to the particle and A is the intensity of the light.

According to the previous equations and the behavior of the LC droplets with the light fields, the expected scenarios of dynamics for an optically isotropic (radial) and optically anisotropic (bipolar) LC droplet by shifting the polarization pattern, are depicted in the figure 2.11. For the radial particles is expected the observation of an optical force modulated along the x axis, showing a displacement of the droplets along $\pm y$, in this case no rotation of the radial droplets is expected. While for bipolar droplets, a combination of both optical linear moment (\vec{F}_{op}) and OAM transfer producing an optical torque ($\vec{\tau}_{op}$), is expected a rotation of the bipolar and also a displacement along the y axis when the polarization pattern is translated.

The scenarios described in the previous paragraph have been experimentally explored using an emulsion of a nematic LC E7 in distilled water, a system already adopted for optical manipulation experiments^[63,83]. Spherical droplets of LC with diameter ranging from 1 to 20 μm can be obtained, which are transparent in the whole visible range. A relevant aspect of this system is that droplets with radial and bipolar nematic configuration (as shown in figure 2.3), can be found in the same emulsion^[83]. The sole optical linear momentum can be transferred to radial droplets, which are optically isotropic with an average refractive index higher than that

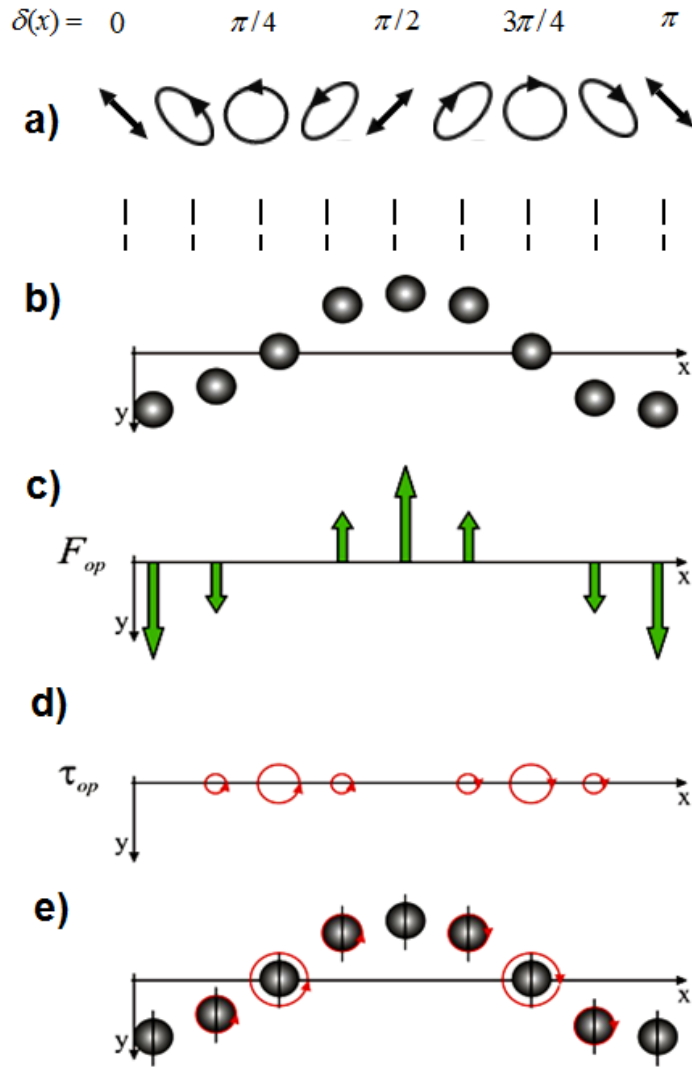


Figure 2.11: Expected dynamics of an optically isotropic (radial) and optically anisotropic (bipolar) LC droplet by shifting the polarization pattern - a) Representation of the polarization; b) Expected behavior on radial LC droplet; c) Modulated optical force \vec{F}_{op} along the x axis; d) Representation of the optical torque ($\vec{\tau}_{op}$) according to the polarization along the x axis, e) Expected behavior on bipolar (anisotropic) LC droplet.

of water. On the other hand, both linear and angular momentum can be transferred to bipolar droplets, which are optically anisotropic. These features enable to test different dynamical behaviours, maintaining almost constant the experimental conditions and the materials parameters, i.e. the average refractive index of the droplets. Liquid crystal droplets with a diameter $d \leq \Lambda/2$, i.e. in the range $2 - 5 \mu\text{m}$, experience the modulated components of the optical force and torque, with a calculated amplitude $0.1 - 1 \text{ pN}$, according to the equation (2.27).

2.3.2 Experimental description

The experimental set-up used to create the above described light fields with the optical forces and torques configurations is presented in the figure 2.12 and showed in the pictures of figure 2.13.

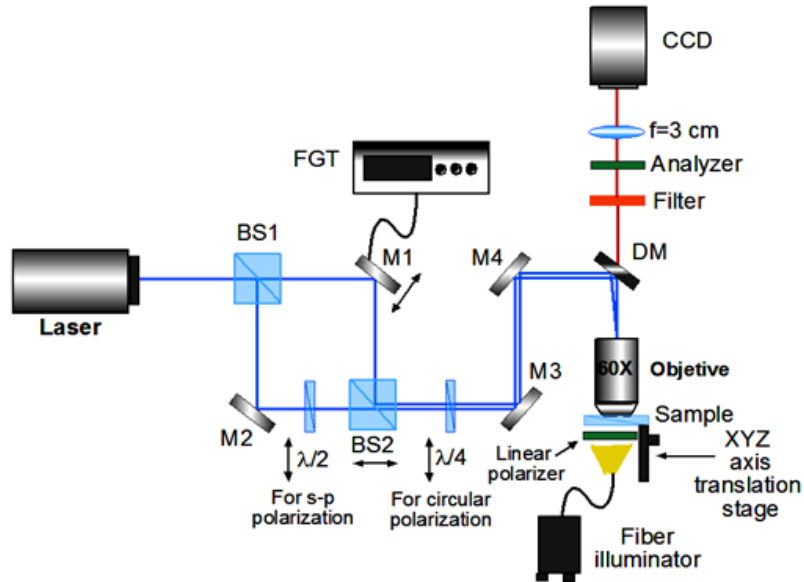


Figure 2.12: Experimental setup with orthogonal polarizations s and p or R and L - It should be notice the similarity and difference with the system for Magnus Force on figure 2.1. Here, is important the use of a HWP to obtain the orthogonal polarizations and the difference using a 60x (N.A=0.85) microscope objective resulting in a smaller spot size.

Two Argon laser beams at $\lambda = 488 \text{ nm}$ are directed towards a 60x microscope objective and interfere on the sample. The beams at the exit of the Mach-Zehnder interferometer have orthogonal s and p linear polarizations, both having the same intensity and crossing at a small angle. While, besides the half-wave-plate (HWP) a quarter-wave-plate (QWP) is introduced before the objective to change the orthogonal linear polarization to the opposite circular polarization configuration. The beams entering on the 60x objective and the illuminated area of the sample are about 2 mm and $40 \mu\text{m}$ in diameter, respectively. The intensity in the interference region is about uniform ($\sim 100 \text{ mW/cm}^2$) and the spatial periodicity of the polarization

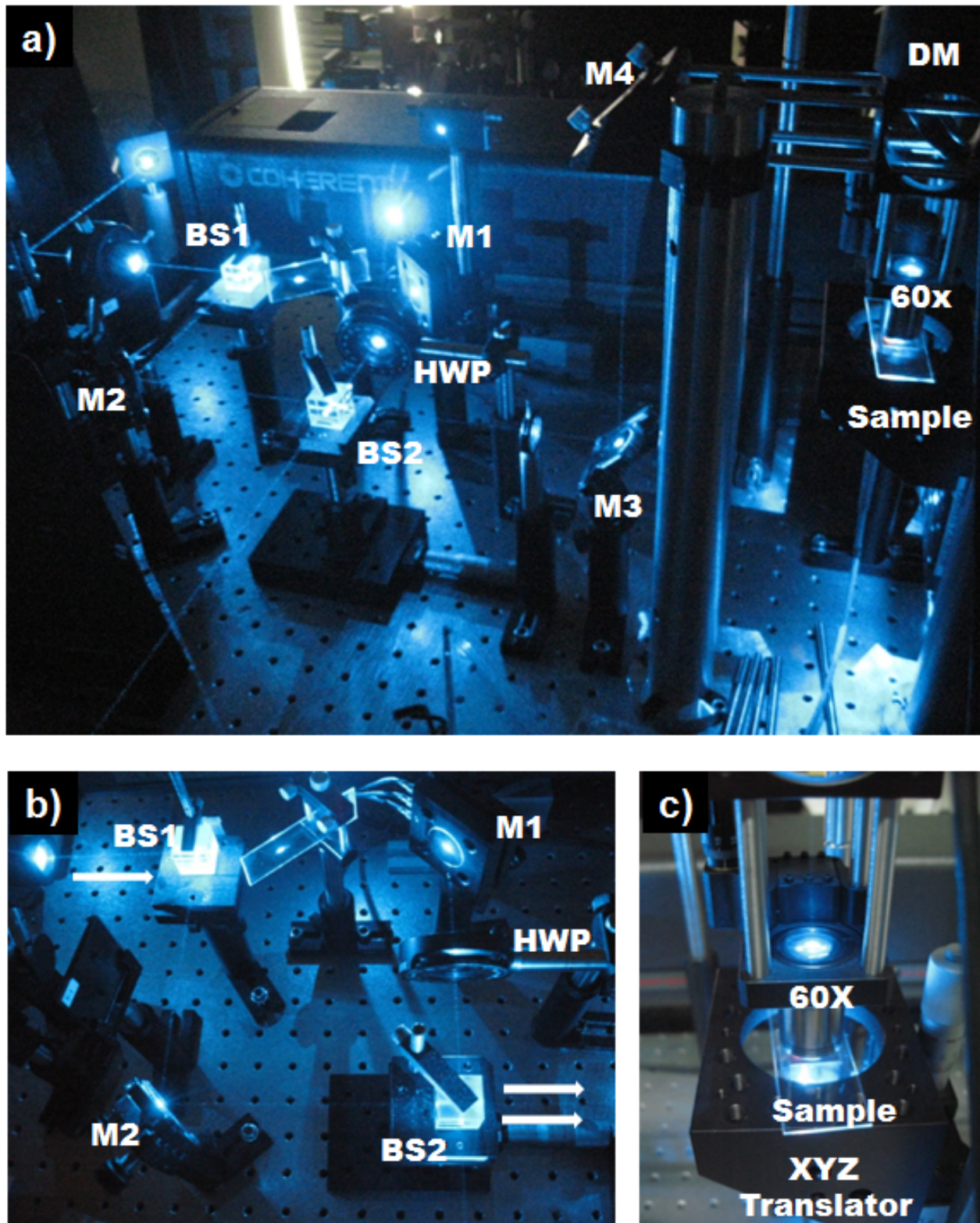


Figure 2.13: Photographs of experimental setup: - For the experiment with s and p polarization. a) Full view of the experimental setup, b) close view of the Mach-Zehnder interferometer with a HWP to obtain the orthogonal polarizations, indicated in white arrows are the used beams, c) close view of the two beams entering on the microscope objective aperture.

pattern is $\Lambda \sim 10 \mu\text{m}$. Again as the previous experiment, the piezoelectric actuated mirror mount, electrically driven by a function generator, allows to move the mirror M1 of the Mach-Zehnder interferometer to translate the interference light fringes. The measurements have been performed moving the interference pattern with a time modulated function.

2.3.3 Results and discussions

Only the optical linear momentum can be transferred to radial droplets, which are optically isotropic with an average refractive index higher than for the water. On the other hand, both linear and angular momentum can be transferred to bipolar droplets, which are optically anisotropic. These features enable to test different dynamical behaviors, maintaining almost constant the experimental conditions and the materials parameters, *i.e.* the average refractive index of the droplets and their diameter in the range of $2\text{-}5 \mu\text{m}$ ($d \leq \Lambda/2$).

To test the mechanical properties of the light polarization pattern resulting from the interference of s and p linear polarization, first is analyzed the effect on a transparent isotropic radial LC droplet, at rest in a circular polarization fringe. No transfer of angular momentum occurs ($\vec{\tau}_{op} = 0$) implying null angular velocity $\vec{\Omega}$. The translation of the polarization pattern along the direction \hat{x} induces a displacement of the particle along $\pm\hat{y}$, due to the birth of the $\vec{F}_{op,y}$, figures (2.11b-c and 2.14). The radial droplets of LC (with $d = 5 \mu\text{m}$) observed between crossed polarizers experience the modulated components of the optical force and torque, with a calculated amplitude $0.1\text{--}1 \text{ pN}$, according to the equation (2.27), are represented in figure 2.14. Starting from a position $x_0 = \pm m\Lambda/4$, with m odd, corresponding to a circular polarization fringe [*i.e.* $F_{op,y}(x_0 = 0)$], when the fringes are moved along $\pm\hat{x}$ an oscillatory displacement of the droplet along $\pm\hat{y}$ is observed.

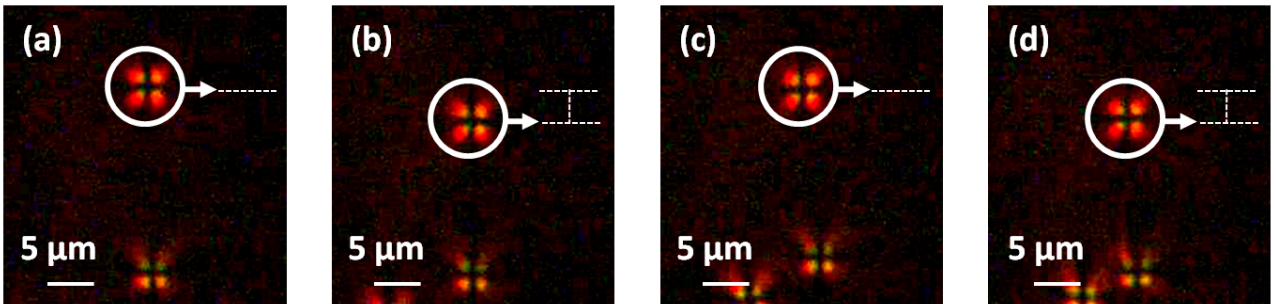


Figure 2.14: Dynamics of an optically isotropic (radial) LC droplet by shifting the polarization pattern - Image showing the maximum displacement of a radial LC droplet. For a non-rotating particle, only the optical force \vec{F}_{op} occurs. Frames (a) to (d) show the droplet displacement along the y -axis induced by the spatially modulated \vec{F}_{op} . The LC droplet moves up and down by $\sim 2 \mu\text{m}$ depending on the $\vec{F}_{op,y}$ direction [See figure 2.11(b)].

When an optically anisotropic particle, *i.e.* a droplet with bipolar configuration is placed in a circular polarization fringe, due to the transfer of the angular momentum ($\vec{\tau}_{op} \neq 0$), it is set in rotation^[59,63]. A uniform angular velocity ($\vec{\Omega} = cte$) can be reached when $\vec{\tau}_D + \vec{\tau}_{op} = 0$, where $\vec{\tau}_D = -8\pi\eta a^3\vec{\Omega}$ is the viscous torque, a is the radius of the particle and η the fluid viscosity. The measured rotation frequency values are few Hz (2 – 5 Hz). In this case, the translation of the polarization pattern induces an unconventional trapping of the spinning particle in the fringe, dragging it along $\pm\hat{x}$. The figure (2.15) shows the trapping of a bipolar droplet rotating clockwise in a circular polarization fringe. The shift of the polarization pattern along $-\hat{x}$ does not show a displacement of the droplet along $\pm\hat{y}$ and the droplet preserves the clockwise rotation, see figure 2.15.

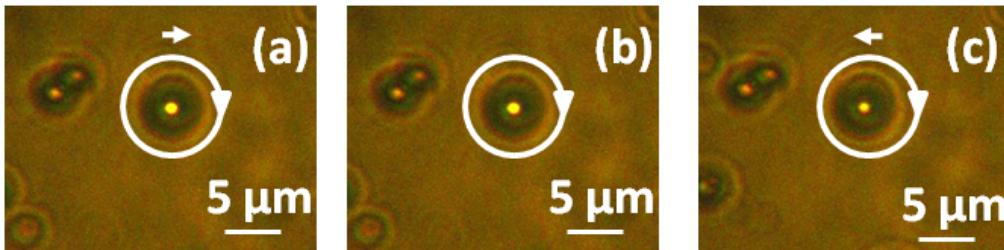


Figure 2.15: Dynamics of an optically anisotropic (bipolar) LC droplet by shifting the polarization pattern - The lift force traps the rotating particle in the circular polarization fringes and without displacement along the \hat{y} direction. Similar behavior is observed when the sample is translated with respect to the polarization pattern

The experimental findings for the isotropic, non-rotating, LC droplets verify how the polarization nature of the light can influence isotropic particles through the vectorial holography; confirming the effect of the optical force coming from the polarization gradient (see equation 2.27). On the other hand, the trapping of the anisotropic particles in the circular polarization fringes, when they are set in rotation by the optical torque (equation 2.28), cannot be accounted for by the mere optical force because of its null x -component. Moreover, even considering the momentum redistribution of the light after passing through the rotating birefringent droplet, the calculated optical force does not exhibit any x -component, which might justify the observed behavior. To give an explanation of the observed unusual trapping we reconsider the influence of the ambient fluid (specifically the influence of the hydrodynamic Magnus force) on the particles dynamics and in the present scenario: together with the polarization pattern, and the optical force field in the x, y -plane, a spherical particle rotating in the plane (x, y) with clockwise sense and the corresponding streamlines of the fluid are shown in figure 2.16. Considering the light interaction with the birefringent particles that locally reorient its optical axis parallel to the linear polarization direction, depending on its position with respect to the polarization pattern. In this case the weak intensity gradient does not show evident mechanical effects.

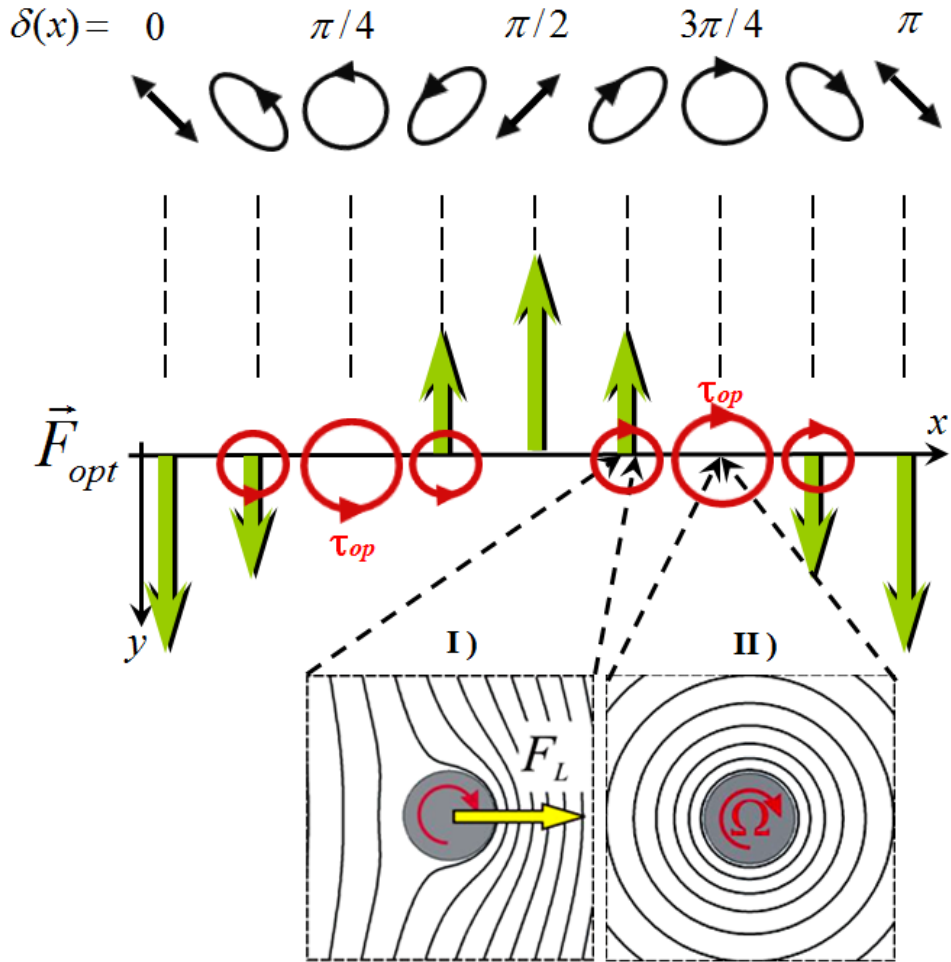


Figure 2.16: Magnus force as restoring force - Representation of the optical torque $\vec{\tau}_{op}$ (red circles with arrows) and the y -component of the optical force $\vec{F}_{op,y}$, felt by a spherical particle with diameter lower than $\lambda/2$. In I) the asymmetric streamlines appear when the particle is centered on an elliptically polarized fringe, due to their linear velocity along the y -axis, and the lift force \vec{F}_L arises along the x -axis, working as restoring force for the rotating particle towards the regions with circular polarization. II) Once the particle reach the circularly polarized fringe, the streamlines appear around the particle, rotating stably with angular velocity $\vec{\Omega}$.

Translating the polarization fringes along \hat{x} , the optical force along $-\hat{y}$ moves the spinning sphere in this direction. The acquired linear velocity \vec{v} of the rotating particle along $-\hat{y}$ generates the lift forces on a perpendicular direction with respect to the velocity, namely \hat{x} , which pushes the particle towards the circular polarization fringe. Indeed, if the polarization fringes were moved in the opposite side, the particle would acquire the linear velocity along \hat{y} and the lift force would occur along $-\hat{x}$. This force could represent the restoring force for the spinning particle toward the circular polarization regions. As a result of the fringes displacement, the birth of the lift force is expected, which may work as a new kind of trap for rotating particles in the polarization pattern.

2.4 Conclusions

In this chapter were reported the experimental investigations of the mechanical properties of optical fields with polarization patterns, *i.e.* polarization holographic tweezers. The use of LC droplets in water enabled to perform optical manipulation experiments without needing to change experimental conditions and material parameters, except for the global optical properties of the droplets connected to the internal molecular arrangement.

The obtained results demonstrate that the hydrodynamics lift force or Magnus force, cannot be neglected at the microfluidic scale if also an external control parameter (such as the light) is present. Moreover, they suggest that new strategies for optical trapping and manipulation, considering the coupling between the hydrodynamic and optical forces, can be established. Multiple opto-hydrodynamical trapping as well as unusual mechanical effects connected to the polarization gradient have been observed, investigating the optical manipulation of LC droplets by means of pure polarization holographic tweezers. Two simple experiments have been used to investigate the features of the polarization holographic tweezers.

In the first experiment, a simple modeling approach and a trajectory method have been devised to demonstrate the Magnus force effect in optical micro manipulation. The experiment with circularly polarized holographic tweezers and optically anisotropic LC droplets, yields towards unequivocal evidences of the Magnus effect, showing that this hydrodynamic lift force is unexpectedly much larger than the one predicted by the existing theories and therefore, it cannot be neglected in some micromanipulation experiments. Only spinning LC particles show a transversal deviation with respect to the direction of the light fringe displacement, according to a scenario where the Magnus force works. As expected, the displacement of the particles depends on the signs of their linear and angular velocities. In addition, the measurement of the maximum transversal displacement of the rotating particle leads to a Magnus force value that is two orders of magnitude larger than the one predicted by the existing theoretical models.

In the second experiment, the mechanical properties of a polarization holographic tweezers based on the interference of two linearly orthogonally polarized beams have been investigated. In this holographic tweezers configuration, no intensity modulation occurs in the superposition region while the polarization ellipticity is strongly spatially modulated, changing from -1 to 1 . That means polarization gradient instead of intensity gradient as principle for the optical control. Interesting and unexpected optical manipulation features for isotropic LC particles emerged in connection with the light polarization, as well as experimental evidence of opto-hydrodynamical trapping where the Magnus force works as a restoring force for birefringent spinning LC particles.

Part 3

Chiral assembled microspheres of LC

3.1 Introduction

Micro- and nano- particles are currently of great interest in many science research areas. In particular, the areas involving the interaction between both light and matter, are fundamental to improve the knowledge and develop future applications.

In optical trapping and manipulation for instance, through different configurations and techniques, a huge variety of micro particles have been employed, passing from purely dielectric, metallic and biological particles *in vivo*^[17–25,93–101], until specific micro particles for microfluidics and nanophotonics^[102–106], sensors^[107–111] and photonics^[112–114]. Nevertheless, although the number of works in optical tweezers has increased, the research tendency is mainly focused in develop new exotic light fields and sophisticated technologies for the traps. Therefore, the common approach usually neglects the structural aspects of the material particles involved or just consider the structures in very simple cases (*i.e.* as homogeneous optically isotropic and anisotropic particles). On the other hand, the majority of researchers working on material colloidal science and soft condensed matter, concentrate their activity in the search of new materials and approaches to develop colloids aggregations without considering a complete study of their photonics phenomena^[115–118].

Is clear from the number of works in the former two research fields, that the applications and mayor advances come from the permutations and combinations in optics, photonics, microfluidics, chemistry, soft matter, colloids and many others, demonstrating that these fields are fast growing and still experiencing significant revolutions^[119–122]. This is partly due to the diversity of influences and partly due to the fact that mixing non-solid media with solid-state fluidic structures provides a nearly limitless range of combinations. Therefore, recognizing that the physical and chemical properties of materials can regulate photonic responses; the confined chiral nematic liquid crystal systems are just one combination in the interdisciplinary effort to

integrate new ideas from soft matter science with photonics and optical control. They have become also interesting by their very unusual structures and defects^[123,124], and because of the easiness to manipulate the internal structure of the CLC droplets by just controlling the chemical properties of the surrounding medium, enabling to have spherical particles that depending on the helical configurations, become optically isotropic or anisotropic chiral particles^[125].

However, because of their intrinsic chirality, structures of chiral nematic systems are more complicated than those of the nematics. Although some structures of chiral nematic droplets and cylinders have been found experimentally, the relations between those structures and the controlling parameters (elastic constants, temperature, surface anchoring strength, external field, or intrinsic chirality) are hardly known^[126]. Recent theoretical studies on chiral nematic droplets^[127–129] provided a good understanding of these systems, nevertheless, some of their derived results are yet to be tested. In this chapter is presented a method based on the polymerization of LC droplets in water emulsion to create solid chiral microspheres exhibiting different internal helical configurations. We have also investigated the internal configuration geometries obtained by controlling the orientation of the LC molecules of the interface with the surrounding medium (water). Besides their characterization in fluid and solid state, some discussion regarding selected physical properties including size, anchoring, optical properties, surface texture and supramolecular internal chirality is also included.

3.2 Chiral liquid crystals

3.2.1 Chirality

Chirality is a relevant aspect of biology, chemistry and physics^[130–133]. An object is considered chiral if its mirror image cannot be brought to coincide with itself by any sequence of simple rotations and translations^[134]. In relation with this, helices are arguably one of the most elegant examples of chiral structures and useful to introduce some important concepts. A helix is characterized by its periodicity (pitch p), defined as the distance necessary to have a rotation from 0 to 2π , its wavenumber $q = \frac{2\pi}{p}$ and by its handedness, which is defined as positive for a right-handed or clockwise twist and negative for a left-handed or counter-clockwise twist (see figure 3.1).

At supramolecular level, chirality is present in molecules^[135,136], clusters^[137], crystals^[138] and metamaterials^[139,140]. It can be detected by differences in the optical response of a substance to right- and left- handed circularly polarized light^[135,136]. In liquid crystals, due to their high capacity of self assembling in a variety of supramolecular arrangements exhibiting high response functions, the chirality is present in the cholesteric liquid crystals (CLC) phases^[1,2,141] and can

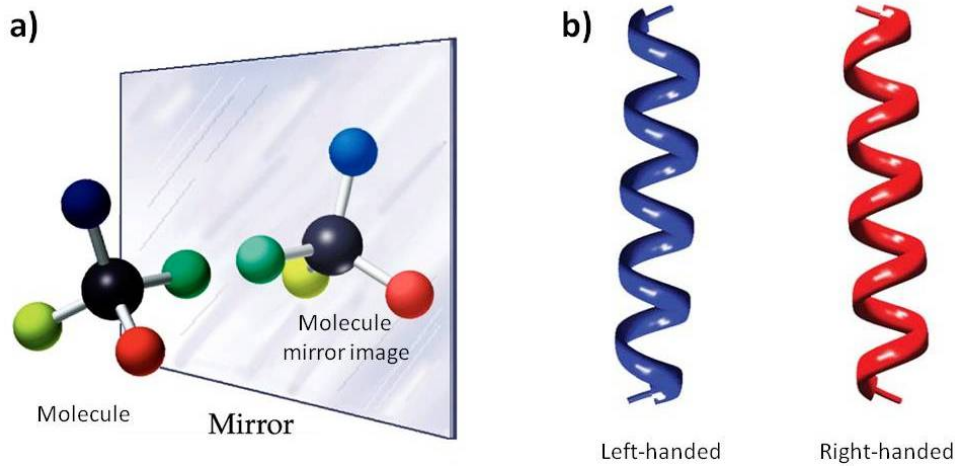


Figure 3.1: Schematic representation of chirality - (a) Is an example of the simplest chiral molecule - a carbon with 4 different atoms bonded to it. The molecule mirror image and the molecule itself cannot be superimposed by the means of rotations. (b) A left-handed and a right-handed helix.

be defined by:

$$q = \frac{1}{p}, \quad (3.1)$$

where p is the pitch of cholesteric LC. Experimentally, chirality can be easily obtained in several different ways, for example, directly introduced within the molecule by incorporation of chiral elements (mostly chiral centers)^[126]. Another popular way, especially for materials used in applications is the addition of a chiral dopant molecule to a non-chiral host phase. This was the method used in our investigation to obtain the two kinds of chiral particles analyzed: cholesteric LC droplets and solid-polymerized cholesteric LC particles.

3.2.2 Doping nematic LCs with chiral molecules

As was described by G. Friedel when discovered the first LC, even a small amount of chiral solute transforms a nematic LC into a cholesteric LC^[142]. The chiral dopant can be mesogenic itself, but not necessarily and it is enough that it dissolves in the nematic host. After dissolving chiral molecules in a nematic LC, the molecular structure undergoes a helical distortion, *i.e.* spatial twisting of the molecules perpendicular to the director, quantified by the helical pitch and handedness, which depends on its chemical structure and absolute configuration^[1,2,141]. The obtained helix might be right-handed or left-handed (according with the choice of chiral dopant).

At low dopant concentration, the inverse pitch increases proportionally to the amount of enantiomerically pure dopant, and the slope is a specific property of each dopant for a given nematic

host. A quantitative description of the cholesteric induction requires the definition of the “helical twisting power” (HTP), which characterizes the ability of a chiral dopant to twist a nematic mesophase:

$$HTP = \frac{1}{p\beta ee} \quad (3.2)$$

where p is the cholesteric pitch, β is the concentration of the chiral dopant and ee its enantiomeric excess. In the case of a mixture of dopants, the resulting HTP is the sum of the individual contributions:

$$HTP = \sum_i x_i HTP_i \quad (3.3)$$

where x_i is the molar fraction of i component ($\sum_i x_i = 1$) and HTP_i is the corresponding helical twisting power. The equation 3.3 applies also when a dopant presents different conformers, which can be seen as a special case of a mixture.

3.2.3 Selective reflection in CLC

Using the previous equations, it is possible to adjust and choose the length range for the required pitch to use on the experiments according to the laser wavelength. If the spatial periodicity (the period of the helix) is close to the wavelength of light, a range of “forbidden” frequencies called a photonic bandgap (PBG) appears. Photons with energies lying in the bandgap cannot propagate through the medium since the wavenumbers are pure imaginary, this gives origin to the unique effect of selective reflection of light. Then, the selective reflection of light is a result of the spatially periodic variation of the dielectric tensor in a helical structure. For light propagating parallel to the helical axis, Bragg reflection occurs when the wavelength is in the following range¹:

$$n_{\perp} p < \lambda < n_{\parallel} p \quad (3.4)$$

where p is the pitch of the CLC structure, $n = (n_{\parallel} + n_{\perp})/2$ is the average refractive index with n_{\parallel} and n_{\perp} being the refractive indices parallel and perpendicular to the director. The Bragg reflected light is circularly polarized if the incident wave propagates along the helical axis. In a left-handed CLC structure, only the right-handed circularly (RHC) polarized component is transmitted through the medium, whereas the left-handed circularly (LHC) component is strongly reflected see figure (3.2).

The polarization state of the reflected and transmitted waves depends on the pitch length and the selectively reflected wave is a helix, such that (at any instant t) the electric field in the reflected light is circularly polarized with the same handedness as the chiral nematic helix. On the contrary, light with the same wavelength but opposite circular polarization is transmitted

¹This spectral regime is called Bragg regime when total reflection occurs. There are three other spectral regimes called: Mauguin regime ($\lambda \ll 0.5p\Delta n$), circular regime ($0.5np\Delta n \ll \lambda \ll p$) and circular regime in the long wavelength ($n_{\parallel}p \ll \lambda$). Each one with a different description and properties^[2].

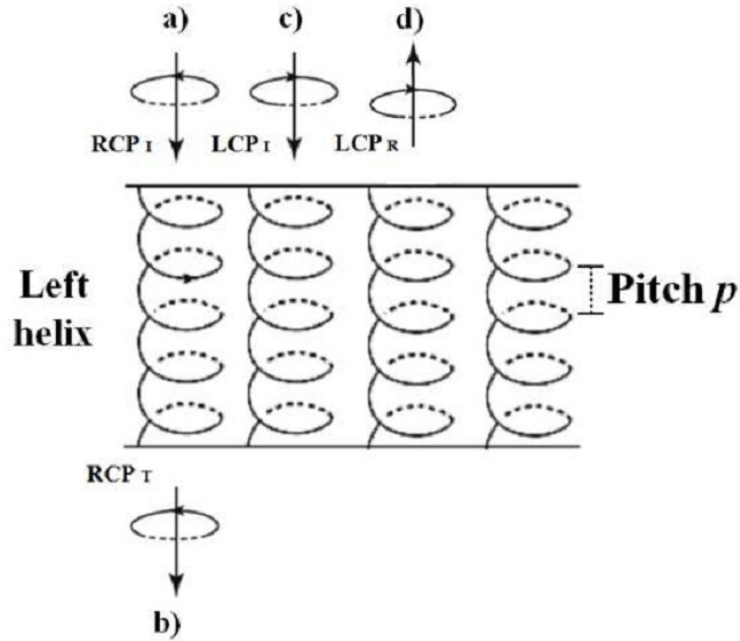


Figure 3.2: Bragg reflection and transmission by a film of left-handed CLC in a glass cell with planar texture - a) The incident right circular polarized light (RCP) is transmitted through the left cholesteric helix; the transmitted light b) goes out practically unchanged. In c) an incident left circular polarized light (LCP) impinges on the sample and the reflected wave d) is an image of the cholesteric helix with LCP, translated upwards.

through the cholesteric helix practically unchanged^[1,2]. This is distinctly different from the reflection from a metal mirror, where it is known that the handedness of a beam of circularly polarized light is reversed on reflection.

The central wavelength λ_0 and the spectral width $\Delta\lambda$ of the reflected light are related to the pitch, the average refractive index n and Δn of the material by the following equations:

$$\lambda_0 = p \frac{n_{\parallel} + n_{\perp}}{2}, \quad (3.5)$$

and

$$\Delta\lambda = p\Delta n, \quad (3.6)$$

where $\Delta n = n_{\parallel} - n_{\perp}$ is the optical anisotropy of the material.

In figure 3.3 are reported the measurements of the optical transmission for several thin films of the material used for the experiments (RMS03-001C by Merck) between glass slides with planar alignment at different concentrations of chiral dopant (ZLI-811, Merck). The graphic shows a shift from red towards blue-violet as the percentage concentration of chiral molecules is increased. The qualitative behavior for the measure at 20% wt is indicated as reference of the shift, but the quality of the sample was not at the level of the others, this explains the different behavior with respect to the other samples.

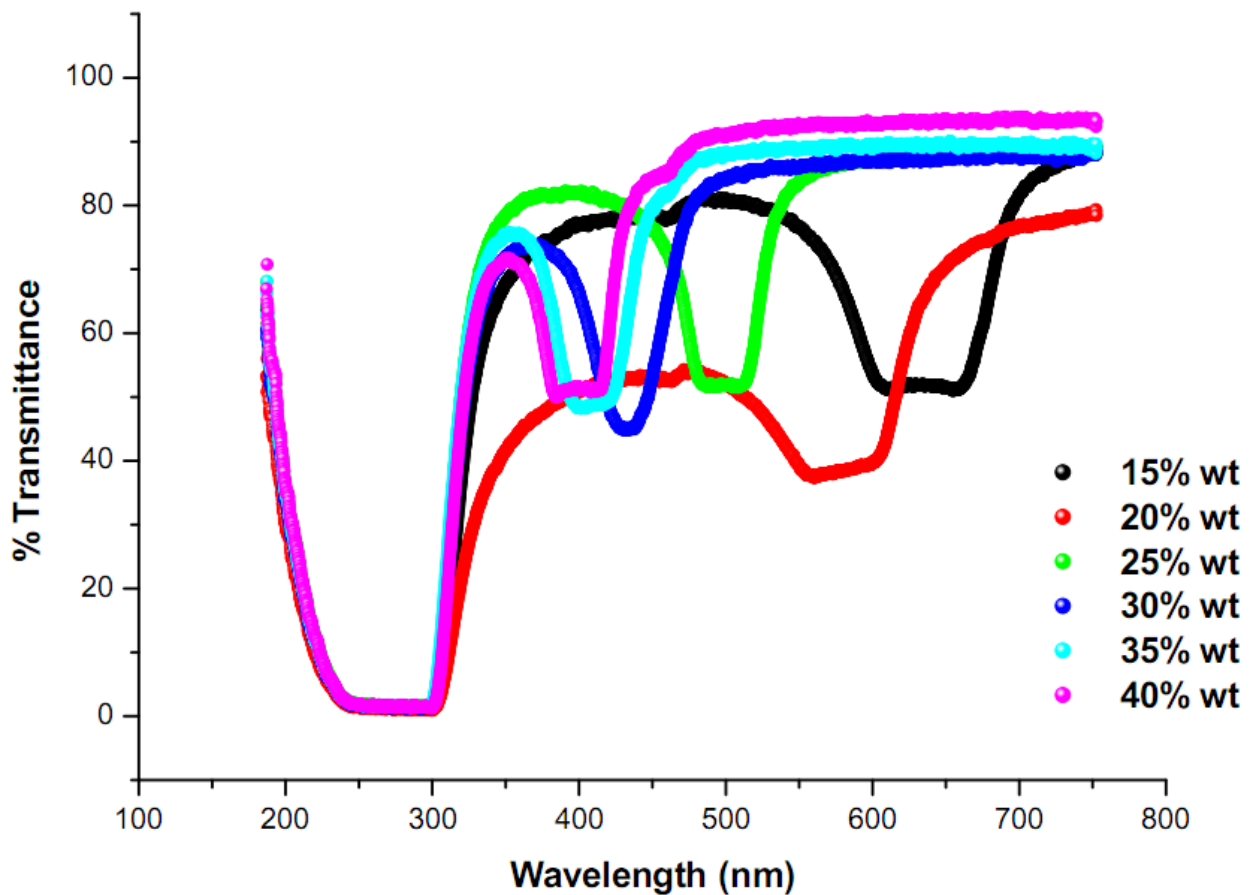


Figure 3.3: Transmission for left-handed CLC films - Spectrum graphic of selective reflectivity versus wavelength for film cells of CLC with planar texture, showing a shift from red towards blue-violet as the concentration of chiral agent increased.

In addition, no difference on the bandgap position was observed for LC cells with planar alignment and non-planar alignment, the position was the same but in planar cells the bandgap was well defined. The reflection band was detected by optical transmission spectroscopy (Avaspec-2048 spectrometer with spectral resolution of 2 nm) and the bandwidth is related to the pitch by equation (3.6). The reflection band of the polymerized film has the same shape that the fluid film before the polymerization process and only shows a blue shift of about 10 nm, connected to a reduction of the cholesteric pitch which can be accounted by the polymer shrinkage. In reflection mode, because λ is in the visible region, the CLC shows an iridescent reflected color which can be influenced by the temperature, the external forces, magnetic field, electric field and chemical compositions. In our case, the selective reflection was directly observed through the color of the cells (as the cell in figure 4.1 in the next chapter).

3.2.4 Cholesteric pitch and particle size diameter

The CLC droplets exhibit complex confined geometries of the chiral structures that result from the combination of several physical-chemical effects and geometrical parameters. The director field configuration within a chiral nematic droplet depends strongly on the droplet diameter d and the helicoidal pitch p . This means that if the diameter d of the particle is comparable with the helical pitch p , as is represented in figure 3.4a, only a single twist of the molecular director structure can be observed, however if the relation between both is such that the pitch is smaller than the diameter. A more complex configuration occurs due to the number of twist or rotations in the helix along the diameter distance inside the sphere (figure 3.4b). For the

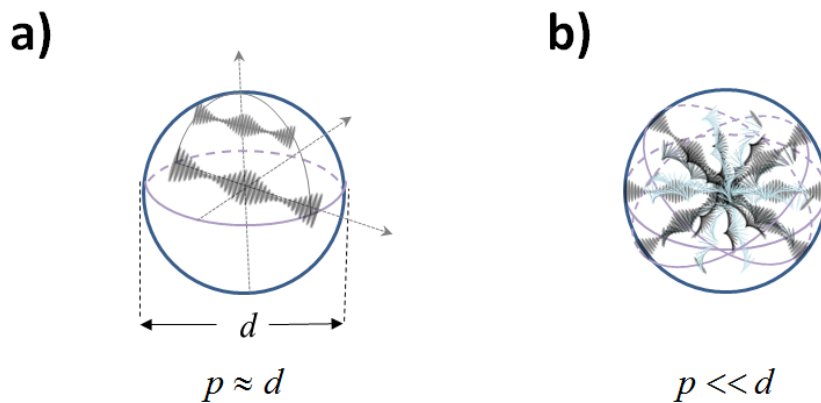


Figure 3.4: Schematic representation in 3D of the internal helix in CLC particles -
a) Simple configuration structure when $p \approx d$; b) complex configuration due to many rotations in the helix along the diameter when $p \ll d$

diameter size and length pitch proportion there are three main regimes, which are showed on figures 3.5 and 3.6.

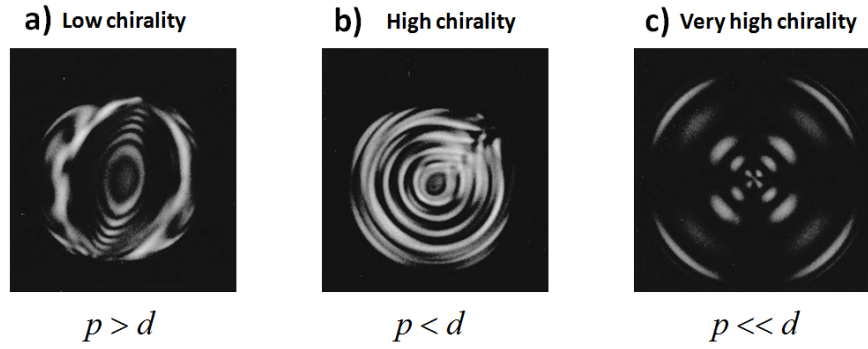


Figure 3.5: Examples of chiral droplets at different dopant concentration - The photographs were taken between crossed polarizers^[126], showing spherical droplets at a) low chirality $p > d$, b) high chirality $p < d$, and very high chirality $p \ll d$.

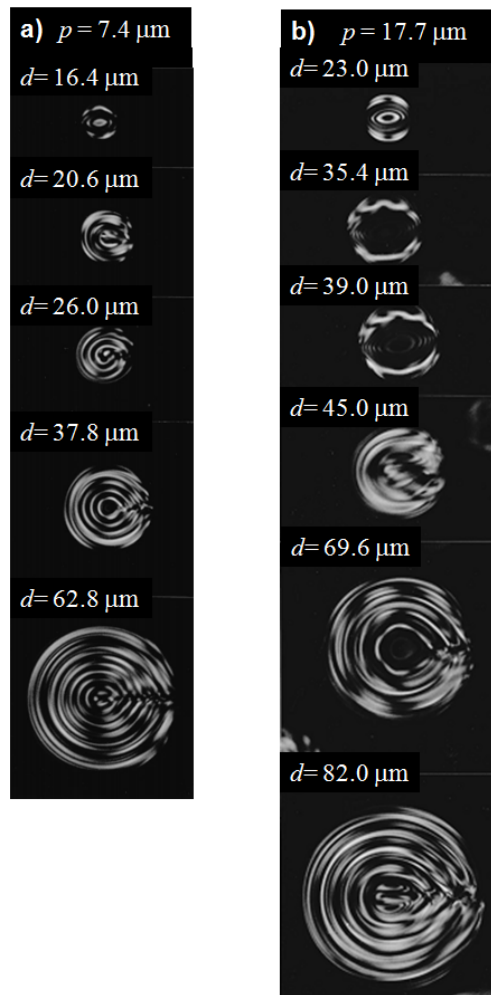


Figure 3.6: Evolution texture with pitch and size diameter - Images taken from reference^[126]

3.3 CLC particles: sample preparation and experimental description

For low chirality ($p > d$) the observed and simulated structure is twisted bipolar according with reference^[127], the structure differs from that for nematic twisted bipolar droplet in that the chiral nematic droplet has more twist than the nematic droplet. For high chirality ($p < d$) the structure is the radial defect or Frank-Price structure; *i.e.* a line defect along a radius, also can be manifested as a line defect along a diameter or as a spiral pattern with no disclination^[126]. The third regime occurs when ($p \ll d$); although the appearance is much different with respect to the former, the structure is still of the kind Frank-Price. The appearance of this CLC droplet observed between crossed polarizers is very similar to that of a nematic droplet with radial director, as was shown in figures 1.10 and 2.3. But in the case of nematic droplets there is radial configuration of the molecular director along the optical axis, while in the case of CLC, the molecular director orientation twist is an helical structure inside the droplets. Other factors that may affect the structure of the droplets are the elastic constant ratios, the surface anchoring strength and the dielectric (or magnetic) anisotropy when an external field is applied^[126].

The particle diameter can often be controlled through physical properties of the materials, such as polymer and surfactant concentration, or through the experimental parameters of the fabrication method, for example the mixing method (vortexing, sonication, stirring), nozzle/capillary diameter and material flow rate. A detailed review of fabrication methods is beyond the scope of this thesis.

On the other hand, the choice of short and long pitches of CLC allow to obtain and identify different kinds of self-organized cholesteric structures. If the helical pitch is smaller than the light wavelength, the periodic medium can be conveniently treated in optics as macroscopically homogeneous, as usual for solid crystals. While, in the case of cholesterics of large pitch, p is typically in the range of $10 - 50\mu m$ and is much larger than the optical wavelength λ .

3.3 CLC particles: sample preparation and experimental description

The cholesteric liquid crystal phases were obtained using the reactive mesogen contained in RMS03-001C solution by Merck, Germany. The pure reactive mesogen was separated from the solvent PGMEA (propylene glycol monomethyl ether acetate) in the RMS03-001C using vacuum evaporation at $90^\circ C$ overnight. The obtained reactive mesogen was mixed with left-handed chiral dopant ZLI-811 (Merck, Germany) at the specific concentration to obtain the selected pitch. After this process, the CLC droplets emulsions were prepared by adding pure water to obtain a 0.5% wt concentration of the chiral active mixture of the mesogen and chiral dopant. Due to its hydrophobicity, the CLC droplets acquired a spherical shape and a parallel anchoring of the LC molecules at the water interface; as the previous section mentioned, the

internal configuration differed depending on the ratio of the diameter of droplets d and the cholesteric pitch p ^[126,143,144]. There was no observable tendency for the director to drive the droplet shape away from that of a sphere inside the emulsion or tendency in the spheres to join between them. Shaking the suspensions at 35 Hz and 60°C for one minute in a laboratory vortex mixer, the obtained droplets diameters d ranged from 1 μm to 40 μm .

The emulsions were prepared to concentrate the observations in two regimes: low chirality ($p > d$) and very high chirality ($p \ll d$). Besides, knowing that the addition of a surfactant promotes perpendicular anchoring at the interface resulting in different supramolecular structures inside the microspheres. A small quantity of a surfactant (cleaning compound Ausilab 300 from Carlo Erba, 0.02% wt) was added in the water to promote the perpendicular orientation of the LC molecules at the interface. The combination between the helical arrangement and the director orientation at the water interface and the LC, results in an ordering reflecting the competition between bulk and interfacial physical-chemical factors. In this way, were obtained optically anisotropic spherical particles, whose formation is driven by interactions arising from the molecular orientation in the spherical volume and we identify the nature of these interactions, demonstrating that they can be controlled by the anchoring of the liquid crystal molecules at the surfaces of the particles.

Two different concentrations of the chiral dopant were used, namely 23% and 10%. The higher concentration gave a reflection band of the CLC within the visible range, centered in the green region, which was used to investigate the optical properties of the chiral spherical particles and the optical control by means of polarized tweezers. The lower concentration, led to the formation of a helical periodicity of the cholesteric in the micrometer range, facilitating the optical microscopy examination of the helicoidal structures. Finally, the solid chiral particles were obtained by exposing the CLC water emulsions of droplets to UV radiation. The polymerization of the CLC droplets was performed using an UV lamp ($\lambda = 365 \text{ nm}$) with an intensity of about 2 mW cm^{-2} and emission centered at 350 nm. The UV curing lasted for 6 hours at room temperature under dry nitrogen flux. A measure of the reflection band on a thin film of the CLC after the polymerization, indicated an expected phase shift of $\sim 10 \text{ nm}$ due to the polymer shrinkage. All the CLC microspheres were stable, preserving their internal structure during the experiments.

3.4 Optical characterization

Optical microscope investigation of the particles was performed to study the internal director configuration of the particles in both cases: CLC droplets and solid microspheres in the short pitch regime. A 100X microscope objective has been adopted. Moreover CLC droplets in

3.4 Optical characterization

pure water emulsion and water-surfactant emulsion before and after polymerization have been studied. The typical diameter of the particle range from 5-20 μm .

For the precursor CLC droplets and solid microspheres with cholesteric pitch in the visible range, a parallel anchoring of the LC molecules was self-organized at the interface in pure water, the microscope observations in transmission mode between crossed polarizers on figure 3.7 (first column) showed the cross pattern. This pattern is typically observed for optically isotropic particles, fluid or solid; in our case, it suggests as in the case of the nematic droplets, an isotropic supramolecular geometry. On the other hand, the observations in reflection mode (second column) on figure 3.7 revealed a central colored spot that was independent of the particle orientation, *i.e.* showed omni directional selective reflection. This last observation suggests that the expected supramolecular isotropic geometry is a radial spherical structure of the cholesteric helical axes with a central bulk defect. On the third column in figure 3.7 is showed a representation on 3D of the helical internal configuration.

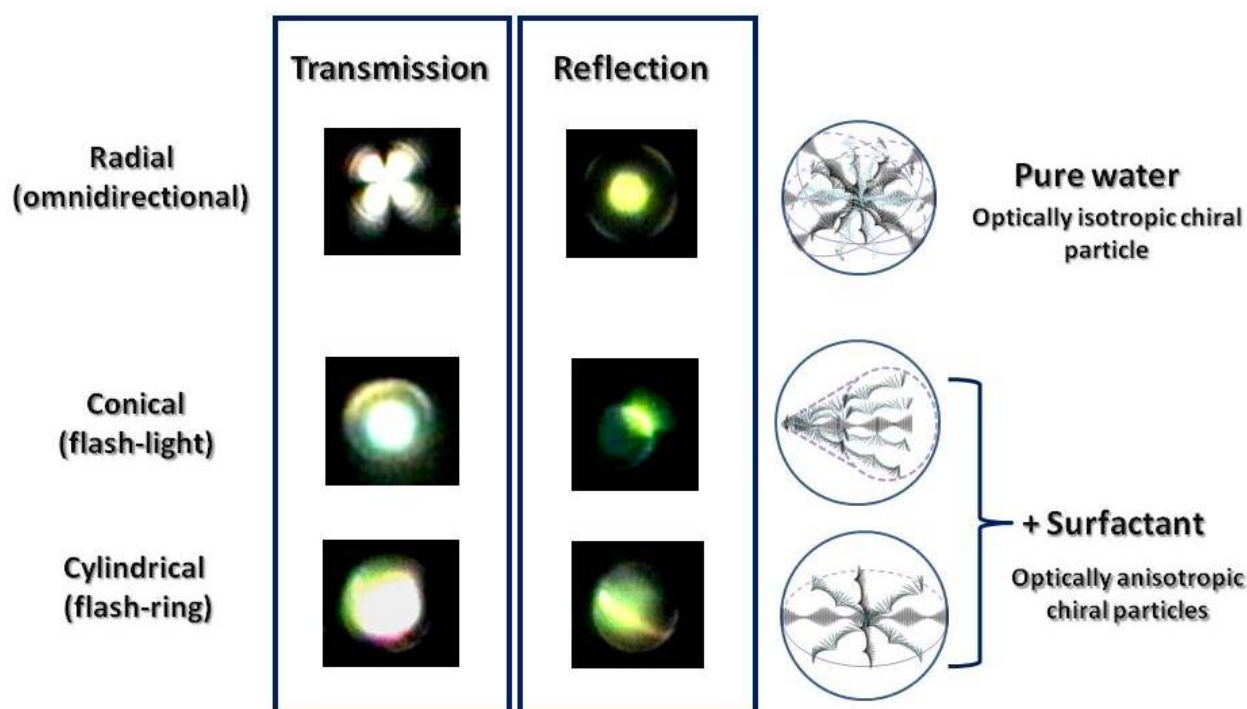


Figure 3.7: Solid chiral microspheres with $p \ll d$ (Short pitch) - In the first column are shown microscopic images taken in transmission view through crossed polarizers. The second column show the observation of the same particles on reflection mode view through crossed polarizers. The last column shows a schematic configuration on 3D of the internal helicoidal structures inside each kind of sphere

In case of CLC droplets and polymeric beads created in water-surfactant emulsions, the microscope observation in transmission mode between crossed polarizers makes evidence of the difference with respect to the radial particles (showed in the first row of figure 3.7). Here, a bright spot of a optically anisotropic (birefringent) particle is observed (second and third row).

For the optically anisotropic particles, two types of organization of the helical structures have been recognized combining this observation with the ones obtained in reflection mode and reported in the reference^[125]. A conical configuration (flash-light type) of the cholesteric helical axes, on the second row, where the central bulk defect move towards a peripheral region of the droplets (or particles), and a diametrical configuration with a cylindrical symmetry and a ring reflection (flash-ring type) on the third row, where the radial helical structure originating from the center of the microsphere with helicoidal axes perpendicular to the surface is present only at an equatorial region, can be envisaged. The observations, suggested that the helicoidal structures with axes almost perpendicular to the droplets surface are preserved only in some regions inside the particle as indicate the 3D diagrams^[125].

To proof that the observed microspheres where really solid after the photo-polymerization, it was investigated the presence of residual spheres on the glass substrate after the water evaporation for two kinds of particles observed with the microscope in reflection mode to distinguish between them, on figure 3.8 are presented the photographs of different samples.

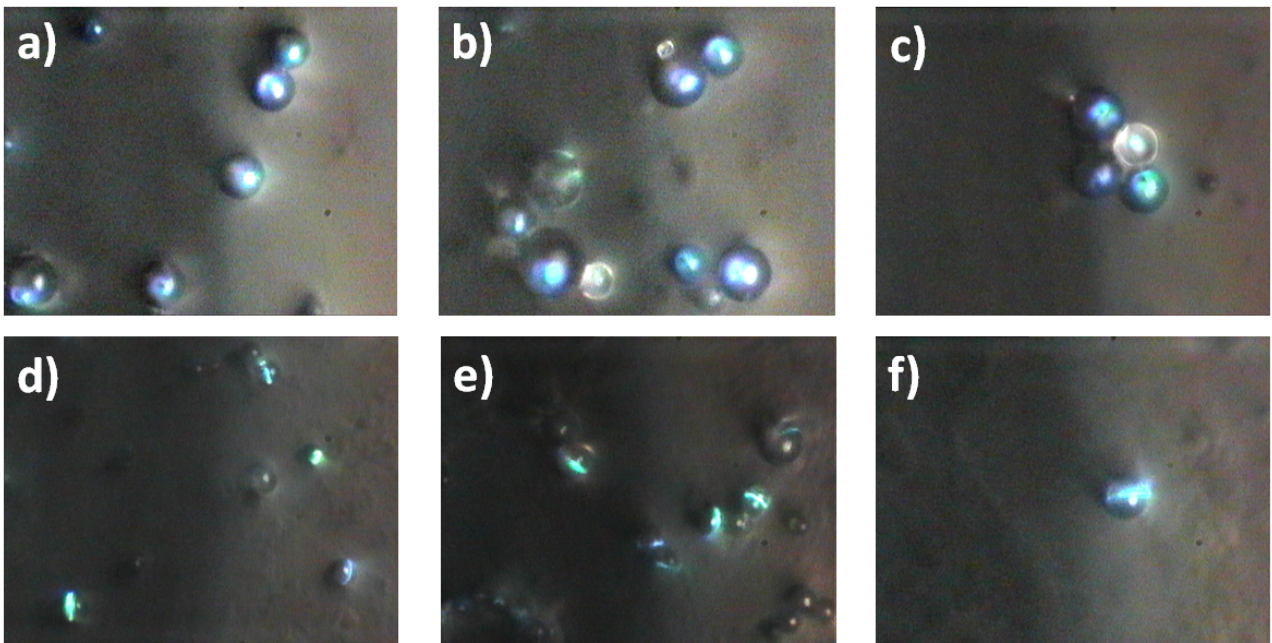


Figure 3.8: Solid chiral microspheres with $p \ll d$ deposited on a glass substrate
 - From a) to c) correspond to prevalent radial solid particles deposited on the glass, when are illuminated with white light, they exhibit an omnidirectional selective reflection; while from d) to f) the prevalent solid particles are optically anisotropic exhibiting the flash-ring reflection at some localized parts.

To get a better understanding of the frozen internal structures on the microspheres, optical microscopy was used to investigate the polymer particles obtained from CLC droplets with helical periods in the micrometer range and again emulsion with and without surfactant. The

figure 3.9 show the different kinds of particles observed when $p < d$ (long pitch) and the representation of the internal structures based on the observations under microscope.

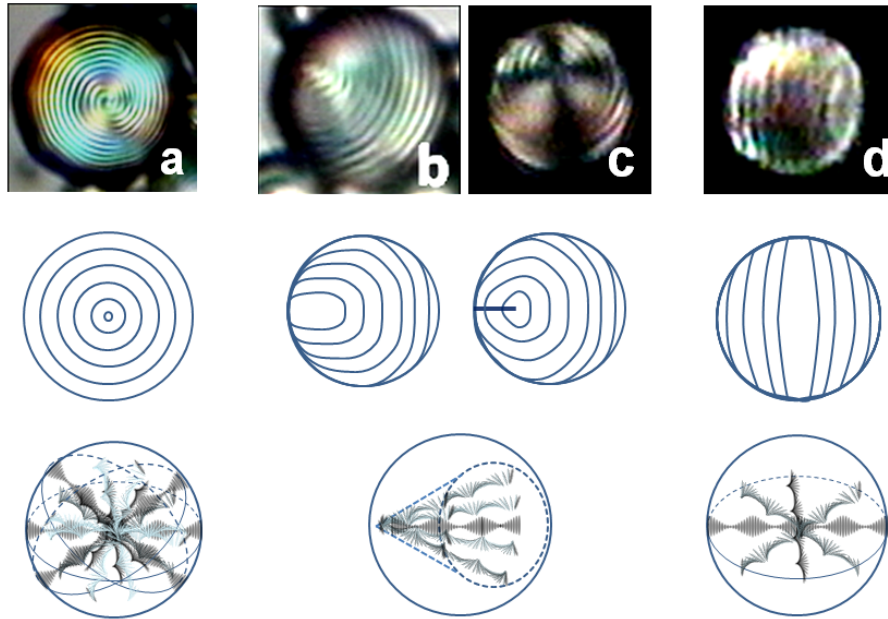


Figure 3.9: Solid chiral microspheres with long-pitch ($p < d$) - In the first row are shown the microscope photographs taken from the different samples. a) CLC in pure water (optically isotropic), from b) to d) the particles are CLC in water with surfactant (optically anisotropic). In the second row is depicted a model for the arrangement of the cholesteric layers on the surface of the spheres. The last row shows a schematic representation on 3D of the internal configuration for the different helicoidal structures inside each kind of sphere

In figure 3.9a appears the microscopy image of a typical solid microsphere obtained in a pure water emulsion. The alternating dark and bright concentric shells suggest a radial helical structure, which is originated from the center of the sphere and give rise to concentric shells of constant refractive index, such that the radial period corresponds to one-half of the cholesteric pitch. The figure 3.9b) and c) show images of the solid microspheres obtained in surfactant-water emulsions, which led to the formation of spherulite-like CLC spheres induced by intermediate (between 0° and 90°) anchoring conditions at the interface^[125,143,145]. Combining the investigations for the cases of short and long pitch microspheres, it was possible to model the internal configurations of the primitive CLC droplets. Figure 3.9b shows the arrangement of the cholesteric layers promoted by a perpendicular orientation of the LC molecules at the interface^[145]; the parallel layers undergo a deformation connected to the curvature of the droplet surface, becoming similar to a cup. As a result, the microsphere looks like a series of nested cups^[145].

For stronger layers deformation (Figure 3.9c and d), some of the cups become closed, giving rise to radial or diametrical singularities^[144]. In such instances, a configuration with a radial helical

structure that originates from the center of the sphere is expected only at an equatorial region^[125,143,145]. Therefore, helicoidal axes perpendicular to the surface are expected only inside an equatorial belt. The schemes reported in Figure 3.9 are consistent with the corresponding short pitch polymeric microspheres in figure 3.7 showing equatorial and conical selective reflection. If the 3D director geometry in figure 3.9d is depicted for all equatorial planes, a schematic representation of the chiral sphere with a global isotropic arrangement of the helical structures can be obtained (3D scheme for figure 3.9a), *i.e.* where the helical axes coming from the center are everywhere perpendicular to the sphere surface. Evidently, this scheme is consistent with the optical properties of the corresponding short pitch polymeric microspheres (Figure 3.7).

Besides the optical microscope characterization, the observation of the chiral particles with alternative and more sophisticated microscopy techniques such as scanning electron microscope (SEM) and transmission electron microscopy (TEM)¹, demonstrate that the internal configuration of the microspheres is fully preserved even after the polymerization. As a result were obtained the following images.

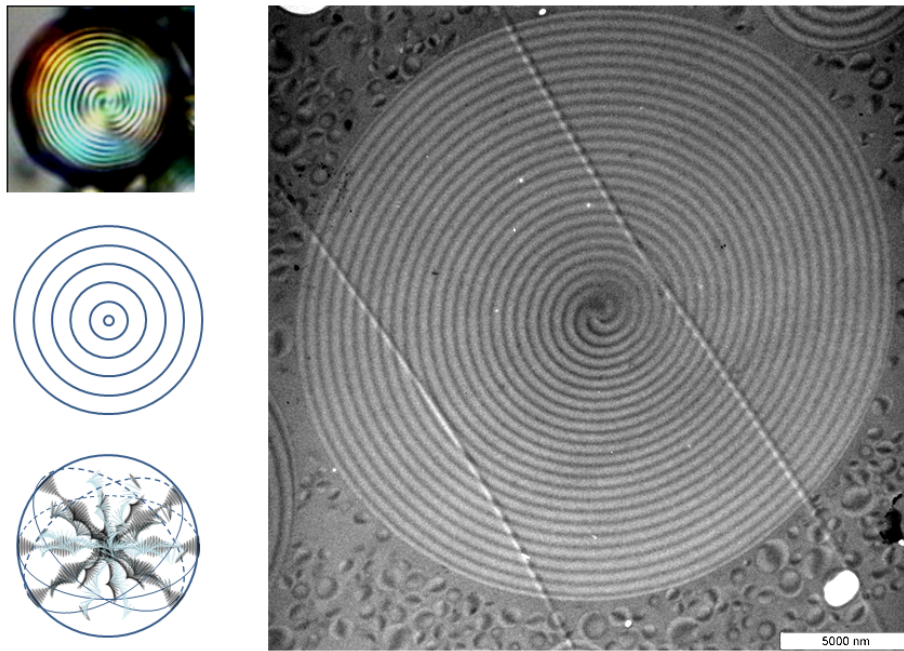


Figure 3.10: TEM observation of a radial chiral microsphere - TEM observation of a radial chiral microsphere, as comparison in the top of the column is shown the microscopic photograph taken in transmission for the radial sphere with diameter $d \sim 20 \mu m$. Below are shown the arrangement of the cholesteric layers and the 3D schematic configuration of the helicoidal structures

¹SEM images were obtained and provided by courtesy of Giovanni Desiderio from Dipartimento di Fisica; and TEM images were obtained and provided by courtesy of Enrico Perrota from Dipartimento di Ecologia e Laboratorio di Microscopia Elettronica, both from University of Calabria.

3.4 Optical characterization

In the case of optically anisotropic particles, more than one kind of structure was observed, in the images are pointed with the arrows the two types that can be easily distinguished. Many of the other kinds of internal arrangements correspond to intermediate configurations between the conical and the cylindrical.

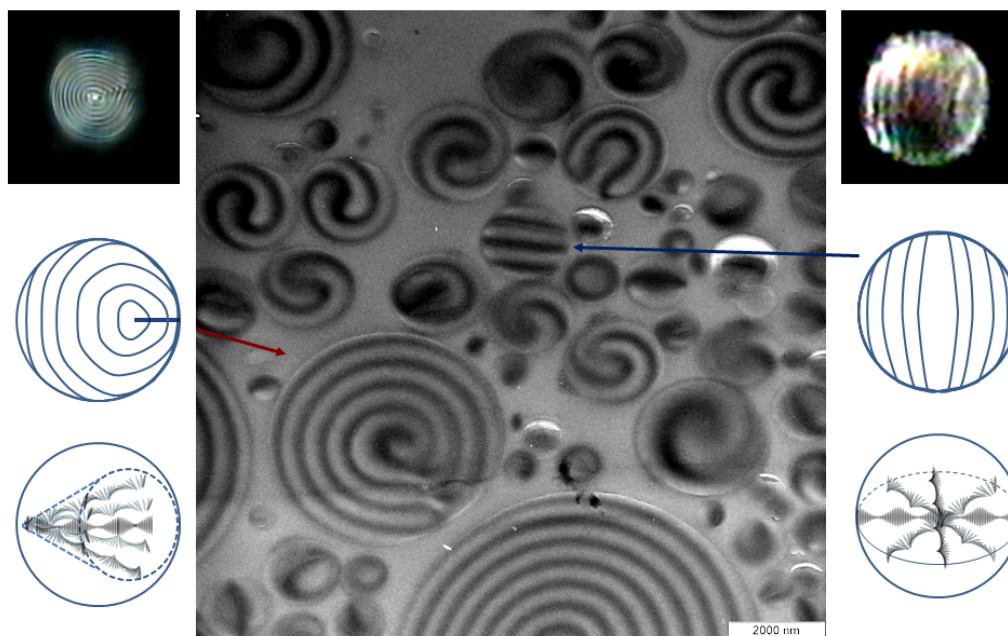


Figure 3.11: TEM observation of anisotropic chiral microsphere - TEM observation of a radial chiral microsphere, as comparison in the top of the column are shown the microscopic photograph taken in transmission mode viewed through crossed polarizers. Below are shown the arrangement of the cholesteric layers and defects and the bottom row shows the 3D schematic configuration of the helicoidal structures

To obtain the TEM images, a beam of electrons was transmitted through an ultra thin layer of the material deposited in a polymeric matrix, interacting with the specimen as it passes through. In our case, the TEM image contrast is due to the absorption of electrons in the material, due to the thickness of the sample and composition of the material revealing the constant refractive index and the concentric shells inside the sphere, suggesting the possibility to use them as optical microcavities, based on spherical Bragg reflectors.

Finally, the morphologies of the polymerized microspheres were examined by scanning electron microscope (SEM). The high resolution SEM images helped to determine the distribution size diameter of the obtained polymerized spheres according to the scale bar as well as a direct observation of the spheres surface.

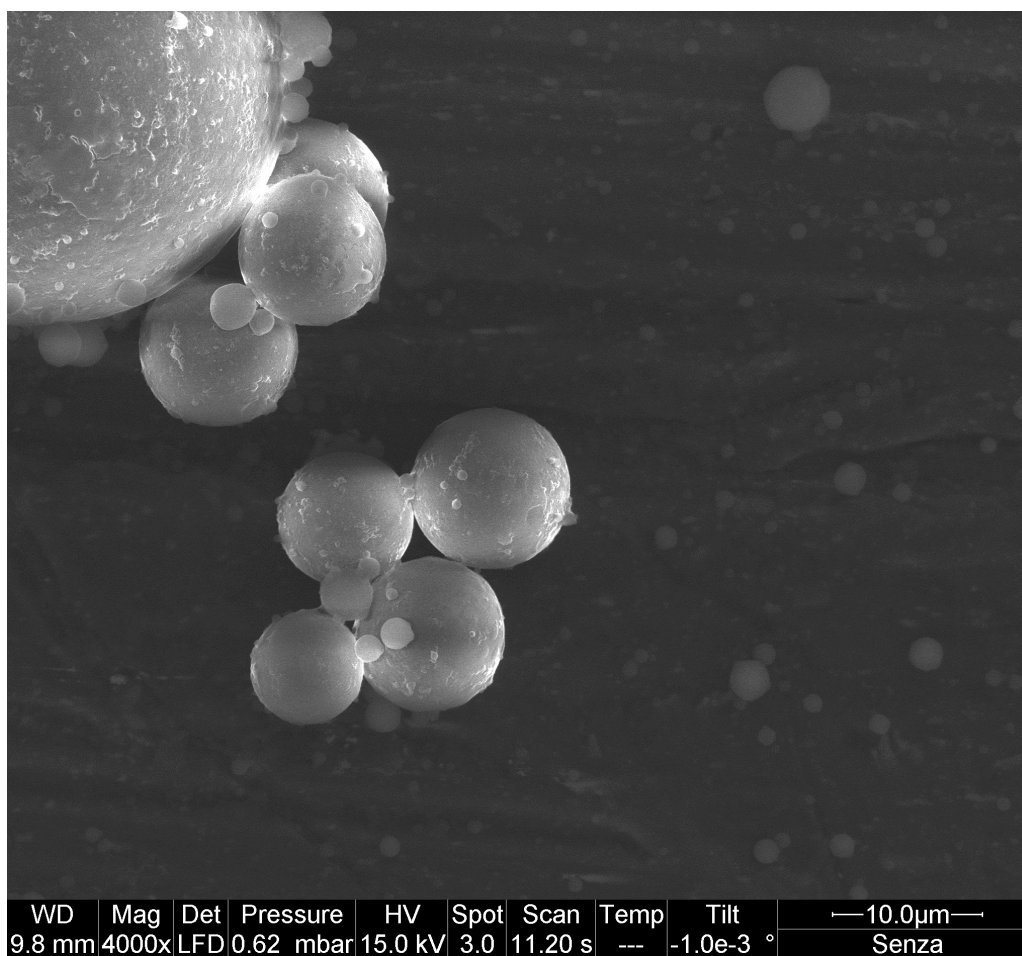


Figure 3.12: SEM observation of the polymerized spheres -

3.5 Conclusions

In conclusion, new chiral microparticles were created via very simple self-assembling processes of soft matter. The developed method is based on the self organization of the LC droplets in water emulsion, where the internal director configuration is controlled by several parameters: the spherical shape is due to the liquid crystal hydrophobicity, the helical structures are related to the presence of a chiral dopant, the orientation of the LC molecules at the surface is established by the physical-chemical properties of the LC water interface.

The use of reactive mesogens enable to solidify the LC droplets in water by means of photopolymerization process. The ability to control the internal helical geometry using dopant agent in the precursor LC emulsion enabled to obtain fluid and solid microspheres with helical structures having radial, conical, and equatorial configurations to which correspond different optical properties.

Polarized optical microscopy, SEM and TEM microscopy techniques enabled to investigate the internal supramolecular structure of the particles and confirmed that the internal molecular configuration of the CLC droplets is fully preserved in the solid microspheres after the polymerization of the droplets.

The methodological approach and the features of these chiral microparticles (both fluid and solid) make them good candidates for developing new concepts in colloidal materials science, microphotronics, microlasers, optical trapping and manipulation, micro- and optofluidics, microsensors, etc. Their unique capabilities will be demonstrated by optical manipulation experiments involving optical tweezers (Chapter 4) and their application as optical microresonators for creating microlasers (Chapter 5).

Part 4

Chiral LC microspheres and optical manipulation

4.1 Introduction

In spite of the increasing attention that has received the effect of optical forces on objects made of chiral materials in connection with new proposed applications, there are only few reports on theoretical treatment and experimental studies^[83,146,147]. In this chapter is presented an investigation of optical manipulation of the chiral LC particles performed with optical tweezers at the proper laser wavelength and polarization. It is demonstrated how the combination of light and the complex internal configuration structures of optically isotropic and optically anisotropic particles (either fluid or solid), results in an exclusive particle dynamics connected with the selective reflection of the cholesteric phase. The chiral particles studied have the optically isotropic configuration (radial) and optically anisotropic configuration (conical, cylindrical and bipolar). leading to characteristic features for each kind of particle.

The promising ability of polarized light to switch repeatedly the dynamics of chiral objects can be used to engineer novel strategies for optical micro systems. The combination of optical manipulation with other control parameters (electric or magnetic), as well as the integration of other functionalities suggest exciting developments for future applications of these micro-devices in the micro and optofluidics, microphotronics and materials science.

4.1.1 Photonic bandgap in CLC

For the optical manipulation experiments and observations were used CLC with concentration at $\sim 25\%$ of chiral dopant because the selective reflectivity is well located on the Bragg selective reflection band for the laser wavelength at 488 nm, which was used for the experiments. As was

described in the previous chapter (Section 3.2.3), the reflection band was detected by optical transmission spectroscopy of a thin film of CLC between two glasses and the bandwidth was established by adjusting the proper pitch using the equation (3.6). In reflection mode, the selective reflection was directly observed through the color of the cells (See figure 4.1).

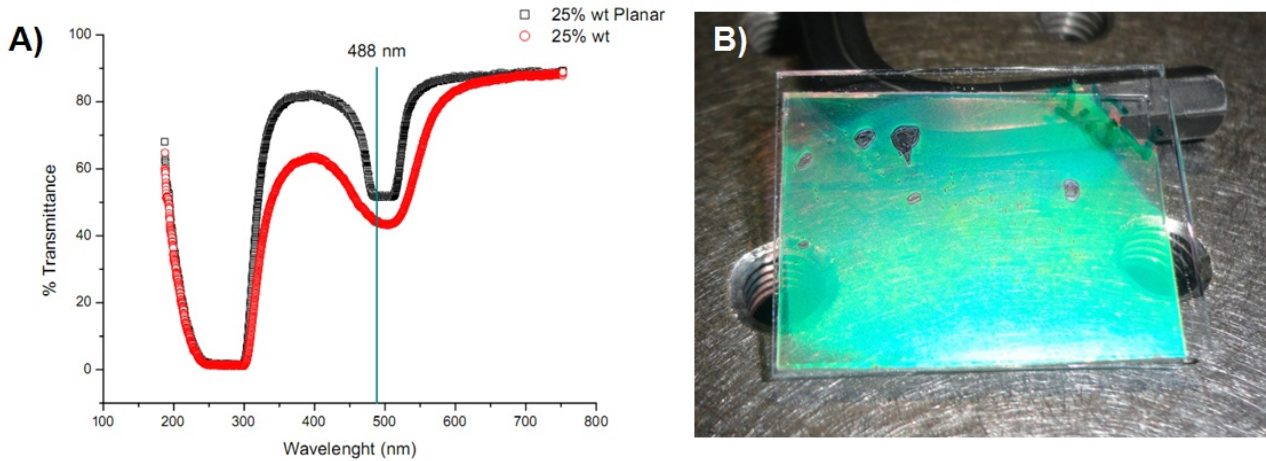


Figure 4.1: Selective reflection for CLC at 25 % - A) Transmission spectrum graphic for a polymerized CLC film between two glass substrates with planar alignment (black line) and without any alignment (red line) for a linearly incident polarized light, the vertical line indicates the value of 488 nm, corresponding at the wavelength of the laser beam used on the experiment. B) Photograph of the cell glass showing a blue-green color due to uniform reflection.

After the characterization of the CLC cell containing the material, the CLC droplets emulsions were obtained following the same procedure described in the section 3.3. In the case of solid particles, taking in account the shrink of the transmission spectrum due to the polymerization process, it was verified that the wavelength of the laser beam used in the optical tweezers still remained inside the spectral regime defined by the equation (3.4) known as bandgap (or stopband).

4.1.2 Optical tweezers setup

The experimental system of optical tweezers employed to investigate the optical manipulation of both chiral isotropic and anisotropic particles, fluid and solid immersed water is depicted on the figure 4.2. It consisted in a single laser beam with circularly polarized light with a wavelength located inside the selective reflection band of our CLC (as shown in the transmission spectrum graphic on figure 4.1). The optical trap was formed using a standard setup for manipulation experiments; *i.e.* an argon ion laser beam at $\lambda = 488 \text{ nm}$ wavelength and power of $\sim 100 \text{ mW}$, was directed towards a $60x$ microscope objective ($N.A. = 0.85$) to focus the beam into a sample chamber containing the CLC droplets dispersed in a water solution. To change the state of polarization of the light beam from linear to circular, a quarter-wave plate ($\lambda/4$) with its axis

oriented at 45° is placed before of the objective; while the insertion of a half-wave plate ($\lambda/2$) before the quarter-wave-plate makes it possible switch from left to right circularly polarized light (LCP and RCP). The sample was placed between a polarizer and the analyzer; illuminated with a white light fiber and imaged onto a charge-coupled device (CCD) camera, the sample position was adjusted using a precision three-axis (x, y, z) translation stage.

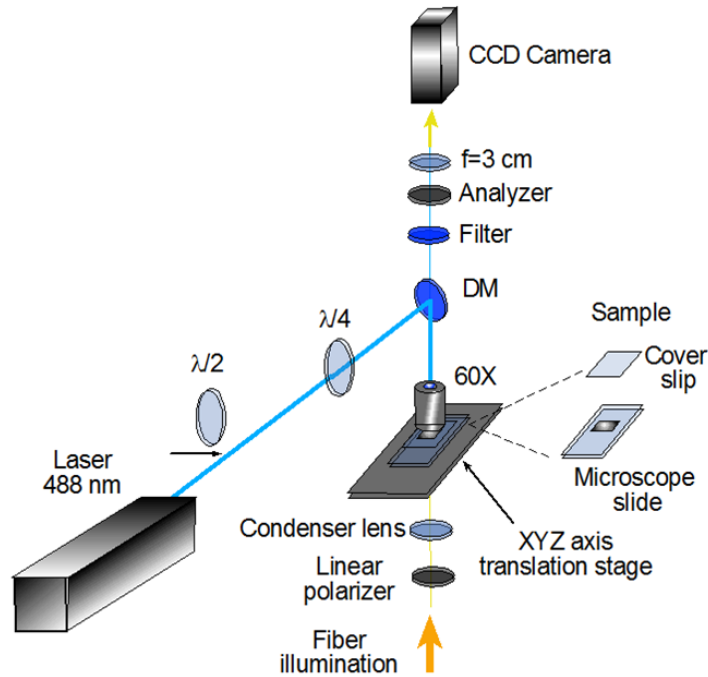


Figure 4.2: Experimental setup -

4.2 Experimental results and discussion

The dynamical behavior of the chiral particles (fluid and solid) with both configurations optically isotropic particles (radial configuration) and optically anisotropic (bipolar, conical and cylindrical configuration) has been experimentally investigated exploiting circular polarization left and right (LCP and RCP), of the optical tweezers. The observation of the same dynamics for both fluid and solid particles and the observation of the particles with microscopy techniques (SEM and TEM from the previous chapter), demonstrate that the internal configuration of the microspheres is fully preserved even after the polymerization. This dynamic never seen before consists in that the light can exert both a repulsive or attractive force on the same particle depending on the handedness of its circular polarization.

4.2.1 Dynamics for radial optically isotropic particles

In the case of microspheres with radial configuration of the cholesteric helices (with the cross pattern when are viewed between crossed polarizers), we observe a contrasting behavior of the same particle, attractive or repulsive with respect to the optical trap only by switching the polarization from right circular to left circular (Figures 4.3 and 4.4).

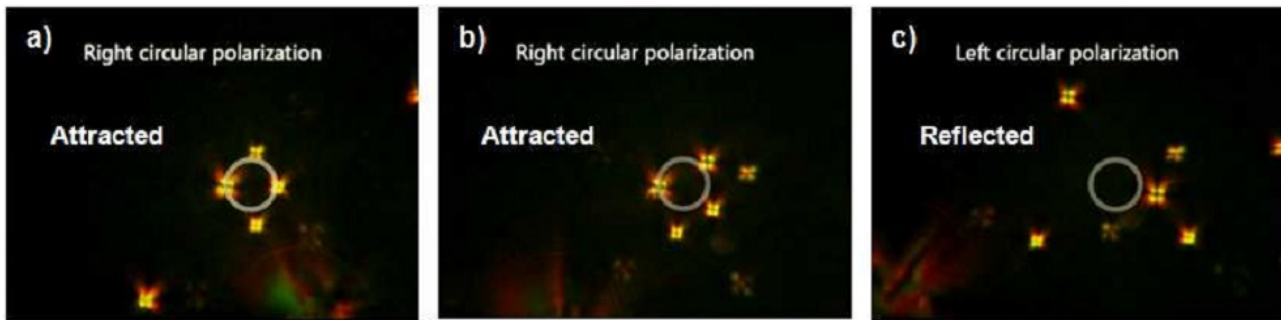


Figure 4.3: Radial isotropic CLC fluid droplets manipulation on circularly right and left polarization - In the figure are shown microscope images of four radial isotropic CLC droplets in water observed between crossed polarizers. a) the usual attractive force aggregates the CLC droplets towards the focal spot (indicated by the circle) of the light beam for right circular polarization, b) due to the strong optical trapping the particles remain in the focal spot and can be translated across the sample, c) changing from right to left circularly polarized light, the droplets experience a strong reflection and the repulsive force dominates, pushing the CLC droplets outside the illuminated region.

As was mentioned for the characterization measurements and according to the experimental observations. No difference was observed on the optical properties for both fluid or solid CLC particles. Although surprising, this unique dynamical behavior can be explained by taking into account the selective reflection of the CLC, the radial configuration of the helical axes inside the particle and the experimental geometry of the optical trap.

In order to explain the particular observed behavior, the optical forces were calculated using a theoretical approach based on the selective reflection property for the cholesteric LC phase and the ray optics approach to simulate the dynamics according to the experimental values and observations. Besides, of great interest is the fact that due to the global-optically isotropy arrangement of the molecules in the particle, no transfer of angular momentum occurs and therefore no rotation of the particle is observed even if it is composed of birefringent material.

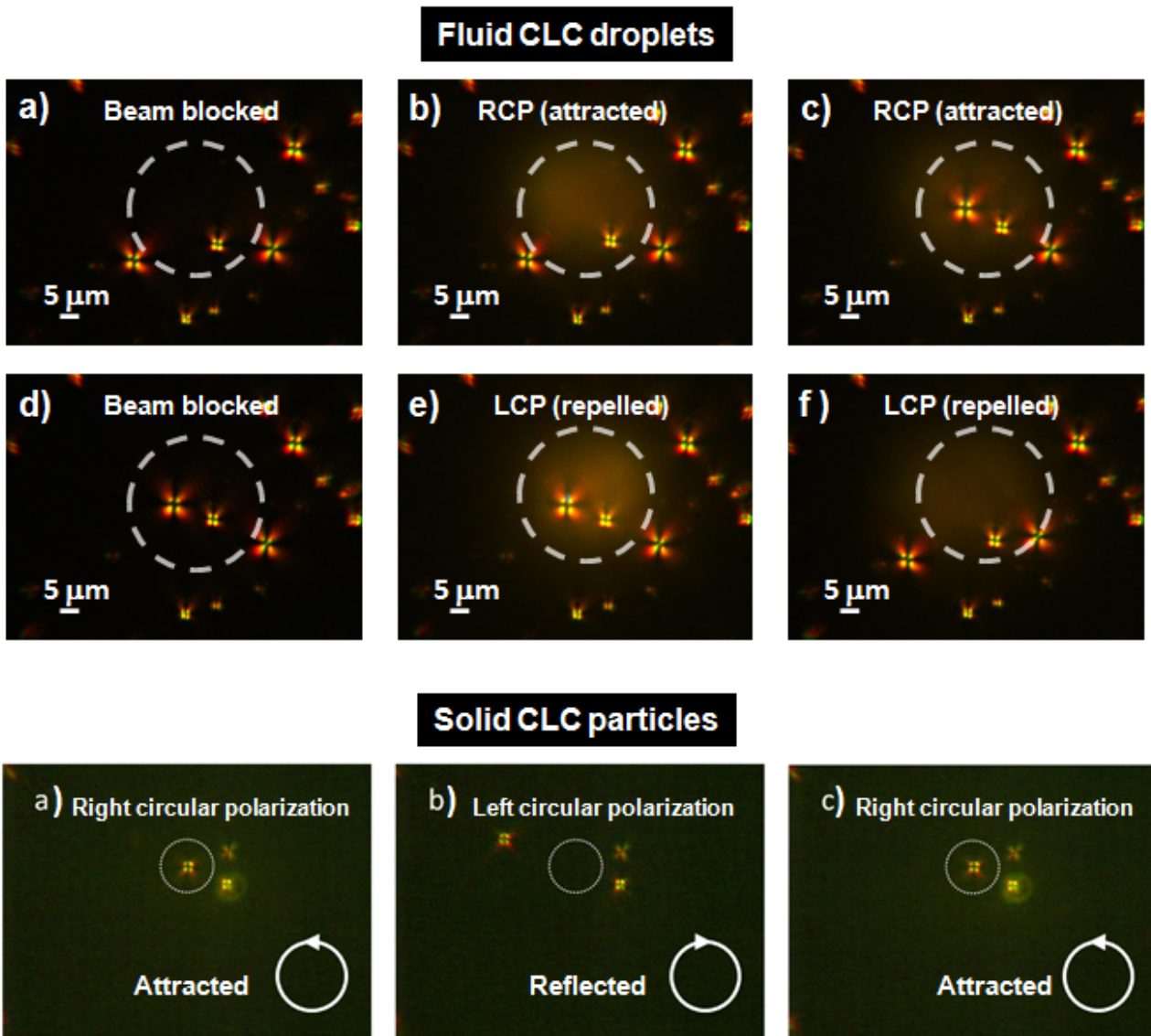


Figure 4.4: Radial isotropic CLC (fluid) droplets and (solid) microspheres attraction-repulsion - Microscope images of radial isotropic CLC particles immersed in water observed between crossed polarizers. In this case the sample is not translated and only the polarization changes. **Fluid CLC droplets:** a) Laser blocked is the initial configuration, b) and c) with laser on; show the particles moving attracted to the spot center for RCP. d) Blocking the beam and changing from RCP to LCP, with the beam passing on e) and f) the particles are moving repelled from the spot, a blue-green dot appears near the center of the particle on e). **Solid CLC microspheres:** For right circular polarization of the laser beam (white solid line circle with arrow) in a) the microsphere is attracted to and held in the optical trap (dotted line circle). In b) the light polarization is switched to left circular and the microsphere moves away from the optical trap, while in c) the light polarization is switched to right circular and the microsphere is trapped again.

4.3 Force simulation for radial isotropic particles

The light that is reflected, refracted or absorbed by small particles in general undergoes a change in momentum, while the particles experience an analogous change in both the direction and magnitude momentum, *i.e.* a resulting force. In order to construct tractable mathematical models of the forces exerted by the light on the particles, it is necessary to resort to a number of simplifications and assumptions. These might include for instance, the assumption of uniformly sized particles, minimal radiometric and heating effects on transparent particles, neglect the Brownian motion of the particles and except for the gravity, consider the absence of extraneous forces such as electrostatic or interfacial forces. In general, good agreement of the theoretical results with available experimental data is usually found in situations where these assumptions are warranted.

On the other hand, the study of the light propagation in a CLC is generally complex, the simple case of propagation nearly along the helical axis, in the Bragg regime, has been deeply studied and described in several papers and books^[1,2]. The selective reflection band at oblique incidence undergoes a blue-shift, ranging from few to tens of nanometers depending on the angle^[2]. However, as long as the wavelength of the laser remains within the stop-band, a deviation from the normal incidence condition, even of some tens of degrees, gives rise to a nearly constant refractive index for circularly polarized wave^[1]. In our experiment, due to the geometry of the radial particles, we can consider this condition satisfied by most of the light rays impinging on the sphere. In addition, since the sizes of the spherical particles are well above the wavelength of the trapping beam, a ray optics model^[26] will be adopted to describe the qualitative behavior of the optical trap and to evaluate the net optical force for both circular polarizations.

Under this approach, the light beam will be decomposed into individual rays that propagate in straight lines in the media. The electromagnetic wave on the frontier of two different mediums with different refractive indices will be separated, one part will be refracted and also will be partially reflected and the other part will be transmitted, the ratio of reflected light and transmitted light is calculated by mean of the transmittance (T) and the reflectivity (R). Following this treatment, we start for considering the force due to a single ray of power P hitting a transparent dielectric sphere at an angle of incidence θ with incident momentum per second of $n_m P/c$ according with the equation (1.6), on the figure (4.5), is represented a scheme of the propagation for a single incident ray of light on a sphere with refractive index higher than the surrounding medium. The total force on the sphere is the sum of contributions due to the reflected ray of power PR and the infinite number of emergent refracted rays of successively decreasing power $PT^2, PT^2R, \dots PT^2R^k \dots$ in terms of the transmittance and reflectivity on the

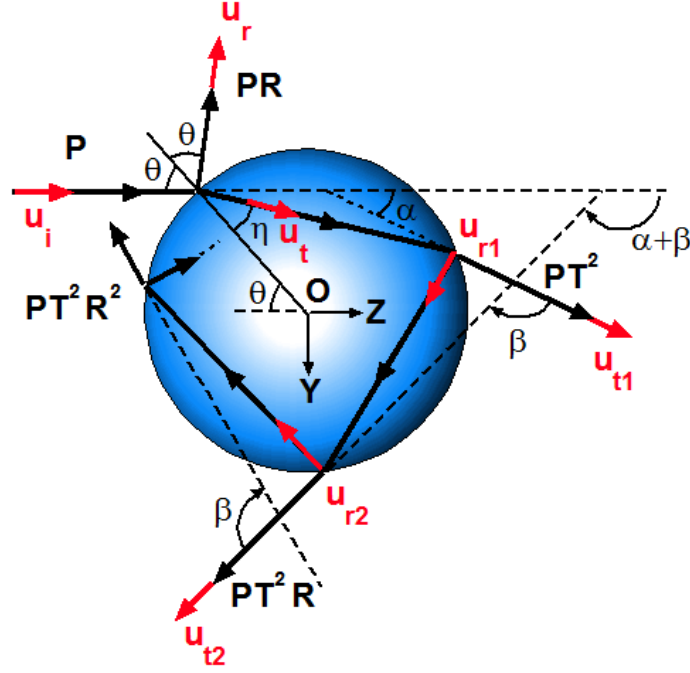


Figure 4.5: Geometry for calculating the force - The scattering of a single incident ray of power P by a dielectric sphere, showing the reflected ray PR and infinite set of refracted rays PT^2R^n

surface, after several internal reflections, the change in the light direction is given by:

$$\begin{aligned} \Delta \hat{\mathbf{k}} = & \{n_m R(\hat{\mathbf{u}}_r - \hat{\mathbf{u}}_i) + T(n_s \hat{\mathbf{u}}_t - n_m \hat{\mathbf{u}}_i) + n_s T R(\hat{\mathbf{u}}_{r1} - \hat{\mathbf{u}}_t) \\ & + T^2(n_m \hat{\mathbf{u}}_{t1} - n_s \hat{\mathbf{u}}_t) + n_s T R^2(\hat{\mathbf{u}}_{r2} - \hat{\mathbf{u}}_{r1}) + T^2 R(n_m \hat{\mathbf{u}}_{t2} - n_s \hat{\mathbf{u}}_{r1}) \\ & + n_s T R^3(\hat{\mathbf{u}}_{r3} - \hat{\mathbf{u}}_{r2}) + T^2 R^2(n_m \hat{\mathbf{u}}_{t3} - n_s \hat{\mathbf{u}}_{r2}) + \dots\}, \end{aligned} \quad (4.1)$$

where n_s and n_m are the respective refractive indices for the sphere and the surrounding medium with the condition ($n_s > n_m$), $\hat{\mathbf{u}}_i$ and $\hat{\mathbf{u}}_r$ (represented by red arrows on the figure) are the unitary vectors pointing in the directions of the incident and reflected rays, respectively. Besides, $\hat{\mathbf{u}}_{rk}$ and $\hat{\mathbf{u}}_{tk}$ correspond to the k -th rays internally reflected and externally transmitted each time that light interacts with the particle interface.

Rearranging the terms on the equation (4.1), we obtain that the contributions coming from the rays propagating inside the sphere cancel between them and the total change of direction for an incident ray of light is:

$$\Delta \hat{\mathbf{k}} = -n_m \{ \hat{\mathbf{u}}_i - R \hat{\mathbf{u}}_r - T^2 \sum_{k=1}^N R^{k-1} \hat{\mathbf{u}}_{tk} \} + n_s T R^N \hat{\mathbf{u}}_{rN}, \quad (4.2)$$

where N is the number of total internal reflections. If N is big enough, the last term is despicable due to the fact that $R^N \rightarrow 0$.

In the case of an incident ray hitting a sphere with radius R_0 , we can split the equation (4.2) in a parallel component Δk_{\parallel} to the incident ray and a perpendicular component Δk_{\perp} , using the R and T we obtain:

$$\Delta k_{\parallel} = -n_m \left[1 - R \cos 2\theta - T^2 \frac{\cos(2\theta - 2\eta) + R \cos 2\theta}{1 + R^2 + 2R \cos 2\eta} \right], \quad (4.3)$$

$$\Delta k_{\perp} = -n_m \left[R \sin 2\theta - T^2 \frac{\sin(2\theta - 2\eta) + R \sin 2\theta}{1 + R^2 + 2R \cos 2\eta} \right], \quad (4.4)$$

where the refraction angle η and incidence angle θ are related by the Snell law, on which according to the angles defined on the figure (4.5) we have $n_m \sin \theta = n_s \sin \eta$.

As we mention before¹, in the work reported by Ashkin^[26], the forces are calculated by mean of the set of equations: $\vec{F}_{scat} = \mathbf{Q}_s \frac{n_m P}{c}$ and $\vec{F}_{grad} = \mathbf{Q}_g \frac{n_m P}{c}$. Such expressions are contained in the previous rays analysis (based on the reference^[148]), on which is demonstrated that $Q_s = \Delta k_{\parallel}$ and $Q_g = \Delta k_{\perp}$. On this approximation the total optical force acting on the transparent spherical particle due to the incident light beam will be the vectorial sum of all the contributions from the incident rays weighted according with the incident intensity distribution on the surface on the sphere, this is^[148,149]:

$$\mathbf{F} = \frac{n_m}{c} \int_{S_1} I(\rho, \varphi, z) \cos \alpha_i \{ \hat{\mathbf{u}}_i - R \hat{\mathbf{u}}_r - T^2 \sum_{k=1}^N R^{k-1} \hat{\mathbf{u}}_{tk} \} dA, \quad (4.5)$$

where ρ is the transversal distance from the optical axis to the incidence point on the sphere, φ is the azimuthal coordinate and S_1 is the part of the surface illuminated by the incident light beam. For this reason, it should be stated the position of the particle with respect to the intensity's beam distribution $I(\rho, \varphi, z)$, for this purpose the next model considers two coordinated systems indicated of figure (4.6):

On the reference frame S on part a) of the figure, the spherical particle of radius R_0 is located on the point C of the coordinate system associated to the light beam. On this coordinate system, the origin corresponds to the symmetry center of the transversal intensity distribution in the beam, which on cylindrical coordinates is given in terms of (ρ, φ, z) . Is also represented the incidence point P of the ray at incidence angle θ and the distance ρ_0 between the z axis and the center of the sphere.

The second reference frame S' is located on the center of the sphere and is not a fixed frame system because it moves along with the sphere. On the figure (4.6), are represented the angles of the sphere where ϕ is the polar angle and Θ is the azimuthal angle. The parameter ρ is the distance between the axis z and the incidence point P . Finally, z_0 is the distance between the reference plane $z = 0$ and the center of the sphere.

¹On section 1.6.1

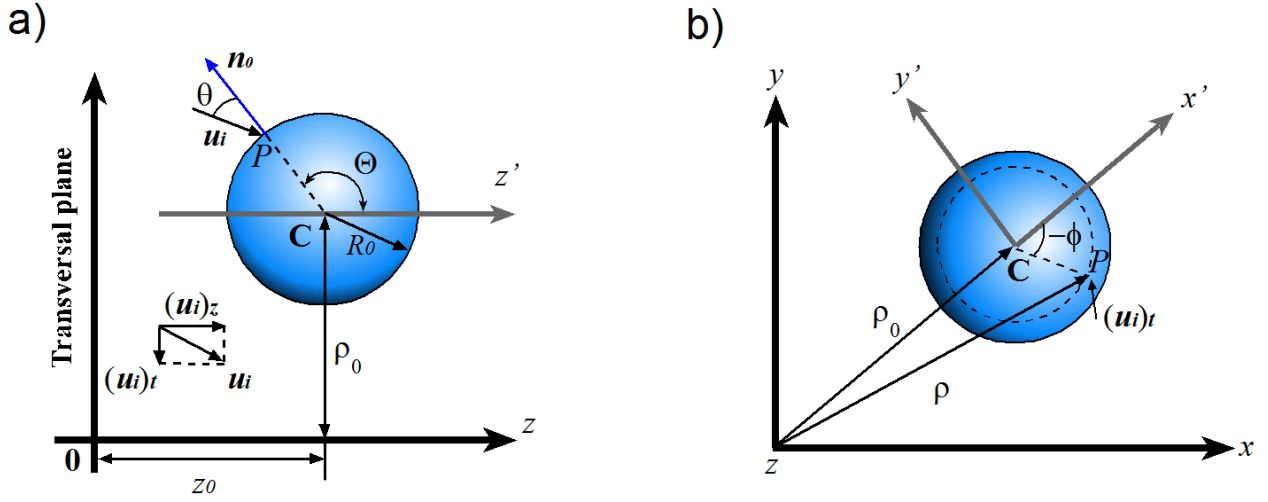


Figure 4.6: Geometrical parameters for ray model - Model with rays for a dielectric sphere under the influence of a light beam propagating along the z direction. a) Side view. b) Front view. ^[148,150]

Then, both reference frame systems are related by:

$$\begin{aligned}\rho &= [\rho_0^2 + R_0^2 \sin^2 \theta + 2\rho_0 R_0 \sin \theta \cos \phi]^{1/2}, \\ z &= z_0 + R_0 \cos \theta.\end{aligned}\quad (4.6)$$

When we consider a Gaussian beam slightly focused, all the incident rays are approximately parallel to the propagation axis. In our experimental conditions, as the trapping beam is focused with a relatively low N.A., we can consider that the scattering force is directed vertically downwards, which is the propagation direction (z), while the gradient force is basically transversal (ρ), *i.e.* in the horizontal plane. The equation to obtain the transversal gradient force exerted by the light beam onto the spherical particle of radius R_0 , in a plane $z = cte$, can be written as:

$$F_g = \frac{n_m R_0^2}{c} \int_0^{\frac{\pi}{2}} \int_0^{2\pi} I(\rho, \varphi, z) \cos \theta \left[R \sin(2\theta) - T^2 \frac{\sin(2\theta - 2\eta) + R \sin(2\theta)}{1 + R^2 + 2R \cos(2\eta)} \right] \cos \phi \sin \theta d\phi d\theta, \quad (4.7)$$

where R_0 is the particle radius of the particle and the integration is performed over the illuminated hemisphere of the particle. In this case, θ coincides with the incidence angle at each point on the sphere's surface and η is the refraction angle. Note that for radial particles, θ is also the angle between the incident ray and the axis of the helical supramolecular structures. Due to symmetry considerations, we can look only at the force along the x direction without loss of generality.

On the other hand, the expression for the component of the scattering force along the propa-

gation direction z axis can be evaluated from:

$$F_s = \frac{n_m R_0^2}{c} \int_0^{\frac{\pi}{2}} \int_0^{2\pi} I(\rho, \varphi, z) \left[1 + R \cos(2\theta) - T^2 \frac{\cos(2\theta - 2\eta) + R \cos 2\theta}{1 + R^2 + 2R \cos(2\eta)} \right] \cos \theta \sin \theta d\phi d\theta, \quad (4.8)$$

The intensity distribution of the incident Gaussian beam is given as function of the distance ρ from the axis beam to the sphere center and their radius R_0 with the following equation:

$$I(\rho, \varphi, z) = I_0 \exp \left[-\frac{2\rho^2}{w^2} \right], \quad (4.9)$$

where I_0 is the maximum intensity on the beam center. The expressions of intensity and the forces are given in function of ρ , to change back to the Cartesian coordinate system, the additional equations relating both coordinate systems are given by:

$$\begin{aligned} x &= x_0 + R_0 \sin \theta \cos \phi, \\ y &= y_0 + R_0 \sin \theta \sin \phi, \\ z &= z_0 + R_0 \cos \theta, \end{aligned}$$

where x_0 and y_0 are the parameters that indicate the displacement of the particle center with respect to the propagation axis.

In the models where the light impinges a transparent-spherical-particle^[148–150], the Fresnel coefficients can be taken as the average of both transversal directions of polarization relatives to the incidence plane for each illuminated element. For circularly polarized waves with wavelength inside the stop-band of the CLC these coefficients and the wave propagation depend strongly on the light handedness with respect to the cholesteric helix handedness^[1,2]. Therefore, following our initial hypothesis, in the microparticles having a CLC left-handed helix, we can suppose that the RCP light propagates with a constant average refractive index $\bar{n} = (n_{\parallel} + n_{\perp})/2$, according to the equation (3.5)^[1]. Using the values $n_{\parallel} = 1.68$ and $n_{\perp} = 1.53$ of the reactive mesogen, the average refractive index and the refraction angle can be evaluated. Then, to account for the circular polarization, the value of R can be calculated as the average over the two orthogonal polarization directions respect to the incidence plane at each point as:

$$R = \frac{1}{2} \left(|r_{\perp}|^2 + |r_{\parallel}|^2 \right) = \frac{1}{2} \left[\frac{\sin^2(\theta - \eta)}{\sin^2(\theta + \eta)} + \frac{\tan^2(\theta - \eta)}{\tan^2(\theta + \eta)} \right]. \quad (4.10)$$

Since the absorption of the liquid crystal at the considered wavelength is negligible, the transmittance T can be easily evaluated from

$$T = 1 - R, \quad (4.11)$$

these expressions for R and T are included in the equations (4.7) and (4.8) to calculate the optical forces F_g and F_s , respectively.

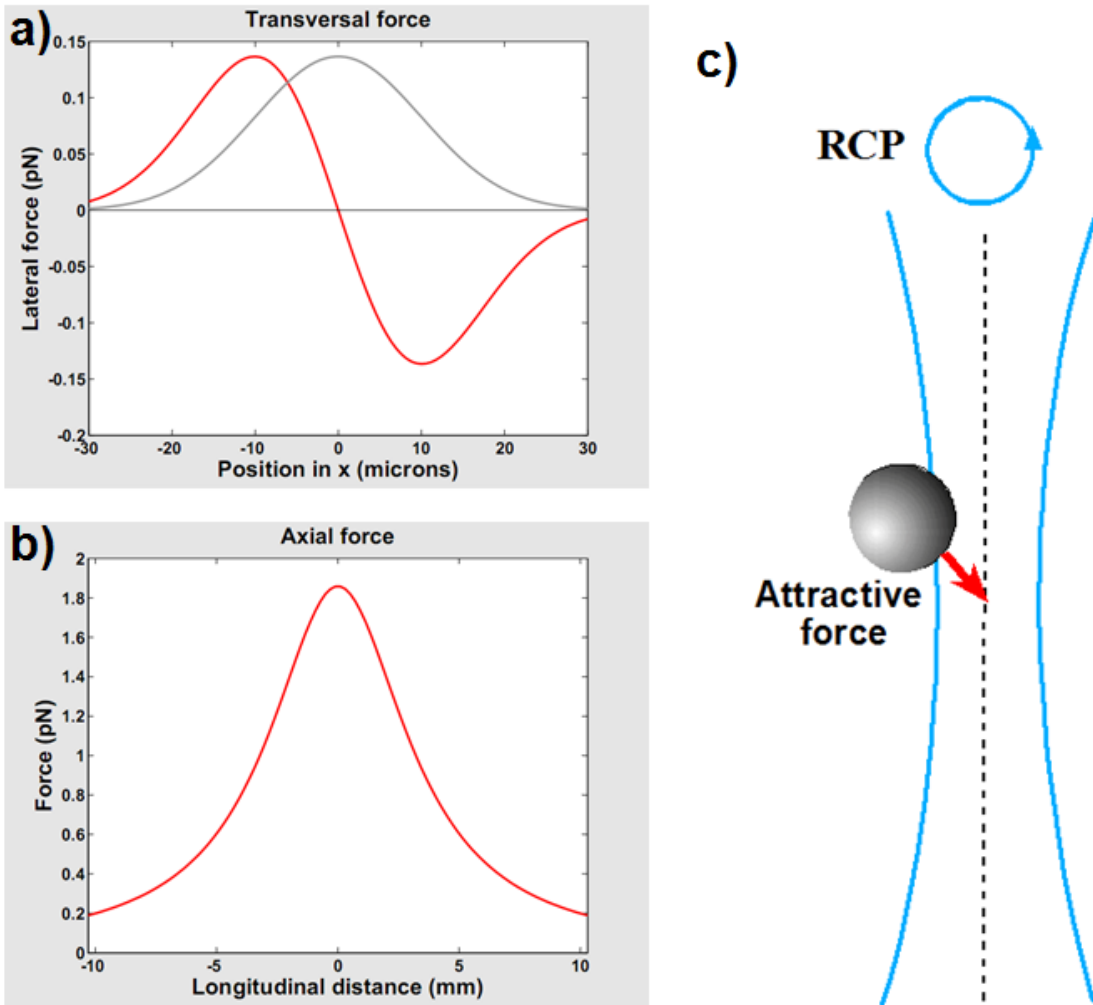


Figure 4.7: Forces for right circular polarization - a) Transverse force on the particle (red line) indicates a stable trap, the center of transversal intensity distribution (gray profile) correspond to the equilibrium point at $x = 0$. b) Longitudinal force along the axis of propagation of the incident beam. c) Representation of the attractive force toward the beam axis. The parameters of the plots are: $\omega_0 = 20 \mu m$, $R_0 = 2.5 \mu m$, $\lambda_0 = 488 nm$ and $P = 100 mW$.

The plots of the forces for right circular polarization as a function of the distance from the trap focusing along the transversal and longitudinal directions are shown respectively, in the figures 4.7a and 4.7b.

According to the calculations, the expected optical forces predict a trapping of the particle towards the highest intensity on the center of the beam axis. The predicted effect is the same observed in the images reported in the figures 4.4 and 4.3 for RCP : the attractive force in the transversal plane aggregates the radial particles towards the focal spot of the light beam with RCP. The radial particles are identified by their typical cross pattern between crossed polarizers. Therefore, in spite of the complex supramolecular structure of the particle, where linear and circular birefringence are present at the mesoscopic scale, due to the Bragg regime, the mechanical effect of the RCP optical tweezers is the same as the attraction of an optically isotropic and homogeneous dielectric sphere with a refractive index higher than that of the surrounding medium.

Nevertheless, by changing the circularly polarized light from right- to left-handed, we observe that the same particles exhibit a strong reflection and a repulsive force dominates, pushing them outside the illuminated region, again in figures 4.4 and 4.3 but in the case of light with opposite (left) handedness. For this circular polarization, the propagation in the CLC Bragg regime is interdicted for waves with wavelength inside the stop-band and the Fresnel reflection coefficient near the center of the stop-band can be now evaluated from the expression reported in [2]:

$$R = \tanh(\beta d) \tag{4.12}$$

where $\beta = \frac{\pi(n_{\parallel}^2 - n_{\perp}^2)\sqrt{2}}{2\lambda\sqrt{n_{\parallel}^2 + n_{\perp}^2}}$ and $d = 2R_0$ is the particle diameter, about $5\mu\text{m}$.

The R value calculated from equation(4.12) using $R = |r^2|$ is about 99.8%, which agrees with the measurements of the transmittance reported in figure (4.1), where the transmittance of linearly polarized light is about 50%. According to these values for transmittance and reflectance, the gradient and scattering forces have been calculated again using equations (4.7) and (4.8). In figure 4.8 is reported the corresponding plots as a function of the distance from the trap focusing along the transverse and longitudinal directions.

As the result indicates, a repulsive force is predicted, in agreement with the experimental observation. In figure 4.4e (fluid), as soon as the light polarization of the laser beam (optical tweezers) turns left-handed, a blue-green dot can be observed in the center of the microsphere that is subsequently pushed out from the optical trap. The bright dot, observed in the center of the particle, can be easily associated with the selective reflection of laser light impinging on the particle. This observation well support the hypothesis adopted in the evaluation of optical forces, *i.e.* that for radial particles most of the rays fulfill the Bragg selective reflection. It is important to notice that no rotation is observed for particles manipulated with circularly polarized optical tweezers, neither RCP nor LCP. This behavior demonstrates that the transfer

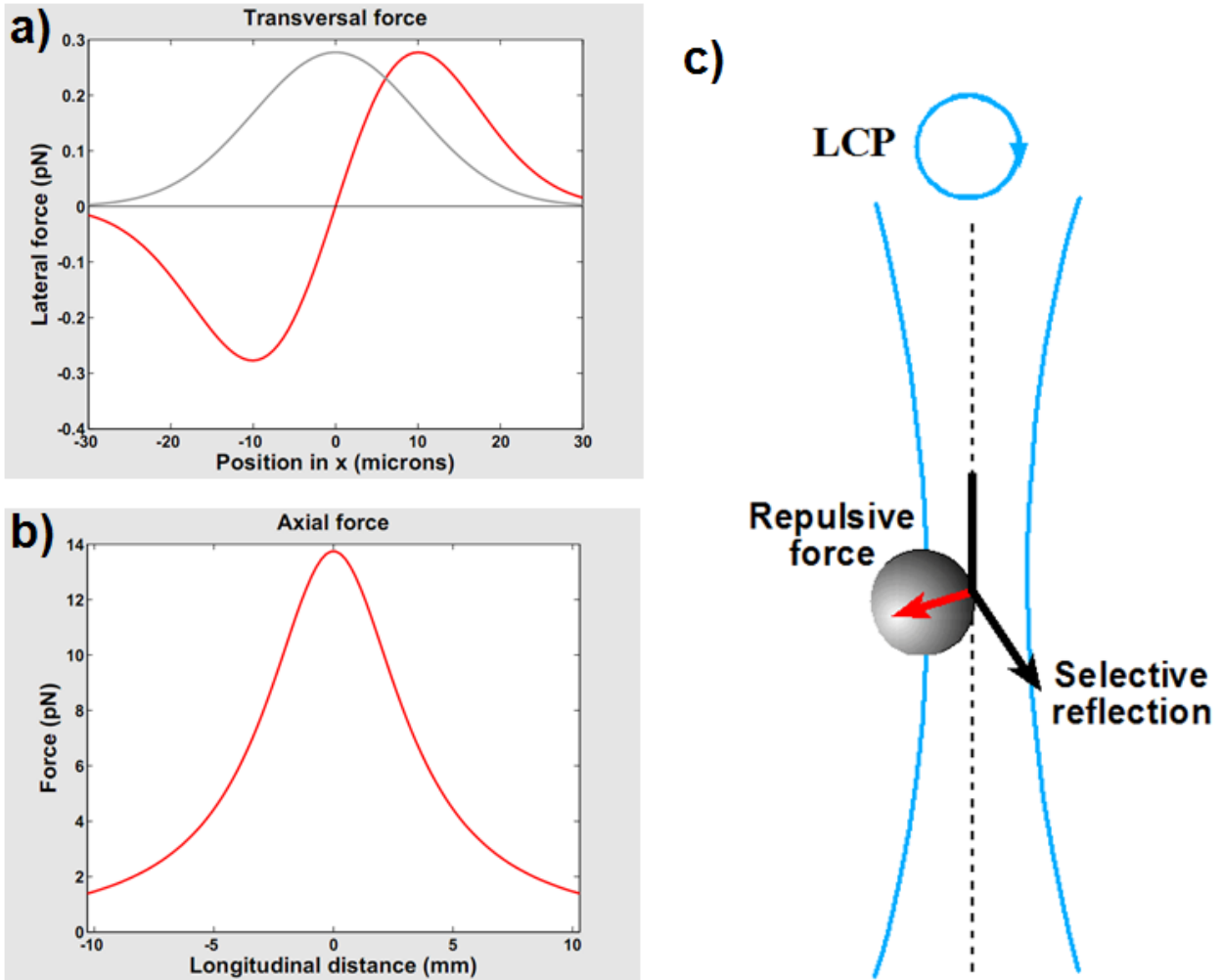


Figure 4.8: Forces for left circular polarization - a) Transverse force on the particle (red line) indicates an unstable trap, the center of transversal intensity distribution (gray profile) correspond to the equilibrium point at $x=0$. b) Longitudinal force along the axis of propagation of the incident beam. As expected the repulsive optical forces are higher in magnitude compared with the case of attractive forces. c) Representation of the repulsive force pulling the particle away from the beam axis. The parameters of the plots are: $\omega_0 = 20\mu m$, $R_0 = 2.5\mu m$, $\lambda_0 = 488nm$ and $P = 100$ mW

of linear momentum dominates with respect to the spin angular momentum transfer that could be expected due to the linear optical anisotropy of the LC polymer.

4.4 Optically anisotropic particles

The presence of surfactants in the water emulsion enables to have microparticles with conical or cylindrical configurations of the helical structures, these configurations give a global-optical anisotropy to the spherical particles. Depending on the light handedness, the light propagation in the microspheres occurs or not, leading to a very complex dynamics of the particles. They behave like Janus spherical particles with dissimilar optical properties, this mean that they behave like dielectric particles formed by a partially transparent surface and a partially reflecting surface. This unique property and the transfer of angular momentum to set in rotation chiral anisotropic particles, reveal the arrangement of the internal helicoidal superstructures combined with the molecular liquid-crystal orientation at the interface on the medium where the particles are dispersed.

In the case of optically anisotropic CLC microspheres (fluid or solid), they represent indeed more complex objects, due to the asymmetric configurations of the internal architectures at the supramolecular scale. As a consequence, the particles acquire a net birefringence, as shown in transmission mode when are observed between crossed polarizers figure (3.7). In this case, is observed a rotation of the particles connected to the transfer of spin angular momentum from the circularly polarized light.

For the optical tweezer with right circular polarization, the light can propagate everywhere inside the particle to trap it in the illuminated region and set it in rotation. However, the observed rotation is not uniform and the motion is different for each kind of internal architecture inside the particle. Of course, the non uniform rotation can be accounted for by an irregular angular momentum transfer due to the asymmetric supramolecular structures of the birefringent material inside the particle, which introduces optical inhomogeneity in the object. For the same reason (the inhomogeneity), the rotational axis does not cross the center of the sphere explaining the precession on the rotation.

For left circular polarization the particles behave like Janus particles^[151,152], whose total surface is partially formed by transparent surface and a reflecting surface (*i.e.* like metallic). When the polarization changes from right to left circular, the rotation sense is reversed, but after a few seconds the particle jumps out of the beam spot on the trap. Depending on the forces, the laser power and also the size of the reflecting surface area, the particle can be attracted to the trap once again and so on (see figure 4.9), or sometimes is even completely expelled from the beam spot figure (4.10).

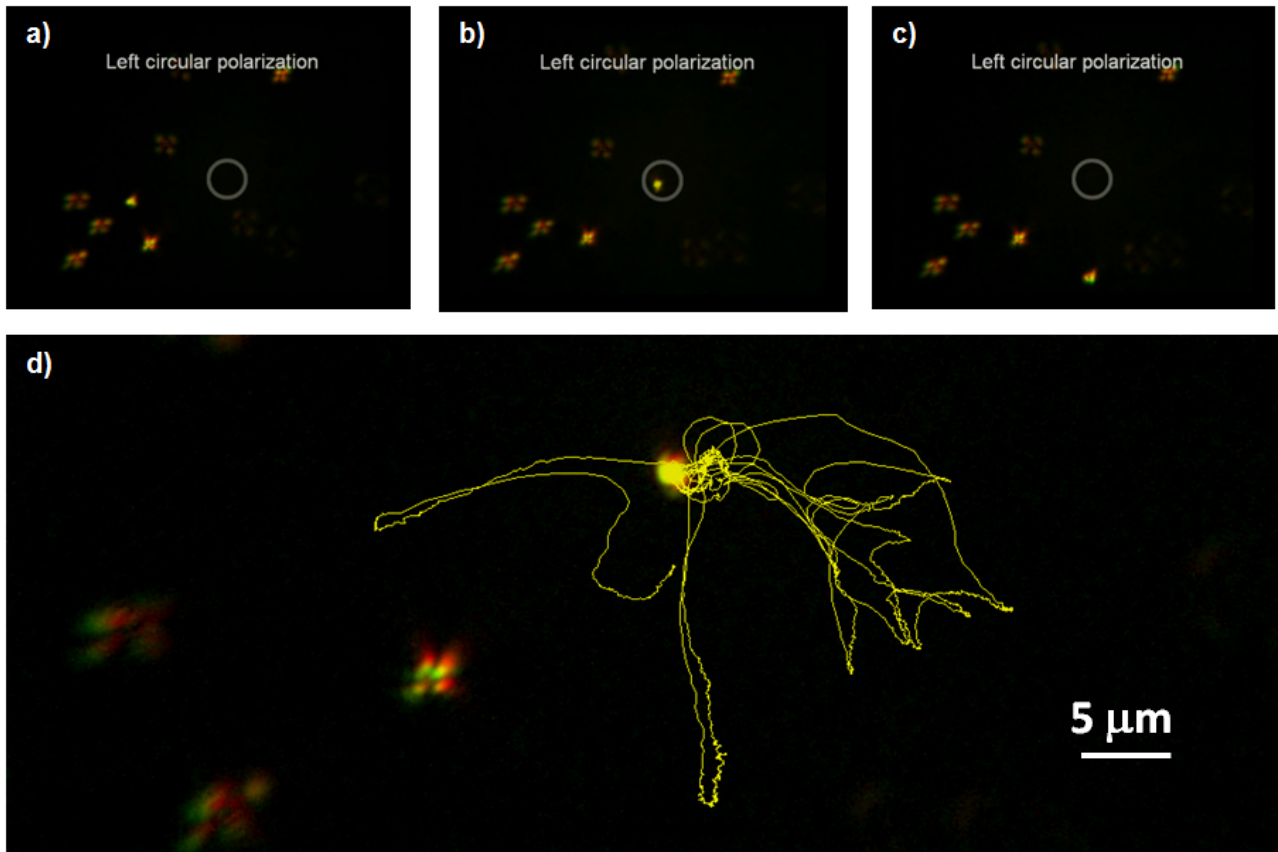


Figure 4.9: Attraction and repulsion behavior on anisotropic CLC immersed in water
 - a) The optically anisotropic CLC droplet is attracted to the beam spot(circle), b) Once there it start to rotate and to change orientation, c) when the orientation is such that repulsive force is generated, the CLC droplet goes out from the trap and the cycle might start again as shown in the movie. Big image shows the trajectory followed by the CLC droplet along the movie.

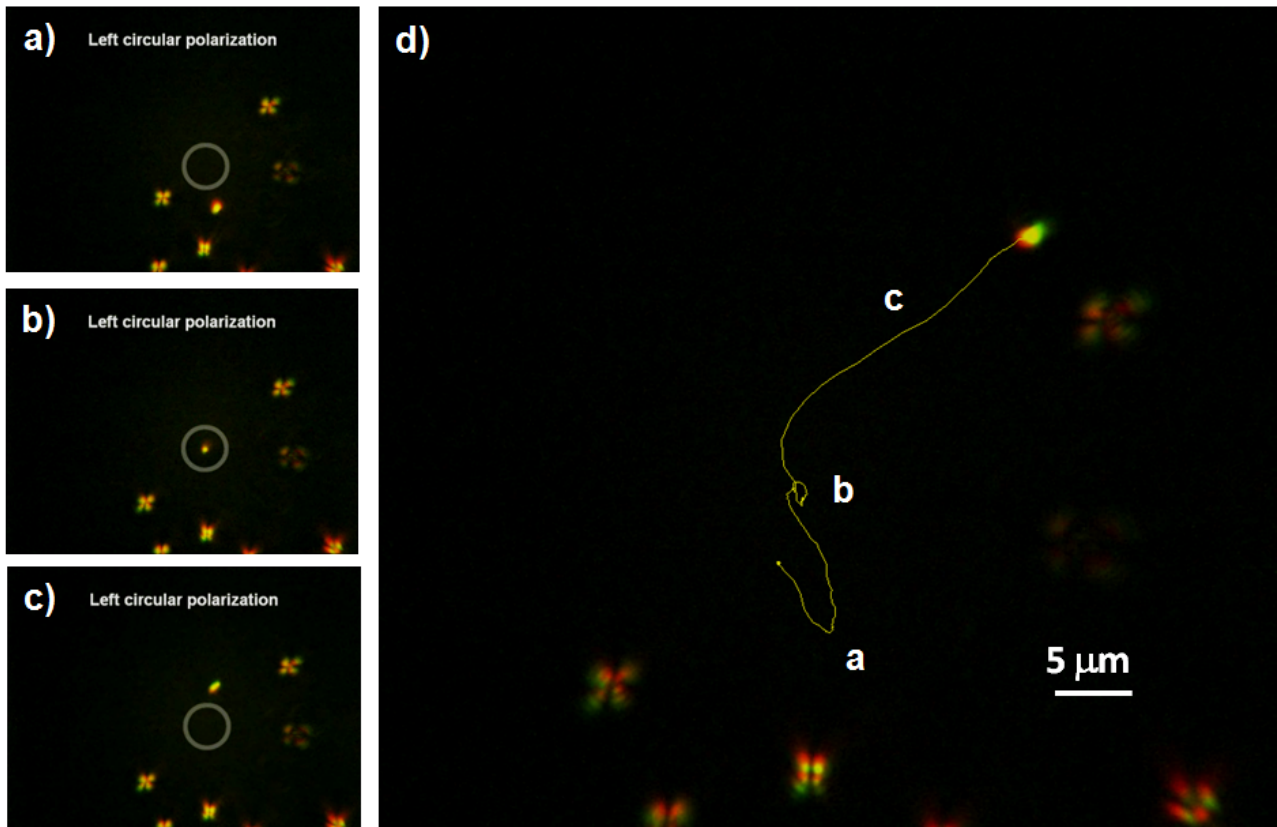


Figure 4.10: Strong reflection for left circularly polarized light - a) The anisotropic droplet is attracted towards the trap region (circle) while the isotropic particles (with the cross pattern) are repelled from this region. b) Once inside the trap the droplet starts to rotate in response to left polarized light, c) after some reorientation when the light impinges on the particle region that exhibits selective reflection, the repulsive force prevails pushing the microsphere out of the optical trap, d) full trajectory (yellow line) described by the particle indicating the position of the former images.

4.4 Optically anisotropic particles

Although in this case the evaluation of both gradient and scattering forces is very complicated and requires a proper modelling and a more accurate theoretical approach for the chiral anisotropic microspheres, the observed dynamical behavior, shown in figure 4.9, can be explained qualitatively using a ray optics scheme.

The figure 4.11a illustrates the situation in which the incident light rays, a and b, propagate in directions not parallel to the helical axes inside the conical region; in the scheme the incident light rays are refracted through the particle and the gradient forces F_a and F_b are applied to the particle due to each ray. The gradient force is balanced by the scattering one and the particle is trapped. The ray optics approach and the scheme evidence the importance of the symmetry of conjugated light rays in optical trap: provided that the gradient force balance the scattering force, the trap is stable. In the present situation the symmetry of this process may be easily broken since it depends on the orientation of the particle with respect to the impinging light rays, whose propagation in the particle is strongly influenced by the non-symmetric and non-homogeneous internal configuration (figure 4.11b).

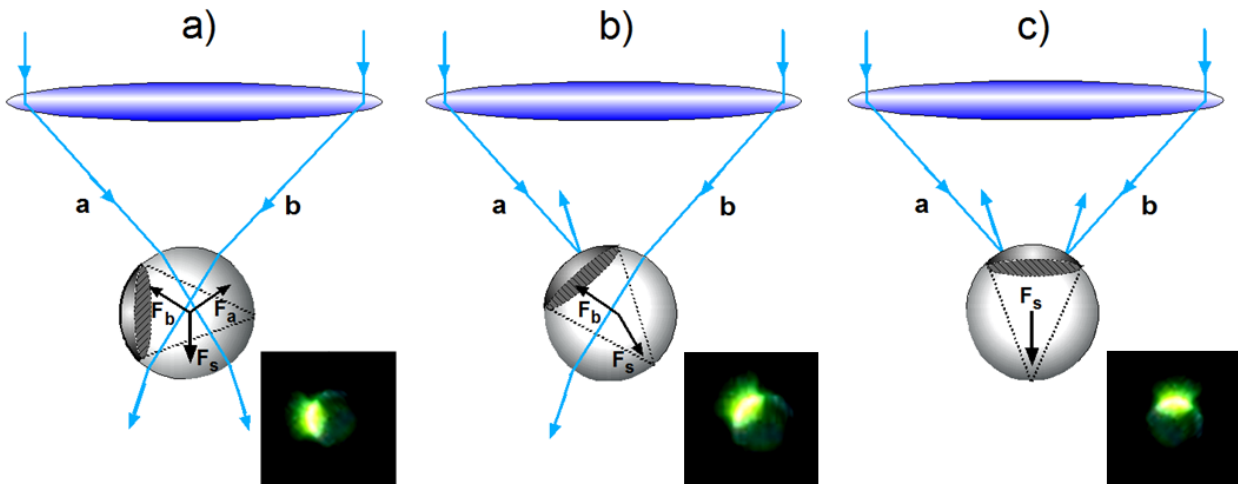


Figure 4.11: Representation with rays for optically anisotropic particles - a) Depicts the balance between gradient and scattering forces due to refraction of light inside the particle resulting in a stable optical trap. b) Shows the case of broken symmetry on forces and torque, depending on the orientation and position of the particle with respect to the optical trap. c) Depicts the extreme situation when the reflecting part of the surface is oriented such that the incident light is reflected and the particle is repelled by scattering force.

This simple ray optics approach make evident the importance of the symmetry of conjugated light rays (**a** and **b**) to establish a stable trapping in the transverse plane. In the present situation, the symmetry of this process may be easily broken since it depends on the orientation of the particle with respect to the impinging light rays, whose propagation in the particle is strongly influenced by the non-symmetric and non-homogenous internal configuration (figure 4.11b). Moreover, as we mentioned, due to the net birefringence of the particles with conical or

cylindrical configuration (figures 3.7b-c, 3.7e-f), the transfer of spin angular momentum occurs, inducing also a torque on the particle that begins to rotate thereby changing its orientation with respect to the impinging light rays. Depending on the particle position and orientation, some rays could not propagate in the particle; this breaks the symmetry, leading to unbalanced torques and forces. The trap becomes unstable and when most of the rays are reflected, figure 4.11b and 4.11c, the unbalance between the gradient and scattering forces pushes the particle out of the trap. The trapping region in this case is not strongly localized and the rotational motion becomes very complex as show the trajectory on 4.9d.

Moreover, due to the global birefringence of the particles with conical or cylindrical configuration (3.7), transfer of spin angular momentum occurs, inducing also a torque on the particle that begins to rotate thereby changing its orientation with respect to the impinging light rays. Depending on the particle position and orientation, some rays could not propagate in the particle, this breaks the symmetry, leading to unbalanced torques and forces. The trap becomes unstable and when most of the rays are reflected, figure 4.11b and 4.11c, the unbalance between the gradient and scattering force push the particle out of the trap. The trapping region in this case is not strongly localized and the rotational motion becomes very complex, figure 4.9 is just one example.

4.4.1 Rotation of optically non symmetric spheres of CLC

It may be argued that the theory of laser tweezers has lagged somewhat behind experimental progress. For example, relatively little theoretical progress has been made on calculating the radiation force and torque on a nonspherical particle. The ability of a material to self-assemble into complex structures is encoded into its architecture. Since CLC particles possess the unique and novel feature of being spheres “non-centrosymmetric” the rotation becomes irregular.

In this section is presented the simple analysis done on the rotation of CLC particles from the former sections, *i.e.* we present the investigation of the rotation of chiral microscopic spheres (liquid and solid) with asymmetric optical properties. The analysis is based on images sequences taken from the videos captured and the use of imaging analysis software, the software Able Particle Tracker was employed for the trajectories. Indeed, it turned out from the observations and analysis that the CLC particles exhibit a variety of complex and partially unexpected dynamics.

4.4.1.1 Fluid particles and trajectories

On this part, the CLC droplets in the emulsions were studied in fluid phase, typical sizes for the diameters of the droplets were ranging from 1 to 50 μm . The power on the sample was about 30 mW on the plane of observation and the beam size diameter ranged from 50-100 μm

as was mentioned in the previous section. In all graphics are presented the values considered from the center of the particle, in a) the X position with respect to the time; b) the Y position with respect to the time, c) the angle between the short and long axis of the particle. In d) a graphic of both X,Y positions vs time, on e) is presented the 3D trajectory showing their evolution on time and in f) is showed the graphic of the projection on the plane (x, y) from the movement of the particle along the axis X,Y.

In the figure 4.12, the CLC droplet rotated in clockwise sense showing a periodic uniform and continuous rotation in time. In the graphics a),b) and c) is clear that the particle follows a periodic oscillatory motion with defined period and amplitude. The observation and the graphics analysis show the expected behavior in the transfer of angular momentum that sets in rotation a typical birefringent particle. This particular case is the simplest case of rotation and have been studied in several references. In our case, serves as reference of the typical rotation behavior.

The result indicates that the particles was not doped with the chiral agent and therefore, the dynamics was like in the case of a bipolar nematic droplet. Another possibility is that the conditions for the wavelength or CLC selective reflection where not fulfill by the particle analyzed. In a future work, will be made a full comparison for the nematic LC and the CLC droplets in rotation.

In the figure 4.13, the CLC droplet rotated also in clockwise sense but with respect to the previous case at the same conditions, the rotation was slowly and showed a small precession in the movement. Comparing the position graphic with the previous case, can be observed a big change in the graphic 4.13a) with the X position. The graphic 4.13b) is more similar to a saw tooth function instead of a smooth sine modulation. This results in a different distribution of displacements along the X and Y axis and a trajectory evolution deformed on figure 4.13e.

The case showed in figure 4.14, reveals a change in the motions and dynamics just by changing the circular polarization state. As can be observed from the graphs on 4.14a) and 4.14b) the CLC droplet rotates with clockwise sense from the beginning until the second 30, then the beam is interrupted and the particle stops. Changing the polarization state to the opposite with anticlockwise rotation. The particle is start to rotate in the opposite sense as expected, but after a few some seconds is repelled from the trap spot. The behavior of repulsion and rotation alternate and the dynamic becomes irregular. On the graphics 4.14c) to f) is clear the dual behavior in the rotation due to the change of circular polarization.

In the figure 4.15, is presented the analysis of the CLC reported on figure 4.9 the particle exhibit the attraction-repulsion dynamics. Because the video analyzed was longer than the other videos and due to the particular behavior the graphics show a unique movement uncorrelated in the displacements along the axis. The regions where the movement has small amplitudes and

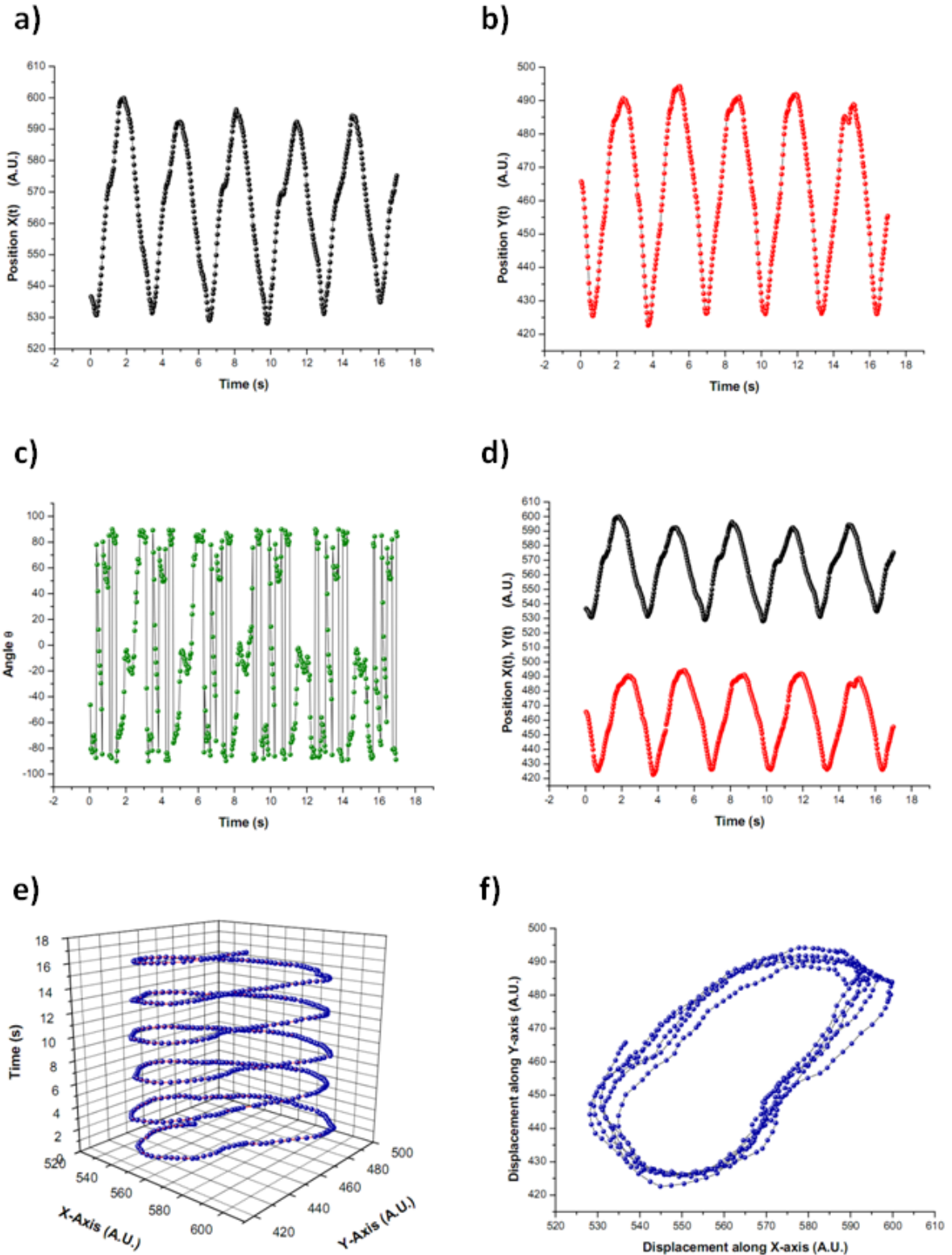


Figure 4.12: Rotation of a fluid CLC droplet I - In the graphics a) is the X position with respect to the time; b) the Y position with respect to the time, c) the angle between the the and the long axis of the particle. In d) a graphic of both X,Y positions vs time, on e) is presented the 3D trajectory showing their evolution on time and in f) is showed the graphic of the projection on the plane (x, y) from the movement of the particle along the axis X,Y.

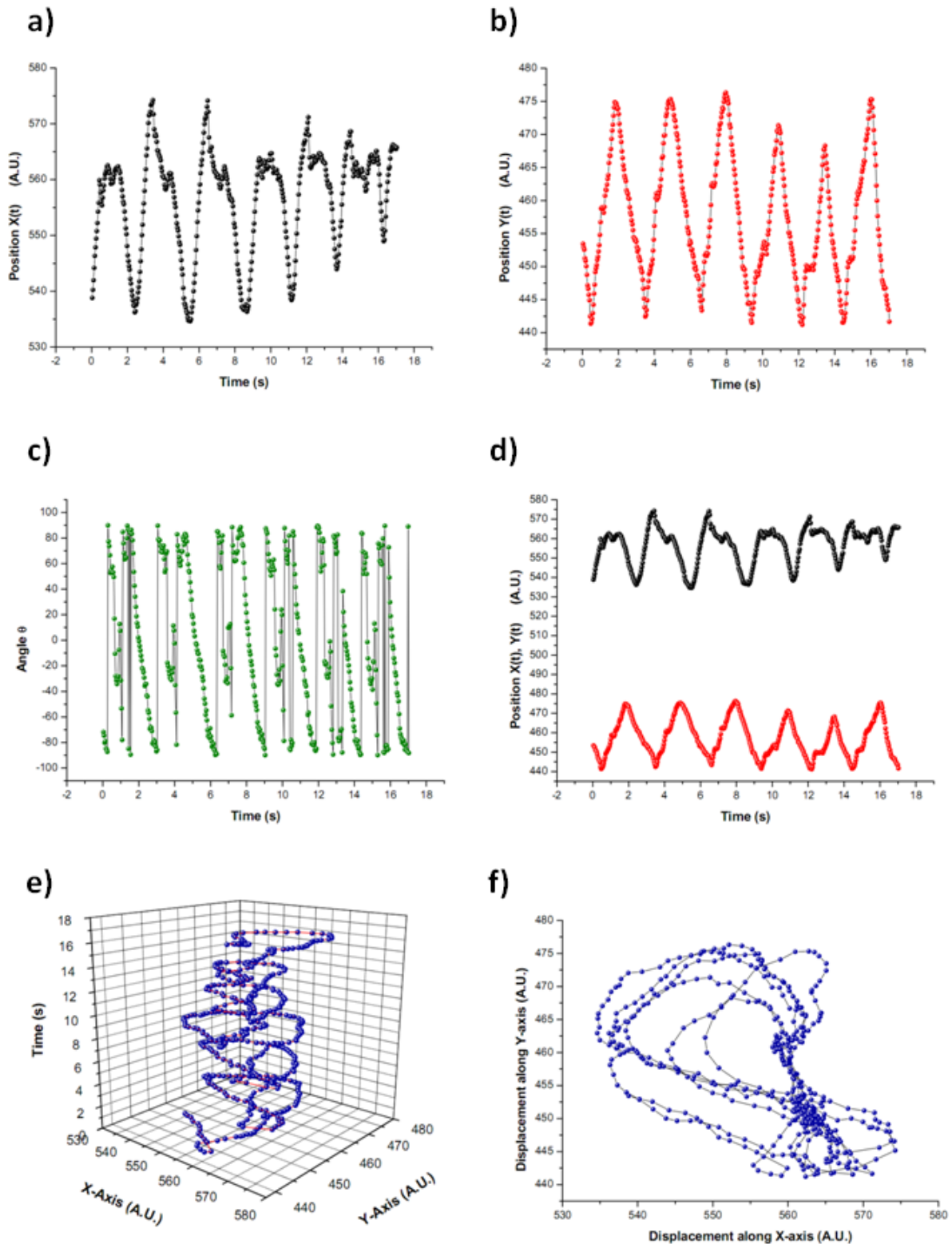


Figure 4.13: Rotation of a fluid CLC droplet II - In the graphics a) is the X position with respect to the time; b) the Y position with respect to the time, c) the angle between the the and the long axis of the particle. In d) a graphic of both X,Y positions vs time, on e) is presented the 3D trajectory showing their evolution on time and in f) is showed the graphic of the projection on the plane (x, y) from the movement of the particle along the axis X,Y.

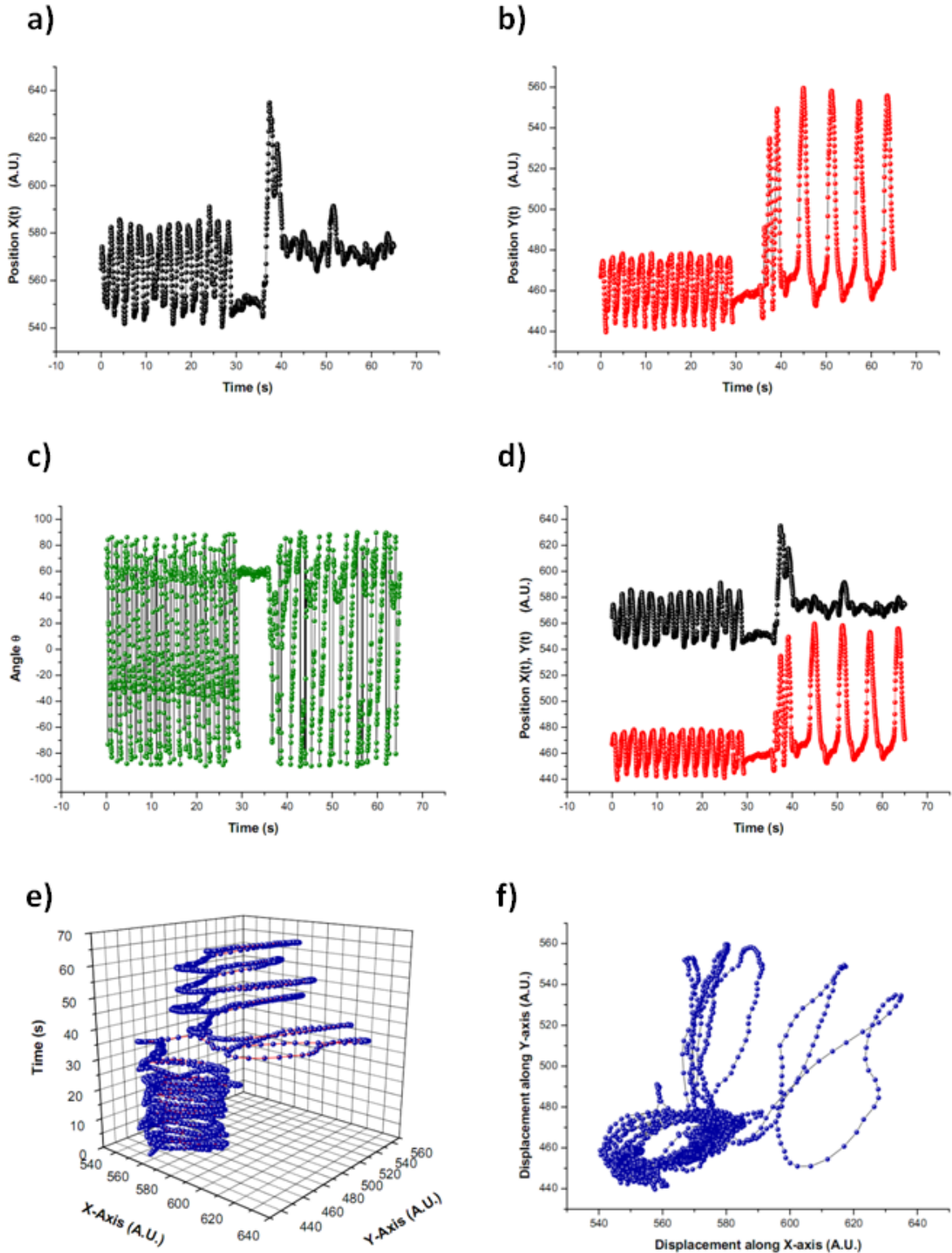


Figure 4.14: Rotation of a fluid CLC droplet II - In the graphics a) is the X position with respect to the time; b) the Y position with respect to the time, c) the angle between the the and the long axis of the particle. In d) a graphic of both X,Y positions vs time, on e) is presented the 3D trajectory showing their evolution on time and in f) is showed the graphic of the projection on the plane (x, y) from the movement of the particle along the axis X,Y.

periodic behavior correspond to the usual attractive and uniform rotation. While the zones with big amplitudes are the regions where the repulsion is present, in this case the repulsion was instantaneous and the time to be attracted again depend on the reorientation of the particle to the trap.

In the figure 4.16, is showed the unbalance between torques and forces, it correspond to a CLC doplet rotating in anticlockwise sense but also with the effects of repulsion. From this combination of movements is observed a very complex dynamic.

4.4.1.2 Solid particles and trajectories

In the case of solid particles obtained after the photo-polymerization process by the UV light. The optical properties do not change and also there wasn't any degradation. The only observable difference besides the endurance was a higher density because after a short time the particles in the emulsion were deposited in the bottom of the container. Another future investigation will develop the characterization of the physical parameters that change in the process from liquid to solid on these spheres, beyond from the observables reported here.

As in the case of the LC droplets, depending on the concentration of material and anisotropy on the particles the rotation changes. In the figure 4.17, the solid CLC sphere rotated in clockwise sense showing a periodic uniform and continuous rotation in time.

In the figure 4.18, the solid CLC sphere rotated in clockwise sense showing a periodic uniform and continuous rotation in time. Not much difference can be observed with respect to the previous case and with respect to the fluid droplets.

Again in the graphics on figure 4.19 starting with a circularly polarized light on the sample, the first part of the dynamic from the second 0 to 15 indicates a rotation with some precession. From the second 15 to 20 the beam was interrupted and the particle stops the movements. Switching on the laser from the second 20 and changing the polarization state, it was observed a change in the dynamics. The repulsion was also dominant with respect to the attraction force, the jumps in this case due to the repulsion and rotation have small amplitudes and the dynamics becomes irregular.

We present a technique for characterizing rotations of trapped microspheres that behave as optically asymmetric objects. Our analysis indicates that the rotations are periodic but with a time varying angular velocity, as can be surmised from the presence of peaks at the fundamental rotational frequency and additionally, at higher order integer harmonics.

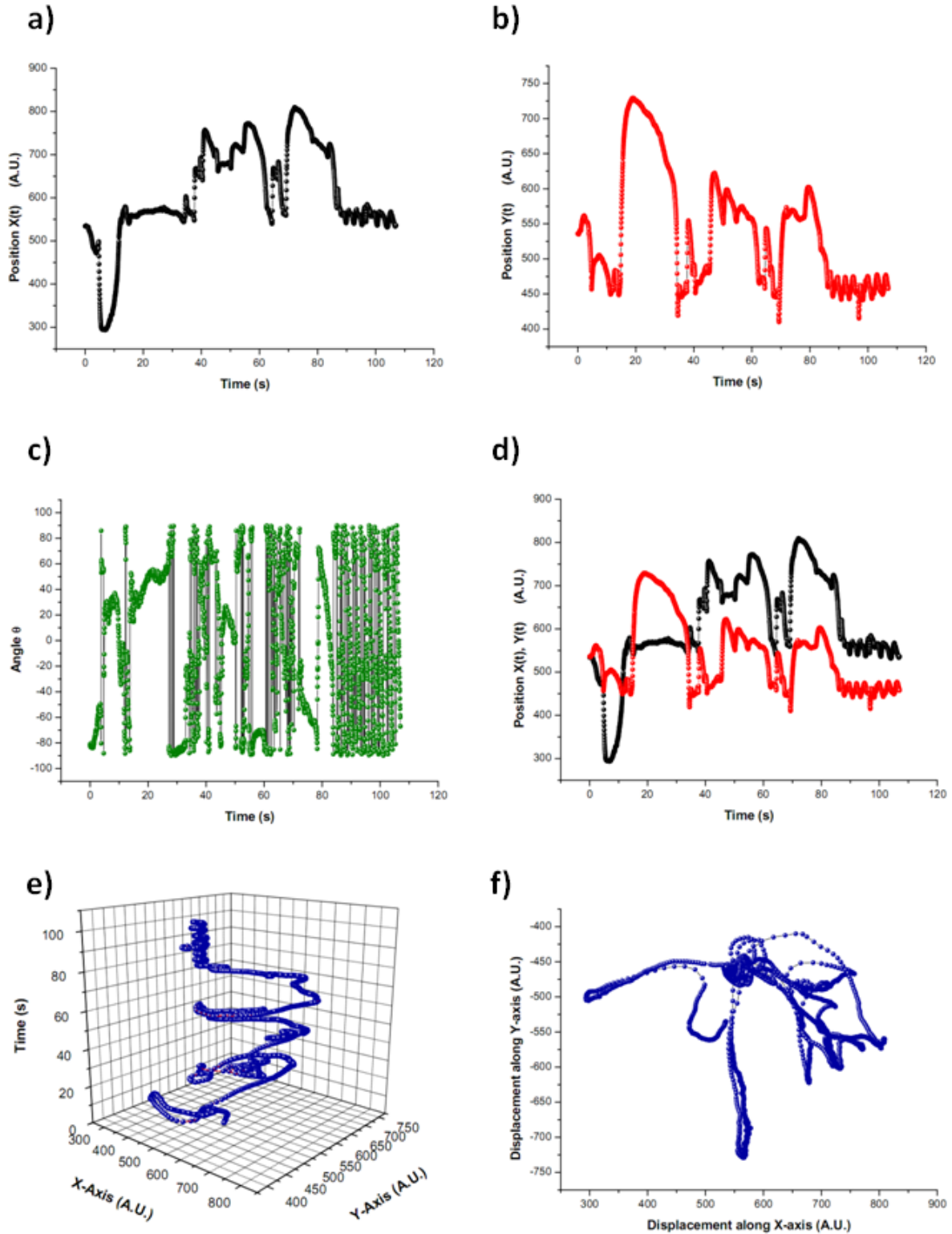


Figure 4.15: Rotation of a fluid CLC droplet III - In the graphics a) is the X position with respect to the time; b) the Y position with respect to the time, c) the angle between the the and the long axis of the particle. In d) a graphic of both X,Y positions vs time, on e) is presented the 3D trajectory showing their evolution on time and in f) is showed the graphic of the projection on the plane (x, y) from the movement of the particle along the axis X,Y. This graphics correspond to the particle presented in the figure 4.9

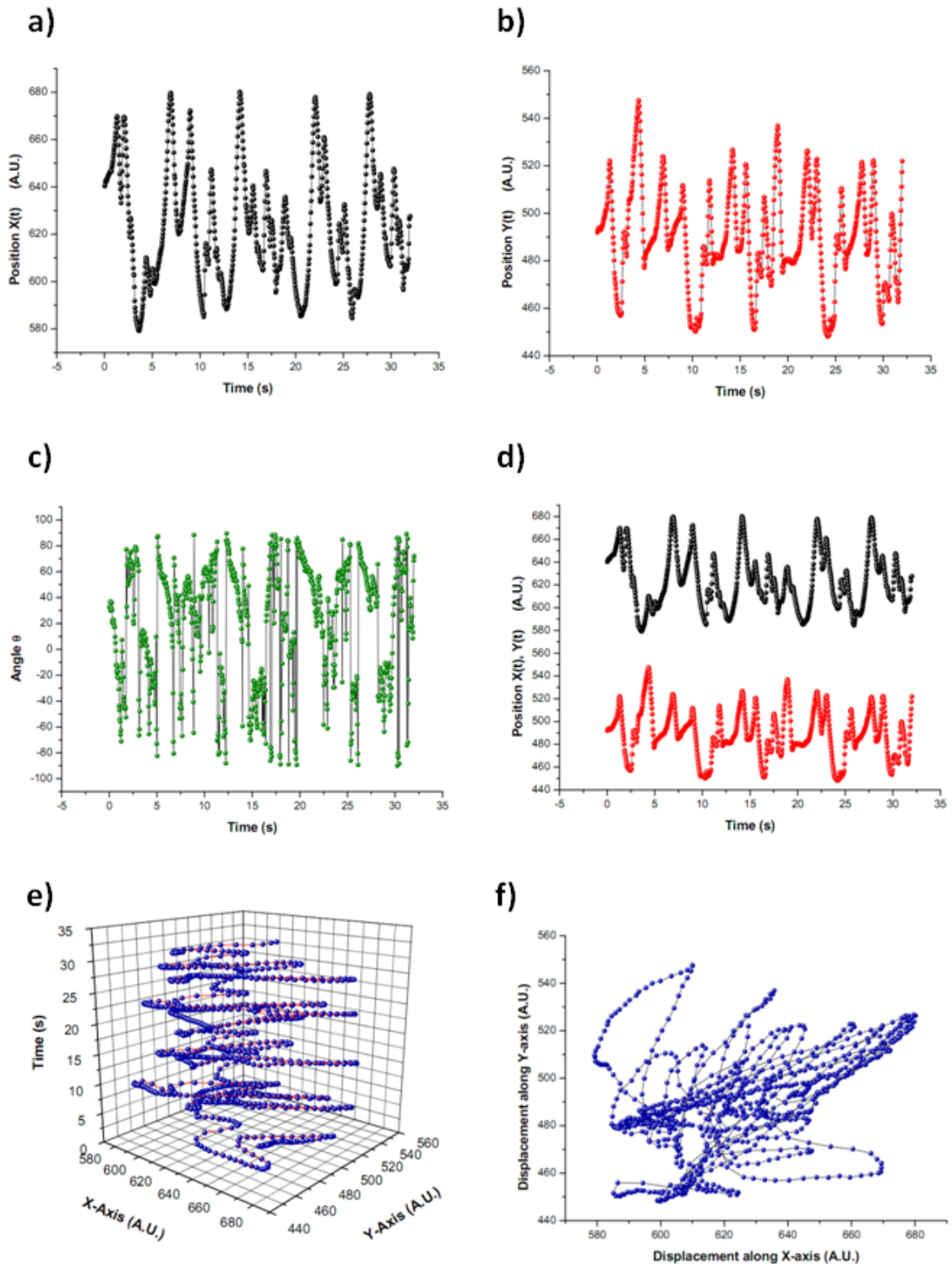


Figure 4.16: Rotation of a fluid CLC droplet IV - In the graphics a) is the X position with respect to the time; b) the Y position with respect to the time, c) the angle between the the and the long axis of the particle. In d) a graphic of both X,Y positions vs time, on e) is presented the 3D trajectory showing their evolution on time and in f) is showed the graphic of the projection on the plane (x, y) from the movement of the particle along the axis X,Y.

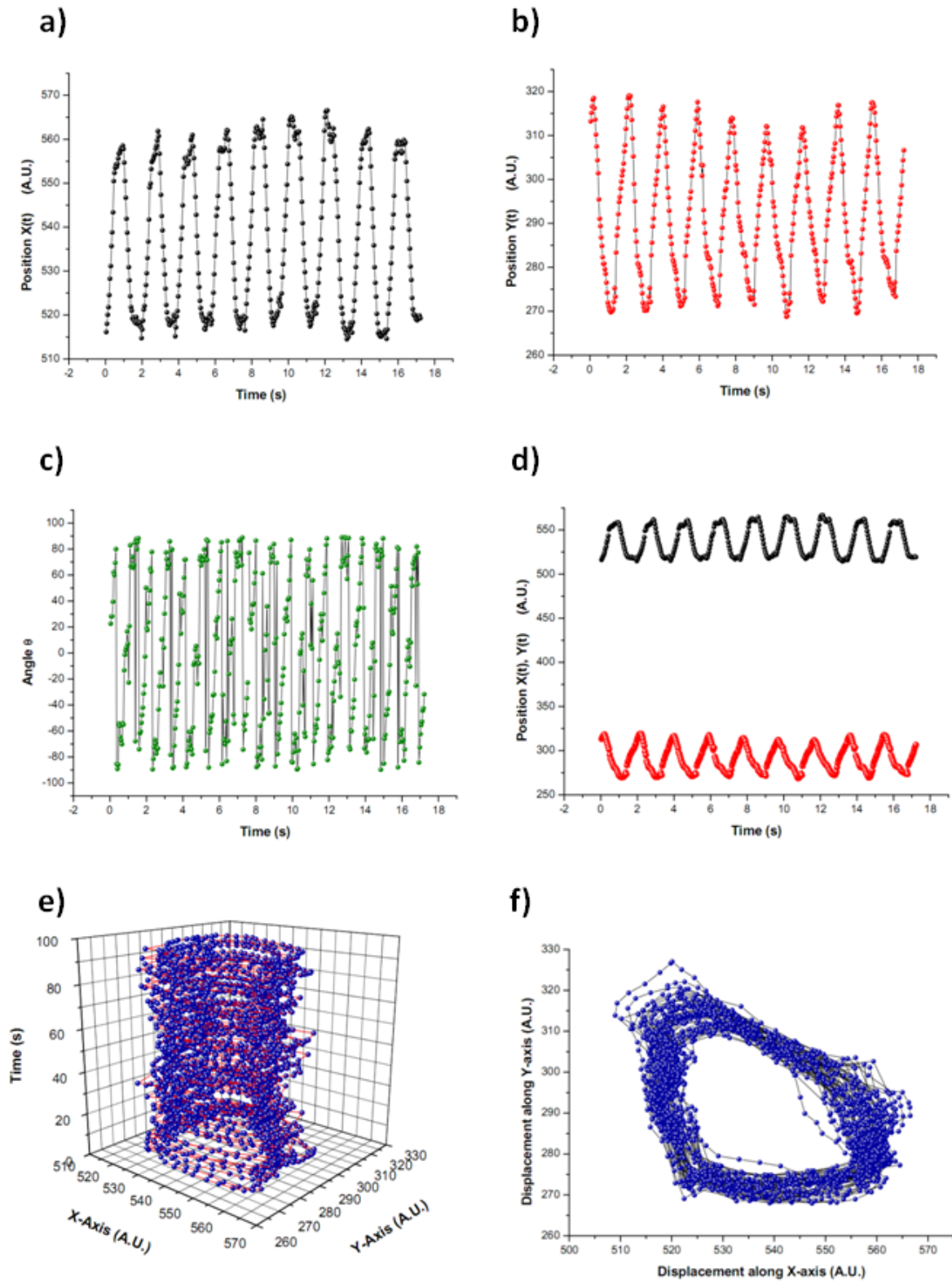


Figure 4.17: Rotation of a solid CLC particle I - In the graphics a) is the X position with respect to the time; b) the Y position with respect to the time, c) the angle between the the and the long axis of the particle. In d) a graphic of both X,Y positions vs time, on e) is presented the 3D trajectory showing their evolution on time and in f) is showed the graphic of the projection on the plane (x, y) from the movement of the particle along the axis X,Y.

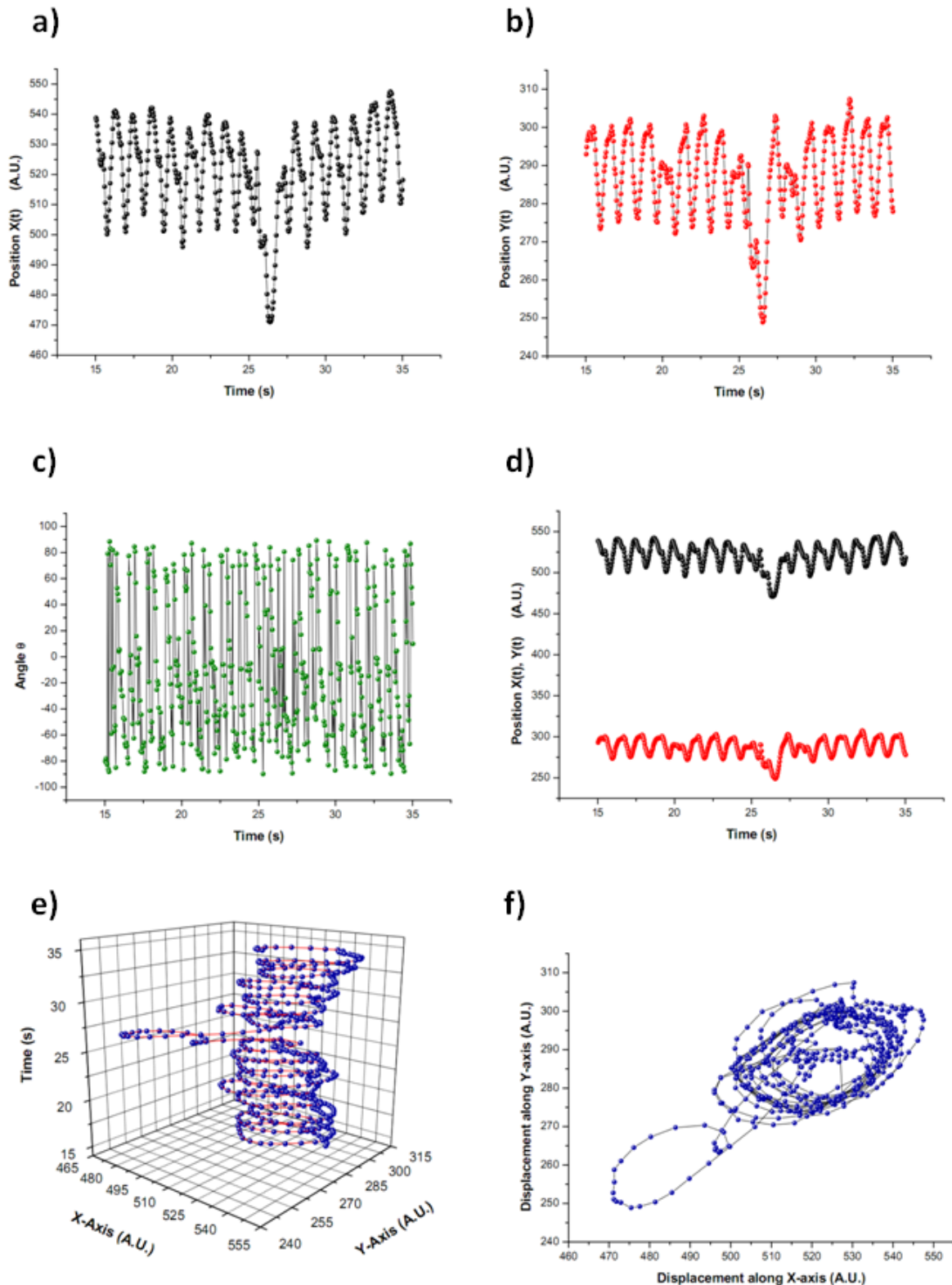


Figure 4.18: Rotation of a solid CLC particle II - In the graphics a) is the X position with respect to the time; b) the Y position with respect to the time, c) the angle between the the and the long axis of the particle. In d) a graphic of both X,Y positions vs time, on e) is presented the 3D trajectory showing their evolution on time and in f) is showed the graphic of the projection on the plane (x, y) from the movement of the particle along the axis X,Y.

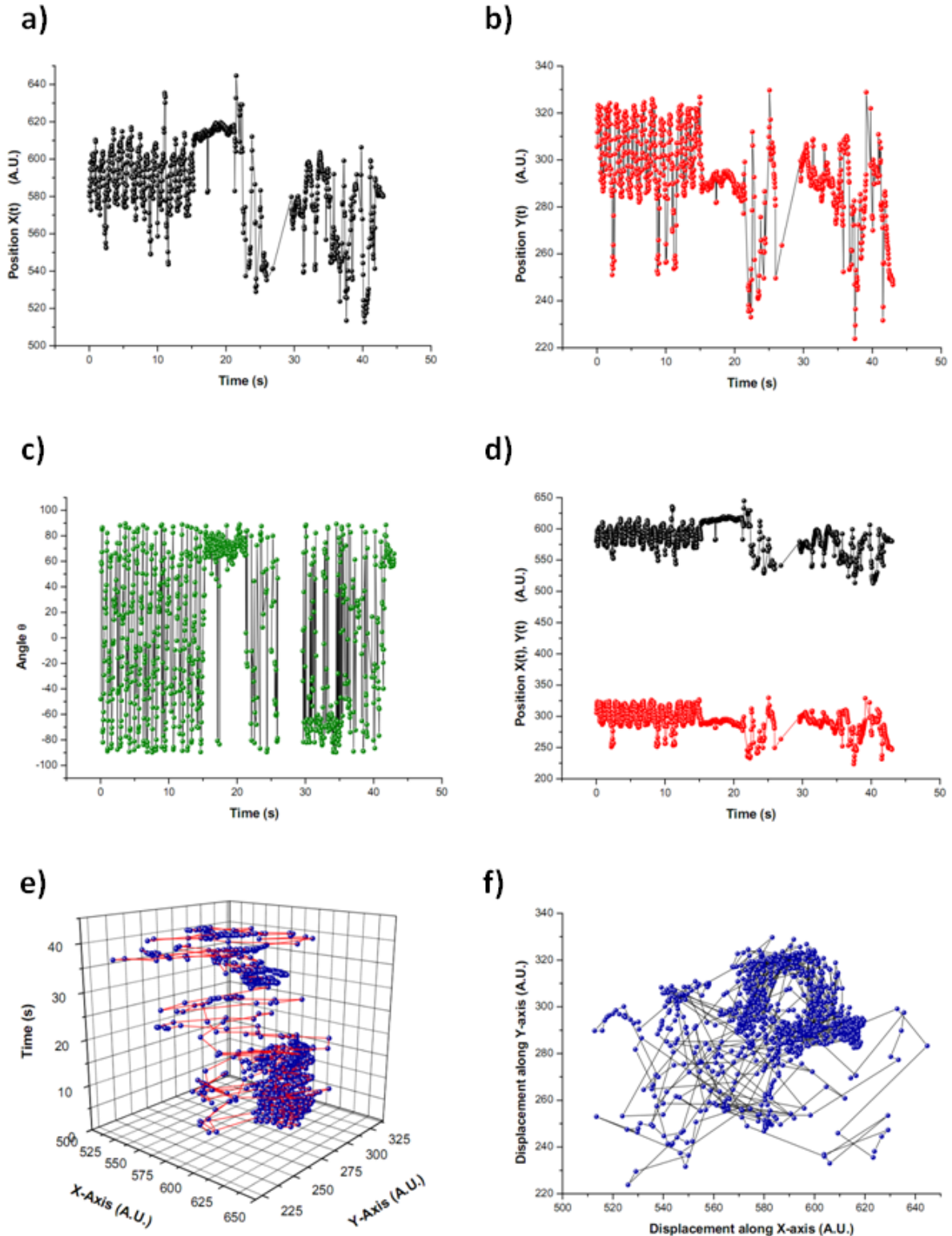


Figure 4.19: Rotation of a solid CLC particle III - In the graphics a) is the X position with respect to the time; b) the Y position with respect to the time, c) the angle between the the and the long axis of the particle. In d) a graphic of both X,Y positions vs time, on e) is presented the 3D trajectory showing their evolution on time and in f) is showed the graphic of the projection on the plane (x, y) from the movement of the particle along the axis X,Y.

4.5 Conclusions

Optical manipulation reveals the exotic behavior that comes from the reflection and transmission properties of chiral droplets depending on the circular polarization state.

We have observed the attractive and repulsive optical forces on CLC micro particles immersed in water with a laser trap. The origin of these forces relies on the interplay between the internal helical structure on the CLC particles and the circular state of polarization of the light. The simple way to exploit the reflection and transmission properties of CLC requires only a spatial periodicity (the period of the helix) close to the wavelength of light to obtain a selective photonic band gap. In optically isotropic chiral left handed particles of liquid crystal, a right circular polarized beam induces an attractive force, while for left circular polarization a repulsive force dominates. For optically anisotropic particles, the normal continuous rotation and trapping occurs only on RCP, while non conventional rotation and repulsive forces were observed reversing the circular polarization to LCP. The combination of these effects not seen before in particles of this type, evidence that such chiral objects with dynamic controlled by light-polarization could be promising media for further research or applications based on all-optical switching devices.

Optically controlled dynamical behavior of fluid and solid microspheres by means of circularly polarized optical tweezers has been investigated. The observed attractive-repulsive behavior of the optical trap comes from the reflection and transmission properties of the investigated chiral and birefringent particles, connected to the cholesteric liquid crystal phase.

We observed very different dynamical behaviors connected to the different internal architectures of the particles. A net attractive or repulsive optical force on the same particle with radial configuration of the helical structures (isotropic chiral particle), was performed depending on the handedness of the CPL. The origin of these forces has been explained taking into account for the interplay between the internal helical structure of the CLC and the light circular polarization, when the cholesteric spatial periodicity is close to the wavelength of optical tweezers beam (inside the selective photonic band gap). Reflection and transmission properties of the CLC have been then considered to evaluate the optical gradient and scattering forces. For optically anisotropic particles, the dual behavior related to the selective reflection of the CPL produces the trapping and a non uniform rotation of the particle for right handed, while unbalanced torques and forces induce a complex dynamics reversing the circular polarization to left handed.

The unique mechanical and manipulation performances of these devices can be certainly improved by taking into consideration different light fields configurations, like complex beams or holographic patterns with proper architectures of the polarization state. Moreover, the well know high sensitivity of the liquid crystals to the external stimuli, like electric or magnetic

fields, suggests the possibility to introduce additional control parameters and to combine, for example, the optical control with the electric and magnetic one.

Finally, the capabilities of these microparticles, here demonstrated by means of optical manipulation experiments, as well as their exclusive properties allowing their passive or even active role in microdevices, make them good candidates for developing new concepts in materials science, colloidal and photonics systems, microlasers, optical control, micro- and optofluidics, microsensors, among many others.

Part 5

Photonic applications of CLC: micro lasers

5.1 Introduction

Optical microresonators and microcavities have attracted a lot of attention because of their promising applications on microlasers, photonics devices, sensors but also for fundamental investigations in quantum electrodynamics^[107–114]. Here we demonstrate lasing emission from three dimensional microresonators created by the self assembling of chiral structures in dye doped solid microspheres. The microparticles with spherical radially periodic dielectric structures are created using the photo-reactive mesogen (RMS03-001C, by Merck) mixed with the chiral dopant (ZLI-811, Merck) to self organize cholesteric droplets in a water emulsion. The photopolymerization of the liquid crystalline droplets enables to freeze the helicoidal supramolecular configurations in spherical solid particles. The internal material structure behaves like a multilayer system, creating spherical distributed dielectric microresonators in the visible range (*i.e.* with distributed Bragg reflection in radial direction).

The easiness of the procedure for assembling the chiral solid microspheres investigated, enable to control the period of the radial dielectric modulations and the size of the microresonators, but also the chirality of the helicoidal-periodic structures to left or right-handed (depending on the kind of chiral dopant). In addition, the incorporation of proper dye molecules into the precursor cholesteric liquid crystal droplets in fluid state, allow to obtain droplets with absorption in selected wavelengths that after can be polymerized to make solid spheres. In this way, laser emission based on optically pumped dye-doped solid microspheres is demonstrated. This chapter is the beginning (with preliminary results) in our investigation about the effects of droplet size and dye concentration on the spectral position of lasing wavelength for solid chiral microspheres. The chiral particles can have different periods and handedness of the helicoidal

structures, to show how these parameters can be used for the emission wavelength tuning, envisaging strategies for innovative light sources and microarchitectures of lasers systems.

5.2 Optical microcavities

One of the most important optical components are optical microcavities and microresonators, their importance and interest goes from the fundamental physics, because of their small mode volume and high quality factor, to the applications for the development of next generation compact size and low-power photonic devices: low threshold microlasers, optical filtering and switching devices, sensors, etc^[112–114].

For many of these applications it is often critical to realize a microresonator with compact size (small modal volume, V), high mode quality factor Q , and large spectral range, that is on the order of the optical wavelength^[153]. The Q -factor is a measure of the resonator capacity to circulate and store light, and is usually defined as the ratio of the energy stored to the energy dissipated in the microresonator^[153–156]. An ideal resonator would have infinitely sharp resonances and would confine light indefinitely, however in the practice resonators like this are not possible because of the loss effects such as absorption and radiation loss. Like mechanical oscillators, the optical microresonators support resonant frequencies that are dependent on their shape and size. By tailoring the resonator shape, size, material composition, etc; the microresonator can be tuned to support a spectrum of optical modes with proper polarization, frequency and emission pattern^[156].

There are three kinds of confinement of light in microcavities, these are: total internal reflection, confinement by a periodic structure and confinement by plasmons^[126,153]. To get the confinement of light in microcavities, many kinds of microresonators with different architectures have been developed and several fabrication techniques have been adopted. The most widely used microresonators are rotationally symmetric structures such as spheres, cylinders, toroids, and disks, which have been shown to support very high-quality factor Q modes, with low threshold, and simple fabrication procedures^[157–163]. They can be fabricated by exploiting either (almost) total internal reflection of light at the interface between a dielectric (*e.g.* semiconductor) material and the surrounding air or, by distributed Bragg reflection from periodical structures such as multilayered structures or arrays of holes. As a result, a very wide range of microresonator shapes has been explored over the years for various applications. In figure 5.1 are listed some of the most popular optical microresonator types as well as their dominant modes and basic features.

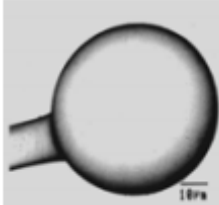
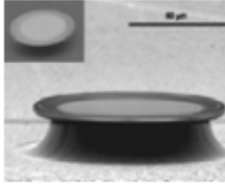

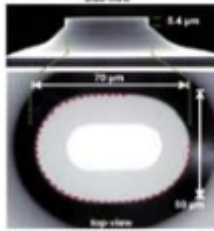
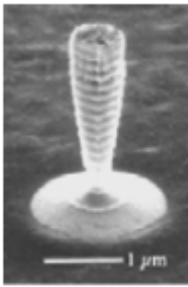
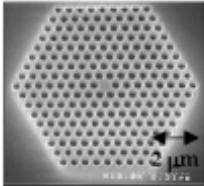
Resonator type	Light confinement Dominant modes Features	Resonator type	Light confinement Dominant modes Features
<p>Microsphere</p>  <p>Lefevre-Seguin, V., 1999, <i>Opt. Mater.</i> 11(2-3):153-165. © 1999 Elsevier B.V.</p>	<p>ATIR</p> <p>WGMs</p> <p>Ultra-high Q-factors ($10^7 - 9 \times 10^9$); large mode volumes; dense modal spectrum (all modes are degenerate); challenging on-chip integration</p>	<p>Microtorus</p>  <p>Armani, D.K. et al, 2003, <i>Nature</i> 421:905-908.</p>	<p>ATIR</p> <p>WGMs</p> <p>Mode volumes lower than for spheres; very high Q-factors (5×10^8); reduced azimuthal-mode spectrum; suitable for on-chip integration</p>
<p>Microdisk (microring)</p>  <p>Baba, T. et al, 1997, <i>IEEE Photon. Technol. Lett.</i> 9(7):878-880. © 1997 IEEE</p>	<p>ATIR</p> <p>WGMs</p> <p>Small mode volumes; high Q-factors ($10^4 - 10^5$); higher-radial-order WG modes are eliminated in the ring resonators; suitable for planar integration</p>	<p>Quadrupolar (racetrack) microresonator</p>  <p>Gmachl, C. et al, 1998, <i>Science</i> 280:1556-1564. © 1998 AAAS</p>	<p>ATIR</p> <p>WGMs, bow-tie</p> <p>Relatively low Q-factors (850-1500), highly directional emission and high FSR of the bow-tie modes; WGM Q-factors lower than in circular microdisks, efficient coupling to planar waveguides</p>
<p>Micropost/pillar</p>  <p>Solomon, G.S. et al, 2001, <i>Phys. Rev. Lett.</i> 86(17):3903-3906. © 2001 American Physical Society</p>	<p>DBR in vertical direction</p> <p>ATIR in horizontal direction</p> <p>Fabry-Perot oscillations</p> <p>Small mode volumes; relatively high Q-factors (1300-2000); easy coupling to fibres</p>	<p>Photonic crystal defect microcavity</p>  <p>Painter, O.J. et al, 1999, <i>J. Lightwave Technol.</i> 17(11):2082-2088. © 1999 IEEE</p>	<p>ATIR in vertical direction</p> <p>DBR in horizontal direction</p> <p>Symmetry-dependent spectrum of defect modes</p> <p>The smallest mode volumes; high Q-factors (4.5×10^4); suitable for planar integration</p>

Figure 5.1: Types and characteristics of optical microresonators - For the light confinement and dominant modes the acronyms are: Almost Total Internal Reflection (ATIR); Whispering Gallery Modes (WGMs); and Distributed Bragg Reflection (DBR). Image taken from reference^[126].

From the previous examples, one of the most common type of microresonators is made of transparent dielectric spheres or planar circular structures with typical radius of 10-50 μm ^[164]. If the refraction index of the sphere is greater than the index of the outside medium, the light can be trapped inside the sphere as a consequence of total internal reflection. If the light is trapped inside a symmetric structure, it can be circulating in the structure and return to the starting point in phase, producing resonant standing waves. This resonant modes are referred to as whispering-gallery modes (WGMs) or morphology-dependent resonances (MDRs)^[126,156]. This kind of resonators won't be considered on this work.

5.2.1 Circular and spherical Bragg microcavities

Apart from light confinement by reflection and total internal reflection such as in WGMs, confinement by photonic periodic structures is even more efficient^[126,153]. If the dielectric photonic structures have a periodic modulation of the refractive index with a period comparable to the wavelength of the light, the periodic structure can be one-, two- or three-dimensional. On each period of the structure a part of incident light is reflected and then constructively or destructively interferes. Therefore, the light can be reflected from the structure, this effect is called Bragg reflection. Bragg reflection is more known by the scattering of X-rays from a crystal lattice, which is exactly the same phenomenon but at shorter wavelengths^[165]. For the wavelength range that is reflected from the structure, we say that the photonic bandgap (PBG) exists and usually changes for different incidence directions. Structures having the PBG are referred to as photonic crystals. The frequencies in this range are forbidden inside the periodic material and if the propagation of the same frequency range is forbidden in all the directions in space and for all the polarizations, we have full photonic bandgap. Typically the structures based on photonic crystals can confine light in a volume much smaller than those in the case of WGMs, however the price to pay is to obtain lower Q -factors, that are up to approximately 10^5 for photonic crystals compared to the factor of 10^{10} for WGMs^[153].

One type of PBG structures are the circular Bragg microcavities^[157-159] and spherical Bragg microcavities^[160-163] made of concentric rings or concentric shells called "onion structure". Such structures are basically one dimensional photonic crystals, but wrapped around the central point. Light going out from this central point is reflected back by the periodic structure and is confined in the center. Spherical Bragg-reflector microcavities, are particularly interesting because of their perfect rotational symmetry in 3D.

Depending on the structure of the cavity we have three basic types of spherical Bragg microcavities (see figure 5.2).

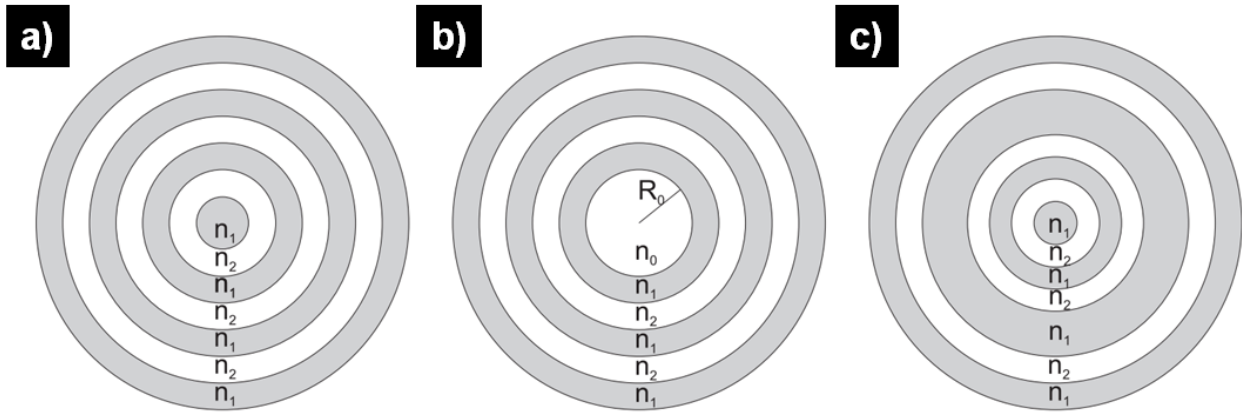


Figure 5.2: Three basic types of spherical Bragg microcavities - a) A normal spherical Bragg microcavity, b) with a defect in the center and c) with a shell defect. Image taken from reference^[156]

The simplest is the structure where the periodic structure fills all the volume of the spherical cavity (figure 5.2a). In the figure is represented the periodic modulation of the refractive index by n_1 and n_2 in the sphere. In the second case there is a defect in the center (figure 5.2b). The size of the defect is characterized by the radius R_0 with refractive index n_0 , this is a sphere that can have the same or different refractive index than the layers. The third type of Bragg microcavity has a shell defect, that means, the case when one of the spherical layers is thicker (figure 5.2c) or has different refractive index. All this structures also have equivalents in 2D, that are referred to as circular, disk and ring Bragg microcavities, respectively^[166].

In the case of microcavity with the central defect, the optical modes are confined into this central region, with the intensity exponentially decaying into the surrounding periodic structure. The resonant frequencies lie in the PBG frequency region, and are therefore called bandgap modes or defect modes. If there is no defect at the center, the modes in such cavity are unlocalized and occupy much of the volume of the cavity and their frequencies lie on the edge of the bandgap or near the band-edge, so they are called band-edge modes.

5.3 Liquid crystal band-edge lasers

Band gaps in materials have long been recognized as important for waves propagating in regular periodic structures. They arise essentially from interference effects between waves as they propagate through the medium in question. Photonic band gap (PBG) structures are also produced in liquid crystals (LCs) where phases with a regular, periodic dielectric structure may be used to generate coherent laser light. Chiral LCs, for example, self organize to give a macroscopic helical phase with a structure that exhibits a PBG, provided that the wavelength of incident light is of the helical periodicity. A typical LC laser consists of an LC host and a

fluorescent laser dye, where the LC host provides the feedback and the laser dye provides the gain. By reflection of light the cavity confines the light in a small space and at the same time defines the possible modes inside it. The gain material amplifies these modes so that lasing is possible.

The original concept of lasing in liquid crystals was put forward by Goldberg and Schnur in a patent in 1973^[167]. However, it took 25 years before LC lasing was experimentally demonstrated by Kopp *et al.* in 1998^[168]. During the years between the prediction and demonstration of lasing in LCs, considerable research was conducted into the optical properties of materials exhibiting a PBG. For example, Yablonovitch^[169] examined the optical properties of the PBG itself, and suggested that photon suppression would occur within the PBG. John^[170] also showed that photon localization and enhancement would occur at the photonic band edges (PBEs) and Dowling and colleagues^[171] reported that, with the inclusion of a fluorescent emitter, spontaneous emission would be suppressed within a PBG and enhanced at the band edges where there is a sharp increase in the density of photon states (DoS). It is here at the PBEs that lasing occurs on the inclusion of such a gain medium, as first reported by Kopp *et al.*^[168].

Thus, the stimulated emission rate is large at the edges. As a result, two possible laser channels exist in an LC laser: one at each band edge. The wide spacing of these two modes because of the presence of the PBG restricts mode hopping, which is a common disadvantage with more conventional lasers, such as the Fabry-Perot laser^[172]. Schmidtke and Stille^[173] showed that the magnitudes of the peaks at the band edges are equal, indicating that both edges are potentially suitable for lasing.

Chirality in an LC can be naturally forming in the bulk material itself or, for an achiral host, can be induced on addition of a high-twisting-power chiral additive. The latter approach allows to control the macroscopic optical properties of the CLC as required, while the chiral additive allows the position of the band edge to be selected for a specific wavelength output. The geometrical confinement of liquid crystals within micrometer-sized systems is a mean to obtain a range of stable molecular configurations exhibiting varied defects topologies^[111–114,174].

The figure 5.3 shows a typical experimental setup where a dye doped CLC planar film is optically pumped with a pulsed laser.

The wavelength of the pump laser must coincide with the absorption of the laser dye. A typical combination is to pump the laser dye optically with a Nd:YAG laser frequency doubled to 532 nm with pulse widths of either nanoseconds or picoseconds. The penetration depth of the excitation beam in the CLC laser sample is maximized by converting the linearly polarized pump laser beam into circularly polarized light through the use of a quarter-wave plate. The CLC laser emission properties can be investigated using a range of components, *e.g.* a spectrometer, energy meter, beam profiler, etc.

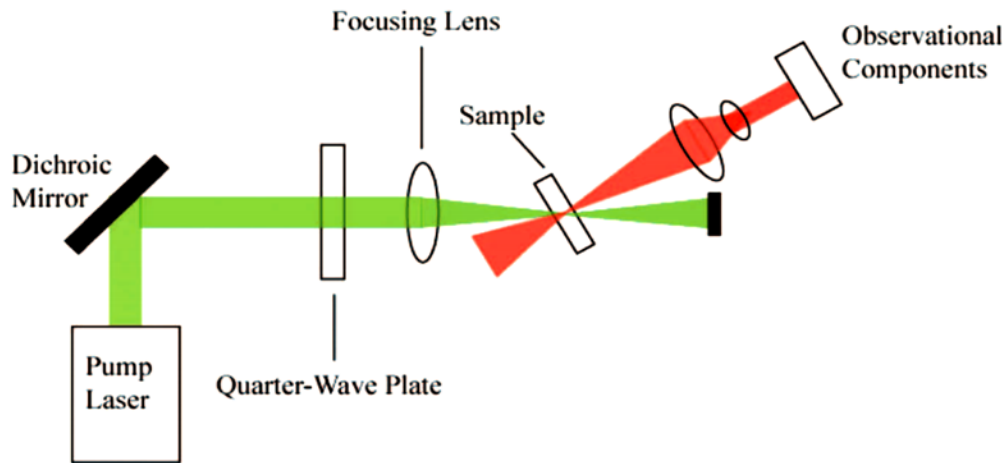


Figure 5.3: Experimental setup for CLC lasers - Experimental setup for lasing on CLC with an pumped system. Image taken from reference^[175]

As is represented in figure 5.4, CLC laser emission always occurs in a direction parallel to the helix axis irrespective of the angle of incidence of the pump beam. This is where the pump beam intersects the LC laser sample at an angle, while the CLC laser emission occurs in a direction parallel to the CLC helix axis. Because of the symmetry of the helical CLC structure, laser emission occurs equally in both the forward and the backward directions.

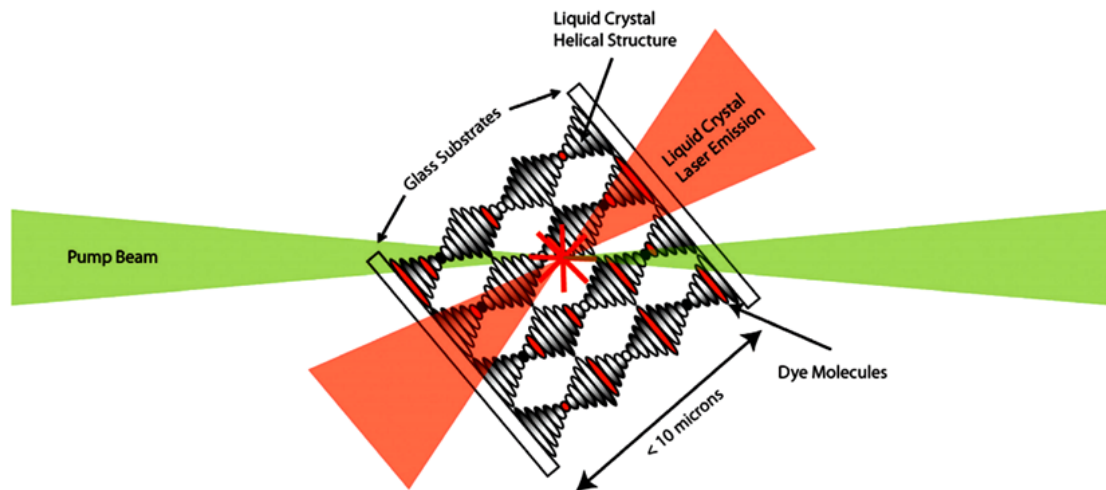


Figure 5.4: LC laser emission parallel to the helix axis of the CLC in both forward and backward directions. - The pump beam is incident at an angle to the helix axis. Image taken from reference^[175]

Exploiting the same principle for CLC laser emission, recently 3D microlasers based on self-assembled CLC micro-droplets suspended in a glycerol or polymeric matrix have been developed^[114,176,177]. Thus, the laser light is emitted from the center of the CLC microdroplet in

all directions (omnidirectional lasing) and the laser is acting as a coherent, point-like source of light.

In our case, we have recently demonstrated a procedure to create solid chiral microspheres with internal refractive index shells configuration (as figure 5.2c), by combining the self-assembling of chiral nematic droplets in water with the photopolymerization process. The self-assembling procedure of the cholesteric droplets in pure water makes possible to create spherical particles with the internal shells configuration of the refractive index connected to the self-organized helicoidal structures addressed by the chiral molecules, suggest also a laser emission omnidirectional. Because the spherical shape and internal structures are fully preserved after droplets polymerization and water evaporation, omnidirectional laser emission is expected in case of dye doped solid microspheres.

Moreover, in the case of the flash-light type and the flash-ring type microbeads where the helical structure with axes perpendicular to the particle surface are preserved in a conical or equatorial region inside the sphere, as showed in the figure 3.7, laser emission is expected to occur in a smaller solid angle range.

5.4 Sample preparation and experimental setup

The investigation of the lasing from the solid CLC microparticles was performed by pumping with a Q -switched pulsed laser Nd-YAG laser (Continuum, Surelite II) with the second harmonic, the beam was focused on the microspheres with a 10 cm focal length lens (L1 as is shown in figure 5.5). The pulse wavelength and width were 532 nm and 6 ns, respectively. The combination of a linear polarizer (P) and a half-wave plate (HWP) at the exit of the beam allowed to regulate the beam intensity.

Two kinds of dye-doped microspheres (with diameters ranging from 5-40 μm) were obtained by mixing 1 wt% fluorescent dye Pyrromethene 567 and 1 wt% fluorescent dye DCM to the respective mixture of reactive mesogen and the left-handed chiral dopant ZLI-811 (Merck). In both cases, the concentration of chiral dopant was chosen so that the longer wavelength edge of the cholesteric PBG overlaps with the emission maximum of the dye used. The position of the PBG of each mixture was determined by measuring the spectrum of white light reflected from a polymerized film of thick $\sim 40 \mu m$ in a planar cell containing the mixture. One of the most important properties of the dyes is their solubility in LCs. The LC emulsion polymerization procedure is the same described in the experimental section (5.5). In figure 5.6 are shown images of the dye doped solid microspheres in water observed between crossed polarizers. The adopted procedure makes use of pure water to obtain the majority of particles with radial configuration, nevertheless the inevitable presence of some impurities is responsible of a small percentage of droplets with different configurations, as shown in the figure.

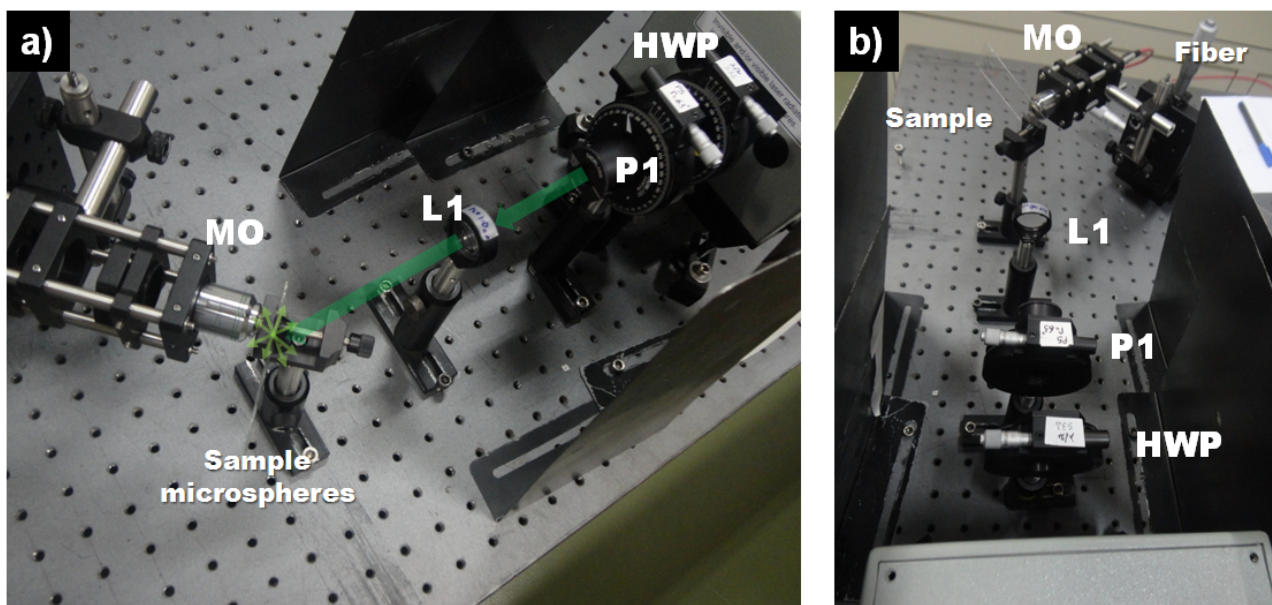


Figure 5.5: Experimental setup - a) and b) Shows some photographs of the experimental system for for CLC lasing, on b) only part of the fiber of the spectrometer is showed. Notice the similarity with the experimental setup on 5.3

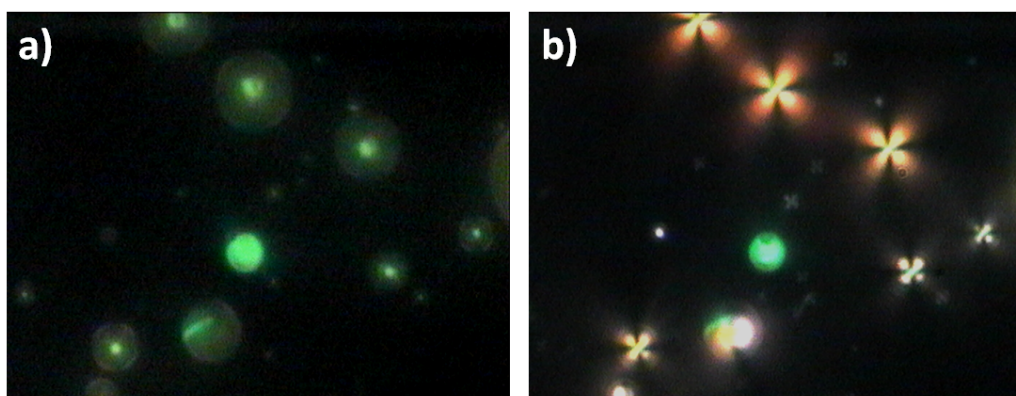


Figure 5.6: Polymerized dye doped particles observed under crossed polarizers - The microscopy images show an emulsion of dye doped chiral solid microspheres in water obtained by photopolymerization. The images were taken between crossed polarizers a) in reflection mode and b) for the same particles under transmission mode.

A small amount of the emulsion containing the particles were put in a glass slide, after the water evaporation the residual microspheres remained as substrate on the glass. The optical fiber spectrometer (Avantes, model Avaspec-2048) with spectral resolution of 2 nm was used to measure the laser intensity from the pump and from the emission on the glass slide containing the dye doped microspheres. To collect a higher amount of light with the fiber a system composed by a microscope objective 20X and lens was used. Removing the optical fiber from this system it was also possible to use a CCD camera connected to a computer to observe the sample and the region where the light was focused.

5.5 Results and discussion

In the graph in figure 5.7, the transmission spectrum of a polymerized film of the CLC is superimposed on the emission spectrum to demonstrate that lasing occurs at the resonance located adjacent to the long wavelength selective reflection band edge. This aspect is foreseen for CLC lasing, confirming that the observed line is due to the laser emissions of the individual microspheres. Furthermore, the frozen helical structures in the solid microspheres improve stability of the laser emission with respect to the usual CLC cells or CLC droplets, where stability problems are mainly related to cholesteric texture deformations due to the absorption of the pumping beam. Figure 5.7 shows the spectrum of the light coming from the sample collected with the fiber spectrometer placed in close proximity to the particles and the experimental scheme.

Notice that, the reflection spectrum was obtained for light propagating along the CLC helix, while the emission spectra was measured at a generic angle with respect the pump beam direction. The laser pump beam at 532 nm appears together with the line at 558 nm, which was emitted by the sample. Although the measured line-width is wider than the reported on reference^[125] ranging from 5 nm to 6 nm, this broadening nevertheless depends on the limit of the instrumental spectral resolution, as demonstrated by the measured line-width of the pumping line. In our case, several factors had an additional contribution like the thickness of the particles substrate, the non uniform distribution in size diameter of the sphere, the resolution time for the instruments and the effect of photobleaching, occurring when the dye molecules are irreversibly converted to a non-fluorescent form.

In the case of isotropic-radial chiral microspheres doped with the dye DCM (Red emission), we observe similar results as indicate the figure 5.8.

As expected, the lasing wavelength is related to the natural helical period of the cholesteric. Omnidirectional 3D or 2D lasing occurs with stimulated emission of light from the dye molecules. The recorded spectrum is composed of the pump laser beam (532 nm line) and by the lasing emission from the dye doped microspheres (558 nm line for Pyrromethene and 606 nm for

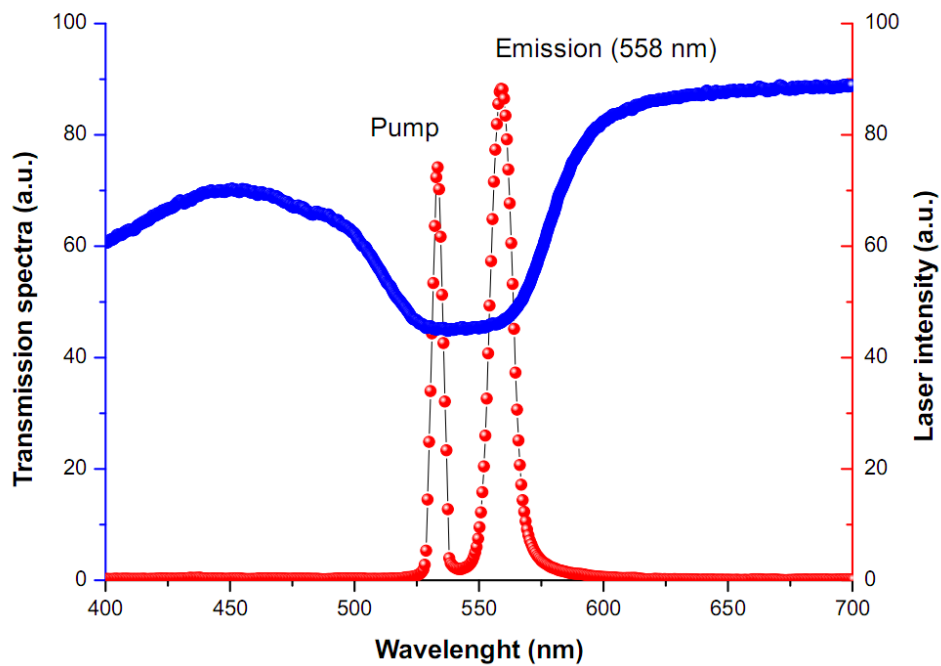


Figure 5.7: Spectrum of the light emitted by the dye doped microspheres (Green emission) - Light intensity spectrum due to the emission from the microspheres and to the pump beam line. The light intensity spectrum is compared to the reflection spectrum of a $10\ \mu\text{m}$ planar film of the same polymerized CLCs. The laser pump beam at 532 nm appears together with the line at 558 nm which was emitted by the sample

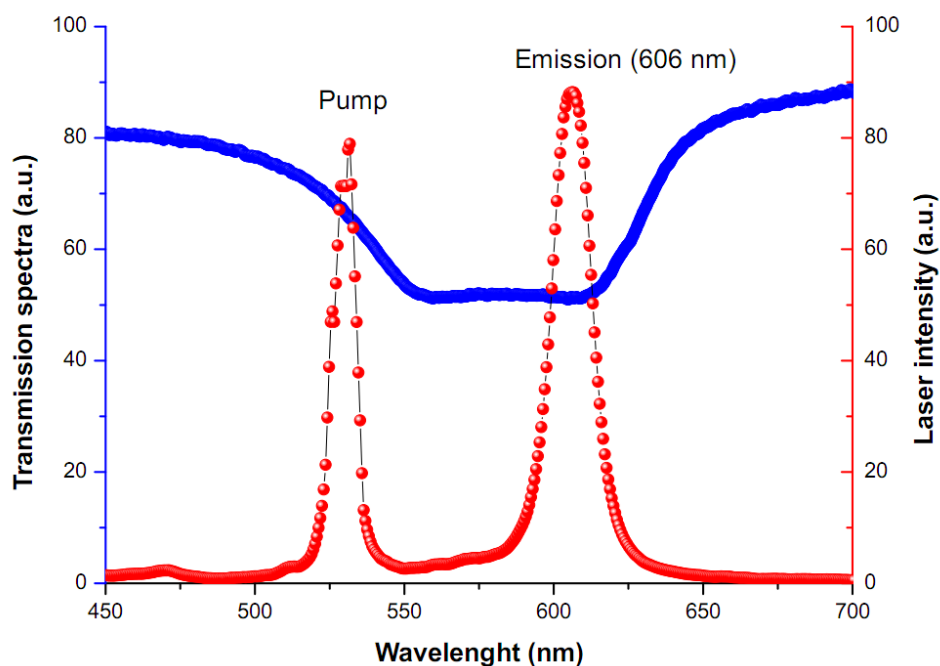


Figure 5.8: Spectrum of the light emitted by the dye doped microspheres (Red emission) - Light intensity spectrum due to the emission from the microspheres and to the pump beam line. The light intensity spectrum is compared to the reflection spectrum of a $10\ \mu\text{m}$ planar film of the same polymerized CLCs. The laser pump beam at 532 nm appears together with the line at 606 nm which was emitted by the sample

DCM) obtained with a few tens of micro-joule pump-energy. Threshold energy lower than $1 \mu\text{J}$ has been observed. Although lasing from CLC microdroplets has been demonstrated, emission from solid micro-spheres represents an innovative concept of a solid microlaser. Additionally a clear advantage of solid spheres over LC fluid state spherical microcavities is the increased stability of the helical structures that guarantees a more stable laser emission.

5.6 Conclusions

Lasing from dye doped solid chiral microparticles has been demonstrated with stimulated emission of light from dye molecules, added to the primitive LC mixture.

The cholesteric LC spheres forms a Bragg-onion optical microcavity when are in an adequate medium and the stimulated emission of light can be obtained from dye molecules incorporated in the liquid crystal mixture. After realize a CLC- pure water emulsion, CLC droplets with a Bragg resonator structure have been created, the subsequent photopolymerization allow to freeze the structures. These solid particles work like Bragg onion microresonators and lasing emission from dye doped microspheres have been observed.

Because of the procedure to create the chiral solid particles by polymerizing LC droplets in water, the spectral position of lasing wavelength can be easily tuned from ultraviolet wavelengths, through the visible range, to infrared wavelengths. We have investigated the effects of helical pitch and dye concentration on to show how these parameters can be used for the emission wavelength tuning. The emission at two different wavelengths has been demonstrated by combining the chiral dopant concentration and the proper fluorescent dye. Furthermore, the frozen helical structures in the solid microspheres improve the stability of the laser emission with respect to the usual CLC cells or CLC droplets, where stability problems are mainly related to cholesteric texture deformations due to the absorption of the pumping beam.

A very large amount of microlasers can be produced in a very simple and fast way. Light polarization and emission spectrum of light sources based on this microphotonic devices can be tuned properly mixing microlasers, emitting light with opposite circular polarizations or different wavelength.

Several improvement can be envisaged both on the performance of the microlasers and on the architectures of microlasers systems for lab on a chip devices. Reduction of the pumping threshold as well as control of the particles dimensions and structures can be achieved through the materials design and selection, and the adoption of microfluidics procedures for the creation of liquid crystal droplets and polymeric beads. A significant reduction in the threshold would increase the number of potential pumping mechanisms that might be available for use, such as a light-emitting diode or white light source, and as consequence the application fields.

Moreover exotic architectures can be designed with these highly versatile, soft-matter microlasers as: arrays of microlasers with different wavelength in the properly designed geometry, white light sources, e-papers, by mention a few.

Part 6

General conclusions and prospectives

In the work of this thesis was presented an analysis of the dynamical properties of the light interacting with liquid crystals particles immersed in water.

The use of liquid crystal as material has many advantages for the investigation due to their richness in self assembling and optical properties.

In the first part of the thesis, nematic liquid crystals where used in combination with holographic polarized optical tweezers. The experiments of optical trapping and manipulation with holographic polarization allowed investigating an alternative approach not based in intensity gradients. As a result, it was demonstrated an unconventional opto-hydrodynamical control on LC droplets, suggesting new strategies for optical trapping and manipulation.

In particular, the experiment presented with circularly polarized holographic tweezers and optically anisotropic LC droplets, yields unequivocal evidences of the Magnus effect at low Reynolds number at the micro scale, showing that this hydrodynamic lift force is unexpectedly much larger than the one predicted by the existing theories. This means that in some situations the Magnus force is comparable to the optical forces. The demonstration of the use and existence of this force could serve to develop new experiments or explain previous results that do not take in account such force.

The micro fluidic control and the development of new applications have recently attracted much interest by the science and emergent technologies: a) because of the grow of commercial, biological, medical systems based on micro-pumps, microchannels and transport or deliver of micro particles and b) because of the necessity to combine micro and nano technologies.

In the second part of the thesis, we used cholesteric liquid crystals based microparticles. We investigated their response properties with polarized light and characterized the internal molecular structures. A new kind of solid-chiral microparticles was created starting from water emulsion of a photo reactive mesogen that becomes solid with the UV light. The orientation of the LC molecules at surface can be freely adjusted by changing the physical-chemical properties of

the LC-water interface. Very different dynamical behaviors have been observed in optical manipulation experiments in connection with the different internal architectures of the particles. It was observed and reported for the first time, a net attractive or repulsive optical force on the same particle with radial configuration of the helical structures (isotropic chiral particle) depending on the circular polarization state of the light. The observed attractive-repulsive behavior of the optical trap comes from the Bragg selective reflection and transmission properties of the investigated chiral particles, connected to the cholesteric liquid crystal phase. Moreover, due to the information obtained from the internal structure, we notice that the same cholesteric LC spheres can be used as Bragg-onion optical microcavity. The stimulated emission of light can be obtained from dye molecules incorporated in the liquid crystal mixture and the photopolymerization allows to freeze the structures. From the solid particles working like Bragg onion microresonators and omnidirectional lasing emission from dye doped microspheres was demonstrated.

Several improvements and future perspectives can be envisaged. The procedure of the creation process of the spheres surely can be improved by the use of controlled micro-droplets generator to obtain a uniform size distribution. Microfluidics solutions can be adopted not only to control the dimension of the droplets, but also to include dopants or particles inside the liquid crystal droplets before the photopolymerization.

Of course, the inclusion of nanoparticles, quantum dots, nanowires, nanocrystals, etc. could open a new and wide field of investigation of these devices both for fundamental aspects and properties and for their applications.

The unique mechanical and manipulation performances reported in this thesis could experience significant enhancement by taking into consideration different light field configurations, like complex beams, vortex beams, and holographic patterns with proper architectures of the polarization state. Furthermore, the high sensitivity of the liquid crystals to the several kinds of external stimuli and their non linear properties can be exploited as additional control parameters for multifunctional manipulation strategies.

6.1 List of publications

The work at hand has resulted in the following publications:

- I. G. Cipparrone, J. Hernández, P. Pagliusi and C. Provenzano; **Magnus force effect in optical manipulation**; Phys. Rev. A 84, 015802 (2011).
- II. R. J. Hernández, P. Pagliusi, C. Provenzano and G. Cipparrone; **Exploring unconventional capabilities of holographic tweezers**, Proc. SPIE 8074, 80740L (2011).
- III. G. Cipparrone, A. Mazzulla, A. Pane, R. J. Hernández, R. Bartolino; **Chiral Self-assembled Solid Microspheres: a Novel Multifunctional Microphotonic Device**; Advanced Materials, Vol. 23, 48, (2011).

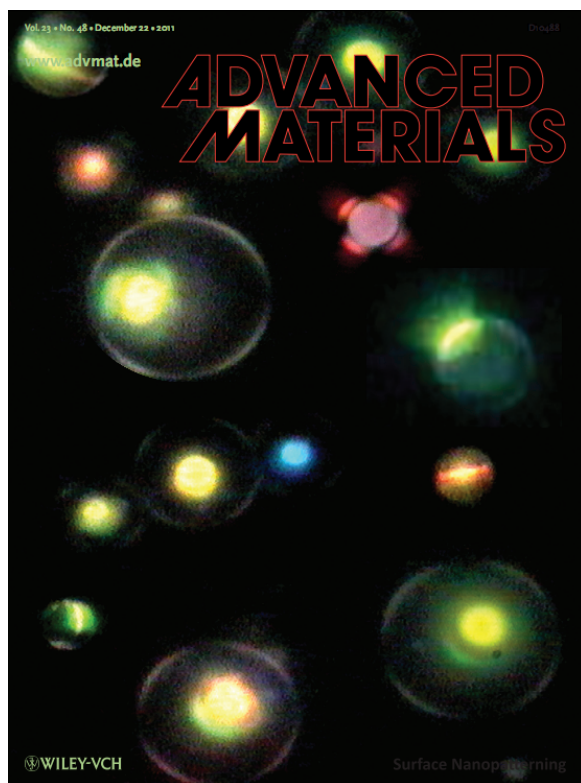


Figure 6.1: Advanced Materials Cover - Advanced Materials, Vol. 23, 48, (2011)

- IV. J. Hernández, C. Provenzano, P. Pagliusi and G. Cipparrone; **Optical manipulation of liquid crystal droplets through holographic polarized tweezers: Magnus Effect**, Molecular Crystals and Liquid Crystals; Vol. 558, Issue 1, (2012).
- V. R. J. Hernández, A. Mazzulla, A. Pane, K. Volke-Sepúlveda, and G. Cipparrone; **Attractive-repulsive dynamics on light-responsive chiral microparticles induced by polarized tweezers**; Accepted for Publication on Lab on a Chip, (2012).

6.2 Participation in Conferences

- I. Action Cost European 2010, Visegrad, Hungary (Oral presentation)
- II. NOMA, Action Cost European 2011, Cetraro Italy (Poster and oral presentation)
- III. II International school of liquid crystals 2011, Erice Italy (Poster)
- IV. Optics for Liquid Crystals 2011, Yerevan, Armenia (Poster and invited talk)
- V. IPCF, General Meeting 2012, Cetraro; Italia (Oral presentation)
- VI. ELOPTO 2012, Gent; Belgium (Oral presentation)

Appendices

Appendix A

Properties of Liquid Crystals (Table)

Liquid Crystal	T ($^{\circ}\text{C}$)	λ (nm)	n_e	n_o	ϵ_{\parallel}	ϵ_{\perp}	k_1 (10^{-12}N)	k_2 (10^{-12}N)	k_3 (10^{-12}N)	Nematic	Range ($^{\circ}\text{C}$)
MBBA ^a	22	589	1.769	1.549	4.7	5.4	6.2	3.8	8.6	20	47
PCH-5 ^b	30.3	589	1.604	1.4875	17.1	5	8.5	5.1	16.2	30	55
		633	1.600	1.4851						30	55
	38.5	589	1.5956	1.4863	16.6	15.3	7.3	4.5	13.2		
		633	1.5919	1.4840							
	46.7	589	1.5849	1.4860	15.9	5.7	5.9	3.9	9.9		
		633	1.5812	1.4836							
K15 (5CB) ^c	25	515	1.736	1.5442	19.7	6.7	6.4	3	10	24	35.3
K21 (7CB) ^d	37	577	1.6815	1.5248	15.7	6	5.95	4	6.6	30	42.8
M15 (50CB) ^e	50	589	1.7187	1.5259	17.9	6.7	6.1	3.74	8.4	48	68
M21 (70 CB) ^f	60	589	1.6846	1.5139	16.3	6.5	6.9		7.7	54	74
M24 (80 CB) ^g	70	589	1.6639	1.5078	14.7	6.2	7.3		9.0	67	80
E5 ^h	20	577	1.736	1.5228	19	5.9				-8	50.5
E7 ⁱ	20	577	1.75	1.5231	19.6	5.1	12	9	19.5	-10	60.5
ZLI-1646 ^j	20	589	1.558	1.478	10.6	4.6	7.7	4.0	12.2	-20	60
ZLI-4792 ^k	20	589	1.573	1.479	8.3	3.1	13.2	6.5	18.3	-40	92
RMS03-001C	75	589	1.684	1.529						25	

^a *p*-Methoxybenzylidene-*p*'-*n*-butylaniline^c Pentylcyanobiphenyl^e Pentylloxycyanobiphenyl^g Octylloxycyanobiphenylⁱ 47%K15+25%K21+18%M24+10%T15^k SFM-TFT mixture^b 4-(trans-4-Pentylcyclohexyl) benzonitrile^d Heptycyanobiphenyl^f Heptyloxycyanobiphenyl^h 45%K15+24%K21+10%M15+9%M21+12%M24^j Phenylcyclohexane and biphenylcyclohexane mixtures

Appendix B

Program for optical forces

In the previous chapters we saw different regimes and approaches to calculate the optical forces, the calculation of optical forces for arbitrary particle sizes $D \approx \lambda$ is nontrivial. For a full arbitrary theory, the solution of Maxwell's equations with the appropriate boundary condition is required. This appendix introduces an alternative method to calculate the forces based on the classical Lorenz-Mie theory and the closely related T-matrix method. The Lorenz-Mie Theory was the first step into that direction and describes scattering of a plane wave by a spherical particle for arbitrary particle size, refractive index and wavelength. Calculation of the radiation trapping force in laser tweezers by use of generalized Lorenz-Mie theory, in which the incident beam is a plane wave, requires knowledge of the shape coefficients of the incident laser beam to be given as^[39]:

$$a_n = \frac{\mu n_{rel} \psi_n(n_{rel}x) \psi'_n(x) - \mu_p \psi_n(x) \psi'_n(n_{rel}x)}{\mu n_{rel} \psi_n(n_{rel}x) \xi'_n(x) - \mu_p \xi_n(x) \psi'_n(n_{rel}x)} \quad (\text{B.1})$$

$$b_n = \frac{\mu_p \psi_n(n_{rel}x) \psi'_n(x) - \mu n_{rel} \psi_n(x) \psi'_n(n_{rel}x)}{\mu_p \psi_n(n_{rel}x) \xi'_n(x) - \mu n_{rel} \xi_n(x) \psi'_n(n_{rel}x)} \quad (\text{B.2})$$

where μ_p and μ are the permittivity of the particle and its surrounding medium, respectively, ψ_n and equation ξ_n are Riccati-Bessel functions, n is an integer that ranges from 1 to $+\infty$ and $x = ka$ is the size parameter of the particle, k being the wave number of the incident wave. The following pages contains a code list of commands and outputs for the software Mathematica to calculate the optical forces for spherical particles with arbitrary particle sizes. It is based on the Generalized Lorenz-Mie Theory (GLMT) from the references^[38,39].

```

%% Program for Optical Forces Calculation %%

Here are presented the analytical results for the paraxial regime at low N.A.

Off[General::spell];

%%%%%%%%%%%%%%%%%%%%%%%%%%%%%%%%%%%%%%%%%%%%%%%%%%%%%%%%%%%%%%%%%%%%%%%% Beam parameters %%%%%%%%%%%%%%%

Numerical Aperture";

NA = 0.85;

Laser wavelength (m) "

 $\lambda = 488 \times 10^{-9}$ ;

Light speed"

 $c = 2.99792458 \times 10^8$ ;

Laser Power (mW)"

P = 100;

Refractive index of medium"

n = 1.333;

Refractive index of particle";

n1 = 1.605;

Particle radii(material or liquid sphere) in meters";

r =  $2.5 \times 10^{-6}$ ;

Wavelength in external medium";

 $\lambda_1 = \frac{\lambda}{n}$ 

 $3.66092 \times 10^{-7}$ 

Wavelength in (sphere)material medium";

 $\lambda_2 = \frac{\lambda}{n_1}$ 

 $3.0405 \times 10^{-7}$ 

Wave number in vacuum in nm-1";

 $K_0 = \frac{2\pi}{\lambda}$ ;

Wave number in external medium in nm-1";

 $K_1 = \frac{2\pi}{\lambda_1}$ ;

Wave number inside the sphere in nm-1";

 $K_2 = \frac{2\pi}{\lambda_2}$ ;

Suitable expansion parameter";

```

$$\text{beta} = \frac{\left(n - \sqrt{n^2 - \text{NA}^2} \right)}{2 n}$$

0.114841

%%%

"Approx. radius of the first dark Airy-ring surrounding the focal point";

$$g = \frac{0.61 * \lambda_0}{\text{NA}};$$

%%% Ricatti-Bessel functions of 1 kind %%

phi[l_, X_] := X SphericalBesselJ[l, X];

psi[l_, X_] := X SphericalHankelH1[l, X];

phi[l_, Y_] := Y SphericalBesselJ[l, Y];

psi[l_, Y_] := Y SphericalHankelH1[l, Y];

%%% Derivate

Ricatti-Bessel functions of 1 kind %%

pphi[l_, X_] := Evaluate[D[phi[l, X], X]];

ppsi[l_, X_] := Evaluate[D[psi[l, X], X]];

pphi[l_, Y_] := Evaluate[D[phi[l, Y], Y]];

ppsi[l_, Y_] := Evaluate[D[psi[l, Y], Y]];

"After this, we have enough information to build the Mie Coefficients"

n̄ = 10; "Number of elements on the series";

a[l_, X_, Y_] = Evaluate[(phi[l, X] * pphi[l, Y] - m * pphi[l, X] * phi[l, Y]) /
(psi[l, X] * pphi[l, Y] - m * ppsi[l, X] * phi[l, Y])] //
Simplify; "%%% a_l %%";

b[l_, X_, Y_] = Evaluate[(m * phi[l, X] * pphi[l, Y] - pphi[l, X] * phi[l, Y]) /
(m * psi[l, X] * pphi[l, Y] - ppsi[l, X] * phi[l, Y])] //
Simplify; "%%% b_l %%";

d[l_, X_, Y_] = FullSimplify[Conjugate[a[l + 1, X, Y]], Element[_Symbol, Reals]];
"%%% a_{l+1} %%";

e[l_, X_, Y_] = FullSimplify[Conjugate[b[l + 1, X, Y]], Element[_Symbol, Reals]];
"%%% b_{l+1} %%";

f[l_, X_, Y_] = FullSimplify[Conjugate[b[l, X, Y]], Element[_Symbol, Reals]];
"%%% b_l %%";

w = 1; "Number of columns for table";

Clear[A, B, j, l, X, Y]; "Clear variables and values";

%%% Sum of Series from l=1 to n
%%%

```

For[j = 1, j ≤ w, j++,
  A_j = Chop[Re[Sum[(2 l + 1) (a[l, X, Y] + b[l, X, Y]) - 2 Sum[{(1 (1 + 2) / (1 + 1) (a[l, X, Y] d[l, X, Y] +
    b[l, X, Y] e[l, X, Y]) + (2 l + 1) / (1 (1 + 1) a[l, X, Y] f[l, X, Y])}]]];
For[j = 1, j ≤ w, j++,
  B_j = Chop[-Im[Sum[(2 l + 1) (a[l, X, Y] + b[l, X, Y]) -
    2 Sum[l (1 + 2) (a[l, X, Y] d[l, X, Y] + b[l, X, Y] e[l, X, Y])]]];
%%%%%%%%%%%%%%%%%%%%%%%%%%%%%%%%%%%%%%%%%%%%%%%%%%%%%%%%%%%%%%%%%%%%%%%%%%
%%%%%%%%%%%%%%%%%%%%%%%%%%%%%%%%%%%%%%%%%%%%%%%%%%%%%%%%%%%%%%%%%%%%%%%%%%;
%%%%%%%%%%%%%%%%%%%%%%%%%%%%%%%%%%%%%%%%%%%%%%%%%%%%%%%%%%%%%%%%%%%%%%%%%% Vs For Scattering %%%%%%%%%%%%%%%%%%%%%%%%%%%%%%%%%%%%%%%%%%%%%%%%%%%%%%%%%%%%%%%%%%%%%%%%%%%;
Vs[Y_, X_] = Table[A_j, {j, 1, w}]; // Simplify
%%%%%%%%%%%%%%%%%%%%%%%%%%%%%%%%%%%%%%%%%%%%%%%%%%%%%%%%%%%%%%%%%%%%%%%%%% Vg For Gradient %%%%%%%%%%%%%%%%%%%%%%%%%%%%%%%%%%%%%%%%%%%%%%%%%%%%%%%%%%%%%%%%%%%%%%%%%%%;
Vg[Y_, X_] = Table[B_j, {j, 1, w}]; // Simplify
Print[" The coefficients are := "];
Vs=Table[A_j, {j, 1, w}];
Vg=Table[B_j, {j, 1, w}];
Print[" V_sc (m, q) = ", Vs];
Print[" V_gr (m, q) = ", Vg]; "
%%%%%%%%%%%%%%%%%%%%%%%%%%%%%%%%%%%%%%%%%%%%%%%%%%%%%%%%%%%%%%%%%%%%%%%%%%
"Relative refractive index between scatterer and medium";
m = n1 / n
1.20405
X = K0 * r
32.1884
Y = m * X
38.7565
%%%%%%%%%%%%%%%%%%%%%%%%%%%%%%%%%%%%%%%%%%%%%%%%%%%%%%%%%%%%%%%%%%%%%%%%%%;
eta[Y_, X_] = Vs[Y, X] / (beta * Vg[Y, X])
{{0.688101}}
"Constant force";

```

$$F0[Y_, X_] = 2 \frac{n P}{c} \text{beta}^3 \frac{Vg[Y, X]^2}{Vs[Y, X]}$$

{ { 4.7363 × 10⁻⁷ } }

"%%"
 "scaled axial position"

$$v[z_] = \frac{2 * \pi * n * \text{beta} * z}{\lambda};$$

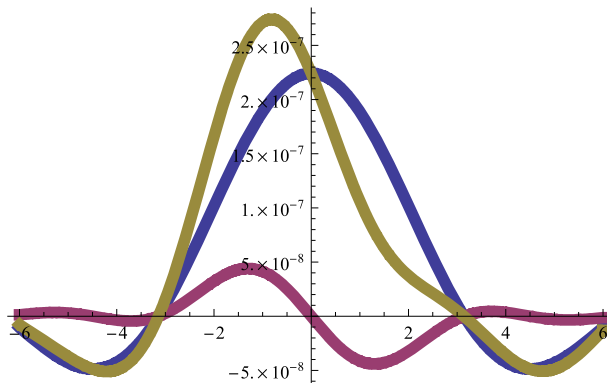
"Then we can express the force as:"

$$F[v_] = F0[Y, X] \left\{ \text{eta}[Y, X]^2 \text{Sinc}[v] + \frac{\text{eta}[Y, X]}{2} D[\text{Sinc}[v]^2, v] \right\}$$

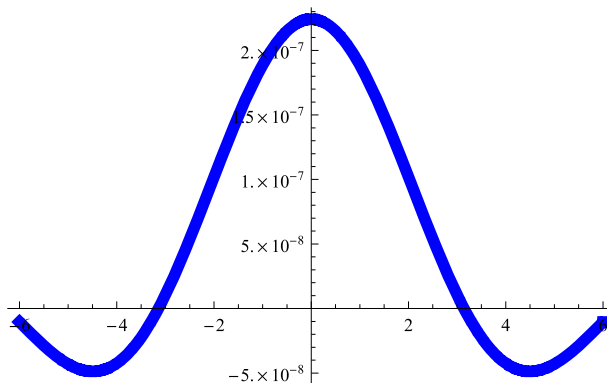
{ { { 4.7363 × 10⁻⁷ (0.473483 Sinc[v] + 0.688101 ($\frac{\text{Cos}[v]}{v} - \frac{\text{Sin}[v]}{v^2}$) Sinc[v]) } } }

Plot[{ F0[Y, X] eta[Y, X]^2 Sinc[v], F0[Y, X] $\frac{\text{eta}[Y, X]}{2} \left(\frac{\text{Cos}[v]}{v} - \frac{\text{Sin}[v]}{v^2} \right) \text{Sinc}[v], F[v] },$
 {v, -6, 6}, PlotStyle -> {Thickness[0.01`]}, PlotRange -> All]

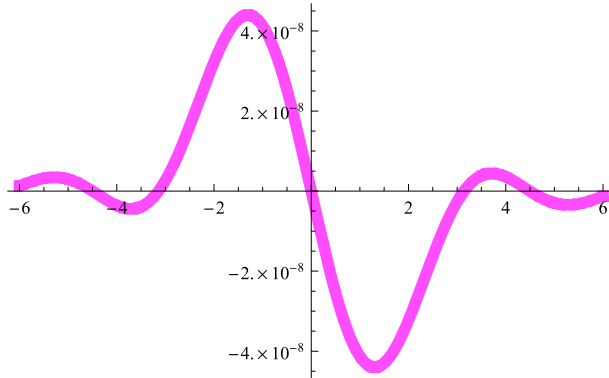
"Green=total force; Blue=Scattering Force; Purple=Gradient Force"



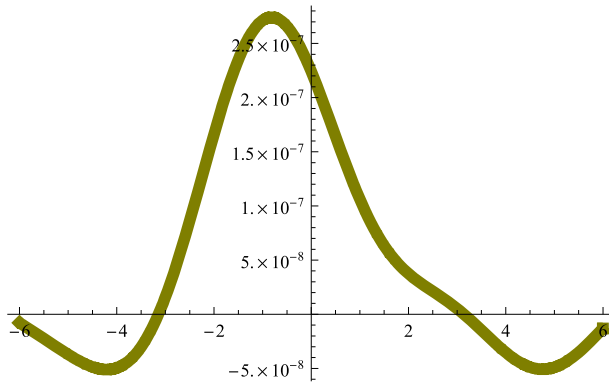
g1[v] = Plot[F0[Y, X] eta[Y, X]^2 Sinc[v], {v, -6, 6},
 PlotStyle -> {RGBColor[0, 0, 1], Thickness[0.01`]}, PlotRange -> All]



```
g2[v] = Plot[F0[Y, X]  $\frac{\text{eta}[Y, X]}{2} \left( \frac{\text{Cos}[v]}{v} - \frac{\text{Sin}[v]}{v^2} \right) \text{Sinc}[v]$ , {v, -6, 6},
  PlotStyle -> {RGBColor[1, 0.3, 1], Thickness[0.01`]}, PlotRange -> All]
```



```
g3[v] = Plot[F[v], {v, -6, 6},
  PlotStyle -> {RGBColor[0.5, 0.5, 0], Thickness[0.01`]}, PlotRange -> All]
```



"Angular frequency"

$$\omega = \frac{2 \pi c}{\lambda};$$

"potential apparently"

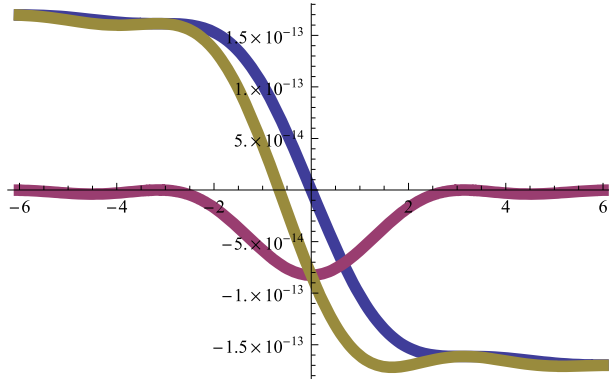
$$U0 = 2 \frac{P}{\omega} \text{beta}^2 \frac{Vg[Y, X]^2}{Vs[Y, X]}$$

{{2.403 x 10⁻¹³}}

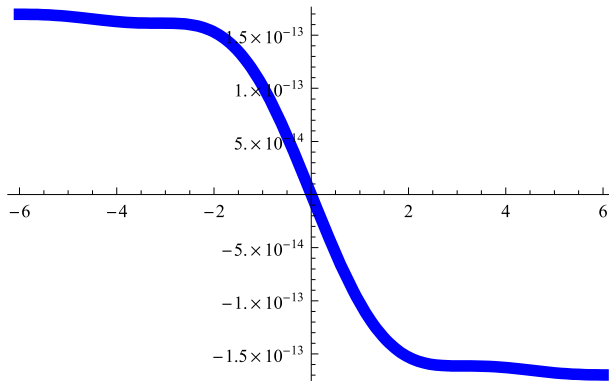
$$U[v_] = U0 \left(\text{eta}[Y, X]^2 \left(\frac{1 - \text{Cos}[2 v] - 2 v \text{SinIntegral}[2 v]}{2 v} \right) - \frac{\text{eta}[Y, X]}{2} \text{Sinc}[v]^2 \right) // \text{Simplify}$$

$$\left\{ \left\{ \frac{1}{v} \left(5.68889 \times 10^{-14} - 5.68889 \times 10^{-14} \text{Cos}[2 v] - 8.26752 \times 10^{-14} v \text{Sinc}[v]^2 - 1.13778 \times 10^{-13} v \text{SinIntegral}[2 v] \right) \right\} \right\}$$

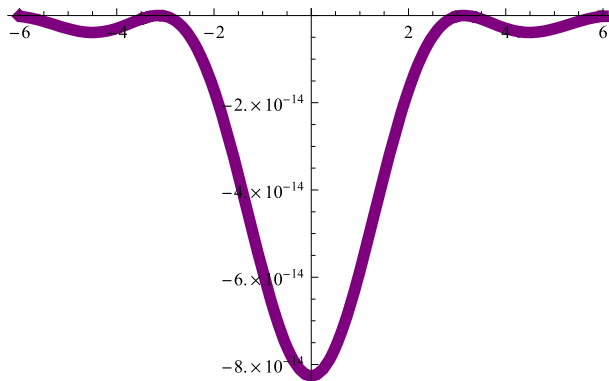

```
Plot[{{U0 eta[Y, X]^2 (1 - Cos[2 v] - 2 v SinIntegral[2 v]) / (2 v), -U0 eta[Y, X] Sinc[v]^2, U[v]},
      {v, -6, 6}, PlotStyle -> {Thickness[0.01`]}, PlotRange -> All]
```



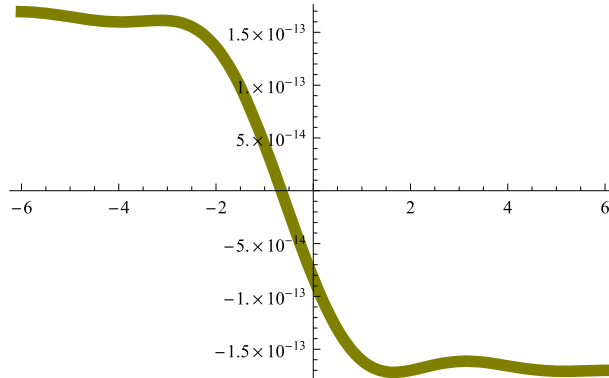
```
g5 = Plot[U0 eta[Y, X]^2 (1 - Cos[2 v] - 2 v SinIntegral[2 v]) / (2 v), {v, -6, 6},
          PlotStyle -> {RGBColor[0, 0, 1], Thickness[0.01`]}, DisplayFunction -> $DisplayFunction]
```



```
g6 = Plot[-U0 eta[Y, X] Sinc[v]^2, {v, -6, 6}, PlotStyle ->
          {RGBColor[0.5, 0, 0.5], Thickness[0.01`]}, DisplayFunction -> $DisplayFunction]
```



```
g4 = Plot[U[v], {v, -6, 6}, PlotStyle -> {RGBColor[0.5, 0.5, 0], Thickness[0.01`]},
  DisplayFunction -> $DisplayFunction]
```



```
"Particle's density (gr/cm^3)"
```

```
sigs = 1.14;
```

```
"Medium's density (gr/cm^3)"
```

```
sig0 = 1;
```

```
"Gravity acceleration (m/s^2)"
```

```
g = 9.8;
```

```
r3
```

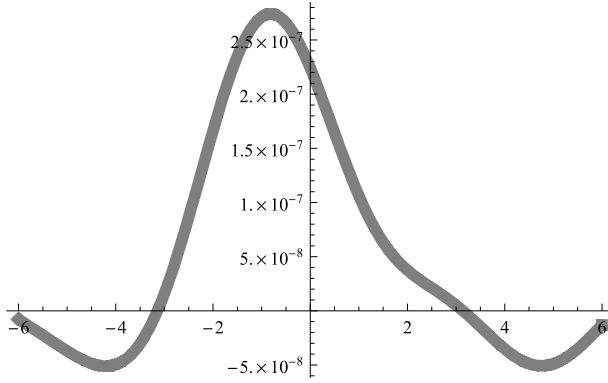
```
1.5625 × 10-17
```

```
"Particle's Weight"
```

$$W = \frac{4\pi}{3} * r^3 * (sigs - sig0) * g / 1000$$

```
8.97972 × 10-20
```

```
g8[v] = Plot[F[v] + W, {v, -6, 6},
  PlotStyle -> {RGBColor[0.5, 0.5, 0.5], Thickness[0.01`]}, PlotRange -> All]
```



"In the Rayleigh-Limit of small spheres ($A/\lambda \ll 1$) simple analytical expressions for the trapping parameter can be obtained:"

$$h = \frac{2}{3 \text{ beta}} \frac{m^2 - 1}{m^2 + 2} x^3;$$

$$f_0 = 6 \text{ beta}^3 \frac{n P}{c};$$

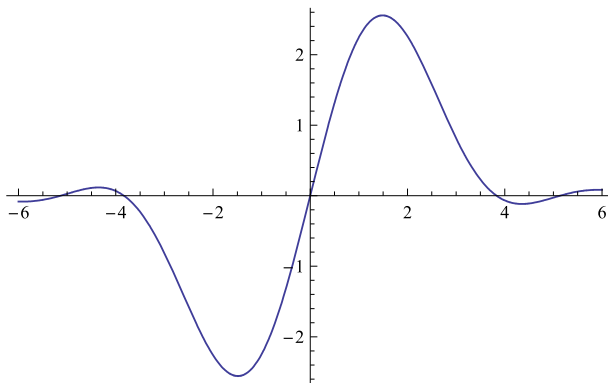
$$u_0 = 6 \text{ beta}^2 \frac{P}{\omega};$$

$$u[z_] = \frac{2 \pi z \text{ NA}}{\lambda};$$

$$A[u_] = 2 (\text{BesselJ}[1, u] / u);$$

$$Fi[u_] = -\frac{\text{NA}}{n \text{ beta}} \{D[A[u]^2, u]\};$$

```
Plot[Fi[z], {z, -6, 6}]
```



List of Figures

1.1	Molecular structure of a) PAA and b) MBBA	2
1.2	Liquid crystal transition	3
1.3	Liquid crystal in nematic phase	4
1.4	Liquid crystal in smectic phase	5
1.5	Liquid crystal in cholesteric phase	6
1.6	Microscope pictures of different textures for different LC phases	6
1.7	Nematic LC observed between polarizer and analyzer	8
1.8	Types of liquid crystals orientation near surface	10
1.9	Elastic distortions in liquid crystals	11
1.10	Examples of nematic liquid crystals confined to spherical droplets at increasing surfactant concentrations	12
1.11	Acceleration and trapping of particles by radiation pressure	14
1.12	Basic principle of optical tweezers in the geometric optics regime	16
1.13	Optical tweezers with a rays model	18
1.14	Basic principle of optical tweezers in the Rayleigh regime	20
1.15	Optical potential and force measurement	22
1.16	Optical tweezers diagram	24
1.17	Conjugated planes system	25
1.18	Particle trapped with optical tweezers	25
1.19	Basic principle of position control in optical tweezers	27
1.20	Transfer of angular momentum by light	29
2.1	Experimental setup	35
2.2	Representation of nematic droplets with radial and bipolar configuration	36
2.3	Liquid crystal droplets with radial and bipolar internal configurations under crossed polarizers	38
2.4	Scheme for Magnus force	40
2.5	Trajectory for anticlockwise spinning LC droplet with diameter $\sim 5 \mu m$ due to Magnus force	41
2.6	Displacement of spinning LC droplet due to Magnus force	42

2.7	Microscope sequence images for a non spinning LC droplet with radial configuration	43
2.8	Trajectory for a non spinning LC droplet with radial configuration	43
2.9	Polarization holography due to the interference of two beams at small angle	46
2.10	Polarization gradient with optical force and optical torque	47
2.11	Expected dynamics of an optically isotropic (radial) and optically anisotropic (bipolar) LC droplet by shifting the polarization pattern	49
2.12	Experimental setup with orthogonal polarizations s and p or R and L	50
2.13	Photographs of experimental setup:	51
2.14	Dynamics of an optically isotropic (radial) LC droplet by shifting the polarization pattern	52
2.15	Dynamics of an optically anisotropic (bipolar) LC droplet by shifting the polarization pattern	53
2.16	Magnus force as restoring force	54
3.1	Schematic representation of chirality	59
3.2	Bragg reflection and transmission by a film of left-handed CLC in a glass cell with planar texture	61
3.3	Transmission for left-handed CLC films	62
3.4	Schematic representation in 3D of the internal helix in CLC particles	63
3.5	Examples of chiral droplets at different dopant concentration	64
3.6	Evolution texture with pitch and size diameter	64
3.7	Solid chiral microspheres with $p \ll d$ (Short pitch)	67
3.8	Solid chiral microspheres with $p \ll d$ deposited on a glass substrate	68
3.9	Solid chiral microspheres with long-pitch ($p < d$)	69
3.10	TEM observation of a radial chiral microsphere	70
3.11	TEM observation of anisotropic chiral microsphere	71
3.12	SEM observation of the polymerized spheres	72
4.1	Selective reflection for CLC at 25%	76
4.2	Experimental setup	77
4.3	Radial isotropic CLC fluid droplets manipulation on circularly right and left polarization	78
4.4	Radial isotropic CLC (fluid) droplets and (solid) microspheres attraction-repulsion	79
4.5	Geometry for calculating the force	81
4.6	Geometrical parameters for ray model	83
4.7	Forces for right circular polarization	85
4.8	Forces for left circular polarization	87
4.9	Attraction and repulsion behavior on anisotropic CLC immersed in water . .	89

4.10	Strong reflection for left circularly polarized light	90
4.11	Representation with rays for optically anisotropic particles	91
4.12	Rotation of a fluid CLC droplet I	94
4.13	Rotation of a fluid CLC droplet II	95
4.14	Rotation of a fluid CLC droplet II	96
4.15	Rotation of a fluid CLC droplet III	98
4.16	Rotation of a fluid CLC droplet IV	99
4.17	Rotation of a solid CLC particle I	100
4.18	Rotation of a solid CLC particle II	101
4.19	Rotation of a solid CLC particle III	102
5.1	Types and characteristics of optical microresonators	107
5.2	Three basic types of spherical Bragg microcavities	109
5.3	Experimental setup for CLC lasers	111
5.4	LC laser emission parallel to the helix axis of the CLC in both forward and backward directions.	111
5.5	Experimental setup	113
5.6	Polymerized dye doped particles observed under crossed polarizers	113
5.7	Spectrum of the light emitted by the dye doped microspheres (Green emis- sion)	115
5.8	Spectrum of the light emitted by the dye doped microspheres (Red emission)	116
6.1	Advanced Materials Cover	121
A.1	Properties of Liquid Crystals	126

Bibliography

- [1] P.G. DE GENNES AND J. PROST. **The physics of liquid crystals.** *Oxford Science Publications*, 1995. 1, 3, 5, 8, 58, 59, 61, 80, 84
- [2] POCHI YEH AND CLAIRE GU. **Optics of liquid crystal displays.** *John Wiley & Sons*, 1999. 3, 5, 6, 58, 59, 60, 61, 80, 84, 86
- [3] CHRISTOPHER J. BARRETT. **Barret Research Group.** 2011. 3
- [4] K. WYNNE. **Ultrafast chemical physics group; University of Glasgow.** 2012. 6
- [5] B. SENYUK. **Liquid Crystals: a Simple View on a Complex Matter.** 2012. 9
- [6] C.W. OSEEN. **The theory of liquid crystals.** *Trans. Faraday Soc.* 29; 883, 1933. 10
- [7] F.C. FRANK. **On the theory of liquid crystals.** *Disc. Faraday Soc.* 25; 19, 1958. 10
- [8] M. HUMAR AND I. MUŠEVIČ. **Surfactant sensing based on whispering-gallery-mode lasing in liquid-crystal microdroplets.** *Opt. Express.*; 19; 21, 2011. 11
- [9] N.A. LOCKWOOD; J.K. GUPTA AND N.L. ABBOTT. **Self-assembly of amphiphiles, polymers and proteins at interfaces between thermotropic liquid crystals and aqueous phases.** *Surf. Sci. Rep.* 63, 255293, 2008. 11
- [10] G.E. VOLOVIK AND O.D. LAVRENTOVICH. **Topological dynamics of defects: boojums in nematic drops.** *Sov. Phys. JETP*, 58 (6), 1159-1166., 1983. 13
- [11] G.E. VOLOVIK. **Topological singularities on the surface of an ordered system.** *Sov. Phys. JETP*, 28, 59-62., 1978.
- [12] D.L. STEIN. **Topological theorem and its applications to condensed matter systems.** *Phys. Rev. A*; 19, 1708-1711, 1979. 13
- [13] J. MAXWELL. **A treatise on electricity and magnetism. vol 2.** *Clarendon Press, Oxford*, 1873. 13
- [14] P. LEVEDEV. **Untersuchungen ber die Druckkrfte des Lichtes.** *Ann Phys* 6:433, 1901. 13
- [15] E. NICHOLS AND G. HULL. **A preliminary communication on the pressure of heat and light radiation.** *Phys Rev (Series I)* 13:307320, 1901. 13
- [16] E. NICHOLS AND G. HULL. **The pressure due to radiation (second paper).** *PhysRev (Series I)* 17:2650, 1903. 13

- [17] A. ASHKIN. **Acceleration and trapping of particles by radiation pressure.** *Phys. Rev. Lett.* 24 (4), 156, 1970. [13](#), [14](#), [57](#)
- [18] R.J. HERNÁNDEZ. **Micromanipulación y separación de partículas utilizando haces de luz.** *B.Sc. Thesis, Universidad Veracruzana-UNAM, México*;, 2003. [14](#)
- [19] A. ASHKIN AND J.M. DZIEDZIC. **Optical levitation by radiation pressure.** *Appl. Phys. Lett.* 19: 283-285, 1971. [15](#)
- [20] A. ASHKIN AND J.M. DZIEDZIC. **Stability of optical levitation by radiation pressure.** *Appl. Phys. Lett.* 24(12): 586-588, 1974. [15](#)
- [21] A. ASHKIN; J.M. DZIEDZIC; J. BJORKHOLM AND S. CHU. **Observation of a single-beam gradient force optical trap for dielectric particles.** *Opt. Lett.* 11, 288-290, 1986. [15](#), [17](#), [19](#), [44](#)
- [22] S.M. BLOCK. **Optical tweezers: a new tool for biophysics.** *Non-invasive Techniques in Cell Biology. Modern Cell Biology Vol. 9: 375-401*, 1990.
- [23] A. ASHKIN. **Optical trapping and manipulation of neutral particles using lasers.** *Proc. Natl. Acad. Sci. U.S.A.* 94 (10): 4853-4860, 1997. [15](#)
- [24] A. ASHKIN AND J.M. DZIEDZIC. **Optical trapping and manipulation of viruses and bacteria.** *Science* 235 (4795): 1517-1520, 1987.
- [25] A. ASHKIN AND J.M. DZIEDZIC. **Optical trapping and manipulation of single cells using infrared-laser beams.** *Nature* 330(6150): 769-771, 1987. [15](#), [57](#)
- [26] A. ASHKIN. **Forces of a single-beam gradient laser trap on a dielectric sphere in the ray optics regime.** *Biophysical Journal* 61(2): 569-582, 1992. [16](#), [17](#), [19](#), [23](#), [80](#), [82](#)
- [27] H.C. V.D. HULST (ED.). **Light Scattering by Small Particles.** *Dover, New York*, 1981. [16](#)
- [28] J. GUCK; R. ANANTHAKRISHNAN; T.J. MOON; C.C. CUNNINGHAM AND J. KÄS. **Optical deformability of soft biological dielectrics.** *Phys. Rev. Lett.* 84:54515454, 2000. [17](#)
- [29] T. NIEMINEN; A. STILGOE; N. HECKENBERG AND H. RUBINSTEIN-DUNLOP. **Approximate and exact modeling of optical trapping.** *SPIE Proc* 7762:77622V, 2010. [17](#), [19](#)
- [30] A. STILGOE; T. NIEMINEN; G. KNONER; N. HECKENBERG AND H. RUBINSTEIN-DUNLOP. **The effect of Mie resonances on trapping in optical tweezers.** *Opt. Express*; 16, 15039-15051, 2008. [17](#)

- [31] T. NIEMINEN; V. LOKE; A. STILGOE; G. KNONER; A. BRANCZYK; N. HECKENBERG AND H. RUBINSTEIN-DUNLOP. **Optical tweezers computational toolbox.** *J. Opt. A: Pure Appl Opt* 9:S196-S203, 2007. [17](#), [21](#)
- [32] K. SVOBODA AND S.M. BLOCK. **Biological Applications Of Optical Forces.** *Annual Review Of Biophysics and Biomolecular Structure*; 23: 247-285, 1994. [19](#), [39](#)
- [33] K. VISSCHER AND G.J. BRAKENHOFF. **A theoretical study of optically induced forces on spherical particles in a single beam trap I: Rayleigh scatterers.** *Optik*, 89, 174-180, 1992. [19](#)
- [34] M. KERKER. **The scattering of light and other electromagnetic radiation.** *Academic, New York, Chapter 3*, 1969. [19](#)
- [35] Y. HARADA AND T. ASAKURA. **Radiation forces on a dielectric sphere in a Rayleigh scattering regime.** *Optics Communications*, 124, 529-541, 1995. [19](#)
- [36] J.D. JACKSON. **Classical Electrodynamics.** *J. Willey & Sons, New York*, 1999. [20](#), [23](#)
- [37] M. WORDEMANN. **Structured Light Fields (Applications in Optical Trapping, Manipulation and Organisation).** *Springer Theses; ISBN 978-3-642-29323-8 (Chapter2)*, 2012. [22](#)
- [38] S. STALLINGA. **Optical trapping at low numerical aperture.** *Journal of the European Optical Society - Rapid Publications* 6, 11027, 2011. [23](#), [127](#)
- [39] JAMES A. LOCK. **Calculation of the Radiation Trapping Force for Laser Tweezers by Use of Generalized Lorenz-Mie Teory. II. On-Axis Trapping Force.** *Applied Optics* 43: 2545-2554, 2004. [23](#), [127](#)
- [40] K.C. NEUMAN AND S.M. BLOCK. **Optical trapping.** *Review of Scientific Instruments* 75, 27872809, 2004. [23](#)
- [41] S.M. BLOCK. **Constructing optical tweezers.** *Cell Biology: A Laboratory Manual; Cold Spring Harbor, NY*, 1998.
- [42] S.P. SMITH; S.R. BHALOTRA; A.L. BRODY; B.L. BROWN; E.K. BOYDA AND M. PRENTISS. **Inexpensive optical tweezers for undergraduate laboratories.** *Am. J. Phys.* 67 (1), 2635, 1999.
- [43] E. FALLMAN AND O. AXNER. **Design for fully steerable dual-trap optical tweezers.** *Appl. Opt.* 36 (10), 21072113, 1997. [23](#)
- [44] K. SASAKI; M. KOSHIOKA; H. MISAWA; N. KITAMURA AND H. MASUHARA. **Pattern-formation and ow-control of fine particles by**

- laser-scanning micromanipulation. *Opt Lett* 16:14631465, 1991. [27](#)
- [45] H. MISAWA; K. SASAKI; M. KOSHIOKA; N. KITAMURA AND H. MASUHARA. **Multibeam laser manipulation and fixation of microparticles.** *Appl. Phys. Lett.* 60:310312, 1992.
- [46] K. VISSCHER; G. BRAKENHOFF AND J. KROL. **Micromanipulation by multiple optical traps created by a single fast scanning trap integrated with the bilateral confocal scanning laser microscope.** *Cytometry* 14:105114, 1993. [27](#)
- [47] C. MIO; T. GONG; A. TERRAY AND D. MARR. **Design of a scanning laser optical trap for multiparticle manipulation.** *Rev. Sci. Instrum.* 71:21962200, 2000.
- [48] U. MIRSAIDOV; J. SCRIMGEOUR; W. TIMP; K. BECK; M. MIR; P. MATSUDAIRA AND G. TIMP. **Live cell lithography: using optical tweezers to create synthetic tissue.** *Lab Chip* 8:21742181, 2008. [27](#)
- [49] E. DUFRESNE AND D. GRIER. **Optical tweezer arrays and optical substrates created with diffractive optics.** *Rev. Sci. Instrum.* 69:19741977, 1998. [27](#)
- [50] E. DUFRESNE; G. SPALDING; M. DEARING; S. SHEETS AND D. GRIER. **Computer-generated holographic optical tweezer arrays.** *Rev. Sci. Instrum.* 72:18101816, 2001. [27](#)
- [51] M. REICHERTER; T. HAIST; E. WAGEMANN AND H. TIZIANI. **Optical particle trapping with computer-generated holograms written on a liquid-crystal display.** *Opt. Lett.* 24:608610, 1999. [27](#)
- [52] J. LIESENER; M. REICHERTER; T. HAIST AND H. TIZIANI. **Multi-functional optical tweezers using computer-generated holograms.** *Opt. Commun.* 185:7782, 2000. [27](#)
- [53] R. BETH. **Mechanical detection and measurement of the angular momentum of light.** *Phys. Rev.* 50:115125, 1936. [27](#), [28](#)
- [54] L. ALLEN; M.W. BEIJERSBERGEN; R.J.C. SPREEUW AND J.P. WOERDMAN. **Orbital angular-momentum of light and the transformation of Laguerre-Gaussian laser modes.** *Phys. Rev. A* 45, 81858189, 1992. [27](#)
- [55] L. ALLEN; S.M. BARNETT AND M.J. PADGETT. **Optical Angular Momentum.** *Institute of Physics Publishing, Bristol*, 2003. [28](#), [34](#)
- [56] J. LEACH; M. PADGETT; S. BARNETT; S. FRANKE-ARNOLD AND J. COURTIAL. **Measuring the orbital angular momentum of a single photon.** *Phys. Rev. Lett.* 88:257901, 2002. [28](#)

- [57] H. HE; M. FRIESE; N. HECKENBERG AND H. RUBINSZTEIN-DUNLOP. **Direct observation of transfer of angular momentum to absorptive particles from a laser beam with a phase singularity.** *Phys. Rev. Lett.* 75:826829, 1995. [28](#)
- [58] M. BERRY. **Paraxial beams of spinning light.** In: *Soskin M (ed) International conference on singular optics, vol 3487. SPIE Proceedings pp 611*, 1998. [28](#)
- [59] S.M. BARNETT. **Optical angular momentum flux.** *J. Opt. B: Quantum Semiclass. Opt.*, 4, S7-S16, 2002. [28](#), [48](#), [53](#)
- [60] T. NIEMINEN; A. STILGOE; N. HECKENBERG AND H. RUBINSZTEIN-DUNLOP. **Angular momentum of a strongly focused gaussian beam.** *J. Opt. A: Pure Appl. Opt.* 10:115005, 2008. [28](#)
- [61] A.T. O'NEIL; I. MACVICAR; L. ALLEN AND M.J. PADGETT. **Intrinsic and extrinsic nature of the orbital angular momentum of a light beam.** *Phys. Rev. Lett.* 88:053601, 2002. [28](#)
- [62] M.E.J. FRIESE; T.A. NIEMINEN; N.R. HECKENBERG AND H. RUBINSZTEIN-DUNLOP. **Optical alignment and spinning of laser-trapped microscopic particles.** *Nature* 394, 348-350, 1998. [28](#), [44](#)
- [63] S. JUODKAZIS; S. MATSUO; N. MURAZAWA; I. HASEGAWA AND H. MISAWA. **Highefficiency optical transfer of torque to a nematic liquid crystal droplet.** *Appl. Phys. Lett.*, 82(26), 46574659, 2003. [28](#), [35](#), [48](#), [53](#)
- [64] G.K. BATCHELOR. **An Introduction to Fluid Mechanics.** Cambridge University Press; Cambridge, 1967. [31](#)
- [65] R. KUROSE AND S. KOMORI. **Drag and Lift Forces on a Rotating Sphere in a Linear Shear Flow.** *J. Flu. Mech.* 384, 183, 1999. [31](#)
- [66] P. BAGCHI AND S. BALACHANDAR. **Effect of free rotation on the motion of a solid sphere in linear shear flow at moderate Re.** *Physics of Fluid*, 14, 2719, 2002.
- [67] B. OERSTELÉ AND T. BUI DINH. **Experiments on the lift of a spinning sphere in a range of intermediate Reynolds number.** *Exp. Fluids* 25, 16-22, 1998.
- [68] E.S. ASMOLOV. **The inertial lift on a spherical particle in a plane Poiseuille flow at large channel Reynolds number.** *J. Fluid Mech.*; 381, 63, 1999. [31](#)
- [69] S.I. RUBINOV AND J.B. KELLER. **The transverse force on a spinning sphere moving in a viscous fluid.** *J. Flu. Mech.* 11, 447-459, 1961. [33](#), [44](#)

- [70] P.G. SAFFMAN. **The lift on a small sphere in a slow shear flow.** *J. Flu. Mech.* 22, 385, 1965. 31, 33
- [71] G. GALILEI. **Dialogues Concerning Two New Sciences (New York: Dover).** 1638. 31
- [72] G.G. STOKES. **On the effect of internal friction of fluids on the motion of pendulums.** *Trans. Camb. Phil. Soc.* 9; 8106, 1851. 31
- [73] I. NEWTON. **Philosophi Naturalis Principia Mathematica (lib.2 prop.33).** 1687. 31
- [74] B. ROBINS. **New Principles of Gunnery.** ed R Hutton (rst printed in 1742), 1805. 32
- [75] G. MAGNUS. **ber die Abweichung der Geschosse, und: ber eine abfallende Erscheinung bei rotirenden Krpern.** *Annalen der Physik;* 164(1) 1-29, 1853. 32
- [76] H.M. BARKLA AND L.J. AUCHTERLONNET. **The Magnus or Robins effect on rotating spheres.** *J. Fluid Mech.;* 47 (03); pp 437-447, 1971. 32
- [77] M. POLIN; D. GRIER AND S.R. QUAKE. **Anomalous Vibrational Dispersion in Holographically Trapped Colloidal Arrays.** *Phys. Rev. Lett.* 96, 088101, 2006. 32
- [78] B. LUKIĆ; S. JENEY; C. TISCHER; A.J. KULIK; L. FORRÓ AND E.-L. FLORIN. **Direct Observation of Nondiffusive Motion of a Brownian Particle.** *Phys. Rev. Lett.* 95, 160601, 2005.
- [79] J. LEACH; H. MUSHFIQUE; S. KEEN; R. DI LEONARDO; G. RUOCCO; J.M. COOPER AND M.J. PADGETT. **Comparison of Faxén’s correction for a microsphere translating or rotating near a surface.** *Phys. Rev. E* 79, 026301, 2009. 32
- [80] G. CIPPARRONE; R.J. HERNÁNDEZ; P. PAGLIUSI AND C. PROVENZANO. **Magnus force effect in optical manipulation.** *Phys. Rev. A* 84, 015802, 2011. 34, 44
- [81] D.G. GRIER. **A revolution in optical manipulation.** *Nature,* 424 (6950), 810816, 2003. 34
- [82] A.E CHIOU; W. WANG; G.J. SONEK; J. HONG AND M.W BERNIS. **Interferometric optical tweezers.** *Opt. Commun.* 133; 7-10, 1997. 34
- [83] N. MURAZAWA; S. JUODKAZIS AND H. MISAWA. **Characterization of bipolar and radial nematic liquid crystal droplets using laser-tweezers.** *Journal of Physics D: Applied Physics,* 38, 2923-2927, 2005. 35, 48, 75
- [84] G. CIPPARRONE; I. RICARDEZ-VARGAS; P. PAGLIUSI AND C. PROVENZANO. **Polarization gradient: exploring an**

- original route for optical trapping and manipulation. *Optics Express*, Vol. 18, No. 6, 608-613, 2010. [35](#), [37](#), [44](#), [45](#)
- [85] P.S. DRZAIC. **Liquid crystal dispersions**. World Scientific Publishing Co., 1995. [36](#), [37](#)
- [86] B.H. KIM AND D.R. WILLIAMS. **Nonlinear coupling of fluctuating drag and lift on cylinders undergoing forced oscillations**. *J. Fluid Mech.*; 559, 335-353, 2006. [44](#)
- [87] A. JONAS AND P. ZEMANEK. **Light at work: the use of optical forces for particles manipulation, sorting and analysis**. *Electrophoresis* 28, 4813, 2008. [44](#)
- [88] V. GARCÉS-CHÁVEZ; D. MCGLOIN; H. MELVILLE; W. SIBBETT AND K. DHOLAKIA. **Simultaneous micromanipulation in multiple planes using a self-reconstructing light beam**. *Nature* 419, 145-147, 2002.
- [89] Y. ROICHMAN; B. SUN; Y. ROICHMAN; J. AMATO-GRILL AND D. G. GRIER. **Optical forces arising from phase gradients**. *Phys. Rev. Lett.* 100, 013602, 2008. [44](#), [45](#)
- [90] L. NIKOLOVA AND T. TODOROV. **Diffraction efficiency and selectivity of polarization holographic recording**. *Optica Acta* 31, 579-588, 1984. [45](#)
- [91] S.G. CLOUTIER. **Polarization holography: orthogonal plane-polarized beam configuration with circular vectorial photoinduced anisotropy**. *J. Phys. D: Appl. Phys.* 38, 3371-3375, 2005. [45](#)
- [92] L.NIKOLOVA AND P.S. RAMANUJAM. **Polarization holography**. Cambridge University Press, 2009. [45](#)
- [93] K. DHOLAKIA AND T. ČIŽMÁR. **Shaping the future of manipulation**. *Nature photonics* 5, 335-342, 2011. [57](#)
- [94] M. PADGETT AND R. BOWMAN. **Tweezers with a twist**. *Nature photonics* 5, 343-348, 2011.
- [95] M. PADGETT AND R. DI LEONARDO. **Holographic optical tweezers and their relevance to lab on chip devices**. *Lab Chip* 11, 1196-1205, 2011.
- [96] A.T. O'NEIL AND M.J. PADGETT. **Three-dimensional optical confinement of micron-sized metal particles and the decoupling of the spin and orbital angular momentum within an optical spanner**. *Opt. Commun.*, 185, 139, 2000.
- [97] H. FURUKAWA AND I. YAMAGUCHI. **Optical trapping of metallic particles by a fixed Gaussian beam**. *Optics Letters* 23, 216- 218, 1998.

- [98] K. SASAKI; M. KOSHIOKA; H. MISAHA; N. KITAMURA AND H. MASUHARA. **Optical trapping of a metal particle and a water droplet by a scanning laser beam.** *Appl. Phys. Lett.*, 60, 807, 1992.
- [99] S. SATO; Y. HARADA AND Y. WASEDA. **Optical trapping of microscopic metal particles.** *Opt. Lett.*, 19, 1807, 1994.
- [100] K.M. HERBERT; W.J. GREENLEAF AND S.M. BLOCK. **Single molecule measurements of RNA polymerase: motoring along.** *Annu. Rev. Biochem.*, 77, 149176, 2008.
- [101] J.R. MOFFITT; Y.R. CHEMLA; S.B. SMITH AND C. BUSTAMANTE. **Recent advances in optical tweezers.** *Annu. Rev. Biochem.*, 77, 205228, 2008. 57
- [102] G.M. WHITESIDES. **The origin and the future of microfluidics.** *Nature* 442, 368-373, 2006. 57
- [103] N. BLOW. **Microfluidics: the great divide.** *Nature methods* 6, 683-686, 2009.
- [104] E. GERSTNER. **Microfluidics: solution for assembly.** *Nature physics*, 7, 98, 2011.
- [105] C. MONAT; P. DOMACHUK AND B.J. EGGLETON. **Integrated optofluidics: A new river of light.** *Nature Photonics* 1, 106, 2007.
- [106] D. PSALTIS; S.R. QUAKE AND C. YANG. **Developing optofluidic technology through the fusion of microfluidics and optics.** *Nature* 442, 381, 2006. 57
- [107] Y. CHEN; L. LEI; K. ZHANG; J. SHI; L. WANG; H. LI; X.M. ZHANG; Y. WANG AND H.L.W. CHAN. **Optofluidics microcavities: Dye lasers and biosensors.** *Biomicrofluidics* 4, 043002, 2010. 57, 105
- [108] A. FRANÇOIS AND M. HIMMELHAUS. **Optical biosensor based on whispering gallery mode excitations in clusters of microparticles.** *Applied Physics Letters* 92, 141107, 2008.
- [109] S. ARNOLD; R. RAMJIT; D. KENG; V. KOLCHENKO AND I. TERAOKA. **Microparticle photophysics illuminates viral bio-sensing.** *Faraday Discussion* 137, 65-83, 2008.
- [110] S. SORIA; S. BERNESCHI; M. BRONCI; F. COSI; G. NUNZI-CONTI; S. PELLI AND G.C. RIGHINI. **Optical Microspherical Resonators for Biomedical Sensing.** *Sensors* 11, 785-805, 2011.
- [111] I-H. LIN; D.S. MILLER; P.J. BERTICS; C.J. MURPHY; J.J. DE PABLO AND N.L. ABBOT. **Endotoxin-induced structural transformations in liquid crystalline droplets.** *Science* 332, 1297-1300, 2011. 57, 110

- [112] M. HUMAR; M. RAVNIK; S. PAJK AND I. MUSEVIC. **Electrically tunable liquid crystal optical microresonators.** *Nature photonics* 3, 595-600, 2009. [57](#), [106](#)
- [113] F. TREUSSART; N. DUBREUIL; J.C. KNIGHT; V. SANDOGHDAR; J. HARE; V. LEFCVRE-SEGUIN; J.-M. RAYMOND AND S. HAROCHE. **Microlasers based on silica microspheres.** *Ann. Telecommun.* 52, 557568, 1997.
- [114] M. HUMAR AND I. MUSEVIC. **3D microlasers from self assembled cholesteric liquid crystal microdroplets.** *Optics Express* 18, 26995-27003, 2010. [57](#), [105](#), [106](#), [110](#), [111](#)
- [115] F. ROMANO AND F. SCIORTINO. **Patchy from the bottom up.** *Nature Materials* 10, 171-173, 2011. [57](#)
- [116] Q. CHEN; S.C. BAE AND S. GRANICK. **Directed self-assembly of a colloidal kagome lattice.** *Nature* 469, 381-384, 2011.
- [117] S.C. GLOTZER AND M.J. SOLOMON. **Anisotropy of building blocks and their assembly into complex structures.** *Nature Materials* 8, 557-562, 2007.
- [118] G.M. WHITESIDES AND B. GRZYBOWSKI. **Self-Assembly at All Scales.** *Science* 295, 2418-2421, 2002. [57](#)
- [119] M.L. JUAN; M. RIGHINI AND R. QUIDANT. **Plasmon nano-optical tweezers.** *Nature Photonics*, 5, 349, 2011. [57](#)
- [120] H. SCHMIDT AND A.R. HAWKINS. **The photonic integration of non-solid media using optofluidics.** *Nature Photonics*, 5, 598, 2011.
- [121] X. FAN AND I.M. WHITE. **Optofluidic microsystems for chemical and biological analysis.** *Nature Photonics*, 5, 591-597, 2011.
- [122] D. ERICKSON; D. SINTON AND D. PSALTIS. **Optofluidics for energy applications.** *Nature Photonics*, 5, 583-590, 2011. [57](#)
- [123] H.S. KITZEROW. **Liquid Crystals in Complex Geometries**, edited by G.P. Crawford and S. Zumer. *Taylor & Francis, London*, 1996. [58](#)
- [124] M.V. KURIK AND O.D. LAVRENTOVICH. **Negative-positive monopole transitions in cholesteric liquid crystals.** *Pis'ma Zhurn. Eksp. Teor. Fiz.*, v. 35, 362-365 [*JETP Lett.*, v.35, p.444-447], 1982. [58](#)
- [125] G. CIPPARRONE; A. MAZZULLA; A. PANE; R.J. HERNÁNDEZ AND R. BARTOLINO. **Chiral Self-Assembled Solid Microspheres: A Novel Multifunctional Microphotonic Device.** *Adv. Mater.*, 2011, 23, 48, 5704., 2011. [58](#), [68](#), [69](#), [70](#), [114](#)

- [126] F. XU AND P.P. CROOKER. **Chiral nematic droplets with parallel surface anchoring.** *Physical Review E* 56, 6853-6860, 1997. 58, 59, 64, 65, 66, 106, 107, 108
- [127] J. BEZIC AND S. ZUMER. **Structures of the cholesteric liquid crystal droplets with parallel surface anchoring.** *Liq. Cryst.*; 11, 593, 1992. 58, 65
- [128] P.J. ACKERMAN; Z. QI AND I.I. SMALYUKH. **Optical generation of crystalline, quasicrystalline, and arbitrary arrays of torons in confined cholesteric liquid crystals for patterning of optical vortices in laser beams.** *Phys. Rev. E* 86, 021703, 2012.
- [129] D. SEC; T. PORENTA; M. RAVNIK AND S. ZUMER. **Geometrical frustration of chiral ordering in cholesteric droplets.** *Soft Matter*, 8, 11982, 2012. 58
- [130] L. ADDADI AND S. WEINER. **Crystals, asymmetry and life.** *Nature* 411, 753 - 755, 2001. 58
- [131] D. ZERROUKI; J. BAUDRY; D. PINE; P. CHAIKIN AND J. BIBETTE. **Chiral colloidal clusters.** *Nature* 455, 380-382, 2008.
- [132] MARCOS; H.C. FU; T.R. POWERS AND R. STOCKER. **Separation of Microscale Chiral Objects by Shear Flow.** *Physical Review Letters* 102, 158103, 2009.
- [133] J.B. PENDRY. **A Chiral Route to Negative Refraction.** *Science* 306, 1353-1355, 2004. 58
- [134] L. KELVIN. **Baltimore lectures on the molecular dynamics and the wave theory of light.** *C.J. Clay & Sons*, 1904. 58
- [135] L.D. BARRON. **Molecular light scattering and optical activity.** *Cambridge Univ. Press*, 2004. 58
- [136] N. BEROVA; K. NAKANISHI AND R.W. WOODY. **Circular Dichroism: Principles and Applications.** *Wiley-VCH, 2nd Edn*, 2000. 58
- [137] N. MICALI; ET AL. **Selection of supramolecular chirality by application of rotational and magnetic forces.** *Nature Chem.*4, 201-207, 2012. 58
- [138] E.C. HSU AND G. HOLZWARTH. **Vibrational circular dichroism observed in crystalline α -NiSO \cdot 6H O between 1900 and 5000 cm^{-1} .** *J. Chem. Phys.*; 59, 4678-4685, 1973. 58
- [139] M. KUMATA-GONOKAMI; ET AL. **Giant optical activity in quasi-two-dimensional planar nanostructures.** *Phys. Rev. Lett.*; 95, 227401, 2005. 58
- [140] E. HENDRY; ET AL. **Ultrasensitive detection and characterization of biomolecules using superchiral fields.** *Nature Nanotech*, 5, 783-787, 2010. 58

- [141] P.J. COLLINGS. **Liquid crystal nature's delicate phase of matter.** *Princeton University Press; Princeton, NJ*, 2002. [58](#), [59](#)
- [142] G. FRIEDEL. **The mesomorphic states of matter.** *Ann. Phys.*, *18*, 273474., 1922. [59](#)
- [143] G.P. CRAWFORD AND S. ZUMER. **Liquid crystals in complex geometries.** *Taylor and Francis, London*, 1996. [66](#), [69](#), [70](#)
- [144] O.D. LAVRENTOVICH. **Topological defects in dispersed words and worlds around liquid crystals, or liquid crystal drops.** *Liquid Crystals* *24*, 117-126, 2001. [66](#), [69](#)
- [145] Y. BOULIGNAD AND F. LIVOLANT. **The organization of cholestric spherulites.** *J. Physique* *45*, 1899-1923, 1984. [69](#), [70](#)
- [146] I.I. SMALYUKH; D.S. KAPUTA; A.V. KACHYNSKI; A.N. KUZMIN AND P.N. PRASAD. **Optical trapping of director structures and defects in liquid crystals using laser tweezers.** *Opt. Express*, *15*(7), 4359-4371, 2007. [75](#)
- [147] S. JUODKAZIS; M. SHIKATA; T. TAKAHASHI; S. MATSUO AND H. MISAWA. **Fast optical switching by a laser-manipulated microdroplet of liquid crystal.** *Appl. Phys. Lett.* *74*, 3627, 1999. [75](#)
- [148] K.P. VOLKE-SEPÚLVEDA. **Light beams with angular momentum and applications in optical tweezers.** *PhD. Thesis, INAOE, México*, 2003. [82](#), [83](#), [84](#)
- [149] R. GUSSGARD; T. LINDMO AND I. BREVIK. **Calculation of the trapping force in a strongly focused laser beam.** *J. Opt. Soc. Am. B*; *9*, 1922-1930, 1992. [82](#)
- [150] V. GARCÉS CHÁVEZ; K. VOLKE SEPÚLVEDA; S. CHÁVEZ CERDA; W. SIBBETT AND K. DHO-LAKIA. **Transfer of orbital angular momentum to an optically trapped low index particle.** *Phys. Rev. A* ; *66*, 063402, 2002. [83](#), [84](#)
- [151] M. CONRADI; M. ZORKO AND I. MUŠEVIČ. **Janus Nematic Colloids driven by light.** *Opt. Express*, *18*, 500, 2010. [88](#)
- [152] R.M. ERB; N.J. JENESS; R.L. CLARK AND B.B. YELLEN. **Towards Holonomic Control of Janus Particles in Optomagnetic Traps.** *Adv. Mater.*, *21*, 4825, 2009. [88](#)
- [153] K.J. VAHALA. **Optical microcavities.** *Nature* *424*, 839-846, 2003. [106](#), [108](#)
- [154] H. COLES AND S. MORRIS. **Liquid crystals lasers.** *Nature photonics* *4*, 676-685, 2010.

- [155] L.M. BLINOV AND R. BARTOLINO. **Liquid crystal micro-lasers.** *Trensworld Research Network, Kerala, India*, 2010.
- [156] MATJAŽ HUMAR. **Liquid-Crystal microdroplets as optical microresonators and lasers.** *PhD. Thesis; Jožef Stefan International Postgraduate School, Slovenia*, 2012. [106](#), [108](#), [109](#)
- [157] A. SHAW; B. ROYCROFT; J. HEGARTY; D. LABILLOY; H. BENISTY; C. WEISBUCH; T.F. KRAUSS; C.J.M. SMITH; R. STANLEY; R. HOUDRE AND U. OESTERLE. **Lasing properties of disk microcavity based on a circular Bragg rector.** *Appl. Phys. Lett.* *75*, 3051-3053, 1999. [106](#), [108](#)
- [158] J. SCHEUER; W.M.J. GREEN; G.A. DEROSE AND A. YARIV. **InGaAsP annular Bragg lasers: theory, applications and modal properties.** *IEEE J. Sel. Top. Quant.* *11*, 476-484, 2005.
- [159] J. SCHEUER; W.M.J. GREEN; G.A. DEROSE AND A. YARIV. **A. Low-threshold two-dimensional annular Bragg lasers.** *Opt. Lett.* *29*, 2641-2643, 2004. [108](#)
- [160] K.G SULLIVAN AND D.G. HALL. **Radiation in spherically symmetric structures, I. The coupled-amplitude equations for vector spherical waves.** *Phys. Rev. A* *50*, 2701-2707, 1994. [108](#)
- [161] D. BRADY; G. PAPAN AND J.E. SIPE. **Spherical distributed dielectric resonators.** *J. Opt. Soc. Am. B* *10*, 644-657, 1993.
- [162] G.N. BURLAK. **Optical radiation from coated microsphere with active core.** *Phys. Lett. A* *299*, 94101, 2002.
- [163] Y. XU; W. LIANG; A. YARIV; J.G. FLEMING AND S.-Y. LIN. **Modal analysis of Bragg onion resonators.** *Opt. Lett.* *29*, 424-426, 2004. [106](#), [108](#)
- [164] A. ASHKIN AND J.M. DZIEDZIC. **Observation of Resonances in the Radiation Pressure on Dielectric Spheres.** *Phys. Rev. Lett.* *38*, 1351-1354, 1977. [108](#)
- [165] LEV M. BLINOV. **Structures and properties of liquid crystals.** *Springer*, 2011. [108](#)
- [166] X. SUN AND A. YARIV. **Surface-emitting circular DFB, disk- and ring- Bragg resonator lasers with chirped gratings: a unified theory and comparative study.** *Opt. Express*; *16*, 9155-9164., 2008. [109](#)
- [167] L.S. GOLDBERG AND L.S. SCHNUR. *US Patent 3,771,065*, 1973. [110](#)

- [168] H.K.M. VITHANA V.I.KOPP; B. FAN AND A.Z. GENACK. **Low threshold lasing at the age of a photonic stop band in cholesteric liquid crystals.** *Opt. Lett.*; 23, 1707, 1998. [110](#)
- [169] E. YABLONOVITCH. **Inhibited spontaneous emission in solid-state physics and electronics.** *Phys. Rev. Lett.*; 58 , 2059-2062, 1987. [110](#)
- [170] S. JOHN. **Strong localization of photons in certain disordered dielectric superlattices.** *Phys. Rev. Lett.*; 58 , 2486, 1987. [110](#)
- [171] J.P. DOWLING; M. SCALORA; M.J. BLOEMER AND C.M. BOWDEN. **The photonic band edge laser: A new approach to gain enhancement.** *J. Appl. Phys.*; 75 , 1896, 1994. [110](#)
- [172] O. SVELTO. **Principles of Lasers.** 4th edition, Plenum Press, New York, 1998. [110](#)
- [173] J. SCHMIDTKE AND W. STILLE. **Fluorescence of a dye-doped cholesteric liquid crystal film in the region of the stop band: theory and experiment.** *Eur. Phys. J. B.*; 31 , 179-194, 2003. [110](#)
- [174] M.P. PILENI. **The role of soft colloidal templates in controlling the size and shape of inorganic nanocrystals.** *Nature materials* 2,145-150, 2003. [110](#)
- [175] A.D. FORD; S.M. MORRIS AND H.J. COLES. **Photonics and lasing in liquid crystals.** *Mater. Today*; 9, 36-42, 2006. [111](#)
- [176] P.J.W. HANDS; D.J. GARDINER; S.M. MORRIS; C. MOWATT; T.D. WILKINSON AND H.J. COLES. **Band-edge and random lasing in paintable liquid crystal emulsions.** *Appl. Phys. Lett.* 98, 141102, 2011. [111](#)
- [177] D.J. GARDINER; S.M. MORRIS; P.J.W. HANDS; C. MOWATT; R. RUTLEDGE; T.D. WILKINSON AND H.J. COLES. **Paintable band-edge liquid crystal lasers.** *Opt. Express* 19, 2432, 2011. [111](#)

Acknowledgements

I would like to express my gratitude to all who have contributed in my life to the accomplishment of this work. Especially, I would like to thank to **Prof. Gabriella Cipparrone**, a woman with brilliant ideas and a huge humankind, for the opportunity to work with her. For her guidance in the work, friendly attitudes, willingness and openness to discuss and accept arguments, for encouraging me to get over many troubles and for support me.

I am very grateful to all my colleagues who I had the pleasure to work with for the stimulating discussions as well as the experiences on these years. In particular, I would like to thank to Dr. Pasquale Pagliusi, for all his comments and suggestions to guide me always in the right direction. To Dr. Clementina Provenzano for all your help, your honest and correct comments and for providing a work environment of joy and unity. To Dr. Alfredo Mazzulla for his help in many of the experimental work and procedures, as well as for the treatment full of cordiality and friendship that always had with me. Also a very special acknowledgment to Eugenia Lepera and Dariia Lysenko for the time that we spent together in the laboratory and office, for sharing the knowledge and making my working days enjoyable. For both of you I wish you a successful PhD work.

I also express my thanks to Dr. Alfredo Pane for all his technical support and the help in the experimental part of my work. With a very special mention to Prof. Roberto Bartolino and Prof. Carlo Versace, for giving me the opportunity to study in Italy in the Bernardino Telesio Doctorate School of Science and Technique. As well for the treatment that always had with me.

To all of them and the people from the Dipartimento di Fisica UNICAL, which I not just consider them as colleagues but as my friends. Including all the people from several places in the world and the Italians that I have met, those who were like a family for me during the time that I spent out of my country.

I would like to thank Prof. Karen Volke that introduced me to the optical tweezers research work in first place and encouraged me to work in science. I will always need an infinite amount of words to thank you.

In a personal way thanks to all my friends in México and my family, for being always with me and for your support.

Each of the named persons and not mentioned, know the appreciation that I have for you as well as my total respect, the achieving of this goal is something that I alone would never achieve and all of you are part of it.

Finally, I express my gratitude to the institutions and persons who provided the financial support for the research project. A great part of the research work was partially supported by the Cooperation Project of Great Relevance, Italy-Mexico 2011 “Optical manipulation strategies in soft matter exploiting holographic tweezers with polarization gradient”, Italian Foreign Ministry.

Declaration

I herewith declare that I have produced this thesis without the prohibited assistance of third parties and without making use of aids other than those specified; notions taken over directly or indirectly from other sources have been identified as such. This thesis has not previously been presented in identical or similar form to any other Italian or foreign examination board.

The thesis work was conducted from 2010 to 2012 under the supervision of Prof. Gabriella Cipparrone at the Photonics Laboratory on Physics Department in University of Calabria.

Rende (Cosenza), Italy December 2012